Absorption Spectroscopy of Sodium through Magnetic Resonant Pulsing:
Notes

Adam Newton Wright

June 1, 2017

Abstract

This documents aim to provide all the resources and notes that I may need for my senior thesis. The first section is my Senior Proposal, as part of an ATEP project. I then include all of the resources that I have used thus far, along with notes for each resource.

Contents

1 Senior Proposal **11**
1.1 Abstract . . . 11
1.2 Statement of Problem and Significance of Research . . . 11
1.3 Plan of Procedure . . . 12

2 Resources **14**
2.1 Optical Magnetometry-Budker . . . 14
2.2 Improving LGS through polarization switching - Fan . . . 23
2.3 Improve Atmospheric Distortion Measurement - Fugate . . . 40
2.4 Kilohertz Picosecond Dye Laser - Gale . . . 44
2.5 Magnetic Resonant Pulsing-Kane . . . 51
2.6 Physics of Sodium LGS - Kibblewhite . . . 59
2.7 Optimization of Pulsed LGS - Rampy . . . 61
2.8 Optimization of CW LGS - Holzlohner (Rampy) . . . 71
2.9 Modular Reconfigurable Dye Laser of Undergrad Lab - AJP . . . 86
2.10 W.M. Keck Observatory AO System . . . 101
2.11 Continuously Tunable Picosecond Dye Laser . . . 130

3 Citations **133**
3.1 Brackman, LambdaChrome . . . 133
3.2 Budker, Optical Magnetometry . . . 133
3.3 Fan, Improving LGS through Polarization Switching . . . 133
3.4 Fugate, Measuring Wavefront Distortion . . . 133
3.5 Gale, Kilohertz Picosecond Dye Laser . . . 133
3.6 Kane, Pulsed Laser Architecture . . . 133
3.7 Kibblewhite, Physics of LGS . . . 133
3.8 Rampy, Toward Optimization of pulsed LGS . . . 133
3.9 Holzlohner, Optimization of CW LGS . . . 133
3.10 Sohl (AJP), Modular Reconfigurable Pulsed Dye Laser . . . 133
3.11 Watanable, Advancement in Adaptive Optics . . . 133
3.12 Wizinowich, W.M. Keck Observatory System . . . 134

SENIOR YEAR RESEARCH PROPOSAL

(Please confine responses to this form only. Use Arial 11 point font.)

Proposer's Name: Adam Newton Wright

Phone: 619.540.9598

Department: Physics

Email: anwright@willamette.edu

Institution Name: Willamette University

Institution Address:
900 State Street
Salem, OR, 97301

Proposed starting date and duration:
August, 2017: 7 months

EDUCATION AND EXPERIENCE: *(Style: "YYYY – Current Institution, Department, City, State, Position" or "YYYY – YYYY Institution, Department, City, State, Degree, Mentor.")*

2014 – 2017, Willamette University, Salem, Oregon, Physics, Michaela Kleinert

TITLE OF PROPOSAL: *(Must fit on two lines and may not exceed 130 characters.)*

Absorption Spectroscopy of Sodium through Magnetic Resonant Pulsing

ABSTRACT: *(Provide a summary of your proposal plan. Maximum 200 words.)*

The newest generation of ground-based telescopes use adaptive optics (AO) systems in which an artificial star is created in the upper atmosphere, emitting light that is emitted and received by the telescope system and used to correct for atmospheric distortion. In earth's mesosphere exists a layer of sodium atoms that is used by astronomers to create a laser guide star (LGS), an artificial star created by the excitation of atoms through laser light. Many LGS systems use optical pumping in order to increase the emission of sodium. However, when the angle between the geomagnetic field and the laser beam approaches ninety degrees, many of the benefits of optical pumping can be eliminated. It has thus been suggested that a laser pulsed at the Larmor frequency of the subject sodium atoms can produce greater emission, a process known as *magnetic resonant pulsed* (MRP) lasing. We propose testing the MRP lasing of sodium atoms under various angles between the laser beam and the magnetic field. By creating an artificial magnetic field, and taking absorption spectroscopy with a MRP dye laser, we seek to experimentally test MRP lasing.

SENIOR YEAR RESEARCH PROPOSAL

PUBLICATIONS AND PRESENTATIONS: *(List all publications, presentations, or conference you attended that are relevant to this proposal. Explain briefly why/how they are relevant.)*

Advanced Techniques in Experimental Physics, Senior Proposal Presentations, Department of Physics, Willamette University, 2017.

Oral presentation to the Department of Physics at Willamette University justifying the legitimacy of my proposed senior project.

Student Scholarship Recognition Day, Senior Theses Presentations, Willamette University, 2017.

Oral presentation detailing the construction, calibration, and applicability of a rhodamine dye laser. This is the same laser that will be used in this proposed project, and knowledge of it will be invaluable in the success of this project.

SENIOR YEAR RESEARCH PROPOSAL

PROPOSED BUDGET: *(All amounts in US dollars. Attach copies of screenshots that show the cost. Listed items should be clearly required for the proposed research. Two semester requests should be itemized per semester.)*

Description:	Fall semester:		Spring semester:	
	Physics Department:	Match (e.g. scholarships):	Physics Department:	Match (e.g. scholarships):
Potassium Titanyl Phosphate – KTP Crystal - *EKSMA Optics*	$88	N/A		
Rhodamine 610 (1 gram) - Sigma Aldrich	$134.50	N/A		
Borosilicate Glass Reference Cells - Thorlabs	$478	N/A		
Silicon Heater Tape (600 C) - Jet.com	$126.50	N/A		
Tenma Amp Bench - *Newark Electronics*	$180.40	N/A		
Magnetic Coil Wires - *Powerwerx*	$7.92	N/A		
Methanol (3.8 L) - *Carolina Biological*	$24.20	N/A		
TOTALS:	**$1,039.52**	**$0**		

Total budget: **$1,039.52**

Less matching funds from scholarships: **$0**

Requested from Physics Department: **$1,039.52**

ADDITIONAL SUPPORT: *(List all scholarships received or requested for this or other research.)*

N/A

BUDGET RATIONALE: *(Include the source of other items [equipment/supplies] that are needed for this research beyond those requested from The Physics Department. Explain travel related to research and other budget items that require further clarification. List any items from the above proposed budget for which a match is being provided and give dollar amount of the match.)*

The crystal is a second harmonic generation crystal, which doubles the frequency of the light and halves its wavelength, which is necessary in order to properly excite Rhodamine 610. This crystal is necessary since the Duetto laser we will be using outputs 1064 nm light whereas Rhodamine needs 532 nm for excitation.

Rhodamine 610 and methanol are needed in order to create a solution that, after excited by the pump laser, emits a wavelength of light resonant with sodium.

The Borosilicate Glass Reference Cell is needed in order to properly contain the Sodium under high temperatures. The glass has a low coefficient of thermal expansion, making it ideal since we will be heating Sodium to high temperatures. The sodium needs to be heated in order to transition it out of solid phase, which is the rationale behind the heater tape.

Lastly, the magnetic coil wires and power supply are needed in order to create an electromagnet for measuring the spectroscopy of sodium in various magnetic fields.

SENIOR YEAR RESEARCH PROPOSAL

STATEMENT OF THE PROBLEM AND SCIENTIFIC SIGNIFICANCE OF THE PROPOSED RESEARCH: *(Provide a summary of your proposed research project. State succinctly the fundamental scientific problem that is to be addressed. Clearly outline the significance of the problem, the originality of the approach, the impact it may have on the field if successful and the hypothesis or primary idea that underpins the proposed work. Use Arial 11 point font. Do not use more than one page.)*

Fundamental Scientific Problem

LGS are artificial star images created for usage in adaptive optics (AO) systems in order to increase the resolution of ground-based telescope imaging. Sodium LGSs are produced by sending laser into the upper atmosphere at the resonant frequency of sodium; this laser light excites a layer of sodium that exists in the mesosphere (Rampy 2015), and is then emitted by these sodium atoms, creating a visible "star." The light from this LGS is then collected by a ground telescope and fed into an AO system where it is used to correct for atmospheric distortions that occur as light enters earth's atmosphere (Fugate, Wizinowich 2009). The AO system corrects for these distortions by measuring the amount of distortion that the LGS light undergoes, and adjusts a deformable mirror to correct for these distortions. It can then use these corrections to collect higher resolution images.

LGSs needs to be sufficiently bright in order for the AO system to collect enough light to correct for distortions (Watanabe 2004). Typical LGS lasers operate at an intensity of $I = 10\ Wm^{-2}$ (Kane 2014) and can be CW or pulsed. The LGS lasers are circularly polarized, which allows the atom, after being excited and emitting a photon, to move to an angular momentum state with increased probability of backscattering; this creates a pumping cycle which in beneficial for greater emission, a process known as optical pumping (Fan, Kane 2014). The fundamental problem, however, is that the benefits of optical pumping can be almost completely eliminated when the angle between the laser light and the magnetic field approaches ninety degrees (Kane 2014); this is due to the fact that the magnetic field reorients the atom before it can properly redistribute its angular momentum.

Significance of the Problem

Unfortunately, the majority of ground-based telescopes are relatively close to the equator, which corresponds to an angle close to ninety degrees when the laser is sent into the atmosphere. This in turn results in decreased emission of sodium atoms in the atmosphere, and a decreased efficiency of the LGS system. In order for AO systems to properly correct for atmospheric distortions, and in turn create higher resolution images, the LGS used must be sufficiently bright. By finding a way to reduce the negative effects of optical pumping at angles of ninety degrees between pump beam and the magnetic field, AO systems can not only function better, but will be much more efficient.

Originality of Approach

It has been suggested that by pulsing the LGS laser at the Larmor frequency of the sodium atom in what is called MRP results in greater emission of sodium at all angles between the laser light and the magnetic field. Sodium has a magnetic moment, and thus, when within a magnetic field, will precess about its magnet moment, in a process called Larmor precession (Rampy 2015). The frequency at which it precesses is known as the Larmor frequency. Furthermore, the Larmor frequency is equal to the energy between the states split by the Zeeman structure; thus, the Larmor frequency corresponds to the inverse of the lifetime an electron is in an excited Zeeman state. Hence, by pumping sodium at this frequency, as soon as an atom has absorbed and emitted a photon, it is excited by another photon, allowing it to stay in its angular momentum state and continue its pump cycle.

Kane et al. used simulation software developed by Rochester Scientific to test MRP lasing. His data show that MRP lasing creates greater emission of sodium for all angles between the magnetic field and the laser light. I in turn propose testing this in the laboratory. By studying these processes in the laboratory, I intend to understand better how light interacts with atoms within a magnetic field and how their Larmor precession plays a role in their absorption and emission of light. Furthermore, understanding these ideas more clearly has direct implications to improving the efficiency and functionality of LGS systems.

To the best of our knowledge, this will be the first experimental testing of the MRP lasing of sodium. This is thus novel not only in regards to understanding how light pulses interact with atoms under the Zeeman structure, but also to creating a more efficient and functional LGS systems.

Hypothesis

In this project I aim to show that the magnetic resonant pulsing (MRP) of sodium within a magnetic field produces greater emission for all angles between the magnetic field and the laser beam than pulsing at a frequency not equal to the magnetic resonant frequency.

SENIOR YEAR RESEARCH PROPOSAL

PLAN OF PROCEDURE: *(Outline the experimental approach to the problem and its feasibility, providing details sufficient to support feasibility. Point out innovative features and relate them to previous work by including pertinent references. Indicate how this plan will contribute to the solution of the broad scientific problem being addressed. Preliminary results can buttress your case but are not required. Use Arial 11 point font. Do not use more than one page.)*

Month 1: We first need to test the feasibility of a MRP dye laser. The Larmor frequency of sodium is given by $w = -\gamma B$ where *B* is the magnetic field and γ is the gyromagnetic ration given by $\gamma = \frac{eg}{2m}$ with *e* being the electric charge, *g* being the g-factor, and *m* being the mass of the atom. For a sodium atom on earth, this corresponds to a frequency of $w = .281\ kHz$. During this first month, we will work on creating a tunable, pulsed dye laser (Sohl, 1997). This dye laser will consist of a dye cell filled will Rhodamine 610, which will enable the laser to emit light around the necessary 589.6 nm (Brackman 2000). Its cavity will consist of two mirrors and a diffraction grating, allowing us to select the corresponding wavelength of light.

Month 2: We need to configure our pump laser so that it will be able to pulse with the corresponding Larmor frequency and have a pulse width in the nanosecond regime; this can be accomplished by using a Duetto Nd:YAG laser. This laser is capable of pulsing on the order of kHz, sufficient for the sodium contained in our magnetic field. However, certain modification will need to be made to obtain this pulse frequency. Furthermore, the Duetto currently outputs 1064 nm laser light; 532 nm light is necessary in order to properly excite the Rhodamine dye and obtain the proper wavelength of light to excite sodium at its 589 nm peak line. We thus need to purchase and configure a second harmonic generation crystal on the Duetto in order to frequency double the light. A KTP crystal can be bought from EKSMA Optics and configured to the laser quite easily.

Month 3: We will next begin configuring our previously constructed dye laser with our MRP Duetto pump laser. The feasibility of this is described by Gale (Gale 1990), but we expect certain difficulties to arise. These difficulties may include the dye not being circulated quick enough, poor beam profile, or poor lasing (Gale 2012).

Month 4: If the previous projects are successful, we will continue with this project and construct a more advanced configuration. We will first use a dye laser capable of producing a cleaner and amplified beam. The dye laser is a Continuum ND6K, with dual amplification cells. This dye laser can be configured and tuned according to the Continuum ND6K User Manual (Continuum). It will also need to be made compatible with the MRP Duetto laser, an aspect which has not been tested on this dye system before.

Month 5: The dye laser output beam will need to be characterized with respect to wavelength, linewidth, and bandwidth in order to ensure it can properly excite sodium. It will also need to be able to produce an intensity of $I = 10\ Wm^{-2}$. Furthermore, the dye laser output beam will need to be circularly polarized (Kane 2012), which requires nothing more than a few quarter wave plates.

Month 6: Once the dye laser is properly established, the sodium reference cell and measurement system will need to be constructed. The reference cell will be a borosilicate glass reference cells available from Thorlabs. This ensures that maximum green light is transmitted, about 80%, and that the cell can withstand a temperature of 100 C, necessary to melt sodium. This cell will be mounted and wrapped in heating tape and filled with a small amount of Sodium. Lastly, a photodiode will be placed perpendicular to the length of the reference cell in order to collect transmitted light. We also will create a magnetic field around the reference cell. This can be done by created Helmholtz coils. We expect to create a magnetic field of $B = 10\ gauss$, which corresponds to a current of approximately $I = 2.1\ A$. We are able to 3D print a coil mount, and wrap this mount in wire and wire it to a power supply, which will need to be bought. The Helmholtz coils will need to be able to rotate around the reference cell, changing the angle between the magnetic field and the laser light.

Month 7: Data will finally be collected The laser light from the dye cell will be directed into the reference frame containing the sodium. The tunability of the dye laser is important, as we will measure the intensity of the light transmitted as a function of varying wavelength. At wavelengths close to 589 nm, the intensity of light should greatly decrease as sodium in absorbing this light and releasing it randomly. We then leave the dye laser at this wavelength and measure the intensity of transmitted light as the angle between the magnetic field and the dye beam is varied. We will then change the Duetto so that its pulse frequency is not at the Larmor frequency and repeat this process.

SENIOR YEAR RESEARCH PROPOSAL

LIST OF REFERENCES: *(Annotate the proposal with a list of at least ten peer-reviewed references from the primary literature. Use only one page for your references; size Arial 10 or 11 point font.* ***Include all authors and titles.****)*

Brackman, Ulrick, “Lambdachrome Laser Dyes,” Lambda Physik 3, 2000

Budker, Dmitry, and Romalis, Michael. “Optical Magnetometry.” Nature Physics 3, 2007.

Fan, Tingwei, Tianhua Zhou, and Yan Feng. "Improving sodium laser guide star brightness by polarization switching." Scientific reports 6 (2016).

Fugate, Robert Q., and D. L. Fried. "Measurement of atmospheric wavefront distortion using scattered light from a laser guide-star." Nature 353.6340 (1991): 144.

Gale, G. M., B. Pedersen, and P. Schanne. "Kilohertz picosecond distributed-feedback dye laser system." Optics Communications 76.2 (1990): 138-142.

Kane, Thomas J., Paul D. Hillman, and Craig A. Denman. "Pulsed laser architecture for enhancing backscatter from sodium." SPIE Astronomical Telescopes+ Instrumentation. International Society for Optics and Photonics, 2014.

Kibblewhite, Edward. "The physics of the sodium laser guide star: Predicting and enhancing the photon returns." In Advanced Maui Optical and Space Surveilance Technologies Conference. 2009.

Rampy, Rachel, Donald Gavel, Simon M. Rochester, and Ronald Holzlöhner. "Toward optimization of pulsed sodium laser guide stars." *JOSA B* 32, no. 12 (2015): 2425-2434.

Sohl, John E., and Stephen G. Payton. "A modular, reconfigurable-cavity, pulsed dye laser for the advanced undergraduate laboratory." American Journal of Physics 65.7 (1997): 640-652.

Watanabe, Makoto, et al. "Proceedings of SPIE-The International Society for Optical Engineering." Advancements in Adaptive Optics. 2004.

Wizinowich, Peter L., David Le Mignant, Antonin H. Bouchez, Randy D. Campbell, Jason CY Chin, Adam R. Contos, Marcos A. van Dam et al. "The WM Keck Observatory laser guide star adaptive optics system: overview." *Publications of the Astronomical Society of the Pacific* 118, no. 840 (2006): 297.

SENIOR YEAR RESEARCH PROPOSAL

LIST OF REVIEWERS: *(The reviewer list should include at least two "outsiders," individuals with whom you have had no substantive contact but who are experts in your area of research, and at least two "insiders," preferably former mentors. The best outside reviewers are frequently corresponding authors from the cited references who are not known to you. Do not hesitate to use a combination of reviewers from academia and non-academic laboratories; including scientists from abroad. Please include complete names (initials are not enough), current titles, mailing addresses, phone and fax numbers, and email addresses. Use size Arial 10 or 11 point font.* ***You must note briefly the nature and extent of your interactions, if any, with each of the outside reviewers. Examples: Met at a meeting, interviewed with, no interaction, never met, etc. Do not use more than one page.****)*

A. Insiders:

Michaela Kleinert
Associate Professor of Physics
Collins Science Center 314
900 State Street
Salem, Oregon 97301
503-370-6338
mkleiner@willamette.edu

Rick Watkins
Professor of Physics; Department Chair
Collins Science Center 310
900 State Street
Salem, Oregon 97301
503-370-6373
rwatkins@willamette.edu

B. Outsiders:

Thomas J. Kane
tom@fasortronics.com
(505) 225-3733
Never met

Edward Kibblewhite
Professor of Astronomy and Astrophysics; University of Chicago
(773) 702-8208
edkoddjob.uchicago.edu
Never met

SENIOR YEAR RESEARCH PROPOSAL

ENDORSEMENT PAGE:

Conditions of Senior Year Research Experience Award:

The award is a contribution to the scientific and academic program of the institution and is to be used for support of work described in the application prepared by the principal investigator (you) and adopted by the institution (Willamette).

Since research by its very nature is unpredictable and may require adaptations in order to exploit promising leads, the principal investigator should feel free to make changes in the emphasis or direction of the work as it progresses. If major changes are contemplated, prior approval should be obtained.

Reallocation of awarded funds between budget categories requires prior approval.

A final polished thesis is due before the end of the spring of the principal investigator's senior year. A polished introductory section of said thesis is due by the end of the fall semester of the previous year. The Principal Investigator must also agree to present their research at least twice during their senior year to peers and faculty of Willamette and Linfield. Failure to provide a satisfactory preliminary thesis on time may result in suspension of the award and a request to return unspent funds.

The principal investigator is urged to publish the findings in the appropriate scientific journals.

Applicant Name: Adam Newton Wright

Project Title: Absorption Spectroscopy of Sodium through Magnetic Resonant Pulsing

Submitted by (institution): Willamette University

Name of institution adopting and assuming responsibility for the above project, believing the principal investigator is qualified to conduct the project, and accepting the Conditions of Award, if an award is approved.

Name and position of authorized financial officer: Michaela Kleinert, Associate Professor of Physics, Willamette University

Signature of financial officer: _____ Date: _____

Signature of Principal Investigator: _____ Date: _____

1 Senior Proposal

1.1 Abstract

The newest generation of ground-based telescopes use adaptive optics (AO) systems in which an artificial star is created in the upper atmosphere, emitting light that is emitted and received by the telescope system and used to correct for atmospheric distortion. In earths mesosphere exists a layer of sodium atoms that is used by astronomers to create a laser guide star (LGS), an artificial star created by the excitation of atoms through laser light. Many LGS systems use optical pumping in order to increase the emission of sodium. However, when the angle between the geomagnetic field and the laser beam approaches ninety degrees, many of the benefits of optical pumping can be eliminated. It has thus been suggested that a laser pulsed at the Larmor frequency of the subject sodium atoms can produce greater emission, a process known as magnetic resonant pulsed (MRP) lasing. We propose testing the MRP lasing of sodium atoms under various angles between the laser beam and the magnetic field. By creating an artificial magnetic field, and taking absorption spectroscopy with a MRP dye laser, we seek to experimentally test MRP lasing.

1.2 Statement of Problem and Significance of Research

Fundamental Scientific Problem

LGS are artificial star images created for usage in adaptive optics (AO) systems in order to increase the resolution of ground-based telescope imaging. Sodium LGSs are produced by sending laser into the upper atmosphere at the resonant frequency of sodium; this laser light excites a layer of sodium that exists in the mesosphere (Rampy 2015), and is then emitted by these sodium atoms, creating a visible star. The light from this LGS is then collected by a ground telescope and fed into an AO system where it is used to correct for atmospheric distortions that occur as light enters earths atmosphere (Fugate, Wizinowich 2009). The AO system corrects for these distortions by measuring the amount of distortion that the LGS light undergoes, and adjusts a deformable mirror to correct for these distortions. It can then use these corrections to collect higher resolution images.

LGSs needs to be sufficiently bright in order for the AO system to collect enough light to correct for distortions (Watanabe 2004). Typical LGS lasers operate at an intensity of (Kane 2014) and can be CW or pulsed. The LGS lasers are circularly polarized, which allows the atom, after being excited and emitting a photon, to move to an angular momentum state with increased probability of backscattering; this creates a pumping cycle which in beneficial for greater emission, a process known as optical pumping (Fan, Kane 2014). The fundamental problem, however, is that the benefits of optical pumping can be almost completely eliminated when the angle between the laser light and the magnetic field approaches ninety degrees (Kane 2014); this is due to the fact that the magnetic field reorients the atom before it can properly redistribute its angular momentum.

Significance of the Problem

Unfortunately, the majority of ground-based telescopes are relatively close to the equator, which corresponds to an angle close to ninety degrees when the laser is sent into the atmosphere. This in turn results in decreased emission of sodium atoms in the atmosphere, and a decreased efficiency of the LGS system. In order for AO systems to properly correct for atmospheric distortions, and in turn create higher resolution images, the LGS used must be sufficiently bright. By finding a way to reduce the negative effects of optical pumping at angles of ninety degrees between pump beam and the magnetic field, AO systems can not only function better, but will be much more efficient.

Originality of Approach

It has been suggested that by pulsing the LGS laser at the Larmor frequency of the sodium atom in what is called MRP results in greater emission of sodium at all angles between the laser light and the magnetic field. Sodium has a magnetic moment, and thus, when within a magnetic field, will precess about its magnet moment, in a process called Larmor precession (Rampy 2015). The frequency at which it precesses is known as the Larmor frequency. Furthermore, the Larmor frequency is equal to the energy between the states split by the Zeeman structure; thus, the Larmor frequency corresponds to the inverse of the lifetime an electron is in an excited Zeeman state. Hence, by pumping sodium at this frequency, as soon as an atom has absorbed and emitted a photon, it is excited by another photon, allowing it to stay in its angular momentum state and continue its pump cycle.

Kane et al. used simulation software developed by Rochester Scientific to test MRP lasing. His data show that MRP lasing creates greater emission of sodium for all angles between the magnetic field and the laser light. I in turn propose testing this in the laboratory. By studying these processes in the laboratory, I intend to understand better how light interacts with atoms within a magnetic field and how their Larmor precession plays a role in their absorption and emission of light. Furthermore, understanding these ideas more clearly has direct implications to improving the efficiency and functionality of LGS systems.
To the best of our knowledge, this will be the first experimental testing of the MRP lasing of sodium. This is thus novel not only in regards to understanding how light pulses interact with atoms under the Zeeman structure, but also to creating a more efficient and functional LGS systems.
Hypothesis In this project I aim to show that the magnetic resonant pulsing (MRP) of sodium within a magnetic field produces greater emission for all angles between the magnetic field and the laser beam than pulsing at a frequency not equal to the magnetic resonant frequency.

1.3 Plan of Procedure

Month 1: We first need to test the feasibility of a MRP dye laser. The Larmor frequency of sodium is given by where B is the magnetic field and is the gyromagnetic ration given by with e being the electric charge, g being the g-factor, and m being the mass of the atom. For a sodium atom on earth, this corresponds to a frequency of . During this first month, we will work on creating a tunable, pulsed dye laser (Sohl, 1997). This dye laser will consist of a dye cell filled will Rhodamine 610, which will enable the laser to emit light around the necessary 589.6 nm (Brackman 2000). Its cavity will consist of two mirrors and a diffraction grating, allowing us to select the corresponding wavelength of light.
Month 2: We need to configure our pump laser so that it will be able to pulse with the corresponding Larmor frequency and have a pulse width in the nanosecond regime; this can be accomplished by using a Duetto Nd:YAG laser. This laser is capable of pulsing on the order of kHz, sufficient for the sodium contained in our magnetic field. However, certain modification will need to be made to obtain this pulse frequency. Furthermore, the Duetto currently outputs 1064 nm laser light; 532 nm light is necessary in order to properly excite the Rhodamine dye and obtain the proper wavelength of light to excite sodium at its 589 nm peak line. We thus need to purchase and configure a second harmonic generation crystal on the Duetto in order to frequency double the light. A KTP crystal can be bought from EKSMA Optics and configured to the laser quite easily.
Month 3: We will next begin configuring our previously constructed dye laser with our MRP Duetto pump laser. The feasibility of this is described by Gale (Gale 1990), but we expect certain difficulties to arise. These difficulties may include the dye not being circulated quick enough, poor beam profile, or poor lasing (Gale 2012).
Month 4: If the previous projects are successful, we will continue with this project and construct a more advanced configuration. We will first use a dye laser capable of producing a cleaner and amplified beam. The dye laser is a Continuum ND6K, with dual amplification cells. This dye laser can be configured and tuned according to the Continuum ND6K User Manual (Continuum). It will also need to be made compatible with the MRP Duetto laser, an aspect which has not been tested on this dye system before.
Month 5: The dye laser output beam will need to be characterized with respect to wavelength, linewidth, and bandwidth in order to ensure it can properly excite sodium. It will also need to be able to produce an intensity of . Furthermore, the dye laser output beam will need to be circularly polarized (Kane 2012), which requires nothing more than a few quarter wave plates.

Month 6: Once the dye laser is properly established, the sodium reference cell and measurement system will need to be constructed. The reference cell will be a borosilicate glass reference cells available from Thorlabs. This ensures that maximum green light is transmitted, about 80%, and that the cell can withstand a temperature of 100 C, necessary to melt sodium. This cell will be mounted and wrapped in heating tape and filled with a small amount of Sodium. Lastly, a photodiode will be placed perpendicular to the length of the reference cell in order to collect transmitted light. We also will create a magnetic field around the reference cell. This can be done by created Helmholtz coils. We expect to create a magnetic field of , which corresponds to a current of approximately . We are able to 3D print a coil mount, and wrap this mount in

wire and wire it to a power supply, which will need to be bought. The Helmholtz coils will need to be able to rotate around the reference cell, changing the angle between the magnetic field and the laser light. Month 7: Data will finally be collected The laser light from the dye cell will be directed into the reference frame containing the sodium. The tunability of the dye laser is important, as we will measure the intensity of the light transmitted as a function of varying wavelength. At wavelengths close to 589 nm, the intensity of light should greatly decrease as sodium in absorbing this light and releasing it randomly. We then leave the dye laser at this wavelength and measure the intensity of transmitted light as the angle between the magnetic field and the dye beam is varied. We will then change the Duetto so that its pulse frequency is not at the Larmor frequency and repeat this process.

2 Resources

2.1 Optical Magnetometry-Budker

This paper details optical magnetometry. This related to the the absorbtion spectroscopy of sodium, which will be done later in the project.

Optical magnetometry

Some of the most sensitive methods of measuring magnetic fields use interactions of resonant light with atomic vapour. Recent developments in this vibrant field have led to improvements in sensitivity and other characteristics of atomic magnetometers, benefiting their traditional applications for measurements of geomagnetic anomalies and magnetic fields in space, and opening many new areas previously accessible only to magnetometers based on superconducting quantum interference devices. We review basic principles of modern optical magnetometers, discuss fundamental limitations on their performance, and describe recently explored applications for dynamical measurements of biomagnetic fields, detecting signals in NMR and MRI, inertial rotation sensing, magnetic microscopy with cold atoms, and tests of fundamental symmetries of nature.

DMITRY BUDKER[1,2] AND MICHAEL ROMALIS[3]

[1]Department of Physics, University of California, Berkeley, California 94720-7300, USA

[2]Nuclear Science Division, Lawrence Berkeley National Laboratory, Berkeley California 94720, USA

[3]Department of Physics, Princeton University, Princeton, New Jersey 08544, USA

e-mail: budker@berkeley.edu; romalis@princeton.edu

It has been nearly half a century since optical pumping techniques pioneered by Kastler[1], Dehmelt[2], and Bell and Bloom[3,4] have been applied to sensitive measurements of magnetic fields[5,6]. The general idea of the method is that light that is near-resonant with an optical transition creates long-lived orientation and/or higher-order moments in the atomic ground state, which subsequently undergo Larmor spin precession in the magnetic field. This precession modifies the optical absorptive and dispersive properties of the atoms, and this modification is detected by measuring the light transmitted through the atomic medium. Recent reviews of resonant magneto-optics have been given in refs 7,8.

The fields of resonant magneto-optics and atomic magnetometry have been experiencing a new boom driven by technological developments, specifically by the advent of reliable, small, inexpensive, and easily tunable diode lasers, and by the refinement of the techniques of producing dense atomic vapours with long (in some cases ~1 s) ground-state relaxation times. These advances have enabled atomic magnetometers to achieve sensitivities rivaling[9–11] and even surpassing[12] that of most superconducting quantum interference device (SQUID)-based magnetometers that have been leading the field of ultrasensitive magnetic field measurements for a number of years[13]. As a result, optical magnetometers are starting to explore some of the applications that have previously been in the exclusive domain of SQUID magnetometers. Atomic magnetometers have the intrinsic advantage of not requiring cryogenic cooling, and offer a significant potential for miniaturization. In contrast to SQUIDs, which measure magnetic flux through a pick-up loop, atomic magnetometers measure magnetic field directly and can be used to detect other spin interactions. They can be configured so that their output is directly related to the absolute magnitude of the magnetic field through fundamental physical constants, so that no calibration is required. In contrast, SQUID magnetometers are relative field sensors that can also be configured for direct measurement of magnetic field gradients.

Currently, the most sensitive atomic optical magnetometer is the spin-exchange relaxation-free (SERF) magnetometer, whose demonstrated sensitivity exceeds 10^{-15} T Hz$^{-1/2}$, with projected fundamental limits below 10^{-17} T Hz$^{-1/2}$ (ref. 12). SERF magnetometers also offer a possibility of spatially resolved measurements with millimetre resolution.

The present-day interest in optical magnetometers is driven by numerous and diverse applications, a partial list of which includes tests of the fundamental symmetries of nature, search for man-made and natural magnetic anomalies, investigation of the dynamics of the geomagnetic fields (including attempts at earthquake prediction), investigation of the magnetic properties of rocks, detection of magnetic microparticles at ultralow concentrations, detection of signals in NMR and MRI, direct detection of magnetic fields from the heart and the brain, magnetic microscopy, and measuring magnetic fields in space.

In this review we describe the basic principles and fundamental limits of the sensitivity of optical atomic magnetometers, and discuss several specific applications.

GENERAL FEATURES AND LIMITS OF SENSITIVITY

A general schematic of an optical atomic magnetometer is shown in Fig. 1. In many magnetometers, the resonant medium is a vapour of alkali atoms (Rb, Cs or K) contained in a glass bulb. Because atomic polarization is generally destroyed when atoms collide with the walls of the bulb, cells filled with buffer gas are commonly used. The gas ensures that the atoms optically polarized in the central part of the cell take a long time to diffuse to the walls. Another technique for reducing wall relaxation is application of a non-relaxing coating, typically paraffin, on the cell walls (see below). As mentioned above, the light sources of choice today are diode lasers, however, discharge lamps, the original light sources for atomic magnetometers, are still used in most commercial ones, and can achieve sensitivity comparable to lasers in some research applications[14]. Figure 1 shows separate light

©2007 Nature Publishing Group

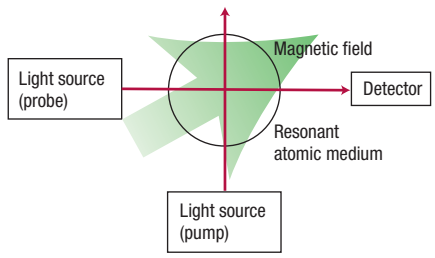

Figure 1 A general schematic of an all-optical atomic magnetometer. Pump light polarizes the atoms, atomic polarization evolves in the magnetic field, and the resultant state of the atoms' polarization is detected by measuring transmission or polarization rotation of the probe light.

sources for pumping and probing with orthogonal light beams. Many magnetometer configurations exist that differ by relative direction and spectral tuning of the pump and probe light. In some schemes, pumping and probing is performed by the same beam. The two most common detection modes are those of monitoring the intensity or polarization of the transmitted probe light. The polarization method has certain intrinsic advantages, such as its ability to detect very small polarization-rotation angles, and a reduced sensitivity to the laser-intensity noise. Shown in Fig. 1 is an all-optical magnetometer; no other electromagnetic fields are applied to the atoms apart from the magnetic field being measured and the pump and probe light. Some magnetometers require additional means for excitation of spin precession. A weak magnetic field oscillating at the Larmor frequency is commonly used for this purpose[3,11]. Other techniques include application of microwave fields[15] and all-optical excitation using various types of modulation of the light beams: intensity, frequency or polarization[4,8].

Quantum mechanics sets fundamental limits on the best sensitivity that can be achieved in a magnetic-field measurement using atoms. One such limit is associated with projection noise resulting from the fact that if an atom is polarized in a particular direction, a measurement of the angular-momentum projection m on an orthogonal direction yields a random result (+1/2 or −1/2 in the simplest case of angular momentum $F = 1/2$). Ignoring factors of order unity that depend on particulars of the system (for example, the total value of the angular momentum F, and the relative contributions of different Zeeman sublevels), the sensitivity of a magnetic-field measurement performed for a time T with an ensemble of N atoms with coherence time τ is

$$\delta B \simeq \frac{1}{g\mu_B}\frac{\hbar}{\sqrt{N\tau T}}, \qquad (1)$$

where μ_B is the Bohr magneton, g is the ground-state Landé factor, and $\hbar$ is Planck's constant. Equation (1) is derived by using the observation that a measurement with a single atom with a duration of τ produces an uncertainty in the Larmor precession angle of the order of 1 rad. With N atoms, this is improved by $\sqrt{N}$, and repeating the measurement multiple times gains another factor of $\sqrt{T/\tau}$.

Recently, a possibility of overcoming the projection noise in magnetometry using the techniques of spin-squeezing was discussed and demonstrated (see ref. 16). Here, quantum states are prepared with unequal distribution of uncertainty between conjugate observables, in this case, the projections of the angular momentum on two orthogonal directions. Unfortunately, an improvement in sensitivity using spin squeezing seems to be possible only on a timescale significantly shorter than the spin-relaxation time[17].

In optical magnetometry, in addition to the atomic projection noise, there is also photon shot noise. For example, if the measured quantity is the rotation angle φ of the light polarization, the shot noise is

$$\delta\varphi_s \simeq \frac{1}{2\sqrt{\dot{N}_{ph}T}}. \qquad (2)$$

Here, $\dot{N}_{ph}$ is the probe-photon flux (in photons per second) behind the atomic sample. Depending on the details of a particular measurement, either the spin noise (equation (1)) or the photon noise (equation (2)) may dominate. However, if a measurement is optimized for statistical sensitivity, the two contributions to the noise are generally found to be comparable[10,18]. Another potential source of noise in atomic magnetometers is the a.c. Stark shift caused by the probe and/or pump laser, which generates a fictitious magnetic field proportional to the degree of circular polarization of the light[19]. Even in the absence of technical sources of intensity or polarization fluctuations, quantum fluctuations generate noise of the fictitious magnetic field[20]. However, the noise due to a.c. Stark shifts can, in principle, be eliminated by choosing a laser frequency where it crosses zero[21], or a geometry where the fictitious field is orthogonal to the measured magnetic field. Nevertheless, in practical implementations of magnetometers, light shifts due to drifts of laser properties are often a significant concern.

The ultimate sensitivity of atomic magnetometers is given by the product of three quantities in equation (1), the magnetic moment of the atoms ($g\mu_B$), the square root of the number of atoms involved in the measurement, and the square root of the spin-relaxation time. Consequently, to improve the sensitivity of a magnetometer, the number of atoms in the system and their spin-relaxation time should be maximized.

There are several mechanisms that limit spin-relaxation time, one of the most important being depolarization caused by collisions with the cell walls that enclose the atomic vapour. Surface relaxation can be reduced by using a coating that has low adsorption energy for atoms, so they spend less time bound to the surface of the cell. Among such coatings, paraffin and other materials with long chains of hydrocarbons were found to work well with alkali metals[22]. In a seminal study[23] Bouchiat and Brossel demonstrated that spin relaxation on paraffin is caused by two effects of comparable size: magnetic dipolar interaction and spin-rotation coupling. Magnetic dipolar relaxation is dominated by interaction between the magnetic moment of the electron and magnetic moments of protons in the coating. They showed that replacing hydrogen with deuterium, which has a nuclear magnetic moment about three times smaller, reduces this type of relaxation. Despite work by several groups over the years, surface coating is still a rather laborious process with some degree of 'black magic' that does not always yield reproducible results. Whereas collisions with bare glass are generally completely depolarizing for alkali atoms, high-quality coatings can allow more than 10,000 bounces before depolarization, which also implies that even if a small fraction of the surface has defects, this will ruin the performance of the coating.

Another way to improve magnetometer sensitivity is to increase the density of alkali-metal atoms. This typically requires increasing the temperature of the cell, although alternative approaches using light-induced desorption have been investigated (see ref. 24). As paraffin coatings do not work at temperatures higher than ~80 °C, high-density magnetometers usually use a buffer gas to slow down the diffusion of alkali-metal atoms to cell walls. Slow atomic diffusion combined with spatially resolved optical detection also allows many independent measurements of the magnetic field inside one cell to be made[12]. As the density is increased, at some point the spin-relaxation time becomes dominated by collisions between alkali-metal atoms and the product $N\tau$ approaches a constant, so that shot-noise sensitivity no longer increases with density. Thus, relaxation due to collisions

©2007 Nature Publishing Group

between alkali-metal atoms represents a fundamental obstacle to improvement in sensitivity for a given cell volume.

Collisions between alkali-metal atoms are dominated by the spin-exchange process in which the electron spins of the colliding atoms rotate with respect to their combined spin, which is conserved in the collision. Even though such collisions conserve the total spin, they can lead to loss of spin coherence. All alkali atoms have non-zero nuclear spin, I, and their ground states are split into two hyperfine-structure components, characterized by the total angular momentum $F = I \pm 1/2$. The direction of magnetic precession, determined by the relative orientation of the electron spin with respect to the total angular momentum, is opposite for the two hyperfine states. Thus, in the presence of a magnetic field, the spin-exchange collisions that randomly transfer atoms between the two hyperfine states normally lead to spin-relaxation, as atomic angular momenta acquire random angles with respect to each other.

As was first realized by Happer[25], it is possible to suppress the effects of spin-exchange relaxation by increasing the rate of spin-exchange collisions until it exceeds the Larmor precession frequency. The effect is quite similar to Dicke narrowing in microwave and optical spectroscopy or motional narrowing in NMR. In the rapid spin-exchange regime, the idea of magnetic precession of atoms in an individual hyperfine state is no longer appropriate. Instead, each atom experiences an average precession in the same direction as would a free atom in the $F = I + 1/2$ state. This is because atoms, while being redistributed among the sublevels, spend more time in this state, which has a higher statistical weight and higher electron-spin polarization. As a result, in a weak external magnetic field, the average angular momentum of the atomic vapour precesses without spin-exchange relaxation, although at a rate that is slower than the precession rate for a free atom. The slowing down of the spin-precession rate depends on the distribution of atoms among magnetic sublevels, and is thus a sensitive function of the optical pumping process[26]. This dependence on local optical pumping conditions may lead to non-uniformity of the spin-precession frequency over the volume of the cell, and broadening of the resonance signal. The problem can be avoided by operating the magnetometer near zero magnetic field.

In this regime the Zeeman resonance linewidth is not broadened at all by spin-exchange collisions, and the alkali-metal density can be increased to about 10^{14} cm^{-3}, four orders of magnitude higher than in traditional atomic magnetometers. Eventually the relaxation time becomes limited by 'spin-destruction' collisions between alkali-metal atoms that do not conserve the total spin of the colliding pair. Several mechanisms of comparable importance have been identified for such relaxation[27], but some aspects of this process remain poorly understood[28]. The measured spin-destruction cross-sections are smaller for lighter alkali-metal atoms and result in a fundamental limit on the sensitivity of a potassium magnetometer of about $10^{-17} V^{-1/2}$ T Hz$^{-1/2}$ (ref. 29), where V is the active volume of the sensor in cm^3.

The spin-exchange relaxation-free regime can be achieved only in a magnetic-field range of less than ~10 nT. At higher magnetic fields such as the Earth's field, it is possible to use a single SERF magnetometer as a three-axis null-detector with external feedback[30]. The possibility of reducing spin-exchange relaxation in a finite magnetic field has also been explored[31]. The idea is to pump most atoms into a stretched state with $m = I + 1/2$ where they cannot undergo spin-exchange collisions due to conservation of angular momentum. This technique works at any magnetic field strength, but it cannot completely eliminate spin-exchange relaxation, because a high optical pumping rate required to put atoms into the stretched spin state in the presence of other relaxation processes also contributes to the resonance linewidth. For an optimal pumping rate, the minimum resonance linewidth is given by the geometric mean of the spin-exchange and spin-destruction rates[18,32]. This method for reduction of spin-exchange broadening has been used for narrowing of a microwave resonance in an alkali-metal atomic clock[32], and to improve the sensitivity of a resonant magnetometer for detection of very weak radiofrequency fields[18]. However, this technique does not significantly improve the sensitivity for measurements of static fields because excitation of large spin coherences, necessary to obtain an optimal signal/noise ratio, removes the atoms from the stretched spin state[33].

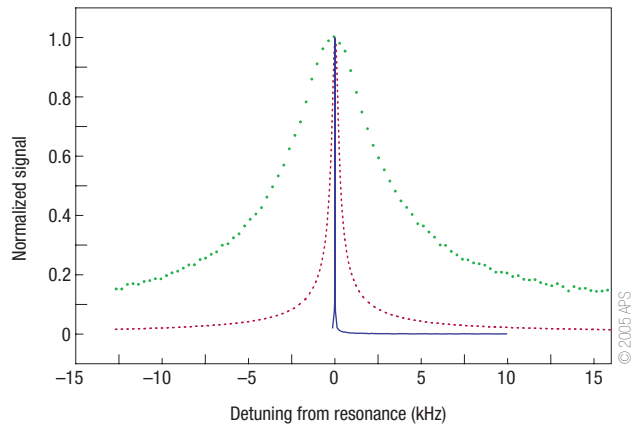

Figure 2 Comparison of Zeeman resonances for different modes of operation in a potassium vapour with density $n = 7 \times 10^{13}$ cm^{-3}. Green points: spin-exchange broadened resonance with a full-width at half-maximum of 3 kHz observed in a magnetic field of 10 μT when spin polarization is low. Red dashed line: resonance is narrowed to a full width of 350 Hz at the same magnetic field by pumping a large fraction of atoms into a stretched state parallel to the magnetic field. Blue solid line: at a field of 5 nT, the resonance width is 2 Hz due to complete elimination of spin-exchange broadening in the rapid spin-exchange regime. (Adapted and printed with permission from ref. 18.)

In Fig. 2 we show the Zeeman resonance curves obtained in a dense alkali-metal vapour in three different regimes. Spin-exchange broadening for low spin-polarization is reduced by a factor of 10 by pumping most atoms into a stretched spin state. The linewidth can be further reduced by a factor of more than 100 in a very low magnetic field, where spin-exchange relaxation is completely eliminated.

ADDITIONAL CHARACTERISTICS OF A MAGNETOMETER

Apart from sensitivity, there are many other characteristics of a magnetometer that are important for specific applications. We have already mentioned that some of the most sensitive magnetometers operate best at relatively small magnetic fields, that is, they have a limited dynamic range. An important benchmark for the magnetometer's dynamic range is the geomagnetic field ~50 μT of interest in many applications. Although traditional radiofrequency–optical double-resonance magnetometers have operated in this range from their inception (see, for example, ref. 5), diode-laser-based all-optical magnetometers for the geophysical range have been also developed recently[34–37]. At geomagnetic fields, sensitive atomic magnetometers have to contend with the complications arising from the nonlinear Zeeman effect caused by the Breit–Rabi mixing of hyperfine energy levels. The nonlinear Zeeman effect leads to a splitting of the magnetic resonance into multiple lines (see, for example, ref. 37). Several approaches have been proposed to alleviate the adverse effects of the nonlinear Zeeman effect in all-optical magnetometers, including synchronous optical pumping at the quantum revival frequency given by the quadratic correction to the Zeeman energies[38], and

©2007 Nature Publishing Group

selective excitation and detection of coherences (which correspond to high-order polarization multipoles) between 'stretched' Zeeman sublevels unaffected by the nonlinear Zeeman effect[39–41].

Another important property of a magnetometer is whether it is scalar or vector, that is, whether it measures the total magnitude, or specific cartesian components of the magnetic field. Although knowing all three vector components of a field provides more complete information about it, a truly scalar sensor has an advantage in that the device is insensitive to the orientation of the sensor with respect to the field, which is important for operation on a mobile platform.

Atomic magnetometers operating in a finite field naturally tend to be of the scalar type as they rely on the resonance between a radiofrequency field or a modulated light field with Zeeman-split energy eigenstates of an atom. However, there is a standard technique[30,42,43] for converting a scalar sensor into a vector one that relies on the fact that if a small bias field is applied to the sensor in a certain direction in addition to the field to be measured, then the change in the overall field magnitude is linear in the projection of the bias field on the main field, and is only quadratic (and generally negligible) in the projection on the orthogonal plane. Thus, on applying three orthogonal bias fields consecutively, and performing three measurements of the overall magnetic-field magnitude, the overall field vector is reconstructed. In practice, it may be convenient to apply all three bias fields simultaneously and modulate them at different frequencies. Synchronous detection of the magnetometer output at a corresponding frequency yields the value of the cartesian component of the magnetic field being measured.

For practical operation at finite fields, atomic magnetometers require a feedback loop to keep the frequency of the excitation locked to resonance as the magnetic field is changing. One approach is to use a phase-sensitive detector with an external feedback loop and a voltage-controlled oscillator. Another approach, which is often simpler, is a self-oscillating magnetometer that uses the measured spin-precession signal to directly generate the radiofrequency field in a positive feedback loop[5]. All-optical self-oscillating atomic magnetometers have been demonstrated recently, using transitions between hyperfine[44] and Zeeman sublevels[45,46].

An important characteristic of a magnetometer is how fast the device responds to a change in the magnetic field. The time response of a passive atomic magnetometer to a small variation in the magnetic field is usually equivalent to a first-order low-pass filter with a time constant τ. Hence the natural bandwidth of such a magnetometer is equal to $(2\pi\tau)^{-1}$ Hz. If it is desirable to make measurements on a time scale $T<\tau$, the operating parameters, such as the probe beam intensity, of the magnetometer can be adjusted so that $\tau = T$. If the number of atoms N is fixed, then according to equation (1), sensitivity is lost as T^{-1} for short times. However, if the number of alkali atoms can be increased and the spin-coherence time is limited by collisions between alkali atoms, then the sensitivity decreases only as $T^{-1/2}$. If the number of atoms or light power are limited for practical reasons, it is possible to increase the bandwidth of a magnetometer with external feedback by using a large gain in the feedback loop. However, if the bandwidth is increased by a factor K over the natural bandwidth, the magnetometer output noise spectral density also increases by the same factor K (ref. 47).

It is also interesting to consider the response of a magnetometer to an instantaneous change in the magnetic field. As Larmor precession has no inertia, a magnetometer based on such precession responds instantaneously to a change in the field. Our knowledge of the new value of the frequency will be at first very uncertain, but will improve with time as $T^{-3/2}$ (the best scaling for the uncertainty of a single-tone-frequency determination from a noisy signal[48]). This is discussed in the context of a practical self-oscillating magnetometer in ref. 46, where the effect of additional noise sources such as photodetector and amplifier noise are also considered.

Many magnetometer applications require operation at frequencies lower than 1 Hz where $1/f$ noise is often dominant. Atomic magnetometers have an intrinsic advantage over other types of sensors in this regard because they use a sensing element with very simple structure that does not generate intrinsic $1/f$ noise, which is usually observed in solid-state systems with many nearly degenerate energy states[49]. In practical situations, significant $1/f$ noise may arise due to external elements, such as laser fluctuations caused by air currents. Such noise may be reduced using spin-modulation techniques[50].

In the case of portable and space-borne magnetometers, important characteristics include 'heading errors' — the dependence of the reading of the magnetometer on the orientation of the sensor with respect to the field being measured, as well as the existence of 'dead zones', that is, spatial orientations where the magnetometer loses its sensitivity. Other parameters of importance include size and power consumption of the sensor system. A recent trend is the use of vertical-cavity surface-emitting lasers (VCSEL) as light sources, which provide on the order of a milliwatt of light resonant with the D-lines of rubidium and caesium, do not require an external cavity, and consume only a few milliwatts of power. Miniaturization of the vapour cells to millimetre scales can be done using fairly standard techniques (see ref. 51 for a description of a prototype optical-rotation magnetometer using a 3-mm-diameter paraffin-coated Cs cell). Another approach, particularly appealing for future mass production of miniaturized low-cost magnetometers, is manufacturing an integrated sensor package incorporating a VCSEL laser, an alkali-vapour cell, optics, and a detector using the wafer-production techniques well-developed by the semiconductor industry. The first magnetometers based on this approach with a grain-of-rice-sized integrated sensor have been recently constructed[52], demonstrating a sensitivity of 50 pT $Hz^{-1/2}$, with anticipated improvement by several orders of magnitude with further optimization.

A favourable feature of magnetometers with a small vapour cell is their reduced sensitivity to magnetic-field gradients, which can otherwise lead to additional spin relaxation, line broadening and performance degradation. Magnetometers using buffer-gas-free anti-relaxation-coated cells are also less sensitive to small field gradients, because each atom samples the volume of the cell during its many bounces between the walls in the course of a relaxation time. This leads to a significant averaging of the magnetic-field inhomogeneities. A systematic study of the effects of the gradients on the Rb ground-state spin relaxation in a coated cell is presented in ref. 53 along with a survey of earlier work.

Spatial resolution of magnetometers is important in applications requiring mapping of magnetic fields or measurements of fields from small, localized sources. Typically, spatial resolution is determined by the size of the vapour cell. In magnetometers using high-density buffer gas it is possible to make multiple measurements in the same cell with a spatial resolution given by the diffusion length in one spin-coherence time[12]. Whereas these techniques can make measurements on millimetre length scales, higher resolution can be obtained with laser-cooled trapped atoms[54,55], as discussed below. Another recently explored approach for high-spatial-resolution magnetometry is to use an evanescent wave to probe atoms very close to an anti-relaxation-coated surface[56].

APPLICATIONS TO BIOMAGNETISM

Detection of magnetic fields of biological origin enable non-invasive studies of the time dependence and spatial distribution of biocurrents. Most biological magnetic-field studies have focused on detection of the fields from the heart and the brain. Measurements of the magnetic fields generated by the heart (magnetocardiography) provide richer diagnostic information about heart function than traditional electrocardiography and do not require placing electrical contacts on

©2007 Nature Publishing Group

the patient[57]. Useful diagnostic information is obtained by measuring the spatial distribution of the magnetic field during different parts of the cardiac cycle. Most magnetocardiography studies have been performed in magnetically shielded rooms, but they are considered too expensive for clinical application, and widespread use of magnetocardiography requires development of relatively low-cost sensors that can operate in an unshielded environment. Measurement of magnetic fields generated by the brain (magnetoencephalography) has been used extensively for functional brain studies[58]. Magnetic fields associated with a particular sensory input, such as auditory, visual or tactile stimulation, are recorded by averaging the signals over many presentations of the same stimulus. Detailed measurements of the spatial distribution of the magnetic field around the head allows the identification of regions of the brain that become active during processing of the sensory input. However, spatial localization is complicated by the fact that the inverse problem of finding the current distribution responsible for a particular magnetic field distribution does not have a unique solution. Additional information, such as MRI data and sophisticated numerical algorithms, are used for spatial localization. Magnetoencephalography also finds increasing use in clinical diagnostic applications, for example for treatment of epilepsy[59].

The first measurements of biological fields with an atomic magnetometer[60] were performed in the 1970s, but this approach was not widely pursued and most biomagnetic applications have relied on SQUID magnetometers. Recent progress in atomic magnetometry has again attracted interest to its application for measurements of biological magnetic fields with non-cryogenic sensors. Figure 3 shows examples of magnetic fields from the heart and the brain detected with atomic magnetometers in a magnetically shielded environment. The cardiomagnetometer is based on optical-radio-frequency double resonance and uses Cs atoms at 30 °C, allowing it to be placed close to a human body[61]. Cardiomagnetic fields are recorded sequentially on a grid of points above the human chest. Measurements of the brain's magnetic field have been performed with a potassium SERF magnetometer, which operates at the vapour cell temperature of 180 °C and uses a multichannel photodetector to simultaneously record the spatial distribution of the magnetic fields[62]. Even though heating is required to maintain the operating temperature of the cell positioned close to the subject's head, it is technically easier and cheaper to do than maintaining cryogenic temperature at the sensor, as required in the case of SQUIDs.

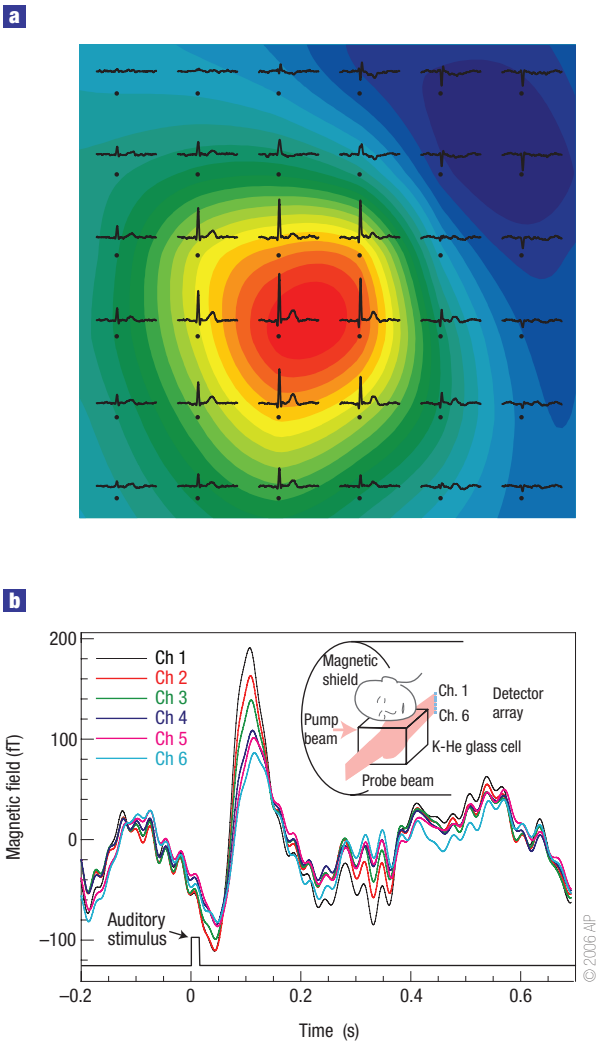

Figure 3 Examples of biological magnetic fields recorded with atomic magnetometers. **a**, Time traces (averaged over 100 heartbeats) of the out-of-chest component of the magnetic field from a human heart recorded on 36 grid points spaced by 4 cm. The underlying map is a snapshot of the field distribution at the moment of strongest magnetic activity (R-peak). The scale of the map ranges from –30 pT (blue) to +60 pT (red). Figure courtesy of A. Weis. **b**, Magnetic fields recorded from a brain in response to an auditory stimulation by a series of short clicks (averaged over about 600 presentations). The prominent feature at 100 ms after the stimulus is the evoked response in the auditory cortex, most clearly seen as a difference in the magnetic fields recorded by different channels. In contrast, ambient field drifts, such as those seen before the stimulus, generate similar signals in all channels. (Adapted and reprinted with permission from ref. 62.)

FUNDAMENTAL APPLICATIONS

Many fundamental interactions reduce at low energy to a spin-coupling similar to magnetic interaction, as the spin is the only vector available in the rest-frame of the particle. Atomic magnetometers are intrinsically sensitive probes of the spin precession and hence are important in tests of fundamental symmetries. An example of the magnetometers' versatile nature is a Cs magnetometer constructed at Amherst. It was used to set limits: (i) on the electric dipole moment (EDM) d of electrons, which violates parity (P) and time-reversal invariance (T) and generates $d\mathbf{ES}$ coupling[63]; (ii) on violation of Lorentz invariance manifested as a spin coupling $\mathbf{bs}$ to a background vector field $\mathbf{b}$ (ref. 64); and (iii) on spin-dependent forces that can be mediated by axions[65].

Magnetometers based on nuclear (rather than electron) spin precession are also important in tests of fundamental symmetries. Although nuclei, such as ^{3}He, have a magnetic moment smaller than that of an electron by three orders of magnitude, they also display a much longer spin-relaxation time τ and thus can be competitive with electron-spin magnetometers in magnetic-field measurements[66]. In the searches for non-magnetic spin interactions, the smallness of the nuclear magnetic moment is actually an advantage, as it reduces the sensitivity to spurious magnetic effects. Measurements of nuclear spin precession of ^{199}Hg have been used to set a limit on the EDM of the mercury atom[67] — which is also the tightest limit on an EDM of any particle — as well as for monitoring magnetic fields in a neutron EDM experiment[68]. These results place stringent constraints on sources of combined charge-parity symmetry violation beyond the Standard Model[69]. Comparison of ^{129}Xe and ^{3}He precession sets the most stringent limit on the Lorentz-violating vector coupling to a nuclear spin[70].

A number of new ideas for tests of fundamental symmetries using atomic magnetometers are currently being explored, such as searches for a permanent electric dipole moment using laser-cooled Cs atoms in an optical lattice[71] or an atomic fountain[72], and the possibility of

©2007 Nature Publishing Group

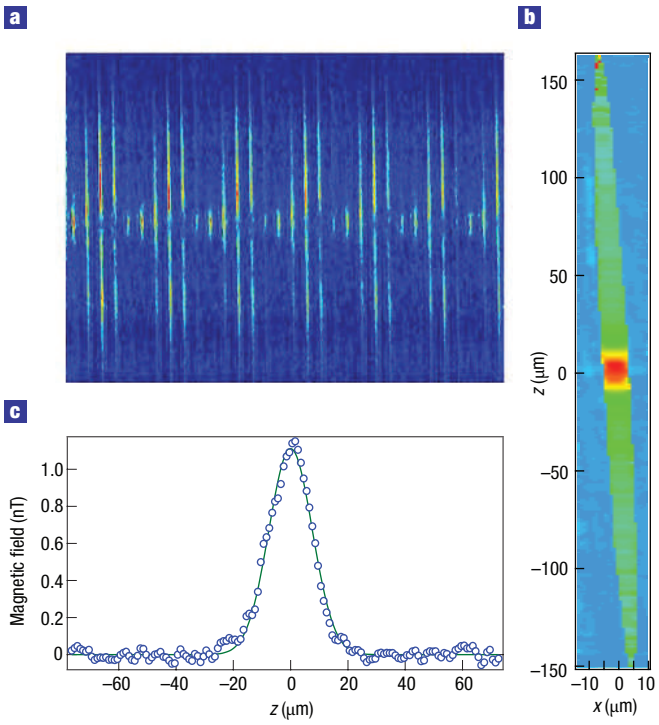

Figure 4 Detection of effective magnetic field by imaging of Larmor precession in a BEC of ^{87}Rb (ref. 55). The condensate contains 1.4 million atoms, optically trapped with trapping frequencies of 4.2 Hz × 155 Hz × 400 Hz. A uniform bias magnetic field of 16 μT is applied, while a far-detuned circularly polarized laser beam with a waist of 7.6 μm is focused onto the condensate to simulate the effects of an additional localized magnetic field. **a**, A sequence of 32 individual normalized atomic-spin-sensitive phase-contrast images taken after an evolution time of 50 ms and spaced in time by 100 μs. The variation of the brightness of the images with a period of about five frames is due to Larmor precession of the atomic spins. **b**, A pseudocolour map of the phase of Larmor precession as a function of position in micrometres. **c**, The effective magnetic field corresponding to the phase in **b**, shown as a function of position in the central portion of the condensate, demonstrating the high resolution and precision of the technique.The gaussian phase shift follows the intensity profile of the far-detuned laser beam, and the solid line is a fit to this profile. Figure courtesy of M. Vengalattore and J. Higbie.

using ultra-sensitive magnetometers for detecting P- and T-violating magnetization in solid-state samples induced by an applied electric field[73] or an internal field of a ferroelectric[74].

MEASURING MAGNETIC FIELDS IN SPACE

Measurements of planetary and interplanetary magnetic fields have been integral to space missions from their early days[75]. The on-board instruments designed for such missions have been able to successfully meet various inherent design challenges, including the necessity to have a very broad dynamic range for the instrument, as the magnetic fields to be measured could vary by many orders of magnitude between planetary fly-bys and the craft's sojourn in interplanetary space. Other challenges include, for example, stringent requirements on reliability, the ability to withstand thermal and mechanical stresses associated with the launch and varying conditions during the flight, limited weight and size, power consumption and the ability to characterize and correct for errors due to the craft spin.

Most spacecraft measuring magnetic fields currently rely on flux-gate magnetometers because of their small size and power consumption. However, optically pumped ^{4}He magnetometers are used in most advanced space applications because of their relative simplicity, reliability and high absolute accuracy. In a ^{4}He magnetometer, a weak electric discharge excites helium atoms to the metastable 2^3S_1 state, and optical pumping with a ^{4}He discharge lamp is used to polarize and detect spin precession of atoms in the metastable state. Such instruments typically have sensitivity of the order of 1–10 pT Hz$^{-1/2}$ and have been successfully flown on Ulysses[76] and Cassini[77] missions, recently providing new information about magnetospheres of Saturn[78] and its moon Enceladus[79]. Laser-pumped ^{4}He magnetometers are currently being developed and have demonstrated sensitivity of 200 fT Hz$^{-1/2}$ (ref. 80); their fundamental sensitivity limit is estimated to be about 5 fT Hz$^{-1/2}$ (ref. 81).

Deployment of more sensitive magnetometers in space will enable magnetic-field measurements to be made in weak-field space environments, as in the outer heliosphere and in the local interstellar medium. At distances from the Sun beyond about 80 astronomical units, the strength of the ambient, nominally d.c., magnetic field could be as low as a few tens of picotesla[82], near the limit of detectability of sensors used at present. Fluctuations of magnetic fields in space are caused by a plasma process and have a bandwidth of the order of 1 Hz, corresponding to typical electron cyclotron frequency in the outer heliosphere. Atomic magnetometers are ideally suited for measurements of such fields.

ATOMIC MAGNETOMETERS AND NMR

One of the rapidly growing applications of atomic magnetometers is detection of NMR signals. NMR is usually detected with inductive radiofrequency pick-up coils whose sensitivity drops at low frequency, precluding many applications of low-field NMR. SQUID magnetometers have been widely used for NMR detection at low frequencies[83], but they still require cryogenic cooling, negating one of the main advantages of low-field NMR — the absence of a cryogenic superconducting magnet. Atomic magnetometers can be used in place of SQUIDs to detect the magnetic field generated by the nuclear magnetization[84–86].

One of the promising applications is 'remote' NMR, where spin polarization, NMR-signal encoding and detection are performed sequentially in different parts of the apparatus[87]. Such remote NMR[88] and MRI[89] have recently been demonstrated with an atomic magnetometer.

For both remote and *in situ* NMR detection, having the NMR sample and the magnetometer sensor spatially separated (as, for example, in refs 88,89) has experimental advantages, such as an ability to apply an independent, relatively strong magnetic field to the sample, which is not 'seen' by the sensor if a proper geometrical arrangement is used. On the other hand, atomic magnetometers can achieve an even higher sensitivity by taking advantage of contact interactions between alkali-metal and nuclear spins. These interactions have been particularly well studied for noble gas atoms[90], and can be described by a scalar Fermi-contact interaction between the two spins. For heavy noble gases, such as ^{129}Xe, this interaction can enhance the magnetic field produced by nuclear magnetization by a large factor of the order of 600. Thus, by allowing noble gas atoms to interact directly with the alkali-metal vapour, high sensitivity to low concentration of ^{129}Xe spins can be obtained[86].

The contact interaction between nuclear and electron spins is also useful for inertial rotation sensing. Nuclear spins make good quantum gyroscopes because of their long spin-coherence time, but their magnetic moment causes significant precession in stray magnetic fields[91]. An alkali-metal magnetometer can then serve two purposes, to measure the ambient magnetic field and to detect the inertial precession of nuclear spins with high sensitivity. The requirement for magnetic field stability is rather stringent. For example, a stray

©2007 Nature Publishing Group

magnetic field of 1 fT would cause a false spin-precession rate for ^{3}He of about 0.04 degrees per hour, more than can be tolerated in a navigation-grade gyroscope. A SERF magnetometer can achieve this level of magnetic sensitivity, allowing it to be used for cancellation of stray magnetic fields and enabling a competitive nuclear-spin rotation sensor[92].

Another new application of atomic magnetometers is for detection of nuclear quadrupole resonance (NQR) signals. In crystalline materials, nuclei with a quadrupole moment are aligned by the electric field gradient and can generate a weak radiofrequency signal following application of a resonant radiofrequency pulse. The physics of this phenomenon can be understood in the language of alignment-to-orientation conversion[93], a process well studied in atomic physics. For practical applications, it is particularly important that NQR signals do not average out in materials with randomly oriented crystallites such as powders. Resonance frequencies are highly material-specific and typically range from 0.1 to 5 MHz. Detection of NQR is a promising technique for identification of explosives, as most explosive materials contain the ^{14}N nuclei, which has a large quadrupole moment. However, widespread use of NQR for this purpose has been limited due to the weakness of the NQR signals, which are typically detected with a radiofrequency coil only after substantial signal averaging[94]. Detection of weak radiofrequency signals requires modification of usual atomic-magnetometer arrangements that are designed for detection of quasi-d.c. magnetic fields. A tunable magnetometer for detection of a weak radiofrequency field can be realized by using a bias field to tune the Zeeman energy splitting to the frequency of the radiofrequency field[18,95]. Recently, such a magnetometer has been built for operation at 423 kHz with a sensitivity of 0.24 fT Hz$^{-1/2}$ and bandwidth of 600 Hz and used to detect NQR signals from ammonium nitride[96]. A detailed analysis of the fundamental limits on sensitivity of a radiofrequency atomic magnetometer[18] and an inductive pick-up coil show that atomic magnetometer has higher sensitivity up to frequencies of about 50 MHz (ref. 97).

MAGNETOMETERY WITH COLD ATOMS

Recent breakthroughs in laser cooling and trapping have opened new avenues for precision measurements using long-lived, near-stationary collections of atoms. In particular, far-off-resonance optical traps provide a benign environment for trapping atoms with negligible photon scattering rates and storage lifetimes in excess of 300 s in an ultra-high-vacuum environment[98]. Thus, the spin-coherence time of laser-cooled and trapped atoms can be substantially longer than the typical value of 1 s obtained in a buffer gas or surface-coated cell. However, due to the small volume of atom traps and limits on atomic number density from cold collisions, the total number of trapped atoms is typically of the order of 10^6–10^8, many orders of magnitude smaller than 10^{11}–10^{15} atoms contained in a centimetre-sized vapour cell. Although trapped atoms do not have the highest sensitivity to uniform magnetic fields, they are particularly well suited for making field measurements with high spatial resolution corresponding to the trap size. Atomic magnetic microscopes can potentially compete with SQUID sensors and Hall probes in such applications as studies of vortices in superconductors[99] and imaging of currents in integrated circuits[100]. Two magnetometery techniques have been recently demonstrated with rubidium Bose–Einstein condensates (BEC). The first involves holding the condensate in a weak magnetic trap so the energy of interaction with the magnetic field to be measured causes a perturbation of the trapping potential and changes the local atomic density[54]. A typical chemical potential in a weak magnetic trap of the order of 1 nK gives a magnetic field sensitivity of about 1 nT. The other technique[55] is similar to measurements done with hot atoms — the BEC is held in an optical dipole trap and spin precession is measured using phase-contrast imaging with an off-resonant circularly polarized probe beam. This non-destructive imaging enables spin precession to be monitored, as shown in Fig. 4. The magnetic field sensitivity obtained with this method is 900 fT (in a single run with 250 ms integration time and an integrating area of 100 μm^2). In both methods, cooling atoms to quantum degeneracy improves measurement sensitivity, but whether the coherence of the BEC plays a direct role is currently an open question.

OUTLOOK

Recent progress in atomic magnetometry techniques can be expected to have a significant impact in four general areas. The first is the development of robust laser-pumped atomic magnetometers, largely driven by recent availability of electronically tunable VCSEL and distributed-feedback semiconductor lasers. Such magnetometers can replace existing discharge-lamp-pumped devices, providing higher sensitivity in geological, military and space applications. The second area is the development of micro-fabricated millimetre-size magnetometers, which will open entirely new applications of magnetic monitoring in a wide range of environments. The third area is the increasing use of atomic magnetometers as sensitive detectors for weak signals, in NMR, biological applications, magnetic microscopy and inertial rotation sensing. The fourth area is the exploration of the frontier of magnetic sensitivity, where atomic magnetometers are already surpassing the best sensitivities that have been achieved by SQUID sensors and can be expected to reach sensitivities significantly below 10^{-17} T Hz$^{-1/2}$. The future of measuring magnetic fields with atoms and light is indeed bright.

doi:10.1038/nphys566

References

1. Kastler, A. Some suggestions concerning the production and detection by optical means of inequalities in the populations of levels of spatial quantization in atoms. Application to the Stern and Gerlach and magnetic resonance experiments. *J. Phys. Radium* **11,** 255–265 (1950).
2. Dehmelt, H. Modulation of a light beam by precessing absorbing atoms. *Phys. Rev.* **105,** 1924–1925 (1957).
3. Bell, W. & Bloom, A. Optical detection of magnetic resonance in alkali metal vapor. *Phys. Rev.* **107,** 1559–1565 (1957).
4. Bell, W. & Bloom, A. Optically driven spin precession. *Phys. Rev. Lett.* **6,** 280–281 (1961).
5. Bloom, A. Principles of operation of the rubidium vapor magnetometer. *Appl. Opt.* **1,** 61–68 (1962).
6. Dupont-Roc, J., Haroche, S. & Cohen-Tannoudji, C. Detection of very weak magnetic fields (10^{-9} gauss) by ^{87}Rb zero-field level crossing resonances. *Phys. Lett. A* **28,** 638–639 (1969).
7. Budker, D. *et al.* Resonant nonlinear magneto-optical effects in atoms. *Rev. Mod. Phys.* **74,** 1153–1201 (2002).
8. Alexandrov, E. B. *et al.* Dynamic effects in nonlinear magneto-optics of atoms and molecules: Review. *J. Opt. Soc. Am. B* **22,** 7–20 (2005).
9. Aleksandrov, E. B., Balabas, M. V., Vershovskii, A. K. & Pazgalev, A. S. Experimental demonstration of the sensitivity of an optically pumped quantum magnetometer. *Tech. Phys.* **49,** 779–783 (2004).
10. Budker, D., Kimball, D. F., Rochester, S. M., Yashchuk, V. V. & Zolotorev, M. Sensitive magnetometry based on nonlinear magneto-optical rotation. *Phys. Rev. A* **62,** 043403 (2000).
11. Groeger, S., Bison, G., Schenker, J. L., Wynands, R. & Weis, A. A high-sensitivity laser-pumped M_x magnetometer. *Eur. Phys. J. D* **38,** 239–247 (2006).
12. Kominis, I. K., Kornack, T. W., Allred, J. C. & Romalis, M. V. A subfemtotesla multichannel atomic magnetometer. *Nature* **422,** 596–599 (2003).
13. Clarke, J. & Braginski, A. I. *The SQUID Handbook* (Wiley-VCH, Weinheim, 2004).
14. Groeger, S., Pazgalev, A. S. & Weis, A. Comparison of discharge lamp and laser pumped cesium magnetometers. *Appl. Phys. B.* **80,** 645–654 (2005).
15. Vershovskii, A. K., Pazgalev, A. S. & Aleksandrov, E. B. The design of a λ-hfs magnetometer. *Techn. Phys.* **45,** 88–93 (2000).
16. Geremia, G. M., Stockton, J. K. & Mabuchi, H. Suppression of spin projection noise in broadband atomic magnetometry. *Phys. Rev. Lett.* **94,** 203002 (2005).
17. Auzinsh, M. *et al.* Can a quantum nondemolition measurement improve the sensitivity of an atomic magnetometer? *Phys. Rev. Lett.* **93,** 173002 (2004).
18. Savukov, I. M., Seltzer, S. J., Romalis, M. V. & Sauer, K. L. Tunable atomic magnetometer for detection of radio-frequency magnetic fields. *Phys. Rev. Lett.* **95,** 063004 (2005).
19. Happer, W. & Mathur, B. Effective operator formalism in optical pumping. *Phys. Rev.* **163,** 12–25 (1967).
20. Fleischhauer, M., Matsko, A. B. & Scully, M. O. Quantum limit of optical magnetometry in the presence of ac stark shifts. *Phys. Rev. A* **62,** 013808 (2000).
21. Novikova, I., Matsko, A. B., Velichansky, V. L., Scully, M. O. & Welch, G. R. Compensation of ac stark shifts in optical magnetometry. *Phys. Rev. A* **63,** 063802 (2001).
22. Robinson, H., Ensberg, E. & Dehmelt, H. Preservation of spin state in free atom-inert surface collisions. *Bull. Am. Phys. Soc.* **3,** 9 (1958).

©2007 Nature Publishing Group

23. Bouchiat, M. A. & Brossel, J. Relaxation of optically pumped Rb atoms on paraffin-coated walls. *Phys. Rev.* **147,** 41–54 (1966).
24. Alexandrov, E. B. *et al.* Light-induced desorption of alkali-metal atoms from paraffin coating. *Phys. Rev. A* **66,** 042903 (2002); Erratum. *Phys. Rev. A* **70,** 049902(E) (2004).
25. Happer, W. & Tang, H. Spin-exchange shift and narrowing of magnetic resonance lines in optically pumped alkali vapors. *Phys. Rev. Lett.* **31,** 273–276 (1973).
26. Savukov, I. M. & Romalis, M. V. Effects of spin-exchange collisions in a high-density alkali-metal vapor in low magnetic fields. *Phys. Rev. A* **71,** 23405 (2005).
27. Erickson, C. J. *et al.* Spin relaxation resonances due to the spin-axis interaction in dense rubidium and cesium vapor. *Phys. Rev. Lett.* **85,** 4237–4240 (2000).
28. Kadlecek, S., Anderson, L. W. &Walker, T. G. Field dependence of spin relaxation in a dense Rb vapor. *Phys. Rev. Lett.* **80,** 5512–5515 (1998).
29. Allred, J. C., Lyman, R. N., Kornack, T. W. & Romalis, M. V. A high-sensitivity atomic magnetometer unaffected by spin-exchange relaxation. *Phys. Rev. Lett.* **89,** 130801 (2002).
30. Seltzer, S. & Romalis, M. V. Unshielded three-axis vector operation of a spin-exchange-relaxation-free atomic magnetometer. *Appl. Phys. Lett.* **85,** 4804–4806 (2004).
31. Appelt, S., Ben-Amar Baranga, A., Young, A. R. & Happer, W. Light narrowing of rubidium magneticresonance lines in high-pressure optical-pumping cells. *Phys. Rev. A* **59,** 2078–2084 (1999).
32. Jau, Y. Y. *et al.* Intense, narrow atomic-clock resonances. *Phys. Rev. Lett.* **92,** 110801 (2004).
33. Smullin, S. J., Savukov, I. M., Vasilakis, G., Ghosh, R. K. & Romalis, M. V. A low-noise high-density alkali metal scalar magnetometer. Preprint at http://arxiv.org/abs/physics/0611085 (2006).
34. Stahler, M., Knappe, S., Affolderbach, C., Kemp, W. & Wynands, R. Picotesla magnetometry with coherent dark states. *Europhys. Lett.* **54,** 323–328 (2001).
35. Andreeva, C. *et al.* Two-color coherent population trapping in a single Cs hyperfine transition, with application in magnetometry. *Appl. Phys. B* **76,** 667– 675 (2003).
36. Alipieva, E. *et al.* Coherent population trapping for magnetic field measurements. *Proc. SPIE* **5830,** 170–175 (2005).
37. Acosta, V. *et al.* Nonlinear magneto-optical rotation with frequency-modulated light in the geophysical field range. *Phys. Rev. A* **73,** 053404 (2006).
38. Seltzer, S. J., Meares, P. J. & Romalis, M. V. Synchronous optical pumping of quantum revival beats for atomic magnetometry. Preprint at http://arxiv.org/abs/physics/0611014 (2006).
39. Alexandrov, E. B., Pazgalev, A. S. & Rasson, J. L. Observation of four-quantum resonance in the Zeeman structure of the ground-state of ^{39}K. *Opt. Spectrosk.* **82,** 14–20 (1997).
40. Yashchuk, V. V. *et al.* Selective addressing of high-rank atomic polarization moments. *Phys. Rev. Lett.* **90,** 253001 (2003).
41. Pustelny, S. *et al.* Pump-probe nonlinear magnetooptical rotation with frequency-modulated light. *Phys. Rev. A* **73,** 023817 (2006).
42. Gravrand, O., Khokhlov, A., Mouël, J. L. L. & Léger, J. M. On the calibration of a vectorial ^{4}He pumped magnetometer. *Earth Planets Space* **53,** 949–958 (2001).
43. Alexandrov, E. B. *et al.* Three-component variometer based on a scalar potassium sensor. *Meas. Sci. Technol.* **15,** 918–922 (2004).
44. Matsko, A. B., Strekalov, D. & Maleki, L. Magnetometer based on the opto-electronic microwave oscillator. *Opt. Commun.* **247,** 141–148 (2005).
45. Schwindt, P. D. D., Hollberg, L. & Kitching, J. Self-oscillating rubidium magnetometer using nonlinear magneto-optical rotation. *Rev. Sci. Instrum.* **76,** 126103 (2005).
46. Higbie, J., Corsini, E. & Budker, D. Robust, high-speed, all-optical atomic magnetometer. *Rev. Sci. Instrum.* **77,** 113106 (2006).
47. Bechhoefer, J. Feedback for physicists: A tutorial essay on control. *Rev. Mod. Phys.* **77,** 783–836 (2005).
48. Rife, D. C. & Boorstyn, R. R. Single-tone parameter estimation from discrete-time observations. *IEEE Trans. Inform. Theory* **20,** 591–598 (1974).
49. Weissman, M. B. 1/f noise and other slow, nonexponential kinetics in condensed matter. *Rev. Mod. Phys.* **60,** 537571 (1988).
50. Li, Z., Wakai, R. T. & Walker, T. G. Parametric modulation of an atomic magnetometer. *Appl. Phys. Lett.* **89,** 134105 (2006).
51. Balabas, M. V., Budker, D., Kitching, J., Schwindt, P. D. D. & Stalnaker, J. E. Magnetometry with millimeter-scale antirelaxation-coated alkali-metal vapor cells. *J. Opt. Soc. Am. B* **23,** 1001–1006 (2006).
52. Schwindt, P. D. D. *et al.* Chip-scale atomic magnetometer. *Appl. Phys. Lett.* **85,** 6409–6411 (2004).
53. Pustelny, S., Jackson Kimball, D. F., Rochester, S. M., Yashchuk, V. V. & Budker, D. Influence of magnetic-field inhomogeneity on nonlinear magneto-optical resonances. *Phys. Rev. A* **74,** 063406 (2006).
54. Wildermuth, S. *et al.* Sensing electric and magnetic fields with Bose-Einstein condensates. *Appl. Phys. Lett.* **88,** 264103 (2006).
55. Vengalattore, M. *et al.* High-resolution magnetometry with a spinor Bose-Einstein condensate. Preprint at http://arxiv.org/abs/cond-mat/0612685 (2006).
56. Zhao, K. F. & Wu, Z. Evanescent wave magnetometer. *Appl. Phys. Lett.* **89,** 261113 (2006).
57. Fenici, R., Brisinda, D. & Meloni, A. M. Clinical application of magnetocardiography. *Exp. Rev. Mol. Diagn.* **5,** 291–313 (2005).
58. Hämäläinen, M., Hari, R., Ilmoniemi, R. J., Knuutila, J. & Lounasmaa, O. V. Magnetoencephalography theory, instrumentation, and applications to noninvasive studies of the working human brain. *Rev. Mod. Phys.* **65,** 413–497 (1993).
59. Papanicolaou, A. C., Castillo, E. M., Billingsley-Marshall, R., Pataraia, E. & Simos, P. G. A review of clinical applications of magnetoencephalography. *Int. Rev. Neurobiol.* **68,** 223–247 (2005).
60. Livanov, M. N. *et al.* Recording of human magnetic fields. *Doklady Akademii Nauk SSSR* **238,** 253–256 (1977).
61. Bison, G., Wynands, R. & Weis, A. A laser-pumped magnetometer for the mapping of human cardiomagnetic fields. *Appl. Phys. B.* **76,** 325–328 (2003).
62. Xia, H., Baranga, A. B., Hoffman, D. & Romalis, M. V. Magnetoencephalography with an atomic magnetometer. *Appl. Phys. Lett.* **89,** 211104 (2006).
63. Murthy, S. A., Krause, J., D., Li, Z. L. & Hunter, L. R. New limits on the electron electric dipole moment from cesium. *Phys. Rev. Lett.* **63,** 965–968 (1989).
64. Berglund, C. J. *et al.* New limits on local Lorentz invariance from Hg and Cs magnetometers. *Phys. Rev. Lett.* **75,** 1879–1882 (1995).
65. Youdin, A. N., Krause, J., D., Jagannathan, K., Hunter, L. R. & Lamoreaux, S. K. Limits on spin-mass couplings within the axion window. *Phys. Rev. Lett.* **77,** 2170–2173 (1996).
66. Gilles, H., Monfort, Y. & Hamel, J. ^{3}He maser for earth magnetic field measurement. *Rev. Sci. Instrum.* **74,** 4515–4520 (2003).
67. Romalis, M. V., Griffith, W. C., Jacobs, J. P. & Fortson, E. N. New limit on the permanent electric dipole moment of ^{199}Hg. *Phys. Rev. Lett.* **86,** 2505–2508 (2001).
68. Baker, C. A. *et al.* Improved experimental limit on the electric dipole moment of the neutron. *Phys. Rev. Lett.* **97,** 131801 (2006).
69. Pospelov, M. & Ritz, A. Electric dipole moments as probes of new physics. *Ann. Phys.* **318,** 119–169 (2005).
70. Bear, D., Stoner, R. E., Walsworth, R. L., Kostelecký, V. A. & Lane, C. D. Limit on Lorentz and CPT violation of the neutron using a two-species noble-gas maser. *Phys. Rev. Lett.* **85,** 5038–5041 (2000); Erratum. *Phys. Rev. Lett.* **89,** 209902 (2002).
71. Chin, C., Leiber, V., Vuletić, V., Kerman, A. J. & Chu, S. Measurement of an electron's electric dipole moment using Cs atoms trapped in optical lattices. *Phys. Rev. A* **63,** 033401 (2001).
72. Amini, J. M., Munger, C. T. Jr & Gould, H. Demonstration of a cold atom fountain electron electric dipole moment experiment. http://arxiv.org/physics/0602011 (2006).
73. Lamoreaux, S. K. Solid-state systems for the electron electric dipole moment and other fundamental measurements. *Phys. Rev. A* **66,** 022109 (2002).
74. Budker, D., Lamoreaux, S. K., Sushkov, A. O. & Sushkov, O. P. On the sensitivity of condensed-matter P- and T-violation experiments. *Phys. Rev. A* **73,** 022107 (2006).
75. Acuna, M. H. in *Encyclopedia of Planetary Sciences* (eds Shirley, J. H. & Fairbridge, R. W.) 406–410 (Chapman & Hall, London, 1997).
76. Balogh, A. in *IEE Colloquium on Satellite Instrumentation* Digest No. 12, 2/1–3 (IEE, London, 1988).
77. Dunlop, M. W., Dougherty, M. K., Kellock, S. & Southwood, D. J. Operation of the dual magnetometer on Cassini: science performance. *Planet. Space Sci. (UK)* **47,** 1389–1405 (1999).
78. Dougherty, M. K. *et al.* Cassini magnetometer observations during Saturn orbit insertion. *Science* **307,** 1266–1270 (2005).
79. Dougherty, M. K. *et al.* Identification of a dynamic atmosphere at Enceladus with the Cassini magnetometer. *Science* **311,** 1406–1409 (2006).
80. Slocum, R. E., Kuhlman, G., Ryan, L. & King, D. in *IEEE Proc. Conf. Oceans 2002* Vol. **2,** 945–951 (IEEE, London, 2002).
81. McGregor, D. D. High-sensitivity helium resonance magnetometers. *Rev. Sci. Instrum.* **58,** 1067–1076 (1987).
82. Burlaga, L. F. *et al.* A transition to fast flows and its effects on the magnetic fields and cosmic rays observed by Voyager 2 near 70 au. *Astrophys. J.* **618,** 1074–1078 (2005).
83. Greenberg, Y. S. Application of superconducting quantum interference devices to nuclear magnetic resonance. *Rev. Mod. Phys.* **70,** 175–222 (1998).
84. Cohen-Tannoudji, C., DuPont-Roc, J., Haroche, S. & Laloë, F. Detection of the static magnetic field produced by the oriented nuclei of optically pumped ^{3}He gas. *Phys. Rev. Lett.* **22,** 758–760 (1969).
85. Yashchuk, V. V. *et al.* Hyperpolarized xenon nuclear spins detected by optical atomic magnetometry. *Phys. Rev. Lett.* **93,** 160801 (2004).
86. Savukov, I. M. & Romalis, M. V. NMR detection with an atomic magnetometer. *Phys. Rev. Lett.* **94,** 123001 (2005).
87. Moulé, A. J. *et al.* Amplification of xenon NMR and MRI by remote detection. *Proc. Natl Acad. Sci. USA* **100,** 9122–9127 (2003).
88. Xu, S., Rochester, S. M., Yashchuk, V. V., Donaldson, M. H. & Budker, D. Construction and applications of an atomic magnetic gradiometer based on nonlinear magneto-optical rotation. *Rev. Sci. Instrum.* **77,** 083106 (2006).
89. Xu, S. *et al.* Magnetic resonance imaging with an optical atomic magnetometer. *Proc. Natl Acad. Sci. USA* **103,** 12668–12671 (2006).
90. Schaefer, S. R. *et al.* Frequency shifts of the magnetic-resonance spectrum of mixtures of nuclear spin-polarized noble gases and vapors of spin-polarized alkali-metal atoms. *Phys. Rev. A* **39,** 5613–5623 (1989).
91. Woodman, K. F., Franks, P. W. & Richards, M. D. The nuclear magnetic resonance gyroscope: a review. *J. Navigation* **40,** 366–384 (1987).
92. Kornack, T. W., Ghosh, R. K. & Romalis, M. V. Nuclear spin gyroscope based on an atomic comagnetometer. *Phys. Rev. Lett.* **95,** 230801 (2005).
93. Budker, D., Kimball, D. F., Rochester, S. M. & Urban, J. T. Alignment-to-orientation conversion and nuclear quadrupole resonance. *Chem. Phys. Lett.* **378,** 440–448 (2003).
94. Garroway, A. N. *et al.* Remote sensing by nuclear quadrupole resonance. *IEEE Trans. Geosci. Remote Sens. (USA)* **39,** 1108–1118 (2001).
95. Ledbetter, M. P. *et al.* Detection of radio frequency magnetic fields using nonlinear magneto-optical rotation. *Phys. Rev. A* **75,** 023405 (2007).
96. Lee, S.-K., Sauer, K. L., Seltzer, S. J., Alem, O. & Romalis, M. V. Subfemtotesla radio-frequency atomic magnetometer for detection of nuclear quadrupole resonance. *Appl. Phys. Lett.* **89,** 214106 (2006).
97. Savukov, I. M., Seltzer, S. J. & Romalis, M. V. Detection of NMR signals with a radio-frequency atomic magnetometer. *J. Magn. Res.* **185,** 227–233 (2007).
98. O'Hara, K. M. *et al.* Ultrastable CO_2 laser trapping of lithium fermions. *Phys. Rev. Lett.* **82,** 4204–4207 (1999).
99. Moler, K. A., Kirtley, J. R., Hinks, D. G., Li, T. W. & Xu, M. Images of interlayer Josephson vortices in $Tl_2Ba_2CuO_{6+\delta}$. *Science* **279,** 1193–1196 (1998).
100. Chatraphorn, S., Fleet, E. F., Wellstood, F. C., Knauss, L. A. & Eiles, T. M. Scanning SQUID microscopy of integrated circuits. *Appl. Phys. Lett.* **76,** 2304–2306 (2000).

Acknowledgements

This work is supported by DOD MURI grant No. N00014-05-1-0406. We are grateful to E. B. Alexandrov, M. V. Balabas, G. Bison, S. Bale, W. Gawlik, J. Higbie, M. Ledbetter, I. M. Savukov, D. Stamper-Kurn, A. Sushkov, M. Vengalattore and A. Weis for providing valuable input for this review.

Competing financial interests

The authors declare no competing interests.

©2007 Nature Publishing Group

2.2 Improving LGS through polarization switching - Fan

Article | OPEN

Improving sodium laser guide star brightness by polarization switching

Tingwei Fan, Tianhua Zhou & Yan Feng

Scientific Reports **6**, Article number: 19859 (2016)
doi:10.1038/srep19859
Download Citation

Adaptive optics Astronomical instrumentation
Astronomical optics Atom optics
Atomic and molecular interactions with photons

Received: 07 July 2015
Accepted: 17 December 2015
Published online: 22 January 2016

Abstract

Optical pumping with circularly polarized light has been used to enhance the brightness of sodium laser guide star. But the benefit is reduced substantially due to the precession of sodium atoms in geomagnetic field. Switching the laser between left and right circular polarization at the Larmor frequency is proposed to improve the return. With ESO's laser guide star system at Paranal as example, numerical simulation shows that the return flux is increased when the angle between geomagnetic field and laser beam is larger than 60°, as much as 50% at 90°. The proposal is significant since most astronomical observation is at angle between 60° and 90° and it only requires a minor addition to the delivery optics of present laser system.

Introduction

What is the nature of the dark matter and dark energy and how many Earth-like and habitable planets populate the Galaxy are the examples of big questions to be answered in astronomy in next decades[1]. As a powerful tool for comprehensive understanding of the Universe, the ground-based large-aperture telescopes advanced rapidly with higher sensitivity and higher spatial resolution[2] and achieved significant observations[3]. The high spatial resolution is possible thanks to a technology known as adaptive optics (AO), which corrects blurred images introduced by atmospheric turbulence in real time[4]. Laser guide star (LGS) technique enables the creation of artificial beacons, so that AO observations of astronomical targets that are themselves too faint to be used for such measurement can be performed[5]. The so-called sodium LGS is generated by exciting the mesospheric sodium atom layer at 90 km above the sea level with a 589 nm laser, which is widely used at present astronomical telescopes and considered best choice of beacons[6,7].

The brightness of the artificial star is one of the key parameters determining the performance of AO. Improving sodium excitation efficiency by optimizing the spectral, temporal and polarization characteristics of the 589 nm laser beam has been a focus of study in the astronomical community. The use of circularly polarized laser was proposed to have brighter guide star utilizing the optical pumping process. The increase in return photons for circularly over linearly polarized light has been reported both experimentally and theoretically[8,9,10].

The benefits of optical pumping are substantially reduced with the presence of geomagnetic field, because the sodium atoms precess along the magnetic field[11,12,13]. The precessing atoms are reoriented faster than the time it takes to establish a beneficial distribution. Precession of the angular momentum does not occur when the laser beam is parallel to the magnetic field, but is maximized for the perpendicular case. Unfortunately, large angles are more typical in astronomical observing. Thomas J. Kane *et al.* proposed to use a laser source pulsed at the Larmor frequency for improving the brightness of sodium LGS[14]. It works because it allows the laser light to interact with the atoms at a fixed point in the precession cycle. Their simulation shows a photon return double that of an optimized cw laser at the same average power for large angles between laser beam and geomagnetic field. But sodium guide star lasers pulsed at this frequency range are not available and technically challenging to develop.

In this paper, we propose a method of “magnetically resonant pumping” with currently available cw laser to overcome the problem induced by the magnetic field. Magnetically resonant pumping is achieved by switching the polarization of the cw guide star laser between left and right circular polarization at a rate of Larmor frequency. Numerical simulation with ESO’s laser guide star system at Paranal as example shows that the return flux can be increased at most astronomical observation angle and as much as 50%. Note that the gain in LGS brightness is achieved with only minor modification to the optics after the currently installed cw laser.

Results

The proposal

The proposal of magnetically resonant pumping by polarization switching is sketched in Fig. 1. Figure 1a illustrates the energy levels of $3^2 P_{3/2}$ and $3^2 S_{1/2}$ involved in the sodium D_2 transitions[15]. The D_2a transition from F = 2 ground state is usually chosen in LGS application for higher oscillation strength. When the laser beam is left circular polarization (σ+), population migrates toward the $3^2 S_{1/2}$ (F = 2, m = 2) substate due to transition selection rules. Finally the atoms cycle on the transition from $3^2 S_{1/2}$(F = 2, m = 2) to the $3^2 P_{3/2}$(F = 3, m = 3), which has the highest transition cross section, and effectively become a two-level system[16]. This beneficial redistribution of angular momentum states is called “optical pumping”.

Figure 1: Schematic diagram of the polarization switching method for improving the sodium excitation.

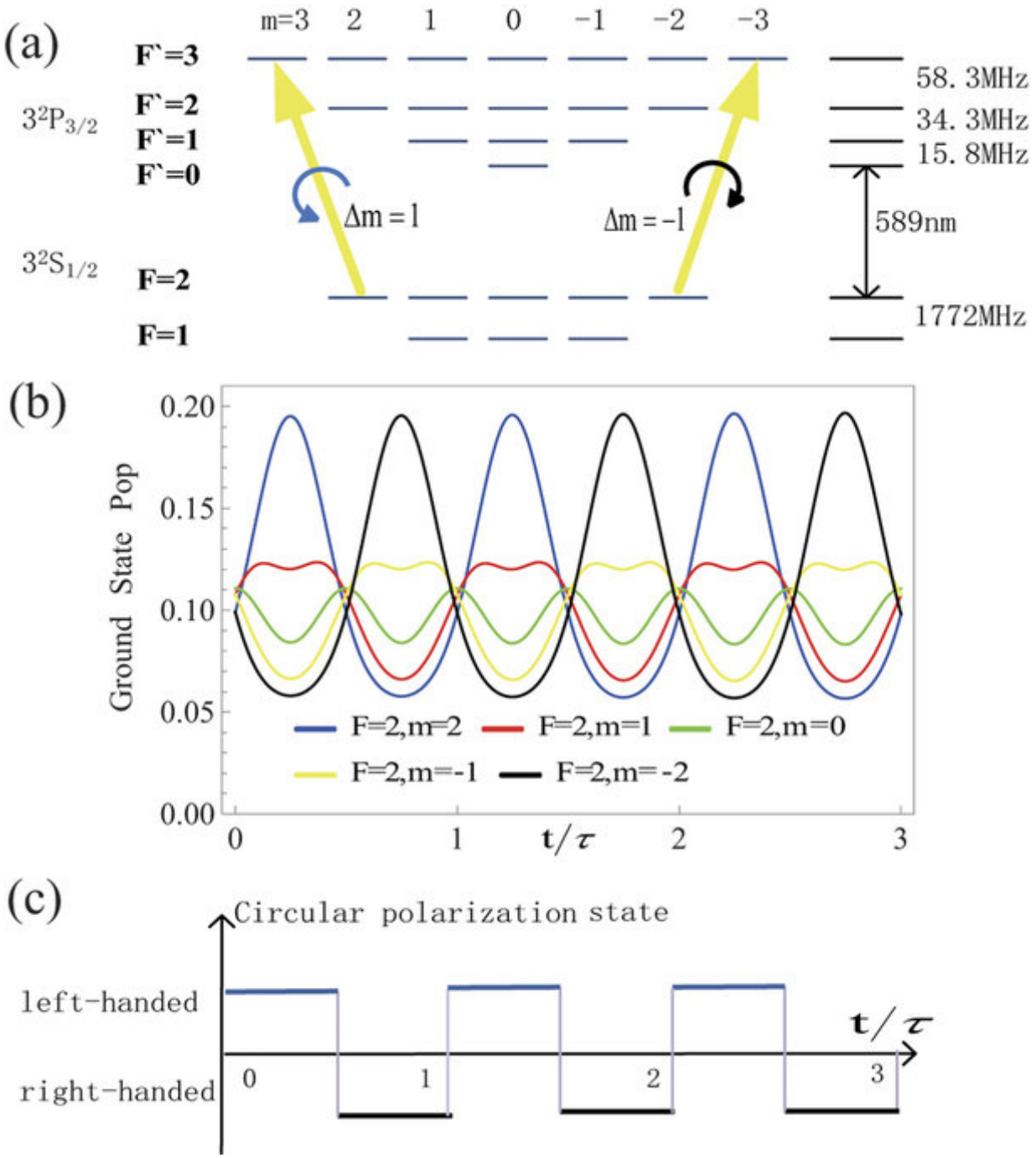

(**a**) the sodium D_2 transitions and energy levels. (**b**) Population dynamics on the five F = 2 ground state magnetic sublevels when the angle between laser beam and magnetic field θ is $\pi/2$. τ is the period of Larmor precession. (**c**) The timing diagram of laser polarization switching.

However, sodium atoms with angular momentum precess around the geomagnetic field. The population oscillates between m substates at a Larmor frequency. Therefore, the benefits of optical pumping are reduced to a large extent, especially for the case of large angle between the beam and the magnetic field (θ). The benefit of optical pumping is almost completely eliminated if the beam is perpendicular to the field. Unfortunately, angles closer to perpendicular are more representative in astronomical observing.

We propose a method to overcome the influence of geomagnetic field by switching the polarization of a cw guide star laser between left and right circular polarization at a rate of Larmor frequency. Figure 1c illustrates the proposed polarization switching pattern, the Larmor precession period in a magnetic field B equals $\tau = (2\pi\hbar)/(g_F\mu_B B)$, where μ_B is the Bohr magneton (9.274×10^{-24} J/T), and g_F is the Landé factor. The polarization of the laser switches between left and right circular at a half of Larmor period. Figure 1b shows the corresponding population dynamics on the magnetic sublevels when $\theta = \pi/2$. The groundstate populations oscillate at the same period of Larmor precession. When the $3^2 S_{1/2}(F = 2, m = 2)$ substate has higher than average population, the laser polarization is $\sigma+$. The laser excites sodium atom from $3^2 S_{1/2}(F = 2, m = 2)$ to $3^2 P_{3/2}(F = 3, m = 3)$, which has the highest transition strength. When the $3^2 S_{1/2}(F = 2, m = -2)$ substate has higher population, the laser polarization is right circular polarization ($\sigma-$). The laser then excites sodium atom from $3^2 S_{1/2}(F = 2, m = -2)$ to $3^2 P_{3/2}(F = 3, m = -3)$, which again has the highest transition strength. By this way, the sodium atoms are excited at a magneto-optical resonance. Higher excitation rate and fluorescence return is expected.

Such polarization switching can be implemented in existing cw laser guide star systems rather readily. A quarter wave plate is usually inserted in the laser delivery path to generate a circular polarized beam from a linearly polarized beam for optical pumping. To achieve polarization switching, one can exchange the quarter wave plate with an electro-optic phase modulator, and align the polarization of the laser at 45° angle with the optical axis of the electro-optic crystal. Applying voltage on the crystal will produce a variable phase delay between the ordinary and extraordinary field components. Therefore, if one applies appropriate voltage on the crystal to produce a phase delay of $-\pi/2$ and $\pi/2$ alternately, the laser will be switched between left and right circular

polarization. The required switching frequency is on the level of 100 kHz. Such electro-optic phase modulator is commercially available.

The numerical model

Simulations of the interaction of sodium atoms with laser have been implemented by many researchers[10,17,18,19]. To calculate the observed fluorescence, the evolution of the atoms is modeled using the optical Bloch equations for atomic density matrix, which describes the statistical state of the atomic ensemble. The simulation is based on the open-source LGSBloch package for Mathematica[20]. Program for the polarization switching is implemented to carry out the calculation. A piecewise function is used to define the polarization switching as instantaneous square-wave switching. Similar results are expected for square wave switching with nanosecond leading and falling edges. Sine-wave modulation of polarization is also simulated, but the improvement in the return flux is not obvious. So sine-wave polarization modulation is not to be discussed here. The fluorescent photon flux per solid angle emitted at a given direction is found as the expectation value of a fluorescence operator.

In our simulation, part of atomic, atmospheric, and mesospheric parameters are standard parameters as defined in Table 1 of ref. 10. Taking ESO's laser guide star system at Paranal as an example, the laser parameters are as follow: laser power centered at D_2a line is 18 W, the repumping light is 2 W (power fraction q = 10%), and the laser linewidth is <5 MHz. The geomagnetic field at 90 km above Paranal is 0.22750 G, which means the precession frequency of sodium atoms is 159.207 kHz. Table 1 lists all simulation parameters relevant to the simulation in this paper. Furthermore, the return flux in our simulation results is defined as $\psi = \Psi/I$ in unit of photons/s/sr/atom/(W/m^2), which is the number of photons per unit time, per solid angle, per atom and per laser irradiance spontaneously emitted in the direction of the launch telescope, as observed in the mesosphere.

Table 1: Simulation parameters and their standard nominal values.

Simulation results and discussion

The return flux versus laser irradiance is calculated for different polarization states and different angles between laser beam and geomagnetic field. Some of the results are shown in Fig. 2. At a low irradiance level below 0.01 W/m^2, the distribution of sodium states is not affected by the laser. The best return is achieved with a laser exactly centered on the peak of the sodium D_2a line at 589.159 nm. The goal of optimization is to maintain or even exceed the return flux at low irradiance level over a wide range of laser irradiance. In this case, the return signal can increase linearly or even faster with increasing laser power.

Figure 2: Calculated return flux for different conditions.

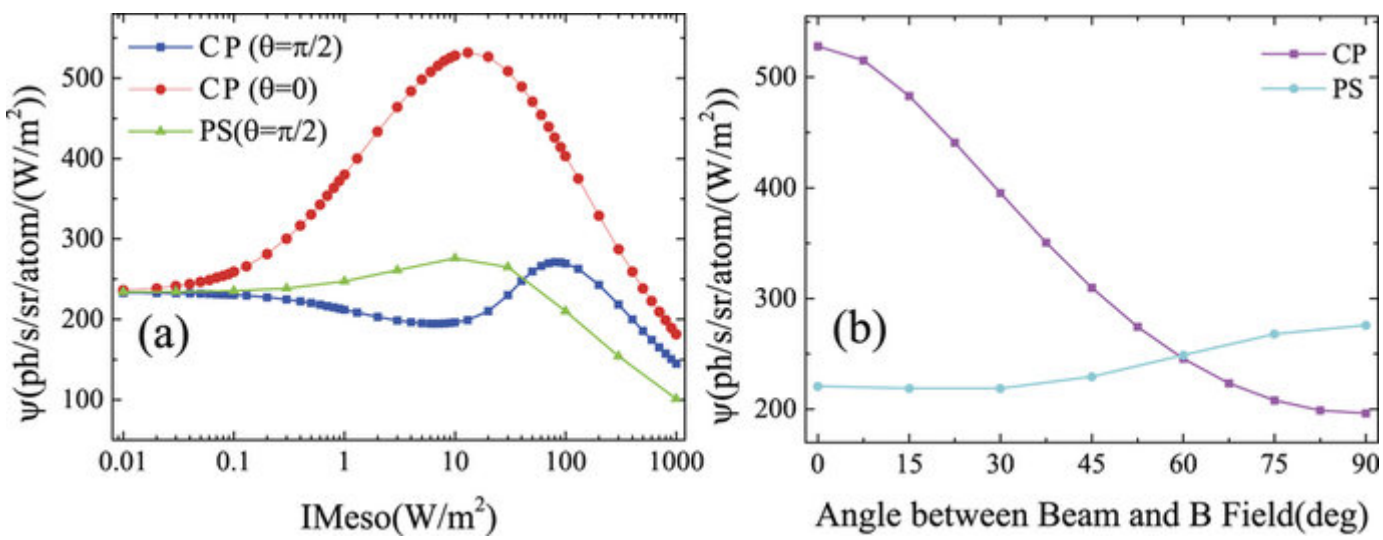

(**a**) Specific return flux ψ(I) for different polarization conditions and different angles between laser beam and magnetic field θ. CP stands for circular polarization, and PS stands for polarization switching. (**b**) The calculated return flux ψ versus θ at a laser power intensity of 10 W/m^2 with repumping power fraction of 0.1.

When the laser is circularly polarized and projects parallel to the geomagnetic field (θ = 0), Larmor precession is absent and the return flux increases with laser power and reaches a maxima at around 10 W/m^2 due to optical pumping. However, when the laser is perpendicular to the geomagnetic field ($\theta = \pi/2$), the effect of optical pumping is completely suppressed by Larmor precession. The return flux decreases with respect to laser power and reaches a minima at 10 W/m^2 instead. Also shown in Fig. 2(a) is the results for the proposed polarization switching case at $\theta = \pi/2$. The return flux increases

with respect to laser power and maximizes at 10 W/m^2. The result shows that polarization switching can indeed compensate for the inhibition on optical pumping by Larmor precession. Figure 2(b) shows the return flux versus angle between laser beam and geomagnetic field θ for the cases of cw circularly polarization and polarization switching. When θ is small, circular polarization is better than polarization switching. When θ is greater than 60°, the situation reverses. The gain in the return flux with polarization switching increases with angle θ, and is as much as 50 % at an angle of 90°.

Although the range of angle in which polarization switching has gain is only from 60° to 90°, most telescopes operate in the 60°–90° range in most of the time. Therefore, the proposal is significant, considering it only requires a minor modification to the present cw guide star laser systems installed at telescopes like VLT at Paranal, Chile. In case that the telescope operates below 60° and the influence of Larmor precession is small, one can simply turn off the polarization switching and gain the benefit of optical pumping.

The population dynamics is investigated to understand the mechanism of return flux improvement better. Figure 3(a,b) shows occupation probabilities evolution of the eight ground state magnetic sublevels for $\theta = \pi/2$ after switching on the laser, with and without polarization switching, respectively. Without polarization switching, populations on the five F = 2 magnetic sublevels decrease gradually, while populations on the three magnetic sublevels of F = 1 increase. Population oscillation is seen for the F = 2 sublevels, which is the sign of Larmor precession. The population becomes stable in about 50 Larmor periods. With polarization switching, the populations of the magnetic sublevels (F = 2, m = 2) and (F = 2, m = −2) oscillate and become the highest alternatively during one Larmor period. The laser switches between left and right circular polarization within one Larmor period correspondingly. That is why it can excite the sodium atom more efficiently. The populations on the F = 2 and m = 1, 0, −1 sublevels also oscillate but in a smaller scale, and decline slowly. Populations on the three magnetic sublevels of F = 1 increase gradually as well, which indicates that the down pumping effect is obvious when the repumping power fraction is 0.1. The repumping power is not high enough.

Figure 3: Occupation probabilities of the eight ground state's magnetic sublevels as functions of the normalized time $\tilde{t} = t/\tau$ for $\theta = \pi/2$ and I = 10 W/m^2.

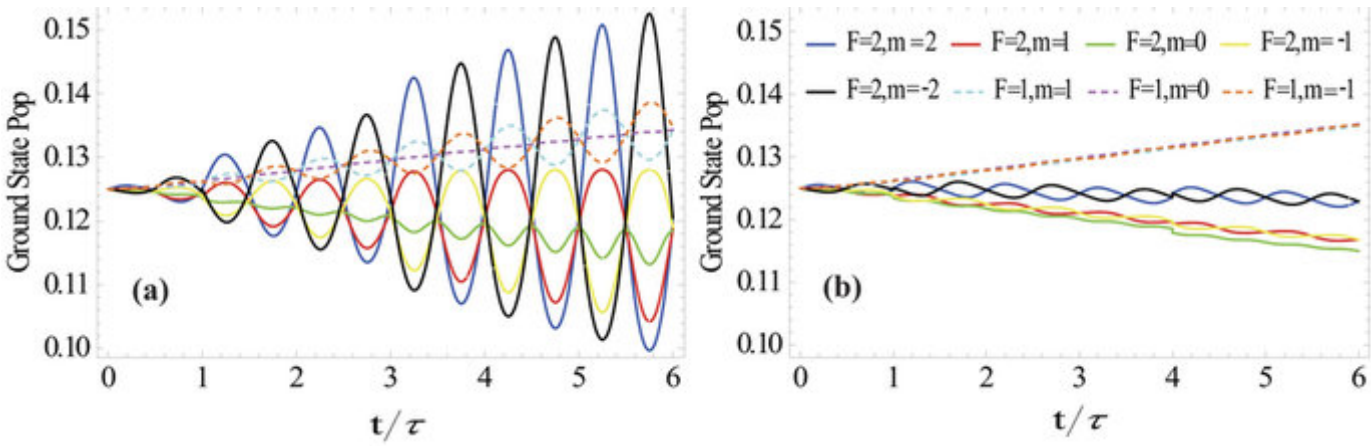

(a) Polarization switching at Larmor frequency of 159.207 kHz, (**b**) cw laser of single polarization state.

Keeping the total laser power constant at 20 W, the return flux versus repumping fraction q is then calculated and shown in Fig. 4(a). The optimum repumping laser fraction is found to be about 20%. Since photon return does not vary significantly with repumping ratio q, only about 5% for q value from 0.1 to 0.2, in practice q can be optimized empirically. The return flux versus angle (as Fig. 2(b)) is calculated again for the case of 20% repumping. The results are shown in Fig. 4(b). For both cw circularly polarization and polarization switching cases, the return fluxes increase slightly at large θ. The benefit of the polarization switching remains at angle >60°. Fig. 4(c,d) shows the population dynamics of the eight ground state's magnetic sublevels in the cases of q = 0.1 and q = 0.2 for comparison. It is clear that, for the q = 0.2, populations on the three magnetic sublevels of F = 1 are relatively low. The populations on the F = 2 sublevels (m = 2 and −2 magnetic sublevels in particular) are higher due to better repumping, which explains the higher return flux.

Figure 4: Specific return flux in case of $\theta = \pi/2$ and I = 10 W/m^2.

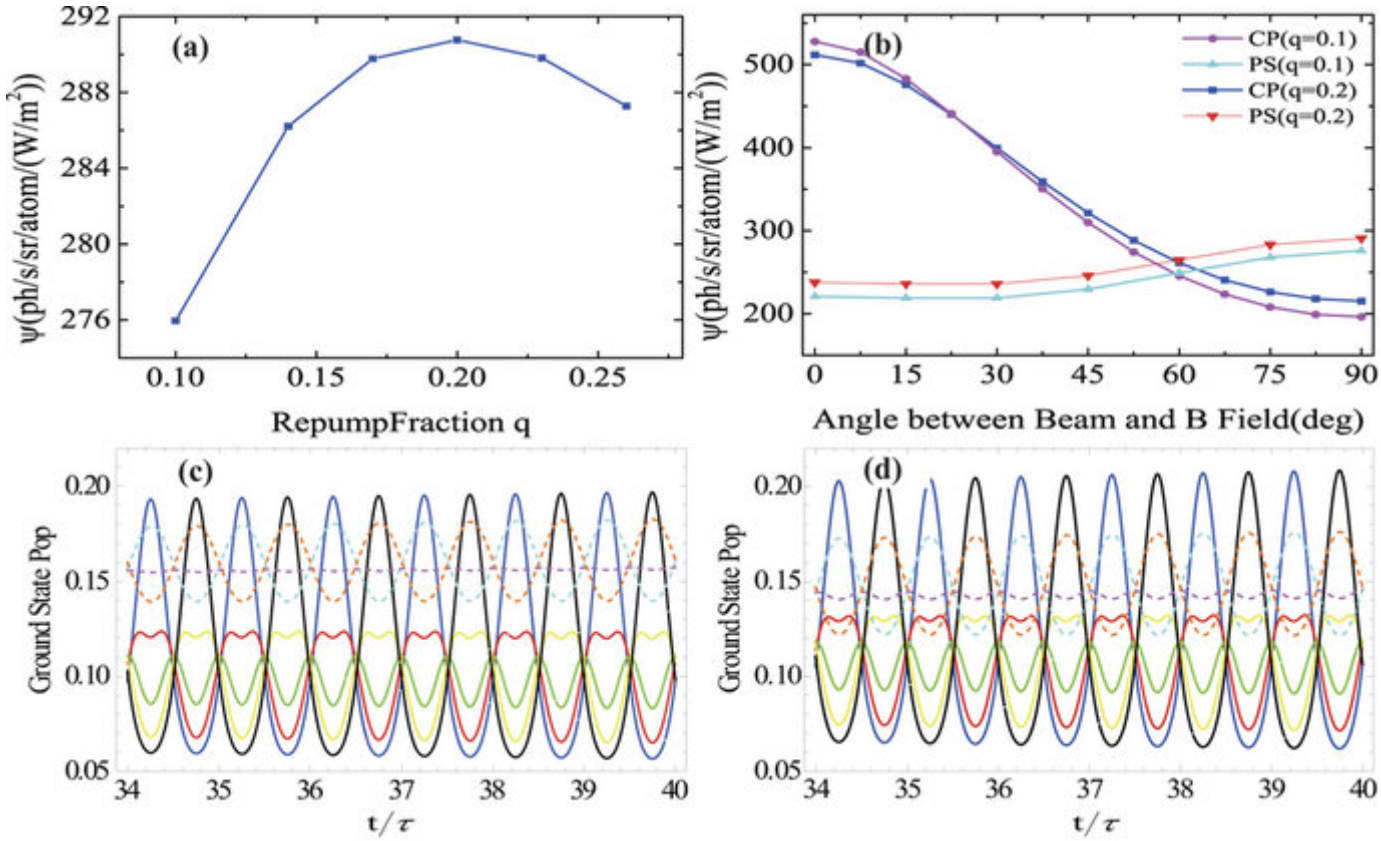

(**a**) return flux ψ as function of repumping fraction q, and (**b**) calculated return flux ψ versus angle between laser beam and magnetic field for both q = 0.1 and q = 0.2. Occupation probabilities evolution of the eight ground state's magnetic sublevels at (**c**) q = 0.1 and (**d**) q = 0.2. The figure (**c**,**d**) share the same legend as in Fig. 3(b).

In above calculations, the polarization switching frequency is set to resonant with the Larmor precession. However, the Larmor frequency is proportional to the local geomagnetic field at the sodium layer, and therefore varies with the laser projection direction. Is it necessary to adjust the switching frequency with different observing direction? The dependence of return flux on the polarization switching frequency is therefore calculated, the result is shown in Fig. 5.

Figure 5: ψ as a function of the polarization switching frequency at I = 10 W/m^2 and $\theta = \pi/2$.

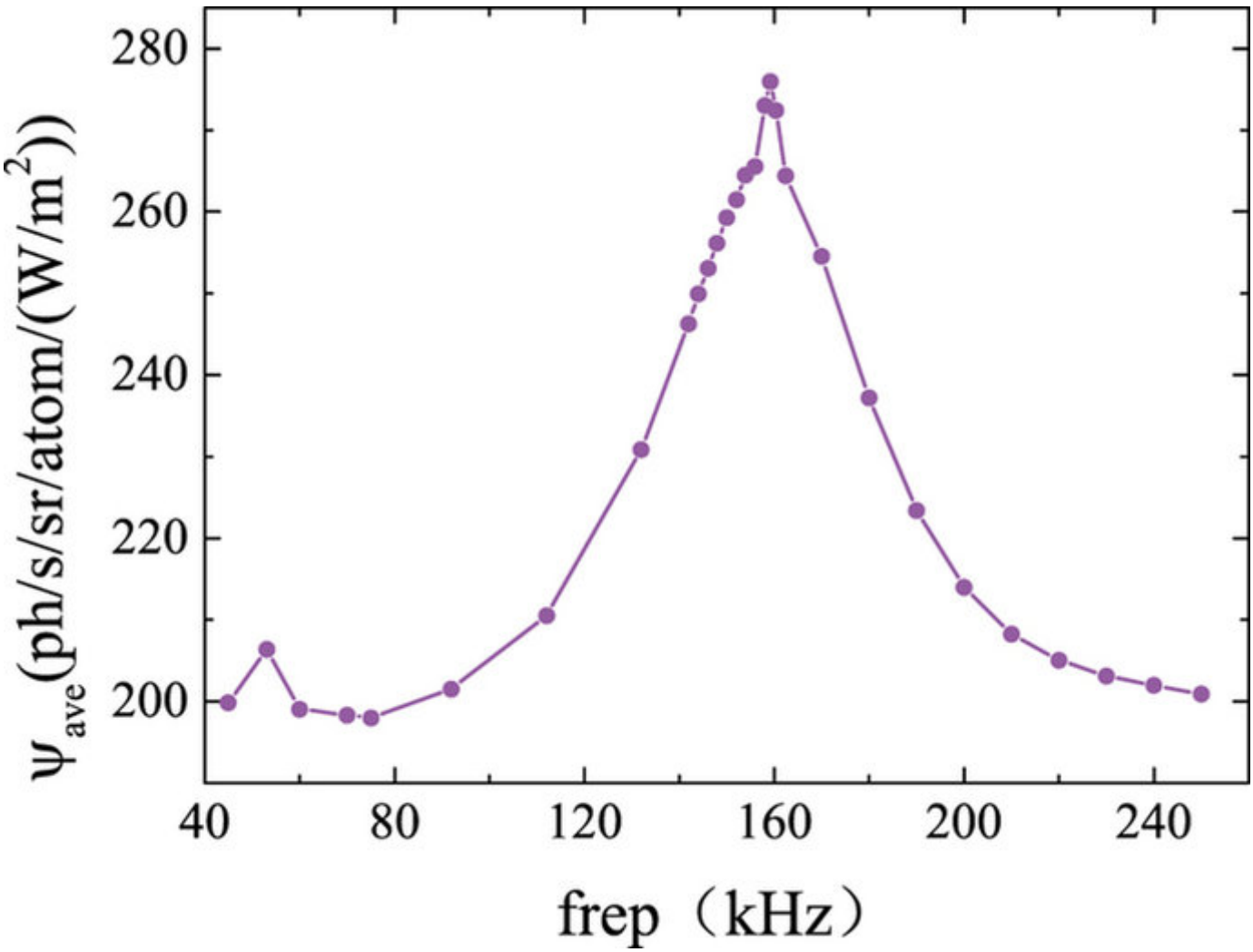

The return flux peaks at Larmor frequency f_L as expected. Interestingly, there is a small peak at $f_L/3$ as well, but no peak at $f_L/2$. This observation is different from the pulsed laser pumping method, where the return flux peaks at all the subharmonics of Larmor frequency[14]. When the frequency is f_L, the laser switches the polarization every half Larmor period as illustrated in Fig. 1. The population dynamics is driven synchronously. If the frequency is $f_L/2$, the laser switches every full Larmor period. As seen in Fig. 1, the groundstate populations oscillate a full circle in one Larmor period, so the enhancement in sodium excitation is lost. If the frequency is $f_L/3$, the laser switches the polarization every 1.5 Larmor period. A reduced resonant peak is expected. The full width half maximum width of D_2a line "polarization magneto-optical resonance" is found to be

about 40 kHz. In Paranal, a ± 30° scanning range of telescope means a geomagnetic field variation of about 100 nT at sodium layer[21], which corresponds to a Larmor frequency change of only 0.7 kHz. The wide polarization magneto-optical resonance is beneficial for the Na laser guide star application, because it suggests that there is no need to adjust the switching frequency when observing astronomical objects at different directions.

The magneto-optical resonance of Na excitation has been proposed for remote measurement of magnetic field. In ref. 22, J. M. Higbie *et al.* considered to measure the magnetic field at the height of sodium layer by shining a pulsed 589 nm laser and resolving the resonant pulse repetition rate. Since Na guide star laser pulsed at Larmor frequency (a few hundred of kHz) is not available at present, chopping of a cw laser is to be used as excitation source. Since the optimum laser duty cycle is about 20%, according to their calculation, a majority (80%) of the laser power is lost. Obviously, polarization switching of currently available cw laser can also be used to measure the magnetic field by finding the Larmor frequency. It has an advantage of no laser power lose and, therefore, higher return signal, which is technically important for such photon hungry application.

In conclusion, we propose to improve the brightness of the cw sodium LGS by switching the laser between left and right circular polarization at a Larmor frequency. For the cw laser system installed at ESO Very Large Telescope at Paranal as example, numerical simulation shows that the return flux is improved when the angle between geomagnetic field and laser beam is larger than 60°, by 50% at an angle of 90°. Polarization switching can partly compensate the inhibitory effect of Larmor precession on optical pumping, and brighter sodium laser guide star can be generated. Since most astronomical observation is at angle between 60° and 90° and it only requires a minor addition to the laser launch optics, the polarization switching method is significant for astronomical community and telescope sites where cw Na guide star has been or will be installed. A by-product of the proposal is that the polarization switching method may also be a preferred method for remote measurement of magnetic field.

Additional Information

How to cite this article: Fan, T. *et al.* Improving sodium laser guide star brightness by polarization switching. *Sci. Rep.* **6**, 19859; doi: 10.1038/srep19859 (2016).

References

1. Norvig, P. *et al.* 2020 visions. *Nature* **463**, 26–32 (2010).
2. Cunningham, C. Future optical technologies for telescopes. *Nat. Photon.* **3**, 239–241 (2009).
3. Meyer, L. *et al.* The shortest-known-period star orbiting our Galaxy's supermassive black hole. *Science* **338**, 84–87 (2012).
4. Babcock, H. W. The possibility of compensating astronomical seeing. *Publ. Astron. Soc. Pac.* **65**, 229–236 (1953).
5. Ageorges, N. & Dainty, C. *Laser Guide Star Adaptive Optics for Astronomy. Ch.* 4, 67–87, (Springer: Netherlands, 2000).
6. Max, C. E. Image improvement from a sodium-layer laser guide star adaptive optics system. *Science* **277**, 1649–1652 (1997).
7. Happer, W., Macdonald, G. J., Max, C. E. & Dyson, F. J. Atmospheric-turbulence compensation by resonant optical backscattering from the sodium layer in the upper-atmosphere. *J. Opt. Soc. Am.* A **11**, 263–276 (1994).
8. Rabien, S. *et al.* The ALFA laser and analysis tools. *Exp. Astron.* **10**, 75–88 (2000).
9. Drummond, J. *et al.* The Sodium LGS brightness model over the SOR. AMOS Technical Conference: Adaptive optics, Wailea, Maui, Hawaii. Proceedings of the AMOS Technical Conference: S. Ryan. p. 581–589 (2007, September 12–15).
10. Holzlöhner, R. *et al.* Optimization of cw sodium laser guide star efficiency. *Astron. Astrophys.* **510**, A20 (2010), doi: 10.1051/0004-6361/200913108.

11. Morris, J. R. Efficient excitation of a mesospheric sodium laser guide star by intermediate-duration pulses. *J. Opt. Soc. Am.* A **11**, 832–845 (1994).

12. Milonni, P. W., Fearn, H., Telle, J. M. & Fugate, R. Q. Theory of continuous-wave excitation of the sodium beacon. *J. Opt. Soc. Am.* A **16**, 2555–2566 (1999).

13. Moussaoui, N., Holzlöhner, R., Hackenberg, W. & Bonaccini Calia, D. Dependence of sodium laser guide star photon return on the geomagnetic field. *Astron. Astrophys.* **501**, 793–799 (2009).

14. Kane, T. J., Hillman, P. D. & Denman, C. A. Pulsed laser architecture for enhancing backscatter from sodium. *Proc. of SPIE* **9148**, 91483 G (2014). doi: 10.1117/12.2055632.

15. Steck, D. A., *Sodium D Line Data, revision* 2.1.4(2010) Available at: http://steck.us/alkalidata. (Accessed: 15th September 2014).

16. Bradley, L. C. Pulse-train excitation of sodium for use as a synthetic beacon. *J. Opt. Soc. Am.* B **9**, 1931–1944 (1992).

17. Holzlöhner, R. *et al.* Simulations of pulsed sodium laser guide stars: an overview. *Proc. of SPIE* **8447**, 84470 H (2012), doi: 10.1117/12.924882.

18. Rochester, S. M. *et al.* Modeling of pulsed-laser guide stars for the Thirty Meter Telescope project. *J. Opt. Soc. Am.* B **29**, 2176–2188 (2012).

19. Rampy, R., Gavel, D., Rochester, S. & Holzlöhner, R. Investigations of long pulse sodium laser guide stars. *Proc. of SPIE* **8447**, 84474L (2012), doi: 10.1117/12.926621.

20. Rochester Scientific, LLC (2015). AtomicDensityMatrix and LGSBloch packages. El Cerrito, CA, USA. URL http://budker.berkeley.edu/ADM/.

21. Thébault, E. *et al.* International geomagnetic reference field: the 12th generation. *Earth, Planets Sp.* **67**, 79–97 (2015).

22. Higbie, J. M. *et al.* Magnetometry with mesospheric sodium. *Proc. Natl. Acad. Sci. USA* **108**, 3522–3525 (2011).

Author information

Affiliations

Shanghai Institute of Optics and Fine Mechanics, Chinese Academy of Sciences, and Shanghai Key Laboratory of Solid State Laser and Application, Shanghai 201800, China

Tingwei Fan, Tianhua Zhou & Yan Feng

University of the Chinese Academy of Sciences, Beijing 100049, China

Tingwei Fan

Contributions

T.F. performed the simulation. Y.F. and T.F. wrote the manuscript. T.Z. provided technical support and advice on the work. Y.F. proposed the idea and supervised the project. All authors discussed the results and commented on the manuscript.

Competing interests

The authors declare no competing financial interests.

Corresponding author

Correspondence to Yan Feng.

Comments

By submitting a comment you agree to abide by our Terms and Community Guidelines. If you find something abusive or that does not comply with our terms or guidelines please flag it as inappropriate.

This work is licensed under a Creative Commons Attribution 4.0 International License. The images or other third party material in this article are included in the article's Creative Commons license, unless indicated otherwise in

the credit line; if the material is not included under the Creative Commons license, users will need to obtain permission from the license holder to reproduce the material. To view a copy of this license, visit http://creativecommons.org/licenses/by/4.0/

Scientific Reports ISSN 2045-2322 (online)

SPRINGER NATURE

© 2017 Macmillan Publishers Limited, part of Springer Nature. All rights reserved.

partner of AGORA, HINARI, OARE, INASP, ORCID, CrossRef and COUNTER

2.3 Improve Atmospheric Distortion Measurement - Fugate

Measurement of Atmospheric Wavefront Distortion Using Scattered Light from a Laser Guide-Star
Fugate, R Q;Fried, D L;et al
Nature; Sep 12, 1991; 353, 6340; ProQuest
pg. 144

Measurement of atmospheric wavefront distortion using scattered light from a laser guide-star

R. Q. Fugate*, D. L. Fried†, G. A. Ameer†, B. R. Boeke*‡, S. L. Browne†, P. H. Roberts†, R. E. Ruane*‡, G. A. Tyler† & L. M. Wopat*

* Starfire Optical Range, Phillips Laboratory/LTE, Kirtland AFB, New Mexico 87117-6008, USA
† Optical Sciences Company, PO Box 1329, Placentia, California 92670, USA
‡ Present address: Rockwell Power Systems, Albuquerque, New Mexico 87117, USA

THE possibility of using an artificial 'guide-star' to measure optical wavefront distortion caused by atmospheric turbulence has been discussed for some time[1–4], but few experimental data are available[5]. Here we report experimental results demonstrating that atmospheric wavefront distortion can be measured by taking fast 'snapshots' of a guide-star formed by light scattered from a laser beam focused in the upper atmosphere. These results agree with a theoretical prediction[6] that the mean-square wavefront error created by using an artificial guide-star at a finite distance rather than a real (infinitely distant) star is proportional to the five-thirds power of the telescope aperture. Using this understanding of the physics, we have demonstrated continuous, real-time atmospheric compensation of a 1.5-m telescope using a high-pulse-rate laser, pulse-synchronized wavefront sensor and deformable mirror, and have been able to resolve the 1.3-arcsecond binary star 53 ξ Ursa Majoris in an exposure time of only one second.

The US Department of Defense has been developing laser guide-star adaptive optics since October 1981, but has allowed public release of information only since May 1991. The programme started following a suggestion made by Julius Feinleib of Adaptive Optics Associates for creating artificial stars from the Rayleigh scattering of a laser beam focused in the upper atmosphere. Because rays from the laser guide-star beacon may travel along a different-path from those of the star under observation, the effects of atmospheric turbulence may be quite different in each case, resulting in focus anisoplanatism. Fried assessed the usefulness of such a finite-range guide-star, and showed that useful performance could be achieved even with the wavefont-distortion error caused by focus anisoplanatism. In 1982, laser excitation of mesospheric sodium was suggested[9] as a means of generating artificial guide-stars at a significantly higher altitude to reduce the focus anisoplanatic error. The Defense Advanced Research Projects Agency (DARPA) sponsored two experiments—one to test the Rayleigh scattering idea and the other to test the resonant mesospheric sodium concept. Here we report the results of the Rayleigh guide-star experiment conducted at the Starfire Optical Range (SOR) in New Mexico during 1983. The sodium experiment was conducted at White Sands Missile Range, New Mexico, during 1984[10]. In 1985, independently of the work of the Department of Defense, the idea of using the Rayleigh and sodium laser guide-stars concepts was suggested[1]. Thompson and Gardner[5] generated a mesospheric sodium guide-star and verified radiometric predictions. In mid-1988, the Massachusetts Institute of Technology Lincoln Laboratory showed atmospheric compensation on a 0.6-m aperture using a Rayleigh laser guide-star operating at a few pulses per second and a special 'go-to' control system for their adaptive optics system. In February 1989, our group at Phillips Laboratory demonstrated high-bandwidth, closed-loop atmospheric compensation on the SOR 1.5-m telescope using a high-repetition-rate Rayleigh laser-guide-star. We analysed stellar images formed at an average wavelength of 0.88 ± 0.05 μm while operating the adaptive optics at a closed-loop bandwidth of 30–65 Hz using a laser guide-star at a range of 10 km. We achieved Strehl ratios (ratio of actual peak intensity to diffraction limited peak intensity) of >0.2, full-width-half-maximum resolution of 0.18 arcsec, and image intensity improvements of nearly an order of magnitude in the presence of visible wavelength atmospheric seeing conditions of 2 arcsec (R.Q.F. *et al.* manuscript in preparation). Figure 1 shows the improvement in a binary star image achieved with the laser guide-star adaptive optics operating on the 1.5-m telescope.

The primary objective of our first laser guide-star experiment performed in 1983 was to determine whether a laser beam focused in the atmosphere really could be used as a beacon to

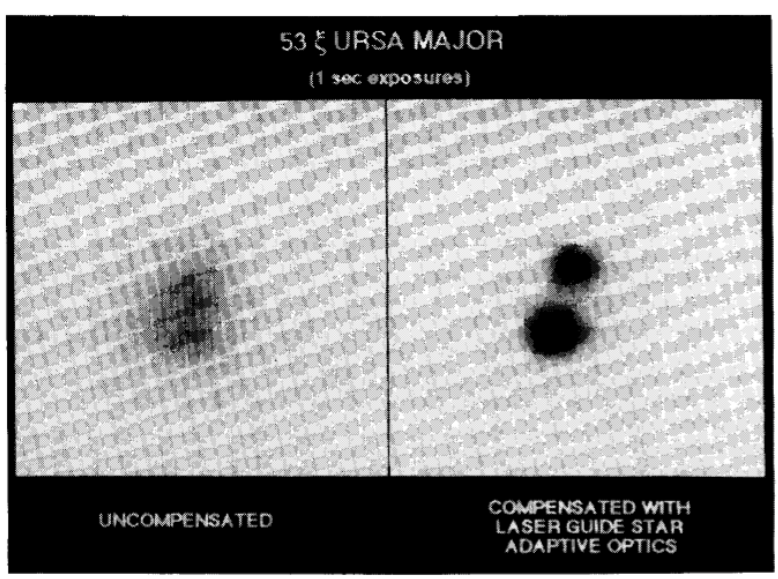

FIG. 1 Charge-coupled-device camera images of the binary star 53 ξ Ursa Majoris (m_v=4.2 and 4.5, separation ~1.3 arcsec) made through the SOR 1.5-m telescope. Each image is 6.24 arcsec square exposed for one second at an average wavelength of 0.88 μm and spectral bandwidth of 0.1 μm. The laser guide-star adaptive optics was operated at 65-Hz closed-loop bandwidth. The peak intensity in the compensated image is 8.6 times the peak intensity in the uncompensated image. The Strehl ratio of the compensated image is ~0.1 and the full-width-half-maximum size of the bright star image is 0.48 arcsec. Full-width-half-maximum image sizes of <0.2 arcsec were achieved for exposures of ~20 ms. The degradation at long exposures is due largely to imperfect overall tilt compensation provided by a separate tracker and steering mirror.

Reproduced with permission of the copyright owner. Further reproduction prohibited without permission.

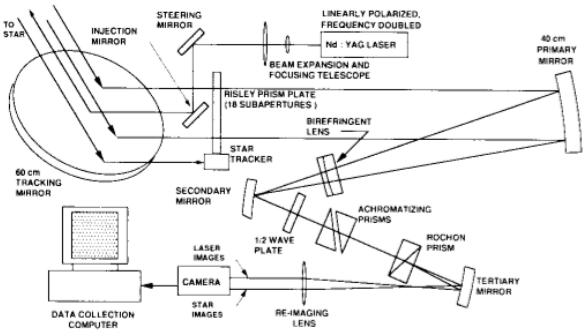

FIG. 2 Schematic diagram of the experimental set-up used for Rayleigh laser guide-star measurements of atmospheric-turbulence-induced wavefront distortion. With the exception of the 60-cm tracking mirror, all components were mounted on a large optics table. The 40-cm-diameter wavefront-distortion-sensing telescope consisted of an off-axis paraboloidal primary mirror and a convex secondary mirror. Hartmann sensor subapertures for measurement of wavefront distortion were defined by 18 Risley prisms mounted in a large plate in front of the 40-cm primary mirror. The subapertures were arranged on two concentric circles with 12 on the outer ring and six on the inner ring. The telescope optics focused all the light on a split photocathode intensifier coupled to a charge-injection-device sensor array. Because of the different settings of each of the Risley prisms, 18 distinct images of a point source were formed. The set of 18 associated centroids defined the wavefront tilt at each of the subapertures. The birefringent lens compensated for the difference in focus between the laser and star beacons.

measure atmospheric-turbulence-induced wavefront distortion, and to assess the quality of the measurement values it produced. The reference (or 'truth') results for this experiment were provided by simultaneous wavefront-distortion measurements using a star as the beacon. Wavefronts determined using the laser beacon were compared with simultaneous wavefront-distortion measurements made using on-axis starlight, the r.m.s. discrepancy between the two wavefronts being compared with theory. The optics were arranged so as to direct the laser beam within a few microradians of the star, thereby, ensuring that light from both the star and the laser guide-star beacons propagate through nearly identical turbulence.

Figure 2 shows the essential features of the experimental set-up. The tracking mirror was positioned by a two-axis gimballed mount under the control of a low-bandwidth star tracker which kept the optical axis of the 40-cm phase-measurement telescope within one micoradian of the star's average position. We used the star Polaris for these experiments because the two-axis gimbal was limited to $\pm 1°$ of total motion in each axis. The 300 mJ per pulse, Q-switched laser beam which we used was expanded to 10-cm diameter, in nearly collimated form, and directed out of the centre of the 40-cm wavefront-sensing aperture, and aligned to be parallel to its optical axis. The beam was focused at a range of 5 km for most tests and the sensor was range-gated to accept backscattered light from 4.5 to 5.5 km.

The wavefront sensor consisted of an 18 subaperture Hartmann-type arrangement, each subaperture defined by an 8-cm diameter Risley prism. The subaperture geometry consisted of two concentric circles with 12 subapertures on the outer circle and six on the inner circle. Each subaperture produced its own distinct image of a beacon, the location of each of the images being determined by the setting of the corresponding Risley prism. The prisms were rotated in their mounts to provide adequate space between the 18 subaperture images formed at the focal plane of the 40-cm diameter telescope. Two distinct sets of 18 such images were formed, one set being images of the laser guide-star and the other being images of the star.

To measure wavefont distortion simultaneously with the star and laser beacons, light from the two sources, after passing through the subapertures, was spatially separated by polarization, using the Rochon prism. This light, now sufficiently divided so as to be able to form two distinct sets of 18 spots, was imaged onto separate halves of a specially made, independently gated, split photocathode intensifier coupled to a charge-injection-device sensor array. All the light from the laser return was directed to one photocathode (where 18 suitably separated, laser spot images were formed) as the Rayleigh backscatter process does not depolarize the linearly polarized outgoing laser beam. The starlight was equally divided by the Rochon prism between the two halves of the photocathode as this light is randomly polarized—but the starlight going to the laser half of the photocathode was in effect neglected because of the shortness of the time for which that part of the photocathode was on. The laser-range gate was on for only a few microseconds,

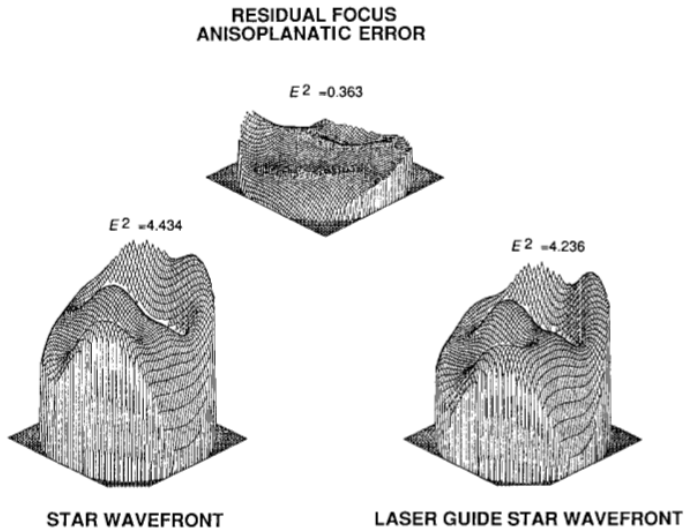

FIG. 3 Representative sample of measured wavefront distortions and distortion difference. The lower-left plot shows the wavefront distortion measured using the starlight whereas the lower-right plot shows the wavefront distortion measured using the laser light—the Rayleigh laser guide-star. These distortions have mean square values of 4.434 rad^2 and 4.236 rad^2 respectively. The centre plot shows the difference between these two wavefronts. Its mean-square value of 0.363 rad^2 is a measure of the magnitude of the focus anisoplanatism—in this case for a 40 cm diameter aperture, viewing at a 35° elevation angle, using a guide-star at 5 km range, and with wavefronts corresponding to a wavelength of 0.53 μm.

Reproduced with permission of the copyright owner. Further reproduction prohibited without permission.

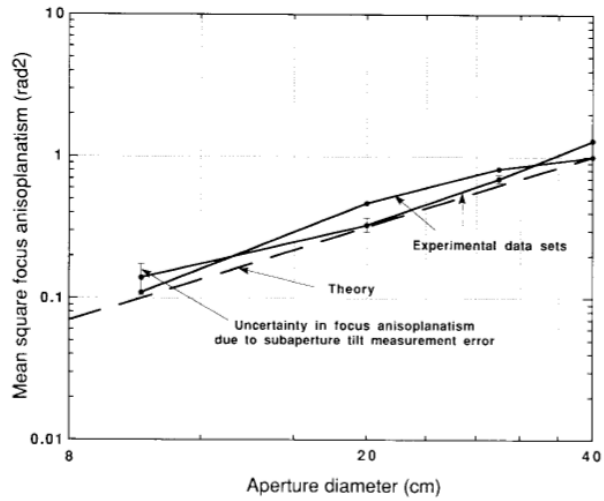

FIG. 4 Mean square focus anisoplanatism error. The term focus anisoplanatism refers to the fact that wavefront distortion measured with a laser guide-star will be somewhat different from what is needed to correct the turbulence induced wavefront distortion of light from a co-aligned star or other source more distant than the laser guide-star. When a laser guide-star is used to control an astronomical adaptive optics system, the focus anisoplanatism will result in a wavefront correction error. We show here the measured focus anisoplanatism for viewing a laser guide-star at 35° elevation and 5 km range, the error being expressed in radians^2 for a wavelength of 0.53 μm. The points shown represent two sets of data each formed by averaging over 35 wavefront distortion measurements. The broken straignt line represents a theoretical prediction [cf. equation (1)] for which $d_0 = 0.39$ m. The measurement data not only shows the predicted five-thirds power dependence on aperture diameter, but also lies surprisingly close to the $d_0 = 0.39$ m theoretical curve. The uncertainty in our measurement of focus anisoplanatism is indicated by the error bars associated with one of the data sets. These errors were computed using a theoretical treatment of induced mean-square error asssociated with the difference of two reconstructed wavefronts [15, 16]. This theory utilizes the rms subaperture tilt measurement error—experimentally determined for this experiment to be 650 nanoradians by comparison of identical wavefront exposures (i.e. star-star and laser-laser) on each half of the split photocathode sensor. The subaperture tilt error was dominated by sensor noise and the fact that the size of the laser-guide-star images were somewhat larger than the diffraction limit.

whereas the starlight gate had to be on for a few milliseconds in order to collect enough light. The starlight gate 'on' period was centred in time on the laser range gate (but was off during the laser firing period). Using this timing and polarization arrangement, only starlight images were formed on one side of the split photocathode, and only laser light images on the other. The birefringent lens compensated the focus for the difference in range to the laser and to the star beacons. A desktop computer and custom-made timing electronics controlled the laser firing, the individual photocathode gating, and the digital data collection by a frame grabber attached to the charge-injection-device sensor.

We processed many frames of raw image data to determine, for each, the centroid position of each spot and thus the tilts (wavefront gradients) for each subaperture. The gradient data were used to reconstruct the wavefornt distortion over the 40-cm aperture, once for the laser beacon data and once for the star data. Figure 3 is a representative example of the wavefront distortion as determined for the star (truth) and for the laser beacon; also shown is the difference between these two, corresponding to what would be the residual error in an adaptive-optics-corrected star wavefront if the laser-beacon data had been used to control the deformable mirror used in the adaptive optics set-up. These results demonstrate qualitatively that laser guide-star beacons are effective in measuring atmospheric-turbulence-induced wavefront distortion.

Theoretical analysis carried out before this experiment predicted that the mean square difference between the tilt-removed laser-beacon wavefront distortion and the star-beacon wavefront distortion should increase with aperture diameter to the five-thirds power[6]. According to theory, a constant of proportionality, d_0, was defined in such a way that

$$\langle E^2 \rangle = (D/d_0)^{5/3} \qquad (1)$$

where D is the aperture diameter and $\langle E^2 \rangle$ is the aperture-averaged square phase difference between the star wavefront and the laser-beacon wavefront, ensemble averaged over turbulence realizations. The parameter d_0 depends on the wavelength of interest, the height of the laser beacon above the ground, and the height dependence of the index of refraction structure function, C_N^2. Physically, one can think of d_0 as the size of a real aperture for which the wavefront error incurred by using the laser guide-star would be one radian (r.m.s.).

Equation (1) represents the mean square error incurred by using the laser guide-star beacon when a real guide-star beacon is not available for use by an adaptive optics system. The error results from the fact that the two sources are at different ranges so rays from the two sources follow different paths through the atmosphere to each point in the aperture. Consequently, at the edge of the aperture, rays from the laser beacon sample the atmospheric turbulence along a (potentially singificantly) different path than do rays from the star. Figure 4 shows $\langle E^2 \rangle$ derived from the experimental measurements, as a function of aperture diameter[13]. The experimental data are in excellent agreement with the theory predicting a $D^{5/3}$ dependence.

The value of d_0 is easily calculated from the data in Fig. 4 and equation (1) as being 0.39 m. The theoretical estimate of d_0 for our wavelength, zenith angle and backscatter altitude, using a nighttime turbulence profile model is 0.39 m[14]. Experiments performed in more benign atmospheric conditions and with a range gate at 15 km, produced mean-square-wavefront errors as low as 0.18 rad^2 and a d_0 of 1.1 m, which is good enough to allow wavefront correction to 1/15 of a wave over our 40-cm aperture. □

Received 23 May; accepted 6 August 1991.

1. Foy, R. & Labeyrie, A. *Astr. Astrophys.* **152**, L29–L31 (1985).
2. Séchaud, M. *et al.* in *Very Large Telescopes and their Instrumentation, Proceedings* Vol II (ed Ulrich, M. H.) 705–714 (European Southern Observatory, Garching, 1988).
3. Beckers, J. M. in *Very Large Telescopes and their Instrumentation Proceedings* Vol II (ed Ulrich, M. H.) 693–703 (European Southern Observatory, Garching, 1988).
4. Gardner, C. S., Welsh, B. M. & Thompson, L. A. *Proc. IEEE* **78**, 1721–1743 (1990).
5. Thompson, L. A. & Gardner, C. S. *Nature* **328**, 229–231 (1987).
6. Belsher, J. F. & Fried, D. L. *Rep. No. TR-576* (Optical Sciences Company Placentia, 1984).
7. Fugate, R. Q. *et al. Bull. Am. Astr. Soc.* **23**(2), 898 (1991).
8. Fried, D. L. & Roberts, P. H. *Rep. No. TR-460* (Optical Sciences Company Plancentia, 1982).
9. Happer, W. & MacDonald, G. *JASON* Rep. No. *JSR-82-106* (MITRE Corp, McLean 1983).
10. Humphreys, R. A. *et al. Optics Lett.* (submitted).
11. Primmerman, C. A., *Bull. Amer. Astron. Soc.* **23**(2), 898 (1991).
12. Primmerman, C. A. *et al. Nature* **353**, 141–143 (1991).
13. Fugate, R. Q. *et al. High Energy Laser Review Group/Propagation Sub-Panel Adaptive Optics Workshop* (Albuquerque, 1984).
14. Tyler, G. A. *Rep. No. TR-582* (Optical Sciences Company, Placentia, 1984).
15. Tyler, G. A. 1983 *Rep. No. TR-545* (Optical Sciences Company, Placentia, 1983).
16. Tyler, G. A. & Fried, D. L. *Rep. No. TR-514* (Optical Sciences Company, Placentia 1983).

ACKNOWLEDGEMENTS. We thank Rhettig P. Benedict Jr and other DARPA officials for sponsoring parts of this work and Donald Hanson of the Air Force Rome Air Development Center for technical discussions and loan of critical test equipment.

Reproduced with permission of the copyright owner. Further reproduction prohibited without permission.

2.4 Kilohertz Picosecond Dye Laser - Gale

A light paper on a kilohertz picosecond dye laser.

ILL Article Request - Courier Free

3/13/2017 3:00.58 PM

Call #: QC350 .O584 v.74-76 (1989 DEC-1990 MAY)
Location: Compact Shelves

OSU ILLIAD TN#: 969132

Journal Title: Optics communications.
Volume: 76
Issue: 2
Month/Year: 1990
Pages: 138-142

ILL Number: 174864023

Borrower: OWS

Article Author: Gale, Pedersen, Schanne
Article Title: Kilohertz picosecond distributed-feedback dye laser system

Odyssey: 158.104.100.188

Borrower: OWS
Lending String:
*ORE,ORZ,NTD,OHS,NNM,PSC

Email: ILL@WILLAMETTE.EDU

Patron:
Maxcost: 10.00IFM

Email: ill@willamette.edu

This item will be invoiced at the end of the month

Photocopy/Loan/Invoice/Postage Charges: **Exempt**

NOTICE:
When available, we have included the copyright statement provided in the work from which this copy was made.

If the work from which this copy was made did not include a formal copyright notice, this work may still be protected by copyright law. Uses may be allowed with permission from the rights-holder, or if the copyright on the work has expired, or if the use is "fair use" or within another exemption. The user of this work is responsible for determining lawful use.

Oregon State University
OSU Interlibrary Loan -- Phone: (541) 737-4488 Email: valley.ill@oregonstate.edu Fax: (541) 737-8267 Ariel:

Pagers:

Initials: _____ NOS: _____ Lacking: _____

BC: Checked Table of Contents: _____ Checked Index: _____

Scanners:

Initials: _____ Date:

KILOHERTZ PICOSECOND DISTRIBUTED-FEEDBACK DYE LASER SYSTEM

G.M. GALE, B. PEDERSEN [1] and P. SCHANNE [2]

Laboratoire d'Optique Quantique du CNRS, Ecole Polytechnique, 91128 Palaiseau, France

Received 8 December 1989

Dual distributed-feedback oscillator–amplifier systems, pumped by a *Q*-switched, mode-locked, cavity-dumped Nd:YAG laser, provide independently tunable, Fourier-transform-limited, synchronized picosecond pulses at megawatt power levels with a repetition rate in kilohertz range.

1. Introduction

The requirement for kilohertz repetition rate, microjoule energy range, tunable picosecond pulses has led to the development of correspondingly high repetition rate pump sources for dye amplification of cw mode-locked dye laser output. These pump sources include *Q*-switched, mode-locked, and cavity-dumped Nd:YAG or Nd:YLF lasers [1–4].

However, these systems are inherently complex as they need two pump lasers (one for the cw dye oscillator and another for the amplifiers) and, in the optimal case of short amplifier pump pulse width, necessitate the precise synchronization of the amplifier pump and the dye oscillator pulses. Further difficulties may arise if two independently tunable amplified pulse trains are required, as temporal jitter [4] between the two trains may cause problems in certain experiments.

We present here a novel system providing two independent, one kilohertz repetition rate, amplified, tunable, picosecond pulse trains, which are essentially Fourier-transform limited and jitter free. This system is based on a single *Q*-switched, mode-locked and cavity-dumped Nd:YAG laser which drives twin distributed-feedback dye laser (DFDL) oscillator–amplifier chains. Because the DFDL requires no external mirrors the experimental set-up is also spatially compact.

[1] Visiting student from the Norwegian Institute of Technology, Trondheim.

[2] On leave from the research section of the French Defence Department.

2. The pump source

The Nd:YAG laser system is drawn schematically in fig. 1. The double lamp continuously-pumped YAG head (Microcontrôle) is placed between two

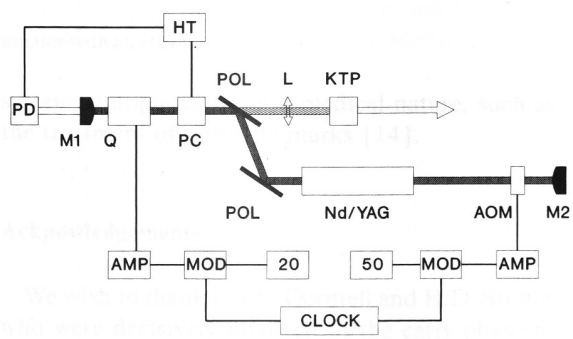

Fig. 1. Schematic of the cavity-dumped, mode-locked, *Q*-switched, continuously-pumped Nd:YAG laser. PD: photodiode. HT: high-voltage triggered Pockels driver. M_1: 800 mm radius 100% convex mirror. Q: acoustic-optic Ar-coated *Q*-switch. PC: lithium niobate AR coated Pockels cell. POL: dielectric polarization-sensitive mirrors. L: lens. KTP: frequency doubling crystal. Nd:YAG: 4×100 mm YAG rod. AOM: Brewster angle acousto-optic mode-locking crystal. M_2: 1200 mm radius 100% convex mirror. AMP: rf amplifier. MOD: rf modulator. CLOCK: 1kHz 8 and 80 μs synchronization pulses for the rf drivers. The numbers in boxes give the rf frequencies employed in MHz.

0030-4018/90/$03.50 © Elsevier Science Publishers B.V. (North-Holland)

divergent reflectors of 800 and 1200 mm radius of curvature, at a distance of 600 mm left and 900 mm right respectively. This leads to a moderately large mode volume inside the YAG rod mode diameter decreasing towards each reflector. Laser emission is polarized by two dielectric polarizers in reflection mode. With a right mirror transmission of 10% and no other elements in the cavity, polarized laser output is 16 W TEM_{00}.

The laser is Q-switched and mode-locked at 50 MHz by quartz acousto-optic elements. The Q-switch is operated at a frequency of between 1 and 2 kHz with an open time of 8 μs. The mode-locking rf of 3 W power is pulsed on during 80 μs in end-synchronism with the Q-switch. Good quality mode-locking and pulse-train energy depend critically on the level of prelasing (intertrain lasing) which may either be adjusted electronically or by orienting the Q-switch.

A single pulse is switched out of the Q-switched, mode-locked pulse train using an antireflection coated lithium Pockels cell. The Pockels cell is driven to quarterwave voltage in 5 ns, just after the passage (from left to right) of a laser pulse, using a high voltage triode triggered by a photodiode detecting end-leakage from the cavity. The switched-out pulse exists the cavity through the dielectric polarizer.

With 100% end-reflectors, the single pulse energy is 800 μJ at 1 kHz (0.8 W) and 500 μJ at 2 kHz (1.0 W). Infrared pulse duration is 70 ps due to the high peak rf power in the mode-locking crystal. The TEM_{00} output is frequency doubled to 532 nm by slightly focussing into a KTP crystal to obtain second harmonic energies of 450 μJ (0.45 W) at 1 kHz and 300 μJ (0.6 W) at 2 kHz. Second harmonic duration is 65 ps in a clean pulse with no detectable leading or trailing satellites. Output energy is remarkably stable, exhibiting short-term fluctuations of the order of ±2%. The laser is normally operated at 1 kHz.

The energies cited above are limited by two factors. The first is the fragility of the antireflection coatings of the lithium niobate crystal which in our system will damage at power levels more than 50% over the stated operating point. Interruption of cavity dumping will also damage the Pockels cell in a few seconds. The second limitation is caused by pump-induced birefringence in the YAG rod which constrains the usable mode volume. Both these restrictions could be somewhat eased by employing Nd:YLF as the active medium, as the lower strain-induced birefringence of this material allows larger beam diameters.

3. The dye laser system

The picosecond dye lasers are based on a modified version of the distributed feedback oscillator described in ref. [5]. The oscillator is schematically drawn in fig. 2. The microjoule energy pump beam at 532 nm, with a duration of 65 ps, is divided into two equal-delay equal-intensity beams which interfere in the dye cell after deviation by a prism and reflection from a rotatable mirror. The rotation axes of the mirrors chosen to minimize beam movement at the dye cell while tuning the laser. A 60° quartz coupling prism is fixed to the quartz dye cell using Canada balsam. The beams are focussed into the dye using either a cylindrical or spherical lens, depending on the required excitation length. Production of short pulses demand short pumped lengths and we employ a spherical lens with the focus on the dye cell wall. In this case the transverse dimension may be adjusted by rotating the two prisms away from the minimum deviation position.

The principle of operation of the DFDL has already been described in detail elsewhere [5–7] and we simply recall here that the total gain of the system

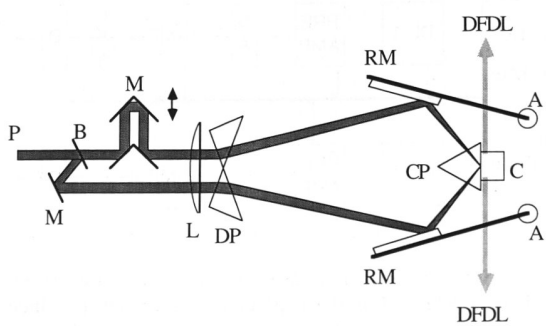

Fig. 2. Outline of the distributed-feedback dye oscillator. P: microjoule energy 65 ps 1 kHz pump at 532 nm. M: 100% plane reflector. B: 50% beam splitter. L: cylindrical or spherical focussing lens. DP: orientable beam-deviation prisms. RM: co-rotating 100% tuning mirrors. CP: coupling prism. C: dye circulation cell. A: rotation axes of co-rotating mirrors. DFDL: twin dye laser output beams.

and the transient induced distributed grating reflectivity vary in a very non-linear fashion with the inversion of the dye medium. Depending on pumping intensity, this leads to the emission of one or more dye laser pulses, which in general are significantly shorter than the pumping pulse width. Because the DFDL pulse evolves inside a high-visibility distributed reflection grating, this pulse is usually near Fourier-transform limited, regardless of its temporal width [5].

The duration of the emitted tunable DFDL pulse depends strongly on the length of the interference fringe system inside the dye cell (and implicity on dye concentration which must be adapted to the pumping level [5]). With a pumped length of 8 mm, obtained using a cylindrical lens, and an inversion close to first threshold, we obtain 25 ps long pulses. These long pulses may be amplified up to energies in excess of 10 μJ by a two stage amplifier (fig. 3, without saturable absorber) pumped by 10% (pre-amplifier) and 35% (main amplifier) respectively of the single pulse doubled YAG output. Small signal gain of the amplifier chain is of the order of 10^4. To reduce thermal effects in the amplifiers and the DFDL oscillators we normally use a 70/30% water/ethanol mixture as a solvent for the dyes. Long pulse tunability from 550 to 650 nm can be readily achieved using appropriate dyes.

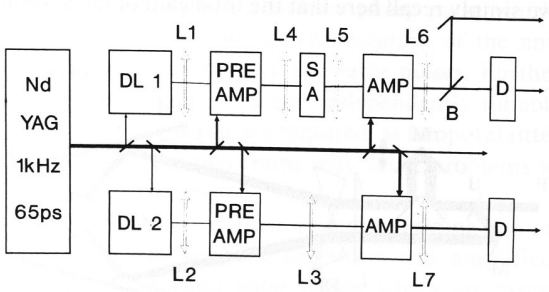

Fig. 3. Simplified schema of the complete dual dye laser system. Nd:YAG: 1 kHz 65 ps 450 μJ pump at 532 nm. DL 1, 2: independent distributed-feedback dye oscillators. L1, L2: 70 mm focal length DFDL beam collector lenses. PRE-AMP: 10 mm long dye pre-amplifiers pumped by 10% of the YAG energy. L3: 1000 mm coupling lens. L4, L5: 50 mm focussing lenses for the saturable absorber. SA: 1 mm long saturable absorber cell. AMP: 20 mm long dye amplifiers pumped by 35% of the YAG energy. L6, L7: 1000 mm collimating lenses, B: beam-splitter. D: adjustable delay lines. In the real system the amplifiers are forward pumped at a small angle to the dye laser beam.

For a DFDL pumped length of 0.5 mm excited to just below the threshold for second spike generation the output pulse width is about 10 times shorter than above. With a high-gain amplifier system and in the absence of a saturable absorber this pulse is broadened to approximately 4 ps after amplification. The introduction of a saturable absorber between the pre-amplifier and the main amplifier (fig. 3) and avoidance of excessive gain saturation allows the production of amplified pulses less than 2 ps in duration with an energy greater than 2 μJ (peak power > 1 MW).

Fig. 4 shows the autocorrelation trace, measured by non-linear second harmonic generation, of such an amplified pulse, where we plot the logarithm of the autocorrelation signal $S_A(t_d)$ as a function of relative delay t_d in picoseconds. Laser wavelength was 572 nm, obtained using rhodamine 6G in the oscillator and amplifiers and DODCI in ethanol as saturable absorber. The autocorrelation curve yields a pulse duration of 1.8 ps, assuming a sech pulse shape [5], as suggested by the observed shape and exponential wings of the autocorrelation trace. Any slight asymmetry of the pulse which might be introduced by the saturable absorber could only be detected in a higher order correlation experiment (see below) and should have a negligible influence on the deduced pulse-width. Because dye concentrations are required to be high for short pulse generation in or-

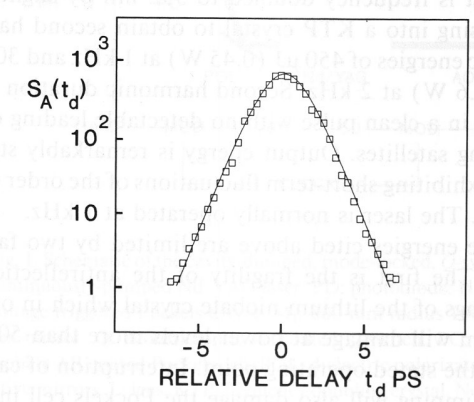

Fig. 4. Auto-correlation trace of amplified dye laser 1 for a 0.5 mm DFDL pumped length. The auto-correlation signal is plotted on a $\log_{10}$ scale against relative delay in picoseconds. The full line is calculated for a pulse width of 1.8 ps assuming a pulse shape of the form $\mathrm{sech}(t/t_p)$.

der to support adequate gain over small pumped length, self-absorption of the laser wavelength becomes an important factor and it is necessary to pump the dye close to the edge of the dye cell to minimize the length of unpumped dye between the lasing region and the cell wall. For this reason it is also difficult to obtain short pulses at a wavelength of less than 565 nm using rhodamine 6G.

With DFDL compression ratios of more than 30, it is important to address the problem of the relative jitter between two independent DFDL oscillators, as this can be a determining factor for time-resolution in many experiments. We may readily calculate the relative movement of a DFDL spike inside the pumping pulse envelope, as a function of pump intensity, using the formalism described in ref. [5]. For short pulse generation this movement is insensitive to pulse duration, a typical value being -0.7 ps/percent increase of pump power. Moreover this value only varies slowly with absolute pump intensity, by about 10 fs/percent change of pump level. This means that two DFDL oscillators with the same operating point above threshold, within 10%, would have a relative jitter <100 fs/percent of pump power. For the $\pm 2\%$ fluctuation, typical of our doubled YAG laser, this leads to a calculated jitter $< \pm 200$ fs, fairly independent of pulse duration.

This prediction is borne out by experimental measurement of auto- and cross-correlation curves for the two amplified DFDL systems, without any saturable absorber. In short-pulse generation conditions, when both oscillators are adjusted to just below second-spike threshold, we are unable to distinguish autocorrelation and cross-correlation traces and we conclude that any jitter must be negligible compared to the 4 ps pulse width. Note that this result represents a significant improvement over that obtained for synchronously-pumped dye laser systems, where relative jitter may easily be several picoseconds [4].

4. Improving time-resolution

One obvious way to improve the time-resolution of the present system is to decrease the duration of the pumping pulse. A factor of two overall decrease in pulse width might be achieved by replacing the YAG rod with a YLF rod. A similar improvement can be obtained at the expense of increased jitter between the dye lasers. This method involves pumping the DFDL oscillators above the threshold for generation of secondary pulses, but with different pumping levels so that the secondary pulses are not time-coincident. Higher pumping level increases the rate of rise of the inversion in the dye medium and is initially equivalent to a shorter pumping pulse.

Fig. 5 shows the result of a non-resonant time-resolved CARS experiment using the set-up of fig. 3 and differentially over-pumping the DFDL oscillators beyond second-spike threshold. In this experiment the shorter amplified dye laser pulse (I_1) is divided into two, to provide both excitation and probe beams, leading to the following correlation function,

$$S(t_d) = \int_{-\infty}^{+\infty} \mathrm{d}t\, I_1(t) I_2(t) I_1(t - t_d) \,.$$

The observed signal $S(t_d)$, which is plotted on a logarithmic scale as a function of t_d in picoseconds, exhibits a decay time of 490 fs over four orders of signal magnitude and is subsequently limited by system noise out to at least 25 ps delay. The slight asymmetry of the above curve may be fitted (full line in fig. 5) by assuming that the I_1 pulse, which traverses a saturable absorber, rises about 30% faster than it

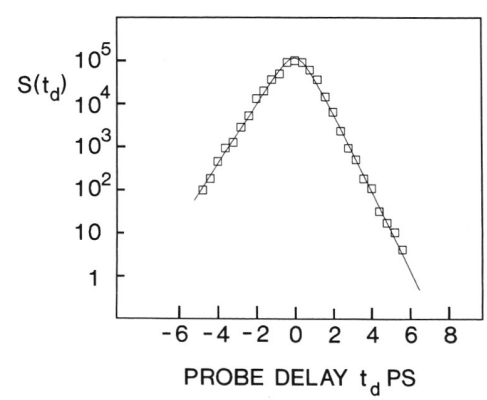

Fig. 5. Three-pulse cross-correlation trace obtained by non-resonant time-resolved CARS and using differentially over-pumped DFDL oscillators. The CARS signal decays over four decades with a time-constant of 490 fs. Each point represents the average of 1000 laser shots or one second of experimental time. The full line is calculated (see text).

falls. The pulse widths used in the fit are 0.7 ps (I_1) and 1.3 ps (I_2). This particular correction function is insensitive to jitter between I_1 and I_2 and jitter manifests itself mainly through increased shot-to-shot fluctuation of signal intensity. Further improvement in time resolution can be obtained if spurious signal structure at large delay, due to secondary pulse overlap, is acceptable.

5. Conclusions

We have developed a dual distributed-feedback dye laser system, pumped by a single 65 ps, 532 nm pulse from a stand-alone YAG laser, and providing independently tunable, synchronized, megawatt power level, kilohertz repetition-rate pulse trains. Single pulse widths of less than 2 ps and CARS time-resolution better than 0.5 ps have been obtained. We believe that his system represents an attactive alternative to existing technology for non-linear picosecond spectroscopy in the time and frequency domain.

References

[1] R.J.Miller, L. Min and A. Shragowitz, Optics Comm. 62 (1987) 185.
[2] L. Min, Q. Bao and R.J.D. Miller, Optics Comm. 68 (1988) 427.
[3] V.J. Newell, F.W. Deeg, S.R. Greenfield and M.D. Fayer, J. Opt. Soc. Am. B6 (1989) 257.
[4] T. Juhasz, J. Kuhl and W.E. Bron, Optics Lett. 13 (1988) 577.
[5] G.M. Gale, P. Ranson and M. Denariez-Roberge, Appl. Phys. B 44 (1987) 221.
[6] Z. Bor, IEEE J. Quantum Electron. QE-16 (1980) 517.
[7] G. Szabo and Z. Bor, Appl. Phys. B47 (1988) 299.

2.5 Magnetic Resonant Pulsing-Kane

This first paper I believe is the most important paper to this project. It details magnetic resonant pulsing, and provides a lot of the background and theory behind the process.

Pulsed laser architecture for enhancing backscatter from sodium

Thomas J. Kane*, Paul D. Hillman, Craig A. Denman
FASORtronics LLC, 1400 Eubank Blvd SE, Albuquerque, NM 87123-3340

ABSTRACT

The brightness of a laser-generated guide star is determined not only by the power of the laser, but also by the spectral and temporal properties of the laser. We show that a guide star laser pulsed at the Larmor frequency of the sodium atoms enhances guide star brightness by up to 2X, compared to an optimized cw laser at the same average power. We describe a frequency-addition source of optical radiation that can provide such pulsed light, while providing any desired spectral shape.

Keywords: Guide star, laser, pulsed, Q-switch, sodium, Larmor

1. INTRODUCTION

Next-generation ground-based telescopes require sophisticated adaptive optical systems, and a "guide star" laser is an essential component in these systems. The performance of the adaptive optical system, and thus of the telescope, depends on the amount of guide star light collected by the telescope, and thus on the brightness of the guide star created in the mesosphere. Models of sodium return show how to optimize return for a given level of laser power.[1]

1.1 Backscatter efficiency at low irradiance used as reference level

At a mesospheric irradiance level below 0.01 W/m^2, the laser does not perturb the distribution of sodium states, and the best return is achieved with a narrow spectrum exactly centered on the peak of the sodium line, at 589.159 nm. Under very low irradiance, laser polarization does not matter. The level of backscatter efficiency under this condition of very low irradiance will be used as a reference level. A goal is to maintain or exceed this level of efficiency over a wide range of laser irradiance, so that return signal rises linearly with laser power, or faster.

1.2 "Optical Pumping" with circularly polarized light enhances return

As the irradiance of the light in the sodium layer increases, it becomes advantageous to use circularly polarized light. Atoms that scatter circularly polarized photons move to angular momentum states which enhance their probability of backscattering subsequent photons. "Optical pumping" is the term often used for this beneficial redistribution of angular momentum states. Holzlöhner et. al.[2] showed that at a mesospheric sodium irradiance of 10 W/m^2 this effect can improve backscatter efficiency by a factor of 2, relative to the low-irradiance efficiency, for atoms that do not precess in the Earth's magnetic field. To achieve the benefits of optical pumping at the lowest possible irradiance, a laser with a linewidth below the lifetime-broadened sodium linewidth of 10 MHz is necessary, to ensure that the laser is interacting only with atoms in a narrow range of velocities. By interacting with fewer atoms, it is easier to significantly perturb their distribution of states, and to achieve the benefits of optical pumping.

1.3 Geomagnetic field substantially defeats the benefit of "Optical Pumping"

The benefits of optical pumping are substantially reduced when the atoms precess due to the geomagnetic field. The precessing atoms are reoriented in a time fast compared to the time it takes to establish a favorable distribution. Precession of the angular momentum imparted by laser photons does not occur when the laser beam is parallel to the magnetic field, and is maximized for the perpendicular case. Unfortunately, angles closer to perpendicular will be more typical. For the case of the beam perpendicular to the field, the benefit of optical pumping is almost completely eliminated.[2]

It would be desirable to find a way to maintain the benefit of optical pumping at all orientations of the laser and the magnetic field.

*tom@fasortronics.com; phone (505) 225-3733; fasortronics.com

Adaptive Optics Systems IV, edited by Enrico Marchetti, Laird M. Close,
Jean-Pierre Véran, Proc. of SPIE Vol. 9148, 91483G · © 2014 SPIE
CCC code: 0277-786X/14/$18 · doi: 10.1117/12.2055632

Downloaded From: http://proceedings.spiedigitallibrary.org/ on 02/24/2017 Terms of Use: http://spiedigitallibrary.org/ss/termsofuse.aspx

1.4 "Downpumping" reduces backscatter efficiency, but "Repumping" can defeat downpumping

Another effect, known as downpumping, results in reduced backscatter efficiency at higher irradiance. The sodium atom has two ground state energies, creating two distinct lines of absorption and emission, separated by 1.72 GHz. The stronger and redder line is referred to as the D_2a line, and the weaker and bluer as D_2b. If atoms are pumped only at the D_2a transition wavelength, the D_2a ground states will become partially depleted, as atoms accumulate in the lowest ground state that feeds only the D_2b line. This is "downpumping." Holzlöhner et. al.[2] showed that at 47 W/m^2 irradiance, downpumping can reduce backscatter efficiency by 70%, relative to the low-irradiance efficiency, for the "bad" magnetic orientation (field perpendicular to laser beam). The effects of downpumping can be ameliorated by also pumping the D_2b transition, a technique known as "repumping." Repumping has been accomplished by directing two distinct lasers at the same volume of the mesosphere[3], but it is more conveniently done by putting sidebands on a single laser, by phase modulation, intensity modulation, or ideally, a combination of the two, which would create a single, blue-shifted sideband. (If two sidebands are created, one will not interact with sodium at all, since it will be outside the Doppler width for both lines.) Holzlöhner et. al. showed that the optimum fraction of light at the D_2b wavelength is in the range 8-25%, depending on the strength of the magnetic field. At a cw irradiance of 47 W/m^2, for the "bad" magnetic orientation, repumping improves backscatter efficiency by 3.5X, bringing it back to the low-irradiance reference level.

1.5 At high irradiance, stimulated emission will reduce backscatter

Another effect that leads to lower backscatter efficiency occurs when a significant fraction of the sodium atoms are in the excited state. Atoms in the excited state will emit by stimulated emission, and two photons will uselessly travel into space. This effect, called saturation, leads to a 10% loss of efficiency at an irradiance of 46 W/m^2, for a laser linewidth well below 10 MHz. At higher irradiance, the loss of efficiency increases. The effects of saturation can be countered by broadening the linewidth of the laser. Holzlöhner et. al. evaluated the tradeoff between the good effect of optical pumping and the bad effect of saturation, and advises that the laser linewidth be broadened by 1 MHz for each 6 watts of laser power, for typical guide star spot sizes. At 20 watts cw, with optimum mesospheric beam size, the recommended laser linewidth of 3.3 MHz is below the 10 MHz sodium natural linewidth, so no observable effect is expected due to laser linewidth broadening. But as laser power increases, due to pulsing or larger average power, a broadened linewidth will be desired.

2. MODELING OF PULSED GUIDE STAR

2.1 "Magnetically Resonant Pumping" provides large benefit at most field orientations

Holzlöhner et. al. analyzed backscatter efficiency for cw guide star lasers. Using code developed by Rochester Scientific for the analysis of pulsed guide star lasers,[4] we have shown that by pulsing the laser at the magnetic precession frequency, often called the "Larmor frequency," it is possible to maintain the benefits of optical pumping regardless of magnetic field orientation. We call this technique for enhancing guide star backscatter efficiency "magnetically resonant pulsing."

For a typical geomagnetic field of 0.25 to 0.5 gauss, the Larmor frequency is between 175 and 350 kHz, linearly proportional to field magnitude. Magnetically resonant pulsing works because it substantially reduces the effect of precession, by allowing the atoms to interact with the laser light at a fixed point in the precession cycle, analogously to how a strobe light illuminating a rotating wheel can make it appear to stop. Subharmonics of the Larmor frequency are also usable, just as they would be in the strobe light analogy.

Figure 1 shows the results of our calculations. The vertical axis is the backscatter efficiency, in the units typically used. For reference, backscatter efficiency as irradiance approaches zero is 240, in the same units. The horizontal axis is the angle between the laser beam and the magnetic field. The upper trace, with red squares, is the case of magnetically resonant pumping, with other parameters optimized. The blue circles show the cw case, also with parameters optimized. For large angles, the benefit is a factor of two. Most telescopes will be operating in the 60°-90° range most of the time, since the magnetic field in the tropics is more nearly horizontal than vertical, and also due to the simple geometric fact that given any axis on a sphere, most of the sphere is more than 45° away from the axis.

Downloaded From: http://proceedings.spiedigitallibrary.org/ on 02/24/2017 Terms of Use: http://spiedigitallibrary.org/ss/termsofuse.aspx

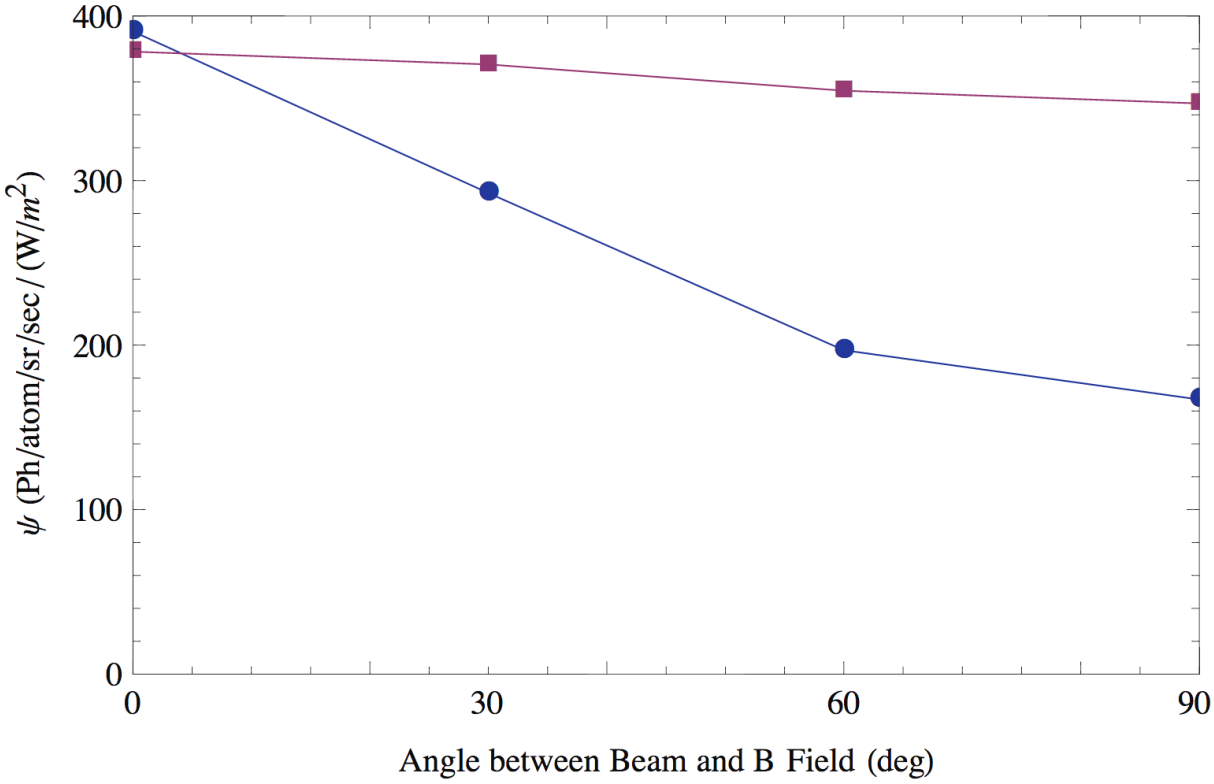

Figure 1. Backscatter efficiency as function of angle between laser beam and B field, calculated with pulsed model.
Red squares: Pulsed at Larmor frequency (350 kHz), 9% duty cycle, linewidth 150 MHz, D_2b fraction 9.2%.
Blue circles: cw, linewidth 9 MHz, D_2b fraction 15%.
Both: Average irradiance 47 W/m^2, B field 0.5 gauss.

Note that at an angle of 0°, the cw case is slightly better, because the broader linewidth of the pulsed laser reaches wavelengths farther out on the Doppler-broadened sodium line, where there are fewer atoms. But for the vast majority of possible orientations, the backscatter efficiency with the pulsed laser is better.

2.2 Countering "Recoil" with "Frequency Chirp" found not to be beneficial

One last technique for enhancing backscatter efficiency takes advantage of the fact that sodium atoms change velocity when they scatter a photon. This "recoil" effect depletes the number of atoms that are at the right velocity to scatter subsequent photons at the same wavelength. If the laser is chirped in wavelength toward the blue, it can reduce its interaction with the depleted velocity class, taking advantage of the enrichment of the velocity class receiving the recoiled atoms. The Rochester Scientific modeling code was augmented to allow the effects of wavelength chirping, sometimes called snowplowing, to be modeled. In this model, a sawtooth-shaped frequency chirp can be applied to the light interacting with the sodium atoms. We carried out calculations, which we will not present in any detail, since the main topic of this paper is the benefit of magnetically resonant pumping. The benefits of snowplowing are reduced as laser linewidth increases. But we found that the benefits of magnetically resonant pumping are lost due to saturation if the linewidth is not broadened, and thus the potential benefits of snowplowing must be foregone. Given a choice between magnetically resonant pumping and snowplowing, the former is much more valuable. The snowplow modeling code is available from Rochester Scientific.

Downloaded From: http://proceedings.spiedigitallibrary.org/ on 02/24/2017 Terms of Use: http://spiedigitallibrary.org/ss/termsofuse.aspx

3. FASOR ENABLES ALL TECHNIQUES FOR EFFICIENCY ENHANCEMENT

A FASOR is a Frequency Addition Source of Optical Radiation. Figure 2 shows a FASOR architecture that can provide pulsed light at the desired pulse repetition frequency and duty cycle for magnetically resonant pumping, while also providing a continuously variable linewidth, a single-sideband for D_2b excitation, and easy tunability, if chirping for snowplowing is desired. This design sums the 1319 nm and 1064 nm wavelengths of Nd:YAG in a crystal of lithium triborate (LBO), as do previous FASOR systems.[5] An important feature distinguishing this from previous FASOR architectures is that while the 1319-nm light is resonated, the 1064-nm light is not, and is converted in a single pass through the LBO.[6] The 1064-nm light can have any desired phase, frequency and amplitude modulation, unconstrained by the necessity of being resonant, and this modulation will also appear on the generated 589-nm light. The 1319-nm light is resonant within the laser resonator where it is generated. An acousto-optic Q-switch causes the 1319-nm light to be pulsed.

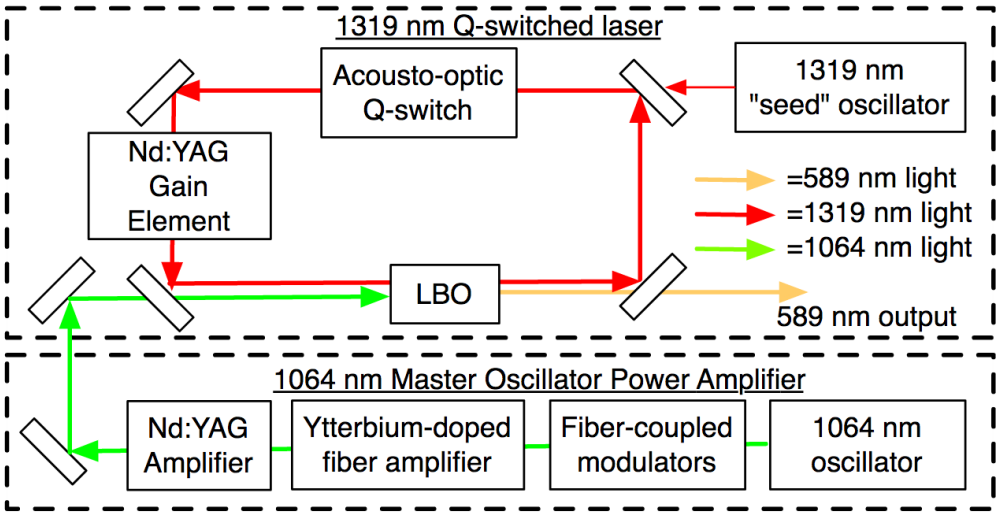

Figure 2. FASOR Architecture. 589 nm is generated by the summation of 1064 nm and 1319 nm in an LBO nonlinear crystal. The 1064-nm light makes a single pass through the LBO crystal. The 1319-nm light makes multiple passes through the LBO, since the LBO is internal to the 1319-nm laser resonator. 1319 nm is generated by a Nd:YAG laser, while 1064 nm is generated in an oscillator-amplifier chain.

The 1319-nm Q-switched laser oscillates at a single frequency due to injection-seeding by a low-power single-frequency cw oscillator, typically a nonplanar ring oscillator.[7] Injection-seeding of a Q-switched laser has considerably relaxed tolerances on power and frequency matching as compared to injection-locking of a cw laser.[8]

The modulated 1064-nm light is provided by an oscillator-modulator-amplifier chain. The oscillator is a single-frequency cw oscillator, again, typically a nonplanar ring oscillator. Conceptually, there are two phase modulators and two amplitude modulators, though in reality it may be better to combine signals in the RF domain and halve the number of optical modulators. Following modulation, the light is amplified. Most of the gain, and as much of the power as possible, is provided by fiber amplifiers. A final amplification stage in a bulk neodymium-doped gain element will be needed if peak output power is greater than 100 watts.

3.1 Modulation to achieve optimized spectrum

Figure 3 shows the function of the modulators. The modulators would be fiber-coupled, waveguide modulators of the type used in telecommunication systems. The first phase modulator receives electrical pulses that create phase modulation of either $+\pi/2$ or $-\pi/2$, with no dead time between pulses and a defined rate of pulsing. The sign of the phase of each pulse is random (or pseudo-random). Such randomly phased modulation will create light of a linewidth roughly

Downloaded From: http://proceedings.spiedigitallibrary.org/ on 02/24/2017 Terms of Use: http://spiedigitallibrary.org/ss/termsofuse.aspx

equal to the defined rate of pulsing. Since fiber-coupled waveguide phase modulators can easily achieve modulation well above 1 GHz, the entire Doppler-broadened sodium line is accessible.

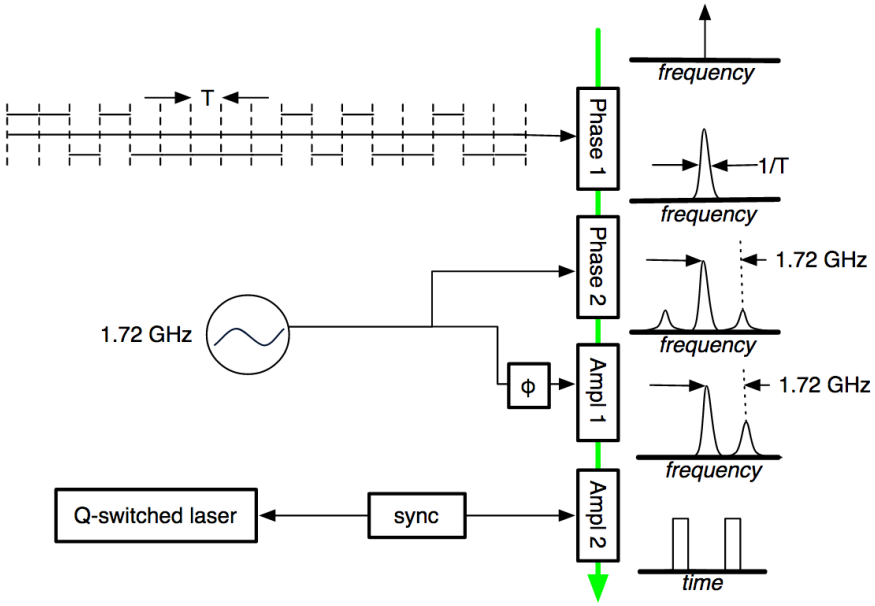

Figure 3. Modulators are fiber-coupled electro-optic waveguide modulators, such as are used for fiber communication. Signals could be combined in RF domain to halve the number needed. First modulator is driven by random pulses creating $\pm\pi/2$ phase shift. This broadens the linewidth. Second two modulators create a single sideband, blueshifted 1.72 GHz. Final modulator slices light into pulses at the Larmor frequency.

The second phase modulator is driven at 1.72 GHz, the frequency split between the D_2a line and the D_2b line. Phase modulation alone will place sidebands on both sides of the input. Since the desired amount of power in the D_2b line is about 9%, this leads to a waste of 9% of the power - since the red-shifted sideband is useless. By amplitude modulating the signal as well as phase modulating, at the same frequency and with a controlled phase difference, a single sideband can be created, blueshifted but not redshifted, saving 9%. This is the purpose of the first amplitude modulator.

The second amplitude modulator slices the light into pulses, synchronized with the pulses in the 1319-nm Q-switched laser, at a pulse repetition frequency that is adjusted to be at the peak of the magnetic resonance.

By placing the amplifiers after the modulators, all power lost to modulation is recovered at low cost. The power is then further amplified to a level adequate to efficiently extract power from the 1319-nm beam in the LBO. A final amplification stage using Nd:YAG or Nd:Vanadate bulk crystal amplifiers will be needed to reach peak power above 100 watts, which is the limit on the power of narrowband light in available fibers, due to stimulated Brillouin scattering. With a duty cycle of 9%, and assuming a 50% conversion of 1064 nm, a 20 watt average power 589-nm laser will require 22 watts of 1064 nm average power, and a peak power at 1064 nm of 242 watts. Thus a single final-stage neodymium bulk amplifier with a gain of 3X puts the fiber amplifier into a safe power range. This is not a challenging level of gain for neodymium bulk amplifiers. The Nd:YAG amplifier used for the Laser Interferometer Gravitational Wave Observatory (LIGO) had a gain of 28.5X, with an output power of 20 watts.[9]

The architecture we have presented enables four techniques for return efficiency enhancement - D_2b re-pumping, magnetically resonant pumping, linewidth optimization, and, if desired, "snowplowing" for recoil compensation, although we do not expect the latter to be valuable when the laser linewidth is increased as needed for pulsed operation.

Downloaded From: http://proceedings.spiedigitallibrary.org/ on 02/24/2017 Terms of Use: http://spiedigitallibrary.org/ss/termsofuse.aspx

4. PRELIMINARY EXPERIMENTAL RESULTS

A concern with this design is the low gain of Nd:YAG at the 1319-nm wavelength. Low gain makes Q-switching at a high repetition rate difficult. To verify that gain was adequate, we built a 1319-nm acousto-optically Q-switched laser using a single side-pumped Nd:YAG gain element. This laser was operable at pulse repetition rates up to 350 kHz, which is on the high side of what is necessary to reach the sodium Larmor frequency, which varies with geographical location. Figure 4 shows an oscilloscope trace for this laser, with the Q-switch operated at 350 kHz, corresponding to a time between pulses of 2.86 µsec. The pulse duration FWHM is 0.18 µsec, for a duty cycle of 6.3%, near the 9% value used for the calculations of Fig. 1.

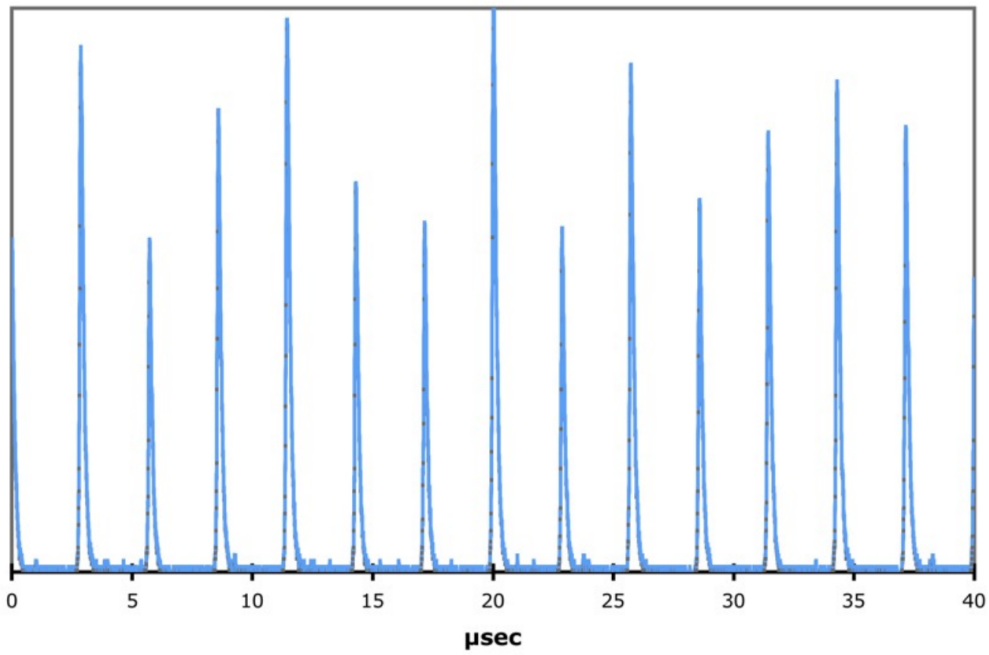

Figure 4. Oscilloscope trace of 1319-nm acousto-optically Q-switched laser. Pulse repetition frequency is 350 kHz, pulse duration FWHM is 0.18 µsec.

The pulse-to-pulse variation in Fig. 4 may be improved by injection-seeding, which stabilizes the pulses. Pulse-to-pulse stability is not critical, as long as pulse timing is maintained at the Larmor frequency, which is easily accomplished.

5. CONCLUSIONS

We have shown by calculation that a guide star laser pulsed at the Larmor frequency can have enhanced return efficiency compared to an optimized cw system, over almost all orientations of the magnetic field. For magnetic fields perpendicular to the laser propagation direction, the enhancement is a factor of two.

We have proposed a FASOR (Frequency Addition Source of Optical Radiation) architecture that we believe can provide this pulsed format, while also providing a variable linewidth to avoid saturation, and a single sideband for repumping.

We are confident that FASOR systems using the hybrid bulk crystal / fiber architecture we have described can reach an average power of 50 watts. It is exciting to realize that at this high power level, the backscatter efficiency of the sodium layer is not expected to drop off, but instead, when averaged over all magnetic field orientations, will be above the level achieved by any previous guide star laser at any power.

Downloaded From: http://proceedings.spiedigitallibrary.org/ on 02/24/2017 Terms of Use: http://spiedigitallibrary.org/ss/termsofuse.aspx

REFERENCES

[1] Holzlöhner, R., Rochester, S. M., Bonaccini Calia, D., Budker, D., Higbie, J. M., and Hackenberg, W., "Optimization of cw sodium laser guide star efficiency," arXiv.org > astro-ph > arXiv: 0908.1527v1

[2] Reference 2. Figure 3a.

[3] Denman, C. A., et al., "Two-Frequency Sodium Guidestar Excitation at the Starfire Optical Range", talk at Center for Adaptive Optics, Fall Retreat 2006, Fish Camp, California (2006)

[4] Rochester, S. M, Otarola, A., Boyer, C., Budker, D., Ellerbroek, B., Holzlöhner, R., and Wang, L., "Modeling of pulsed laser guide stars for the Thirty Meter Telescope project," JOSA B, Vol. 29, Issue 8, pp. 2176-2188 (2012). Pulsed code is available commercially from Rochester Scientific.

[5] Denman, C. A., Drummond, J. D., Eickhoff, M. L., Fugate, R. Q., Hillman, P. D., Novotny S. J., and Telle J. M., "Characteristics of sodium guidestars created by the 50-watt FASOR and first closed-loop AO results at the Starfire Optical Range", Proc. SPIE 6272, 62721L (2006)

[6] Kane, T. J., "Pulsed, Internal Optical Mixer," US Patent Application 13/859,412, filed April 9, 2013. To be published October 9, 2014.

[7] Kane, T. J., and Byer, R. L., "A Monolithic, Unidirectional Single-Mode Nd:YAG Ring Laser," Opt. Lett., vol. 10, p. 65, 1985.

[8] Park, Y. K., Giuliani, G., and Byer, R. L., "Stable single-axial-mode operation of an unstable-resonator Nd: YAG oscillator by injection locking," Optics Letters, Vol. 5, Issue 3, pp. 96-98 (1980)

[9] Wiechmann, W., Kane, T. J., Haserot, D., Adams, F., Truong, G., and Kmetec, J. D., "A 20-W diode-pumped single-frequency Nd:YAG master oscillator power amplifier for the Laser Interferometer Gravitational Wave Observatory" in Conference on Lasers and Electro-Optics, vol. 6, 1998 OSA Technical Digest Series (OSA, Washington DC, 1998) p. 432, paper CThP2.

Downloaded From: http://proceedings.spiedigitallibrary.org/ on 02/24/2017 Terms of Use: http://spiedigitallibrary.org/ss/termsofuse.aspx

2.6 Physics of Sodium LGS - Kibblewhite

You should read this paper more! Details the physics of LGS, and enters into quantum theory.

THE PHYSICS OF THE SODIUM LASER GUIDE STAR: PREDICTING AND ENHANCING THE PHOTON RETURNS

Edward Kibblewhite
University of Chicago

ABSTRACT

Not all lasers give the same photon return/watt and it is this parameter, rather than the raw power generated by the laser, that is the more important figure of merit. In this paper we outline the physical processes involved in calculating this photon return from different types of laser, starting off with the single frequency CW laser developed at the SOR facility. Methods of increasing the return are then discussed and recent experimental results from chirping experiments at Palomar Observatory presented.

1. INCREASING THE COLUMN DENSITY OF SODIUM ATOMS IN THE MESOSPHERE

About 100 tons of meteorite burn up in the upper atmosphere every day, producing of about 100 kg of sodium metal [1]. The metal is removed by various complex physical and chemical processes, which ionize the atoms at high altitudes and lock the sodium atoms either into chemicals or on the surface of sub-micron sized "smoke" at altitudes below 85 km [1]. The total mass of sodium available in the entire mesosphere for generating a guide star is about 500 kg, implying a lifetime of about 5 days, with significant annual and diurnal variation. Greatly enhanced short-lived sodium abundances , so-called "sporadic" sodium , occur on shorter time scales which can increase the abundance by over a factor of ten for periods of minutes to hours [2]. Typical column densities are between 2 and 7 x 10^{13} atoms/m^2 with peak densities sometimes exceeded 20 x 10^{13} atoms/m^2 [2]. It is remarkable that so little sodium metal can backscatter even a few per cent of the radiation from a laser beam and it is conceivable that a few tens of kg of sodium metal, suitability dispersed, could greatly increase the brightness of the LGS locally but for periods of hours. Should such a technology prove feasible, the use of potassium metal, which occurs at a favorable wavelength for laser technology and could allow two-frequency LGS AO, might be even more effective. Such a strategy would be expensive but might of value for important transient targets. In the meantime the only way to increase the return is to build either more powerful lasers or improve the efficiency of producing photons from the sodium atoms.

2. OPTICAL PUMPING IN THE SODIUM ATOM

It is well known [5] that, for the D_2 line used to produce laser guide stars, the sodium atom has two ground levels, an upper F=2 state and a lower F = 1 state, with 5/8 of the atoms being in the F=2 state under conditions of thermal equilibrium. The upper F levels is split into 4 hyperfine sublevels each separted by some tens of MHz. All levels are additionally divided into different M levels, which have the same energy but different cross-sections to the radiation field. A simplified energy diagram of the atom is shown in figure 1.

If right handed circularly polarized photon of the appropriate frequency excites a sodium atom in the (2,M) ground state to the upper (3,M+1) level, it can decay to the (2,M), (2,M+1) or (2,M+2) ground level. If this is repeated and in the absence of other effects, the atom will then be optical pumped into a stable transition between the (2,2) and (3,3) state after a small number of cycles. Since this transition has the highest cross-section to the radiation field and highest backscattering efficency to ground, this optical pumping mechanism is very useful in increasing the photo return. We should note that the enhanced return is not only because of the enhanced backscatter return for this transition (a factor of 1.5 compared to isotropic scattering) but also because the cross-section is a factor of about 2 higher than the cross-section averaged over all M levels. We expect an increase in photon return of a factor of about 3 and this has been observed at MIT/Lincoln Labs with a suitably tailored laser spectral format and a well resolved spot [3].

However, we can also see from figure 1 that the photon return can be significantly <u>reduced</u> by depopulation of the F=2 ground state by another optical pumping process as follows. If the sodium atom is moving in slightly different direction, the energy diagram may favor transitions from the F =2 ground state to either the F=1 or F=2 upper state. For these excited atoms there is now a choice of ground state; an atom starting in the same ground (2,0)

2.7 Optimization of Pulsed LGS - Rampy

This is the paper where I learned about larmor precession. Lightly touches on MRP as a solution.

Towards optimization of pulsed sodium laser guide stars

Rachel Rampy,[1,*] Donald Gavel,[1] Simon M. Rochester,[2] Ronald Holzlöhner[3]

[1]*University of California, 1156 High St., Santa Cruz, CA, 95064, USA*
[2]*Rochester Scientific, LLC, El Cerrito, CA 94530, USA*
[3]*European Southern Observatory (ESO), Garching bei München, D-85748, Germany*
**Corresponding author: rrampy@keck.hawaii.edu*

Received XX Month XXXX; revised XX Month, XXXX; accepted XX Month XXXX; posted XX Month XXXX (Doc. ID XXXXX); published XX Month XXXX

Pulsed sodium laser guide stars (LGS) are useful because they allow for Rayleigh blanking and fratricide avoidance in multiple-LGS systems. Bloch-equation simulations of sodium-light interactions show that these may be able to achieve photon returns nearly equal to, and in some cases greater than, what is seen from continuous-wave (CW) excitation. In this work, we study the time-dependent characteristics of sodium fluorescence, and investigate the optimal format for the new fiber laser LGS that will be part of the upgraded adaptive optics (AO) system on the Shane telescope at Mt. Hamilton. Results of this analysis are examined in the context of their general applicability to other LGS systems and the potential benefits of uplink correction are considered. Comparisons of simulation predictions with measurements from existing LGS are also presented and discussed.

OCIS codes: *(140.0140) Lasers and laser optics, (350.1260) Astronomical optics, (020.0020) Atomic and molecular physics*

http://dx.doi.org/10.1364/AO.99.099999

1.INTRODUCTION

Use of laser guide stars (LGS) along with adaptive optics (AO) allows large telescopes to significantly improve resolution by correcting image distortion induced by atmospheric turbulence at nearly any location in the sky. Sodium LGS operating at a wavelength of 589 nm employ resonance fluorescence of mesospheric sodium atoms, which are concentrated in a ~10 km-thick layer, centered at an altitude of ~90 km. These are preferable to Rayleigh guide stars due to their high altitude (allowing a larger fraction of the turbulence to be measured). Sodium is preferred as a resonant absorber, compared to the other constituents of the upper atmosphere, since it fluoresces at visible wavelengths and has a large fluorescence cross section–abundance product (Happer et al. 1994). Because powerful diffraction-limited laser beams at 589 nm are expensive to produce, careful attention must be paid to optimizing the laser format (spectrum, polarization, spot size, pulse length and duty cycle) in order to maximize the return signal.

Numerical models allow investigation of the various physical mechanisms occurring in the laser–sodium system that affect the number of photons returned to the telescope. The investigations presented here use a density-matrix calculation with coupled velocity groups, and include the important physical effects of Larmor precession due to the geomagnetic field, radiation pressure (recoil), saturation, and velocity-changing and spin-randomizing collisions (Holzlöhner et al. 2010a). The LGSBloch package runs in Mathematica, and is based on the Atomic Density Matrix package written by S. Rochester*.

Motivation for this research was provided by the upgrade of the AO system on the 3 meter Shane Telescope at Lick Observatory. The Shane hosted the first experiments in sodium LGS AO, with observations starting in 1996, and provides for regular astronomical science observing to this day. The upgraded system incorporates many of the recent advancements in AO technology and lessons learned from laboratory and on-sky experiments in order to provide higher Strehl, improved sensitivity, and greater wavelength coverage for astronomers (Kupke et al. 2012). This second-generation system uses a 32×32 actuator micro-electro-mechanical systems (MEMS) deformable mirror, with a higher sensitivity wavefront sensor (WFS). A new fiber laser that was developed at Lawrence Livermore National Laboratory (LLNL) will soon replace the existing dye laser. The fiber technology is more compact and energy efficient than the current laser, and allows adjustments to the pulse and spectral format for optimal coupling to the mesospheric sodium atoms. The initial and principal goal of this investigation has been to ascertain the ideal values of these parameters, and to estimate the return signal this new laser will produce.

The next section presents the sodium physics relevant to the numerical model, followed by description of endeavors to find the optimal pulse and spectral formats in Section 3. Section 4 addresses the potential benefits of uplink correction of the laser beacon, and gives the projected return flux for the new LGS at Lick Observatory. Section 5 presents

simulation results of the return flux for the 50 W Fasortronics laser at SOR, the current 10 W dye laser on the Shane telescope, and the two ~15 W LGS at the Keck Observatory. In section 6, an idea that may enable pulsed lasers to create brighter LGS than CW is presented. The final section summarizes what has been determined thus far and briefly discusses where future efforts should focus.

2.UNDERSTANDING AND MODELING SODIUM-LIGHT INTERACTIONS

Sodium LGS take advantage of the $3^2S_{1/2}$–$3^2P_{3/2}$ transition in atomic sodium, known as the D_2 line. The ground state consists of two hyperfine multiplets, with 8 magnetic substates combined. The hyperfine states are separated by 1.77 GHz, splitting the D_2 line into the D_2a and D_2b transition groups. These two groups are composed, respectively, of transitions originating from the $F = 1$ and $F = 2$ ground states, where F is the total atomic angular momentum quantum number. The four excited state multiplets ($F = 0, \ldots, 3$) are separated by 16, 34, and 60 MHz from each other, and contain a total of 16 substates. Figure 1 shows the atomic structure of sodium starting from the Bohr model (on the left) and ending with the hyperfine states and energy separations on the far right (Hillman et al. 2008). At mesospheric temperatures of about 190 K, the motions of the atoms result in the D_2a and D_2b lines being Doppler broadened to ~1 GHz each, giving rise to the characteristic two-peaked absorption/fluorescence profile.

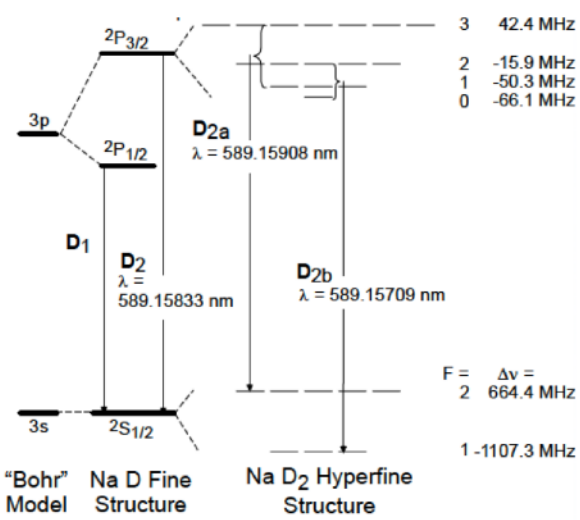

Fig. 1. The atomic structure of sodium, starting from the Bohr model of the atom on the left, and ending on the right with the hyperfine states of the D_2 line. The 1.77 GHz separation of the ground states requires that LGS address both transition groups for optimal coupling to the light field (Hillman et al. 2008).

Circularly polarized laser light can induce higher return flux than linearly polarized light due to the phenomenon of optical pumping (Jeys et al. 1992). When an atom encounters a circularly polarized photon resonant with a transition to the excited state, the value of the magnetic quantum number, m, must change by ± 1 depending on the handedness of the light, as required by conservation of angular momentum. After several cycles of excitation and spontaneous emission (the excited state lifetime is 16.2 ns), the atoms will tend to be locked cycling between the $F = 2, m = \pm 2$ ground state and the $F' = 3, m = \pm 3$ excited state. This confers three main benefits: this cycling transition has the highest cross section of the entire D_2 group, atoms are forbidden by selection rules from decaying from the $F' = 3$ excited state to an $F = 1$ ground state, and the florescence is directed preferentially along the light beam (as for radiation from a dipole rotating about the laser beam axis). However, due to ground-state relaxation and Larmor precession there is never complete polarization in the ground state, resulting in some atoms being excited on other transitions besides the cycling transition. Additionally, spin-exchange collisions tend to equalize the populations between the $F = 1$ and $F = 2$ ground-state hyperfine levels, but this mechanism is slow enough that repumping is still beneficial.

Based on theoretical and experimental considerations, maximizing the number of photons emitted back towards the telescope involves the use of a circularly polarized beam centered on the D_2a line, with ~10% of the light tuned to the D_2b transition (Milonni et al. 1998, Holzlöhner et al. 2010a). With this "repumping," the fraction of atoms that later decay into the $F = 1$ ground state and thus cannot be re-excited by laser light in D_2a is strongly reduced. This optical pumping with repumping strategy allows the most atoms to become trapped in the aforementioned desirable two-state system. Due to the optical pumping effect, the return flux per unit irradiance at first increases with higher laser irradiance. As the irradiance continues to be increased, however, the efficiency eventually falls off, in part due to the increasing fraction of atoms in the excited state (transition saturation). A sodium atom in the excited state that encounters a laser photon may undergo stimulated emission, transitioning back to the ground state by emitting a photon along the laser propagation direction (i.e. off into space). Because of this, the highest efficiency is found near ~10–100 W/m^2 (for 12% repumping). This peak in efficiency represents the middle ground between having high enough light intensity to trap as many atoms as possible into cycling on the two-state optical pumping transition, without causing a substantial fraction to undergo stimulated emission.

There are three main factors that reduce the coupling efficiency of the laser light to the sodium atoms: (1) Larmor precession due to the geomagnetic field, (2) collisions with other constituents of the upper atmosphere, and (3) the aforementioned transition saturation leading to stimulated emission (Holzlöhner et al. 2010a). Also important to consider is the slight change in velocity incurred by an atom from absorption and spontaneous emission of a photon (equivalent to a Doppler shift of ~50 kHz, known as atomic recoil), and the transit of atoms in and out of the light beam. At the location of Mt. Hamilton, the strength of the geomagnetic field is 0.47 Gauss at 90 km altitude, corresponding to a Larmor precession period of ~3.1 μs. The time between collisions is on the order of ~100 μs, and the atoms in the beam are exchanged on a timescale of several milliseconds. Thus, different inhibitory factors will dominate depending on the duration of the laser pulse.

The quantity of returned photons also depends on the amount of atmospheric absorption and the column density of sodium atoms in the mesosphere. These give rise to a directional dependence factor of T_a^{2X}/X, where T_a is the one-way atmospheric transmission at 589 nm at zenith, and $X = 1/\cos(\zeta)$ is the airmass with the zenith angle ζ. For circularly polarized light, the local geomagnetic field also causes significant directional dependence, with maximal reduction of the return flux when the magnetic field and the laser beam are perpendicular. The highest returns are achieved when the laser propagates parallel to the magnetic field. The Na column density is also variable, including a seasonal variation by a factor of ~3 at North American latitudes, with the high around November and low near May (Gumbel et al. 2007).

Modeling sodium-light interactions and predicting LGS brightness also requires accounting for atoms with different Doppler shifts. To accomplish this, the velocity dependence of the density matrix is discretized to describe an appropriate number, n_{vg}, of velocity groups

each with a fixed component of velocity along the laser beam propagation direction. Because coherences between atoms with different velocities can be neglected, the complete density matrix can be thought of as a collection of $n_{vg.}$ separate, but coupled, density matrices, each of dimension 24 × 24, since there are a total of 24 magnetic substates in the D2 transition. In the freely available version of LGSBloch, the system is solved using methods built into Mathematica, based on matrix exponentials (described in detail in Holzlöhner et al. 2012). The fluorescent photon flux per solid angle emitted in a given direction is then found from the steady-state solution as the expectation value of a fluorescence operator (Corney 2006, Holzlöhner et al. 2010a).

To account for a non-uniform irradiance pattern in the mesosphere, LGSBloch assumes a Gaussian intensity distribution, discretized with a user-defined number of irradiance levels. Based on computational experimentation, results do not change significantly when greater than five levels are modeled, so that number is used throughout this work. For the most general format comparisons, results are presented with units of specific return, a measure of local return flux per laser irradiance in the mesosphere, as photons/s/sr/atom/(W/m^2). When quantities such as the irradiance and/or sodium abundance are held constant the units change to reflect that. The vertical distribution of sodium atoms is modeled as Gaussian, and the code used by Rochester Scientific accounts for variations in collision rates with altitude (although this has been found to have a negligible effect). In calculating the photon flux present at a telescope, the fluorescing atoms are assumed to be at the median altitude of the sodium layer near 92 km.

3.OPTIMIZATION OF PULSE LENGTH AND SPECTRAL FORMAT

The first ~30 km of atmosphere strongly scatters light back towards the telescope (Rayleigh scattering), possibly disturbing measurement of the wavefront from the higher-altitude sodium beacon. Rayleigh blanking involves blocking light from entering the WFS during the time the pulse is traveling through this region of air. Fratricide refers to the Rayleigh backscattered light from one LGS entering the WFS of another in systems that contain multiple lasers (such as the Thirty Meter Telescope, Wang et al. 2010), and can be reduced with similar time-gating schemes, or else by launching the laser beams from the side of the primary mirror, as in the European Extremely Large Telescope (E-ELT, Bonaccini-Calia et al. 2014). These background mitigation techniques reduce the WFS measurement error, and thus increase AO system performance.

Until recently, the available laser technology at wavelengths of 589 nm relied heavily on the high peak power in short-pulsed systems to achieve acceptable frequency conversion efficiency levels. As new technologies emerge with greater flexibility available in the temporal format, understanding the costs and benefits of the different format options becomes crucial.

Efforts to determine the optimal pulse duration began with examining how the number of spontaneously emitted photons varies as a function of time. Figure 2 shows results from two 100 μs simulations for a narrow line width laser, zenith pointing at Mt. Hamilton, with the irradiance levels set to be equal to what is present for 10 W average launched power operating at a 20% duty cycle. In the top graph, all the light is on the D_2a transition, and the lower plot is for ~10% of the light tuned to D_2b. For both cases there is an initial enhancement in the specific return (i.e. photons/s/sr/atom/(W/m^2) in the mesosphere). However, in the case of no repumping, the decline begins sooner for all but the lowest irradiance levels, and the peaks are considerably lower. These results suggest that for 10 W average launched power and 20% duty cycle, the most efficient use of the sodium atoms will be with repumping and pulse durations between 10–30 μs. The time between these long pulses (50–150 μs) would be sufficient for pulse-to-pulse effects to be negligible (Rampy et al. 2013). However, if partitioning of the laser light to include the D_2b line is not possible due to engineering constraints, somewhat shorter pulses will be better suited to take advantage of the initial return enhancement.

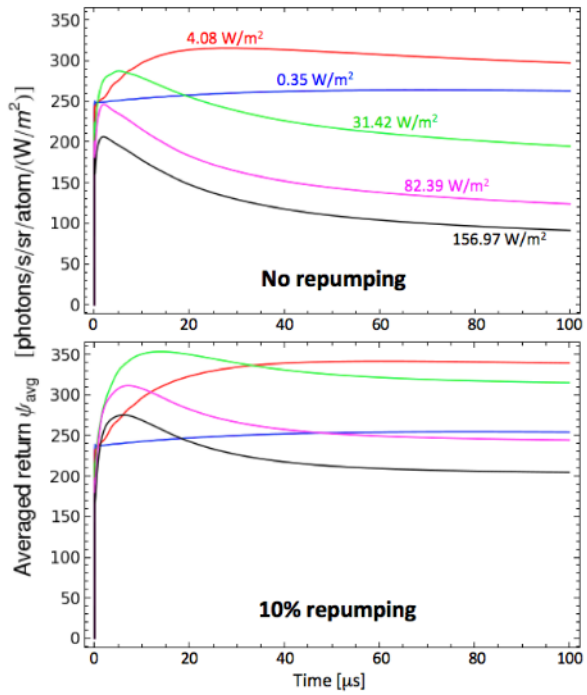

Fig. 2. Time evolution of specific return (in the mesosphere) for different levels of irradiance present for 10 W average power and 20% duty cycle over 100 μs. When no light is resonant with D_2b (top plot), the return peaks and declines quickly. When 10% is tuned to D_2b (bottom plot), the return peaks later, is higher, and decreases less rapidly. These graphs show that certain values of irradiance excite the sodium atoms more efficiently.

It was hypothesized that the peak and decline are in part due to the effects of Larmor precession, since this acts on timescales of a few microseconds. To test this, these simulations were repeated with zero magnetic field. The results showed a lessening in the severity of the decline, and the expected increase in return, but the peak remained prominent. Therefore, other factors are of greater importance, such as the rate of collisions between the sodium atoms and other constituents of the mesosphere. Indeed, altering the rate of collisions changes the shape of the curves in Figure 2, and the predicted return flux, as is discussed below.

Another interesting observation from Figure 2 is that certain irradiance levels are more efficient at optical pumping than others. In the bottom pane of Figure 2 (for 10% repumping) the green line corresponding to 31.4 W/m^2 achieves the highest specific return. The possibility of taking advantage of this circumstance by controlling the irradiance profile using uplink correction will be discussed further in Section 4.

Beyond the consideration of how to most effectively excite the sparse sodium atoms during a single pulse, is the question of what pulse formats allow for the benefits of optical pumping to be maintained between consecutive pulses. Stated differently, what is the length of time necessary for atomic polarizations to return to thermal equilibrium? Based on results of various simulations performed to test

this, the time scale appears to be on the order of ~50 μs, near the center of the sodium layer. Hence, a format with less than this amount of dark time between pulses should be modeled with multiple cycles of the laser, while pulses with larger spacing may be considered independent, i.e., modeling a single pulse will give an estimate within 5 to 10% what is obtained for multiple pulses.

Figure 3 shows a 10-pulse train for pulses of 500 ns, with 10% repumping and a 20% duty cycle. There is collisional relaxation and Larmor precession between pulses, but the ground-state polarization (and possibly also the non-thermal velocity distribution) created by the light during the pulse has not completely relaxed by the time the next pulse comes. The pumping between pulses is evident. Notably, the different irradiance levels (which are the same as in Figure 2) evolve differently as a function of time. The extremal irradiance levels (0.35 and 156.97 W/m^2) remain fairly constant from pulse to pulse, while the in between irradiances (especially the 31.42 and 82.39 W/m^2 curves, in green and magenta, respectively) show the highest return after just a few pulses. These irradiances are most efficient at exciting the sodium atoms.

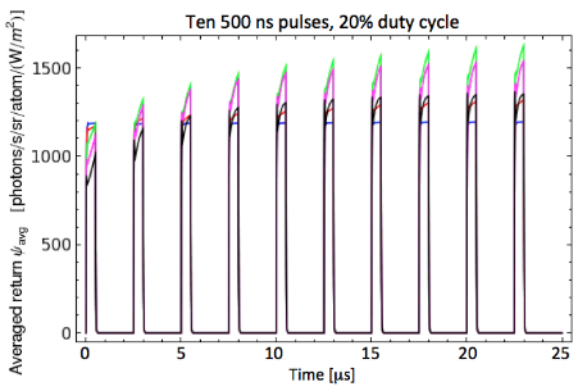

Fig. 3. This intermediate pulse format shows effects of optical pumping between pulses, indicating the sodium atoms maintain their polarization state during the 2 μs dark time. The irradiance levels and colors are the same as in Figure 2. The green (31.42 W/m^2) and magenta (82.39 W/m^2) levels have the highest specific return after a few pulse cycles, indicating they are more efficient than the other levels.

To discover the optimal pulse duration, simulations were carried out for pulses ranging from 200 ns to 60 μs, with 10% repumping, both 10% and 20% duty cycles, for zenith pointing at Mt. Hamilton. In all cases, the 20% duty cycle gave higher return, and the maximum was for the 30 μs pulses. The predicted return flux at the top of the telescope (i.e. before interacting with any optics or detectors) for this format is 12 × 10^6 photons/s/m^2, assuming a sodium column density of 4 × 10^{13} atoms/m^2 and 0.5 m FWHM mesospheric spot size. This value is based on simulation of 3 cycles of the laser (450 μs), although it is the same value obtained for only one cycle. At a pulse length of 60 μs, and the same duty cycle, the time-averaged return flux declined to 11.2 × 10^6 photons/s/m^2. For the 200 ns case (the LLNL fiber laser is currently operating with this pulse length, but at 10% duty cycle), the predicted return flux is 11.3 × 10^6 photons/s/m^2 based on a simulation of 50 cycles (50 μs). This information is displayed in Table 1. For comparison, a 10 Watt CW laser with otherwise identical parameters (repump fraction, location and pointing) is expected to produce 13 × 10^6 return photons/s/m^2.

Table 1. Predicted return flux at the telescope for 200 ns, 30 μs, and 60 μs pulses, with 10% and 20% duty cycles, from a zenith pointing 10 W laser at Mt. Hamilton assuming a sodium column density of 4 × 10^{13} atoms/m^2 and 0.5 m FWHM mesospheric spot.

Pulse length (μs)	Return 10% duty cycle (×10^6 photons/s/m^2)	Return 20% duty cycle (×10^6 photons/s/m^2)
0.2	9.5	11.3
30	10.5	12.0
60	10.2	11.2

The default time between collisions of sodium atoms and other constituents of the upper atmosphere (mainly O_2 and N_2) in LGSBloch is 35 μs for velocity changing and 245 μs for spin randomizing. However, these values are estimates, due to the fact that the relevant cross sections are not well known. To test the effect of changes in this variable on the predicted return flux, the case of 30 μs pulses and 20% duty cycle was examined for collision times 10 times shorter and 10 times longer, in the absence of a magnetic field. The results showed an ~12% decrease in return flux at the telescope when the rate of collisions were an order of magnitude smaller than the default, and only an ~1% increase when collisions were an order of magnitude less frequent. This determines that LGS brightness is not highly disturbed by fluctuations in this parameter.

The above investigation established the 30 μs pulses with 20% duty cycle as part of the goal format to implement on the LLNL fiber laser, since it has the highest predicted return and will also facilitate Raleigh blanking. The 30 μs pulse length corresponds to a distance of 9 km in air, so the pulse will essentially span the entire sodium layer.

The return flux predictions given thus far have been for narrow (<10 MHz) line width lasers. The spectrum of the LLNL fiber laser currently contains multiple lines (modes) spaced at 200 MHz intervals. This multimode format was implemented to mitigate stimulated Brillouin effects (SBS) in the fiber amplifiers. From the standpoint of effective coupling to the Na atoms, in the absence of saturation such a spectrum is generally less desirable than having the light confined within two lines that are tuned precisely to the D_2a and D_2b transitions. Also, the problem of accurately modeling a system with many discrete frequency components using Bloch equations becomes very complex. Hence, the numbers presented thus far should be considered optimistic upper limits on what will actually be achievable with this laser in real on-sky conditions.

There is some flexibility in the fiber laser system as to the number of modes and how far apart they are spaced, and the option exists to convert to a broadband format instead. Because the freely available version of LGSBloch does not have the capability to do multimode time domain calculations, a consulting contract was established with one of the co-authors (SR) through his consulting firm Rochester Scientific to investigate the effects of such changes on the return flux.

Rochester Scientific developed a proprietary extension of the LGSBloch simulation package, where solutions to the density matrix evolution equations are generated with a code written in C that uses an open-source ODE solver (Rochester et al. 2012). This method addresses the stiffness of the system using implicit backward differentiation formulas (Hindmarsh et al. 2005), and significantly decreases the time required for convergence to a solution. Techniques to account for the atoms being subjected to a field with components oscillating at different frequencies have also been included.

Hillman et al. (2006) hypothesized that a mode separation of 150 MHz would give maximal return flux, based on considerations of the sodium hyperfine structure. To investigate this, Rochester Scientific produced a simulation for a three-mode system, with the central frequency tuned

to the center of the D2a line and sidebands with separations ranging from 0 to 500 MHz. The parameters used were for a 10 W laser at Mt. Hamilton with 30 μs pulses, 20% duty cycle, and no repumping. The orange curves in Figure 4 show how the specific return in the mesosphere varies with mode separation, when propagating parallel (top) and perpendicular (bottom) to the geomagnetic field. The blue curves show the changes in return for a broadband laser spectrum, with line width ranging between 0 and 500 MHz.

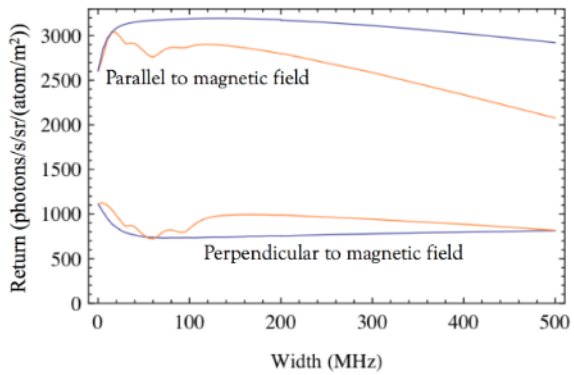

Fig. 4. The predicted return in the mesosphere for a 10 W laser at Mt. Hamilton with 30 μs pulses, 20% duty cycle, and no repumping, varies depending on the spectral format. Return is shown for a multimode LGS as a function of mode separation (orange) and for a broadband LGS as a function of bandwidth (blue), with the laser directed parallel (top lines) and perpendicular (bottom) to Earth's magnetic field. Different formats may be preferable at different locations depending on the orientation to the magnetic field during the majority of observations.

The structure observed in the multimode case can be understood in terms of the energy-level structure of sodium. The local minimum at ~60 MHz is a consequence of the 59.8 MHz separation between the $F' = 2$ and $F' = 3$ excited states. Here, while one of the laser modes (say, the central frequency) is exciting the $F = 2$ to $F' = 3$ transition, an adjacent mode (say, one of the sidebands) is tuned to the $F = 2$ to $F' = 2$ transition for the same velocity group. Because atoms in the $F' = 2$ excited state can decay to the $F = 1$ ground state where they are no longer resonant with the light field, excitations of the $F' = 2$ state are less beneficial, and the competition with optical pumping on the $F = 2$ to $F' = 3$ transition leads to reduced return flux The dips in return near ~30 and ~90 MHz can be understood similarly. When the sidebands are 30 MHz from the central frequency, atoms in a velocity group resonant with the $F = 2$ to $F' = 3$ transition for one sideband will also be resonant with the opposite sideband (spaced 60 MHz away) exciting the $F = 2$ to $F' = 2$ transition. When the modes are separated by 95.3 MHz, a velocity group resonant with a laser mode exciting the $F = 2$ to $F' = 3$ transition will also be resonant with an adjacent mode exciting the $F = 2$ to $F' = 1$ transition. Atoms in the $F' = 1$ excited state can also decay to the $F = 1$ ground state and be lost, leading to reduced return flux due to the competition, as above. The decline in return at larger separations is attributed to the presence of fewer atoms available to interact with the light field near the edges of the Doppler broadened spectrum.

Figure 4 confirms that the ideal line separation in a multimode LGS is either small (less than ~20 MHz) or between about 120 to 150 MHz, depending on the orientation to Earth's magnetic field. This holds implications for what will be the most effective use of laser power depending on the location of an observatory, and what the highest priority science cases are. Near the magnetic equator, a laser may spend the majority of time propagating near perpendicular to the geomagnetic field. At more magnetically polar latitudes, zenith propagation can be much closer to parallel to the field lines. Figure 4 suggests that a broadband LGS (with FWHM between about 50 and 150 MHz) should be the brightest for polar observatories, and an equatorial location may benefit most from a multimode spectrum (with mode separations of ~150 MHz).

Taking into account the lessons learned from the inquiries discussed in this section, the goal format for the LLNL fiber laser is presented in Table 2.

Table 2. Comparison of parameters between current Mt. Hamilton LGS, and lab tested and goal formats of the new laser

	Current dye laser	New fiber laser	
		Lab tested format	Goal format
Output power	9 W	10 W	10 W
Polarization	Linear	Circular	Circular
Spectral format	~2 GHz FWHM bandwidth	9 lines with 200 MHz spacing	Fewer lines and/or smaller spacing
Pulse duration	150 ns	200 ns	30 μs
Duty cycle	0.16 %	10 %	20 %
Fraction of light on D2b	None	None	10%

4.POTENTIAL BENEFITS OF UPLINK CORRECTION

Numerical simulations enable investigation of the possible benefits of uplink control, a technique in which the laser light is reflected off a deformable mirror prior to projection into the atmosphere (Norton et al. 2014). This allows manipulation of the wavefront in order to compensate for imperfections of the outgoing beam shape and projection optics, and aberrations induced by atmospheric turbulence. The potential benefits explored include obtaining a smaller spot to decrease WFS measurement error, and potentially regulating the pattern of irradiance in the mesosphere to maximize efficiency of optical pumping.

In consulting with Rochester Scientific, the issue of quantifying the benefits of uplink control was explored. We investigated manipulating the irradiance profile as well as the spot size, in order to maximize the area in the mesosphere irradiated at levels that lead to the most efficient fluorescence (as discussed in Section 3). This involved modeling a beam profile with the shape of a top hat, and comparing it to the Gaussian profiles used for all modeling results thus far.

In Figure 5, two curves compare the predicted return flux at the top of the telescope of both Gaussian and top hat shaped mesospheric illumination profiles. These were generated for a laser that produces 10 W average power, located at Mt. Hamilton, operating at 20% duty cycle with 30 μs pulses, 3 modes spaced by 150 MHz, 10% of the power in a sideband tuned to D2b, and another 10% lost in the sideband on the far side of the spectrum (this is necessary as a consequence of current laser engineering frequency modulation techniques). The assumed sodium column density is 4×10^{13} atoms/m^2.

We can conclude that there is only a small enhancement in return flux over the Gaussian beam when the irradiance profile is made to approach a constant value. However, full interpretation requires understanding how the shape of the beam in the mesosphere gets translated to a spot size on the WFS detector. For most LGS AO systems currently in operation, there are advantages to using uplink correction to reduce the size of the laser spot.

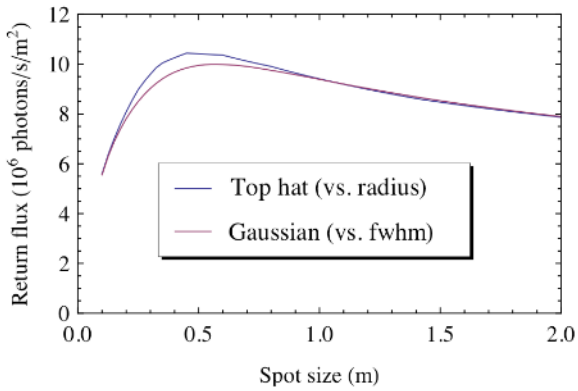

Fig. 5. The predicted return flux at the top of the telescope for Gaussian and top hat shaped mesospheric irradiance profiles shows slight improvement with the top hat profile. This is for the case of 10 W average power, at Mt. Hamilton, 20% duty cycle, 30 μs pulses, 3 modes spaced by 150 MHz, 10% of the power in a sideband at D_2b, and another 10% lost on the far side of the spectrum. The largest benefits of uplink correction will come from the reduction in WFS measurement error associated with a smaller spot size.

The current estimate of the FWHM spot size of the LGS on the Shane telescope is ~2 arcseconds, which means it appears to be ~1 m diameter at the distance of the mesosphere (90 km). Assuming that there are approximately equal amounts of spot broadening from atmospheric turbulence as the light travels back to the telescope as for its trip upward, then the actual physical size of the laser beam in the mesosphere is ~0.6 m. If uplink control could be used to reduce this by a factor of two to a nearly diffraction limited spot, even with the decreased return as indicated in Figure 5, the WFS measurement error would be reduced by a factor of two. Such benefits may be worth the additional complexity of an uplink system. Recall that LGS AO wavefront measurement performance is tied to the guide star radiance (energy per unit area at the telescope), not just the total brightness, so some minor sacrifice of return flux is tolerable if the apparent spot size is reduced.

The best estimate of the LGS brightness expected from the LLNL fiber laser can be deduced from Figure 5. Assuming a roughly Gaussian spot that has ~0.6 m FWHM, approximately 10 × 10^6 photons/s/m^2 should reach the top of the telescope. This is somewhat less than the 12 × 10^6 photons/s/m^2 predicted in section 3, but the difference can be understood as a consequence of the more realistic spectral format used here. Given that the average measured return flux from the current dye laser on the Shane telescope between 2006 and 2010 was 1.16 × 10^6 photons/s/m^2, it appears reasonable to expect the fiber laser to produce 5–10 times the return seen from the current LGS.

5.COMPARISON OF SIMULATION PREDICTIONS TO LGS RETURN MEASUREMENTS

Because the return flux at the telescope scales linearly with the mesospheric sodium column density, C_{Na}, this parameter is a useful gauge in determining how accurately a numerical model reproduces real systems. Results of LIDAR measurements indicate the expected median annual density is 3–4 × 10^{13} atoms/m^2, although sporadic layers may have concentrations up to 10 times greater (Xiong et al. 2003, Moussaoui et al. 2010). It has long been known that the sodium layer has variations that are seasonal, rather than annual, with a winter abundance maximum in both the northern and southern hemispheres (Plane et al. 1999). Perhaps due to the varying intensity of seasonal temperature changes, the strength of variability is a function of latitude, with more extreme changes at larger latitudes (Gumbel et al. 2007).

The LGSBloch model is reported to predict return fluxes in good agreement with measurements for the case of the single frequency 50 W Fasortronics laser at SOR (Holzlohner et al. 2010b). This requires assuming slightly higher than average, but still reasonable, values for the C_{Na}, which are fairly consistent with what has been reported for that site (Drummond et al. 2007). Also, good agreement is seen between model predictions and measurements for the CW laser used in the ESO transportable LGS unit (Bonaccini Calia et al. 2012).

The parameters of the current LGS on the Shane telescope at Mt. Hamilton are given in Table 2. Because of the long dark time between pulses (~91 μs), and long computation times required by LGSBloch, initial modeling endeavors only included one cycle of the laser. They incorporated a Gaussian spot size of 0.6 m FWHM in the mesosphere, a Gaussian pulse shape with 150 ns FWHM, and a Gaussian shaped spectrum with 2.2 GHz FWHM bandwidth. The values of these last two parameters were determined from measurements taken with Mt. Hamilton instruments, although the shape of the laser spectrum is closer to a top hat.

In Figure 6, return flux measurement data from the AO system WFS of this laser, taken between 2006 and 2010, are plotted as a function of month. They show strong evidence for the seasonal variation of the sodium layer. The value of C_{Na} found by comparing the measured data with the prediction from the model was used as a gauge to how well the measurements were reproduced with LGSBloch. The right-hand axis exhibits the implied amount of C_{Na} based on the present stage of modeling. For the seasonal average corresponding to a return flux of 1.16 × 10^6 photons/s/m^2 at the top of the telescope, the average C_{Na} is found to be only 1.5 × 10^{13} atoms/m^2. This small value is interpreted as an indication that the simulations are over-predicting the measurements for this laser by at least a factor of two. Thus, the conclusion is that some physical, environmental, or observational parameters are not being accounted for adequately.

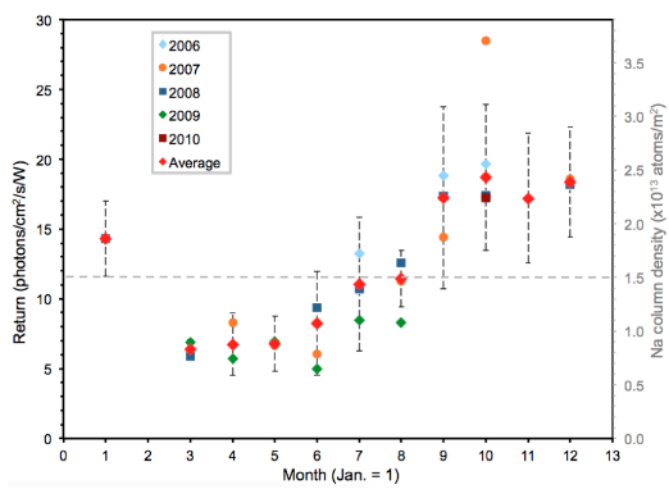

Fig. 6. Data from the dye laser on the Shane telescope show expected seasonal variability. The right axis shows implied C_{Na} based on current modeling with LGSBloch. The horizontal dashed line indicates the predicted average column density for the measured average return of 11.6 photons/cm^2/s/W. These values are considerably lower than expected.

The return flux measurements in Figure 6 are based on data collected with the Shack-Hartman WFS, for zenith pointing observations. The intensity in the fully illuminated subapatures was averaged, and

corrected for detector effects and 40% system throughput. The camera gain is reported to be ~1 electron/count. In 2004, a portable power meter with 633 nm wavelength light was used to measure throughput of the AO system from the primary focus of the telescope to the WFS, which was found to be 55%. In January 2012, observations of several Hayes spectrophotometric standard stars were taken by the observatory staff to re-asses this value. A sodium filter with 0.87 nm FWHM bandpass was placed in the beam path, and resulting photometry measurements were corrected for atmospheric transmission and compared with online spectra†. This analysis yielded an average throughput of 40%, which is consistent with the 2004 measurement when considering the amount of light lost to the primary and secondary mirror surfaces and optics internal to the WFS.

After ensuring the measurement data were being interpreted correctly, some of the less precisely determinable simulation inputs were varied to see how sensitive the predictions were to these assumptions. Making adjustments to parameters such as spot size, bandwidth, and atmospheric transmission, it is possible to somewhat ameliorate the disagreement, but only marginally. For example, the estimate of return for the Shane laser can be reduced 20% by reducing the modeled spot size from 0.7 m to 0.6 m FWHM, and changing the bandwidth from 1.5 GHz (the original target width for the spectrum) to 2.2 GHz FWHM (closer to the measured value). However, the same reduction also occurred when increasing the spot size to 1.0 m FWHM, setting the bandwidth to 2.2 GHz, and decreasing the atmospheric transmission to 85% (the default value is 89%). This is strong evidence for the need to better constrain such variables.

It is worth noting a check of the relative accuracy of LGSBloch was performed by computing the predicted return when the spectrum broadening phase modulators were switched off. In both simulations and experiment this reduced the LGS brightness by a factor of ~3 (presumably due to increased saturation of the sodium layer).

Additional efforts to improve the agreement between theory and measurement were explored when consulting with Rochester Scientific. This entailed reduction of the launched power to 9 W, simulation of multiple cycles of the laser, and inclusion of a more realistic laser spectrum and mesospheric irradiance profile. However, these changes were not able to ameliorate the discrepancy (Rampy 2013).

To help identify whether the source of the discrepancy was related to the measurement data or the model, simulations were also performed for the two LGS at the Keck observatory. The Keck II system began science operations in 2004 (Wizinowich et al. 2006), and has been responsible for ~70% of the refereed science papers published worldwide through 2014 based on data collected with LGS AO systems. The success of this system led to the desire for similar capabilities on the Keck I telescope. This has been recently realized, with the Keck I LGS AO system having begun full science operations in the latter part of 2012 (Chin et al. 2012).

The laser on Keck II is the same technology as the dye laser at the Lick observatory and has essentially the same format, except that it operates with a repetition rate of 26 kHz (the Shane laser is at 11 kHz). A Gaussian spot size of 0.7 m FWHM in the mesosphere was assumed, and parameters based on location, such as observatory altitude, magnetic field direction and strength, were included in the model. For the ~12 W expected to be projected from the launch telescope, the simulations predict 4.2×10^6 photons/s/m^2, for a sodium column density of 4×10^{13} atoms/m^2. However, measurements reported in the literature indicate between ~0.7 and 1.75×10^6 photons/s/m^2 are being received at the telescope (Le Mignant et al. 2006). This again constitutes a factor of 2–3 discrepancy between data and simulation.

The Keck I laser was developed by Lockheed Martin Coherent Technology (LMCT) and is a solid-state mode-locked CW laser, which uses sum-frequency generation (SFG) of beams at 1064 nm and 1319 nm to achieve the 589 nm sodium wavelength (Sawruk et al. 2010). The efficiency of the SFG process increases nonlinearly with input light intensity, so to maximize efficiency the laser is formatted as a train of short pulses to achieve high peak intensity. Each pulse is 300 picoseconds FWHM and the repetition rate is 82 MHz. Though the average launched power is higher for this laser (~ 18 W), the return from the sodium layer is on average nearly equal to, or only slightly higher, than what is seen from the Keck II LGS (Chin et al. 2012). LGSBloch simulations give the over-prediction that 5.2×10^6 photons/s/m^2 should be reaching the top of the telescope. All evidence suggests that this format is even less effective at coupling to the sodium atoms than those used by the dye lasers.

6.CAN PULSED LASERS PRODUCE BRIGHTER LGS THAN CW?

A recent suggestion has raised the possibility that pulsed systems could produce brighter beacons than are achievable with CW lasers. The scheme entails pulsing the laser at the Larmor frequency in order to avoid the detrimental effects of atomic states changing their magnetic quantum number as they precess (Hillman et al. 2012). This is similar to an idea in the field of magnetometry, to use LGS systems with modulated lasers to measure the strength of Earth's magnetic field in the mesosphere (Budker et al. 2007).

Figure 7 presents a preliminary assessment of this technique, for a 10 W average power LGS at Mt. Hamilton (solid lines) and 20 W average power at Mauna Kea (dashed lines). At an altitude of 90 km above Mt. Hamilton, the magnetic field strength and Larmor precession period are $B = 0.47\ G, \tau_L \approx 3.1$ µs (326 kHz), and above Mauna Kea $B = 0.33\ G$ and $\tau_L \approx 4.4$ µs (231 kHz). Pulsed simulations included these values as the repetition rates, with 10% duty cycle, and 10% repumping, for the laser beam pointing parallel and perpendicular to the magnetic field, and towards zenith, for each site. The return flux is compared to CW formats with the same average power and otherwise identical parameters, and also to the goal format in the case of Mt. Hamilton. All simulations included five irradiance levels, integrated over a 0.5 m FWHM Gaussian beam profile in the mesosphere, and propagated back through the atmosphere to the top of the telescope.

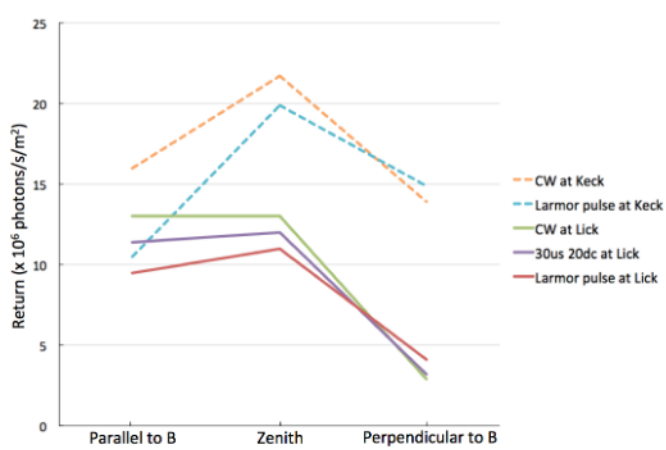

Fig. 7. Comparisons of return flux for 10 W average power at Mt. Hamilton (solid) and 20 W average power at Mauna Kea (dashed) for the Larmor pulse format, a CW format, and at Mt. Hamilton, the goal

† www.eso.org/sci/observing/tools/standards/spectra/stanlis.html

format for the LLNL fiber laser. Simulations were carried out for a laser pointing parallel and perpendicular to the magnetic field, and to zenith.

The largest enhancement is seen for the case of propagation perpendicular to the magnetic field at Mt. Hamilton, where the Larmor frequency pulses produce ~40% higher return than a CW laser with the same average power. At Mauna Kea there is only a 7% increase over CW, likely because the strength of the geomagnetic field is less at this location. These results suggest implementing Larmor frequency pulses at a fairly equatorial site such as Mauna Kea is unlikely to produce significant benefits. However, at the location of Mt. Hamilton, and depending on the science cases of greatest interest, such a technique may warrant further inquiry.

To ensure the repetition frequency used was indeed at the peak of the resonance, several slightly different repetition rates were simulated. This investigation showed that the peak is narrow (only a few kilohertz wide) for a given height in the sodium layer, so experimental investigation of this phenomenon may require the ability to precisely tune the repetition rate of the laser. Future investigation of this method will focus on determining how this enhancement can be most effectively used to increase LGS brightness.

7.DISCUSSION

Sodium laser guide stars (LGS) have emerged as an important tool for advancing ground-based astronomy. The significant cost of these systems necessitates maximizing efficiency, which is an effort that is still in progress. The LGSBloch simulation package (available at http://rochesterscientific.com/ADM/) has permitted new insights into how laser light interacts with mesospheric sodium, including the evolution of the energy level populations, and other physical effects such as Larmor precession, atomic recoil, and collisions with other constituents of the upper atmosphere. Guidelines for current and future system designers have been identified through use of this tool.

Predicted return fluxes from the LGSBloch simulation package have been shown to be reasonably accurate for the case of CW LGS, but to overestimate the return of short pulse systems by a factor of 2–3. The two cases of CW LGS are the 50 Watt Fasortronics laser at the Starfire Optical Range and ESO transportable LGS unit. For short pulse systems, we have modeled the lasers at the Lick and Keck Observatories, and a similar discrepancy was reported for comparison to the LGS system at the Gemini South Observatory (Holzlohner et al. 2012).

The consistency of the discrepancy between four short pulse laser systems with independent assessments raises suspicion that the issue lies in our current understanding of this format regime rather than a measurement calibration error. Because the formats investigated for the new fiber laser at Mt. Hamilton have intermediate pulse lengths (microseconds, instead of nano- or pico-seconds), it is expected the actual return should be less than a factor of 2 reduced from the LGSBloch predictions, assuming its format matches the goal format presented here.

Pulsed laser systems require substantially more complex simulations, and it is possible the discrepancy could be reduced with improved modeling of velocity-changing collisions or other time domain phenomena. It has also been suggested that the problem could be due to some unknown fraction of the light getting lost, or diverted to non-interacting frequencies, between the diagnostic measurements and laser launch. The likeliness of this has been ascertained from plots of the expected return flux as a function of launched laser power. These indicate that ~70% of the power would have to be unaccounted for (assuming the other parameters used are reasonably accurate), a situation that does not seem probable. Other parameters it would be beneficial to double check experimentally include:

- Wavelength stabilization
- Launched power and polarization state
- Beam quality and corresponding irradiance histogram in the mesosphere
- Atmospheric transmission at the time of measurements

An important step in improving our understanding of sodium-light interactions will be accumulating additional experimental information. Dedicated tests to evaluate the effect of changing the power and spectrum of the laser would help illuminate the specific areas of our understanding that require improvement.

References

1. Happer, W., MacDonald, G. J., Max, C. E., and Dyson, F. J., "Atmospheric-turbulence compensation by resonant optical backscattering from the sodium layer in the upper atmosphere," J. Opt. Soc. Am. A 11, 263–276 (1994).
2. Holzlöhner, R., Rochester, S. M., Calia, D. B., Budker, D., Higbie, J. M., and Hackenberg, W., "Optimization of cw sodium laser guide star efficiency," Astron. Astrophys. 510, A20+ (2010a).
3. Kupke, R., Gavel, D., Roskosi, C., Cabak, G., Cowley, D., Dillon, D., Gates, E. L., McGurk, R., Norton, A., Peck, M., Ratliff, C., and Reinig, M., "ShaneAO: an enhanced adaptive optics and IR imaging system for the Lick Observatory 3-meter telescope," Proc. SPIE 8447, Adaptive Optics Systems III, 84473G (September 13, 2012).
4. Hillman, P. D., Drummond, J. D., Denman, C. a., and Fugate, R. Q. "Simple Model, Including Recoil, for the Brightness of Sodium Guide Stars Created from CW Single Frequency Fasors and Comparison to Measurements" Proc. SPIE 7015, Adaptive Optics Systems, 70150L (2008).
5. Jeys, T.H., Heinrichs, R. M., Wall, K. F., Korn, J., Hotaling, T. C., and Kibblewhite, E., "Observation of optical pumping of mesospheric sodium," Optics Letters, Vol. 17, No 16 (1992).
6. Milonni, P. W., Fugate, R. Q., and Telle, J. M., "Analysis of measured photon returns from sodium beacons," J. Opt. Soc. Am. A 15, 217–233 (1998).
7. Gumbel, J., Fan, Z. Y., Waldemarsson, T., Stegman, J., Witt, G., Llewellyn, E. J., She, C. –Y., and Plane, J. M. C., "Retrieval of global mesospheric sodium densities from the Odin satellite," Geophysical Research Letters, Vol. 34, L04813 (2007).
8. Holzlöhner, R., Rochester, S. M., Calia, D. B., Budker, D., Pfrommer, T., and Higbie, J. M., "Simulations of pulsed sodium laser guide stars: an overview," Proc. SPIE 8774, Adaptive Optics Systems III, 84470H (2012).
9. Corney, A., in "Atomic and Laser Spectroscopy," Clarendon, Oxford, (2006).
10. Wang, L., Otarola, A., Ellerbroek, B., "Impact of sodium laser guide star fratricide on multi-conjugate adaptive optics systems," JOSA A., Vol. 27, No. 11, pp. A19-A28 (2010).
11. Bonaccini-Calia, D., Hackenberg, W., Holzlöhner, R., Lewis, S., and Pfrommer, T., "The Four-Laser Guide Star Facility: Design considerations and system implementation," Adv. Opt. Techn., 3,3, pp. 345-361 (2014).
12. Rampy, R., "Advancing adaptive optics technology: Laboratory turbulence simulation and optimization of laser guide stars," Dissertation, University of California Santa Cruz (2013).
13. Rochester, S. M., Otarola, A., Boyer, C., Budker, D., Ellerbroek, B., Holzlöhner, R., and Wang, L., "Modeling of pulsed-laser guide stars for the Thirty Meter Telescope project," JOSA B, Vol. 29, Issue 8, pp. 2176-2188 (2012).
14. Hindmarsh, A. C., Brown, P. N., Grant, K. E., Lee, S. L., Serban, R., Shumaker, D. E., and Woodward, C. S., "SUNDIALS: Suite of nonlinear and differential/algebraic equation solvers," ACM Transactions on Mathematical Software 31, 363–396 (2005).
15. Hillman, P., "Sodium guidestar return from broad CW sources," CfAO Laser Workshop (2006).
16. Norton, A. P., Gavel, D., Helmbrecht, M., Kempf, C., Gates, E., Chloros, K., Redel, D., Kupke, R., and Dillon, D., "Laser guidestar uplink correction using a MEMS deformable mirror: on-sky test results and implications for future AO systems," Proc. SPIE 9148, Adaptive Optics Systems IV, 91481C (2014).

17. Xiong, H., Gardner, C. S., and Liu, A. Z., "Seasonal and nocturnal variations of the mesospheric sodium layer at Starfire Optical Range, New Mexico," Chin. J. of Geophys. 46, pp. 432–437 (2003).
18. Moussaoui, N., Clemesha, B.R., Holzlöhner, R., Simonich, D. M., Calia, D. B., Hackenberg, W., and Batista, P. P., "Statistics of the sodium layer parameters and its impact on AO sodium LGS characteristics," Astron. Astrophys. 511, A31 (2010).
19. Plane, J. M. C., Gardner, C. S., Yu, J. R., She, C. Y., Garcia, R. R., and Pumphrey, H. C., "Mesospheric Na layer at 40°N: Modeling and observations," J. Geophys. Res., 104, 3773 (1999).
20. Holzlöhner, R., Rochester, S. M., Pfrommer, T., Calia, D. B., Budker, D., Higbie, J. M., and Hackenberg, W., "Laser guide star return flux simulations based on observed sodium density profiles," Proc. SPIE 7736, Adaptive Optics Systems II, 77360V (2010b).
21. Drummond, J., Novotny, S., Denman, C., Hillman, P., and Telle, J., "The Sodium LGS Brightness Model over the SOR," AMOS 2007 Conference, pp. E67 (2007).
22. Bonaccini Calia, D., Guidolin, I., Friedenauer, A., Hager, M., Karpov, V., Pfrommer, T., Holzlohner, R., Lewis, S., Hackenberg, W., Lombardi, G., Centrone, M., and Pedichini, F., "The ESO transportable LGS Unit for measurements of the LGS photon return and other experiments", Proc. SPIE 8450, Modern Technologies in Space- and Ground-based Telescopes and Instrumentation II, 84501R (2012).
23. Wizinowich, P. L., Le Mignant, D., Bouchez, A. H., Campbell, R. D., Chin, J. C. Y., Contos, A. R., van Dam, M. A., Hartman, S. K., Johansson, E. M., Lafon, R. E., Lewis, H., Stomski, P. J., and Summers, D. M., "The W. M. Keck Observatory Laser Guide Star Adaptive Optics System: Overview," PASP, 118, 297-309 (2006).
24. Chin, J. C. Y., Wizinowich, P., Campbell, R., Chock, L., Cooper, A., James, E., Lyke, J., Mastromarino, J., Martin, O., Medeiros, D., Morrison, D., Neyman, C., Panteleev, S., Stalcup, T., Tucker, P., Wetherell, E., and van Dam, M., "Keck I Laser Guide Star Adaptive Optics System," Proc. SPIE 8447, Adaptive Optics Systems III, 84474F (2012).
25. Le Mignant, D., Campbell, R., Boucheza, A., Chin, J., Chock, E., Conrad, A., van Dam, M., Doyle, S., Goodrich, R., Johansson, E., Lafon, R., Lyke, J., Melcher, C., Mouser, R., Summers, D., Wilburn, C., and Wizinowich, P., "LGS AO operations at the W. M. Keck Observatory," Proc. SPIE 6270, Observatory Operations: Strategies, Processes, and Systems, 62700C (2006).
26. Sawruk, N. W., Lee, I., Jalali, M. P., Prezkuta, Z., Groff, K. W., Roush, J., Rogers, N., Tiemann, B., Hannon, S. M., Alford, W. J., d'Orgeville, C., Fesquet, V., Oram, R., Adkins, S. M., and Grace, K., "System overview of 30 W and 60 W 589 nm guidestar laser systems," SPIE Proc. 7736, Adaptive Optics Systems II, 77361Y (2010).
27. Hillman, P., "Paths towards a brighter guidestar," CfAO Laser Workshop (2012).
28. Budker, D., and Romalis, M. V., "Optical Magnetometry," Nature Physics 3, 227 - 234 (2007).

2.8 Optimization of CW LGS - Holzlohner (Rampy)

I believe that this is a more in depth paper of the one above. I have not read it yet.

A&A 510, A20 (2010)
DOI: 10.1051/0004-6361/200913108
© ESO 2010

Astronomy & Astrophysics

Optimization of cw sodium laser guide star efficiency

R. Holzlöhner[1], S. M. Rochester[2], D. Bonaccini Calia[1], D. Budker[2], J. M. Higbie[3], and W. Hackenberg[1]

[1] Laser Systems Department, European Southern Observatory (ESO), Karl-Schwarzschild-Str. 2, 85748 Garching b. München, Germany, http://www.eso.org/sci/facilities/develop/lgsf/
e-mail: [rholzloe;dbonacci;whackenb]@eso.org
[2] University of California Berkeley, Department of Physics, Berkeley, CA 94720-7300, USA
e-mail: [simonr;budker]@berkeley.edu
[3] Bucknell University, Department of Physics, 701 Moore Avenue, Lewisburg, PA 17837, USA
e-mail: james.higbie@bucknell.edu

Received 12 August 2009 / Accepted 1 October 2009

ABSTRACT

Context. Sodium laser guide stars (LGS) are about to enter a new range of laser powers. Previous theoretical and numerical methods are inadequate for accurate computations of the return flux, hence for the design of the next-generation LGS systems.
Aims. We numerically optimize the cw (continuous wave) laser format, in particular, the light polarization and spectrum.
Methods. Using Bloch equations, we simulate the mesospheric sodium atoms, including Doppler broadening, saturation, collisional relaxation, Larmor precession, and recoil, taking all 24 sodium hyperfine states into account and 100–300 velocity groups.
Results. LGS return flux is limited by "three evils": Larmor precession due to the geomagnetic field, atomic recoil due to radiation pressure, and transition saturation. We study their impact and show that the return flux can be boosted by repumping (simultaneous excitation of the sodium D_2a and D_2b lines with 10–20% of the laser power in the latter).
Conclusions. We strongly recommend the use of circularly polarized lasers and repumping. As a rule of thumb, the bandwidth of laser radiation in MHz (at each line) should approximately equal the launched laser power in Watts divided by six, assuming a diffraction-limited spot size.

Key words. instrumentation: adaptive optics – methods: numerical – atmospheric effects – telescopes

1. Introduction

Laser guide stars (LGS) are becoming essential in providing artificial beacons for adaptive optics (AO) in large telescopes (Hubin 2009). The generation of 8–10 m class telescopes, such as the Very Large Telescope (VLT) on Cerro Paranal, Chile, or the Keck telescopes on Mauna Kea, has been retrofitted with LGS and is still operated in many observing programs with natural guide stars or no AO at all. The upcoming 30+ m telescopes, such as the 42-m European Extremely Large Telescope (E-ELT) or the Thirty Meter Telescope (TMT), by contrast, are being designed from the start as adaptive telescopes and will require LGS in nearly all of their science operations. At the same time, sensing subaperture sizes of 20–50 cm and near-kHz AO frame rates, designed to provide high Strehl ratios in the infrared or even in the visible, require unprecedented LGS brightness and hence laser power.

Sodium (Na) LGS at 589 nm are most commonly used because of the large fluorescence cross section-abundance product of ca. $10^{-11}\,\mathrm{cm}^2 \times 4 \times 10^{13}\,\mathrm{m}^{-2}$, a fluorescence wavelength in the visible, and the high altitude of the sodium layer around 80–100 km compared e.g. to Rayleigh LGS, (Happer 1994, Table 1), which allows one to sense a large fraction of the turbulent atmosphere column above the telescope with a small number of guide stars. Unfortunately, powerful diffraction-limited laser beams at 589 nm are quite expensive to produce because of the lack of solid-state materials that amplify 589 nm or 1178 nm light. Recently, ESO has demonstrated a frequency-doubled narrow-band Raman fiber laser emitting 25 W at 589 nm (Taylor 2009), and we expect this technology to significantly improve the experimental situation.

Careful dimensioning of the required laser power and optimization of the laser format (spectrum, polarization, spot size) are needed. Numerical simulations are necessary since the experimental situation has so far been unsatisfactory: the sodium layer and atmospheric parameters often fluctuate rapidly (Thomas 2008; Pfrommer 2009), few reliable powerful lasers at 589 nm have been available up to now, and LGS sky experiments lack commonly agreed on measurement standards. Sodium cells cannot easily simulate mesospheric conditions. This work provides optimization rules for the case of continuous wave (cw) lasers over a wide range of laser powers.

Sodium LGS take advantage of the $3^2S_{1/2}$–$3^2P_{3/2}$ dipole transition, known as the D_2 line. The sodium ^2S ground state consists of two hyperfine multiplets with 8 magnetic substates combined, separated by 1.772 GHz, splitting the D_2 line into the D_2a and D_2b transition groups, corresponding respectively to the $F = 1$ and $F = 2$ Na ground states, where F is the total atomic angular momentum quantum number. The four ^2P multiplets ($F = 0 \ldots 3$) are separated by only 16, 34, and 60 MHz (16 magnetic substates, see Ungar 1989). At mesospheric temperatures near 190 K, the D_2a and D_2b lines are Doppler broadened to about 1 GHz each, giving rise to the characteristic double-hump absorption profile (see for instance Bradley 1992, Fig. 11, or Fig. 1 of this work). When the D_2a transition is excited by circularly polarized light at high irradiance (i.e. optical power density, unit W/m^2), a large fraction of atoms is pumped into the $(S, F = 2, m = \pm 2)$ substate, and the atoms cycle on the transition to the $(P, F' = 3, m' = \pm 3)$ substate, with m the magnetic quantum number, so that sodium effectively becomes a two-level system. This situation is twofold desirable because of the large

transition cross section and the directional return light peak towards the laser emitter and the telescope. Numerous studies of optical pumping have been conducted, e.g. by Happer (1972) and McClelland (1985), and the process is well understood.

The effective sodium return flux depends on the environmental conditions such as collisions with constituent gases, temperature, and the geomagnetic field. At higher irradiance, the atoms are driven away from thermal equilibrium, and it is necessary to take effects into account such as saturation, optical pumping, and the recoil caused by radiation pressure. Understanding the complicated interplay of these effects and obtaining quantitative values of the fluorescence efficiency requires numerical simulations. A commonly used method is the solution of the density matrix evolution (Bloch equation) of a multilevel atom.

Milonni & Thode (1992) simplified the D_2 scheme to a 2-level Bloch model which they solve in time domain. Bradley (1992) simulated the full 24-state density matrix, exciting the sodium by a train of short (nanosecond range) laser pulses like Milonni, using Runge-Kutta integration for one pulse period and exploiting the periodicity. Linear and circular light polarizations were treated. However, both works neglect the geomagnetic field. Morris (1994) studied frequency-modulated pulses over a wide range of pulse durations and linewidths up to 3 GHz, hence spanning the entire Doppler broadened D_2 line, employing time domain integration, for both linearly and circularly polarized light. In the end of his paper, he briefly estimates the impact of the geomagnetic field, but he does not include Larmor precession terms into his Bloch equations.

To our knowledge, Milonni (1998, 1999) has published the most advanced and detailed Bloch-equation simulation of sodium LGS to date, later generalized by Telle (2006, 2008). In his 1998 article, Milonni treats the cases of laser pulses that are short, comparable, and long compared to the ^2P lifetime of $\tau = 16.24$ ns, using numerical solution methods similar to Bradley's. His 1999 publication deals with cw excitation only and introduces spin relaxation and Larmor precession into the Bloch equations for the first time. He shows that the Larmor terms due to the geomagnetic field tend to redistribute the magnetic sublevel populations and hence impede optical pumping. All of the works cited in this and the previous paragraph solve the Bloch equations separately for a number of different sodium velocity groups (100−400) and then perform a weighted average over the results, and all neglect recoil.

An alternative method of simulating atomic fluorescence is to use rate equations, either implemented as a set of differential equations, (Pique 2006), (Hillman 2008), or by employing Monte Carlo rate equation techniques[1]. In the latter, one follows a more intuitive approach and tracks the time evolution of a single atom, executing photon absorption and emission events according to steady-state cross sections and branching ratios using a random number generator, while accounting for elapsed physical time and recording the atomic state history. After a sufficient time span Δt has been simulated, one divides the total number of spontaneously emitted photons by Δt to obtain the fluorescent flux. The advantage of this method is that it is easy to understand, and complex physical events such as collisions with different kinds of particles with or without spin exchange can be modeled in a transparent way. Also, the transit of optically pumped atoms across the Doppler spectrum due to velocity-changing collisions and recoil can be easily modeled, hence different velocity groups can be properly coupled, including their atomic polarization exchange (using Bloch equations, such coupling requires the simultaneous solution of sets of 24^2-dimensional equations per velocity group, which we describe in this work for the first time in application to sodium LGS, to our knowledge).

A serious disadvantage of rate equations is that they rely on steady-state atomic cross sections, limiting the scope to the simulation of events slow compared to the sodium transition lifetime, (Milonni 1992), and the combination of the excitation-emission (Rabi) cycling with Larmor precession is hard to implement correctly. Furthermore, when compared to atomic Bloch equations, rate equations neglect the coherences (off-diagonal terms of the density matrix that describe transverse atomic polarization), which is problematic when modeling Larmor precession or linearly polarized light (the latter even for $B = 0$). Finally, Monte Carlo rate-equations need considerable CPU time in order to converge.

There are also approaches that mix aspects of Bloch and rate-equation codes, such as BEACON, which has been adapted to model two-step sodium excitation for polychromatic LGS, (Bellanger 2004). BEACON neglects atomic collisions and recoil. Guillet de Chatellus (2008) reports that it requires on the order of 24 h per run on a 2.6 GHz processor, and that the agreement with a pure rate-equation model can be good in certain cases.

Throughout this paper, we highlight what may be called the "three evils" of sodium LGS, ordered by decreasing importance

1. Larmor precession,
2. Recoil (radiation pressure),
3. transition saturation (stimulated emission),

and we suggest ways of mitigating them. Larmor precession is powerful enough to thwart optical pumping if the angle between the beam and the field lines is large (Drummond 2007), (Moussaoui 2009). The average 50-kHz redshift that one incurs per spontaneous emission due to atomic recoil can lead to spectral hole burning (depopulation of the respective atoms velocity group) in very bright single-frequency LGS (bandwidth <10 MHz, Hillman (2008)), but it also offers the opportunity of "snowplowing" the sodium population towards higher velocities in the laser beam direction, requiring continuous blueshifting (chirping) of the laser as first suggested by Bradley (1992), at the expense of laser complexity. Ultimately, at high spectral irradiance, stimulated emission becomes relevant, limiting spontaneous emission. Photons from stimulated emission are emitted straight into space, hence becoming useless for LGS.

There is some ambiguity in the sodium LGS community about the term "saturation", for it is sometimes used to describe only transition saturation, and sometimes the depopulation of the $F = 2$ upper ground state towards $F = 1$, known as downpumping. Once an atom is in the $F = 1$ state, it can only be excited if the D_2b line is pumped as well, which is known as repumping (either by allocating 10−20% of the laser power to the D_2b line, or by widening a single laser line to ≥2 GHz). Downpumping in the absence of repumping becomes more severe with increasing laser irradiance and reduces the return flux long before the onset of stimulated emission, hence true transition saturation. Spin-exchange collisions can bidirectionally exchange populations between the ground states and within them (transitions between the ($F = 1$, $m = \pm 1$) and ($F = 2$, $m = \pm 2$) ground substates are particularly strong). Repumping has already been experimentally demonstrated to be able to boost the LGS return flux by a factor of 1.6, (Telle 2008 finds a factor 2.4 through Bloch simulations), using two separate laser beams at different frequencies),

[1] "Sodium Laser Guide Star Return Flux Study for The European Southern Observatory", contract study for ESO, E-TRE-KIB-297-0001, 26 August 2008 (available upon request).

and we show in this paper that more than a factor of 3 can be achieved.

To date, the most powerful sodium LGS system is installed at the Starfire Optical Range (SOR) at the Kirtland Air Force Base near Albuquerque, New Mexico, (Denman 2006a), fed by a single-frequency (10-kHz linewidth) cw laser that emits 50 W with circular or linear polarization. Due to its location, the median atmospheric seeing at SOR is significantly worse than at most sites of large astronomical telescopes, causing enlarged LGS spots in the mesosphere, and consequently limiting the irradiance. The upcoming generation of civilian 20-W-class LGS in astronomy, such as for the Adaptive Optics Facility of UT4 of the VLT[2], is therefore expected to venture into unprecedented mesospheric irradiance regimes (much higher laser irradiances have of course been applied to gas cells, albeit at higher gas pressures). Next-generation lasers will emit circularly polarized cw radiation, use repumping, have a linewidth of a few MHz, and are expected to return on the order of 10×10^6 photons/s/m^2 on the ground. Quantifying and optimizing their return flux vs. the laser parameters is one of the principal purposes of this paper.

So far, we have only focused on photon return flux. What is really desired when designing AO systems, though, is a bright guide star, hence high luminosity concentrated in a small spot size. Compared to the uplink laser irradiance in the sodium layer, the above mentioned saturation effects spatially broaden the LGS return fluorescence distribution by emphasizing the low irradiance regions and dimming the peaks. We can show using physical-optics simulations, Holzlöhner (2008), that this effect increases the instantaneous spot sizes on a wavefront sensor by about 0.1″, hence it is not negligible. At large angles between the laser beam and the geomagnetic field, downpumping can be mitigated by repumping.

In this work, we present a Bloch-equation method that models any alkali atom taking into account spontaneous and stimulated emission, Larmor precession due to the geomagnetic field, arbitrary elliptical light polarization, recoil, on the order of 100 coupled velocity groups with velocity-changing collisions and spin exchange, finite atomic dwell time in the beam (atom replacement), arbitrary laser bandwidth, and repumping. We neglect nonlinear Zeeman shifts and hyperfine coherences since we found them to have a small effect on the result. In contrast to the above cited Bloch simulation publications, we directly compute the steady state solution, which is more efficient than time domain solutions (a single run takes about 2 s on a modern PC). The program is written in Mathematica and based on the public-domain Atomic Density Matrix package[3].

In order to validate our results, we have also implemented a Monte Carlo rate-equation simulation called *Exciter* in Matlab, whose results we compare with the Bloch-equation method.

Section 2 describes the Bloch-equation method, Sect. 3 gives details about the simulation parameters, Sect. 4 presents the results, suggesting optimal cw sodium LGS formats, and we conclude in Sect. 5.

[2] Adaptive Optics Facility (AOF) for the VLT, European Southern Observatory (ESO), http://www.eso.org/sci/facilities/develop/ao/sys/.

[3] Rochester, S. M., Atomic Density Matrix package for Mathematica, version 09.08.07 or later, available at http://budker.berkeley.edu/ADM/.

2. Bloch equations

In order to calculate the observed fluorescence from mesospheric sodium atoms, the evolution of the atoms is modeled using the optical Bloch equations for the atomic density matrix. The density matrix describes the statistical state of an ensemble of atoms in the state space of the Na D_2 transition. In order to account for atoms with different Doppler shifts, the density matrix is also considered to be a function of atomic velocity along the laser beam propagation direction. (An additional degree of freedom is included to account for laser line broadening as discussed below.) The calculation is semiclassical in the sense that while the atoms are treated quantum mechanically, the light fields are treated classically (the effect of spontaneous decay must be included phenomenologically since we do not apply field quantization). Because the density matrix describes all populations of, and coherences between, the 24 Zeeman sublevels making up the ground and excited states, the calculation describes, in principle, all saturation and mixing effects for essentially arbitrarily large optical and magnetic fields. (In practice, certain coherences in the system are negligible under our experimental conditions and can be neglected in order to increase the computational efficiency.)

In order to perform numerical calculations, the velocity dependence of the density matrix is discretized to describe an appropriate number $n_{\mathrm{v.g.}}$ of velocity groups, each with a fixed longitudinal velocity. Because coherences between atoms with different velocities can be neglected, the complete density matrix ρ can be thought of as a collection of $n_{\mathrm{v.g.}}$ separate but coupled density matrices, each of dimension 24×24.

The evolution of the density matrix is given by a generalization of the Schrödinger equation:

$$\frac{\mathrm{d}}{\mathrm{d}t}\rho = \frac{1}{i\hbar}[H,\rho] + \Lambda(\rho) + \beta, \tag{1}$$

where $H = H_0 + H_{\mathrm{E}} + H_{\mathrm{B}}$ is the total Hamiltonian, with H_0 the Hamiltonian for the unperturbed energy structure of the atom, $H_{\mathrm{E}} = -\boldsymbol{d} \cdot \boldsymbol{E}$ the Hamiltonian for the interaction of the electric dipole $\boldsymbol{d}$ of the atom with the electric field $\boldsymbol{E}$ of the light, $H_{\mathrm{B}} = -\mu \cdot \boldsymbol{B}$ the Hamiltonian for the interaction of the magnetic moment μ of the atom with the local magnetic field $\boldsymbol{B}$, $\hbar = h/(2\pi)$ where $h = 6.626 \times 10^{-34}$ Js is Planck's constant, and the square brackets denote the commutator. The term Λ in Eq. (1) represents phenomenological terms added to account for relaxation processes not described by the Hamiltonian (Budker 2002). In our case these relaxation processes include spontaneous decay (omitted from the Hamiltonian due to the semiclassical approximation), collisional spin relaxation ("S-damping") proportional to $S^2\rho - S \cdot (\rho S)$ (Happer 1987), and the exit of atoms from the light beam due to motion of the atoms and the beam. In addition, there are terms included in Λ to describe changes in atomic velocity due to collisions and light-induced recoil, as well as an effective relaxation rate that describes dithering of the laser phase in order to simulate a finite bandwidth. These terms are described in more detail below. Each relaxation process described by Λ includes a corresponding repopulation process, so that the trace over the density matrix for all velocity groups is conserved, corresponding to conservation of the total number of atoms. The repopulation process describing the entrance of atoms into the beam is independent of ρ and so is written as a separate term β.

Velocity-changing collisions (vcc) are treated as hard collisions in which the velocity of the colliding atom is rethermalized in a Maxwellian distribution (no speed memory). The internal state of the atom is assumed to be unchanged.

Light-induced recoil is described phenomenologically by causing a fraction $v_r/\Delta v_{v.g.}$ of the excited-state atoms in each velocity group to be transferred upon decay into the next higher velocity group. Here v_r is the recoil velocity and $\Delta v_{v.g.}$ is the width of the particular velocity group. This model relies on the fact that $v_r = 2.9461$ cm/s (equivalent to a Doppler shift of 50.004 kHz) is much smaller than the typical value of $\Delta v_{v.g.}$.

In order to simulate a finite bandwidth laser, a form of phase dithering is used (frequency or amplitude dithering can also be employed). To avoid resorting to a time-domain calculation, the dithering is implemented in the spatial domain: density matrices are written for two "regions" with light fields that are π out of phase with each other, and relaxation terms are included that transfer the atoms between the regions (this doubles the size of the system of equations). The model is that of a laser beam with very fine "speckles" of different phases. The result is an effective laser spectrum of Lorentzian shape with a width proportional to the transfer rate between the regions. This method has been verified by comparison to a time-domain model (implemented for a nuclear-spinless system) in which the light frequency randomly changes with a Lorentzian distribution. Identical results from the two methods are obtained for the case in which the rate that the light frequency changes is faster than the natural decay rate.

Equation (1) supplies a linear system of differential equations for the density matrix elements, known as the optical Bloch equations. Thinking of ρ as a column vector of $n_{v.g} \times 24^2$ density matrix elements, the Bloch equations can be written as $\dot{\rho} = A\rho + b$, where A and b are a matrix and vector, respectively, that are independent of ρ. The vector b corresponds to β and A to the rest of the right-hand side of Eq. (1).

The laser light field has a frequency component tuned near the D_2 $F = 2 \rightarrow F'$ transition group (D_2a), and may have an additional "repump" component tuned near the $F = 1 \rightarrow F'$ transition group (D_2b). Thus the matrix A has components that oscillate at each of these frequencies. Under the rotating wave approximation (Corney 1977), the overall optical frequency is removed from A. However, the beat frequency between the two light-field components remains. This beat frequency can also be removed from the Bloch equations in our case: each frequency component interacts strongly with one transition group and very weakly with the other, so the weak coupling can be neglected for each transition. If, in addition, the small magnetic-field-induced mixing between the two hyperfine ground states is neglected, the beat frequency can be entirely removed from the evolution equations. This makes A time-independent for cw light. To find the steady-state density matrix, we can set $\dot{\rho} = 0$ and solve the linear system $A\rho = -b$. The vectors ρ and b have 322 elements per velocity group (576 if hyperfine states are not neglected), so that the sparse linear equation system has dimension 32 500–65 000 in practice.

To solve the Bloch equations for a particular set of experimental parameters, we first choose an appropriate set of velocity groups. Since the signal is strongly peaked for atoms whose Doppler-shifted resonance frequency is near the light frequency, we can obtain more accurate results for a given number of velocity groups if narrower bins are used for resonant atoms, and wider for off-resonant. We have two methods for doing this.

The first method is to choose two fixed bin sizes, one narrow and one wide, and the number of narrow bins to cluster near each resonance. The wide bins are then used to take up the rest of the Doppler distribution. This method is useful when we don't know beforehand what the spectrum of the signal in velocity space is.

If we have an estimate of the spectrum (obtained using the first method), we can refine it using the second method, which takes advantage of this knowledge. We create a weighting function consisting of three terms: a constant term, which tends to make equal-sized bins, a term proportional to the spectrum, which makes more bins where the signal is large, and a term proportional to the magnitude of the second derivative of the signal, which makes more bins where the signal changes rapidly as a function of velocity. The bin sizes are then found by dividing the integral of the weighting function evenly into the chosen number of bins.

The linear system is solved using the implementation of the iterative BiCGSTAB method (stabilized biconjugate gradient, van der Vorst 1992) built-in to Mathematica. This is a Krylov subspace method in which an initial guess is improved by minimizing the residual over a subspace with dimension much smaller than that of the full system. The rate of convergence of the method is increased by pre-multiplication with a block-diagonal preconditioner (approximate inverse of A), obtained by setting all terms that connect density matrix elements from different velocity groups to zero, and then inverting the block for each velocity group.

The fluorescent photon flux per solid angle emitted in a given direction can be found from the steady-state solution for ρ as the expectation value of a fluorescence operator (Corney 1977).

3. Simulation parameters

3.1. Determination of parameters

Many physical constants and the atomic level diagram of Na have been summarized by Steck[4] and will not be repeated here. Table 1 lists further simulation parameters, and we walk through it to explain some quantities. We work in MKS units, except that we show magnetic field strength in Gauss (1 G = 10^{-4} T) and atomic cross sections in squared centimeters.

The launched laser power P equals the laser device output beam power, diminished by optical losses in the beam train and launch telescope (LT). The value of $I = 46$ W/m^2 is the "50% power in the bucket" irradiance $I_{P/2}$, as explained in the next subsection. We mostly deal with circularly polarized light (the ellipticity angle $\chi = \arctan(\varepsilon) = \pm\pi/4$ denotes respectively LH/RH circular and $\chi = 0$ linear polarization; $\pi/2 - 2\chi$ is the polar angle in the Poincaré sphere, and ε is the ellipticity, hence the major-minor axes ratio of the polarization ellipse). The repumping fraction q is the fraction of the total laser power allocated to the repump beam: the D_2a beam power is $(1-q)P$ and the power in the D_2b beam (tuned Δf_{ab} above the D_2a frequency) is qP.

The geomagnetic-field strength B has a strong impact on the return flux. Its value varies considerably over the world and can be computed for different mesospheric altitudes using the International Geomagnetic Reference Field model[5]. Cerro Paranal in northern Chile, the location of the VLT and the reference site for this work (24.6°S, 70.4°W), has $B \approx 0.23$ G at 92 km altitude, Mauna Kea (Hawaii) has $B \approx 0.35$ G, and the Starfire Optical Range (Albuquerque, New Mexico) has $B \approx 0.48$ G, about twice the field strength at Paranal.

The atmospheric transmission T_a at 589 nm was measured at Paranal to be 0.89 in photometric nights, (Patat 2004). We use a value that is 5% lower to account for higher aerosol levels. The

[4] Steck, D. A., "Sodium D Line Data", version 2.1.1, 30 April 2009, http://steck.us/alkalidata/.

[5] IGRF Release 2005 geomagnetic model online at NOAA website http://www.ngdc.noaa.gov/IAGA/vmod/.

Table 1. Simulation parameters and their standard nominal values.

Variable name	Symbol	Standard value
Laser parameters		
Launched laser power in air	P	20 W
Mesospheric laser irradiance	I	46 W/m^2
Central D_2 vacuum wavelength	λ	589.159 nm
Polarization ellipticity angle	χ	$\pm\pi/4$ (circular)
Laser *FWHM* linewidth	Δf	0
Repumping power fraction	q	0.12
Repumping frequency offset	Δf_{ab}	1.7178 GHz
Atomic, atmospheric, and mesospheric parameters		
Outer turbulence scale	L_0	25 m
Geomagnetic field in mesosphere	B	0.228 G
One-way transmission at λ at zenith	T_{a}	0.84
Average mesospheric temperature	T_{Na}	185 K
Sodium centroid altitude (a.s.l.)*	H_{Na}	92 km
Sodium column density	C_{Na}	4.0×10^{13} m^{-2}
Na beam dwell velocity	v_γ	38 m/s
Beam atom exchange rate	γ_{ex}	1/(6.0 ms)
Na–N_2 v.c.c.† cross section	$\sigma_{\mathrm{Na-N_2}}$	0.71^{-14} cm^2
Na–O_2 v.c.c.† cross section	$\sigma_{\mathrm{Na-O_2}}$	0.70×10^{-14} cm^2
Weighted v.c.c.† rate	γ_{vcc}	$1/(35\,\mu$s)
Na–O_2 spin exchange cross sect. at T_{Na}	$\sigma^{\mathrm{S}}_{\mathrm{Na-O_2}}$	0.50×10^{-14} cm^2
Weighted spin-exchange rate at T_{Na}	γ_S	$1/(490\,\mu$s)
Launch telescope (LT) parameters		
Zenith angle	ζ	30°
LT altitude (a.s.l.)*	H_{tele}	2650 m
LT aperture	D	40 cm
LT beam radius ($1/e^2$)	w	$0.36D = 14.4$ cm
Launched beam rms wavefront error	WFE	100 nm $\approx \lambda/6$
Polar angle of $\boldsymbol{B}$ (laser $\parallel z$)	θ	$\pi/2$
Azimuth of $\boldsymbol{B}$ (laser $\parallel z$)	ϕ	$\pi/2$

Notes. (*) a.s.l. = above sea level. (†) v.c.c. = velocity-changing collision.

mesospheric temperature, as well as partial gas densities, can be derived using the MSISE-90 model[6].

Our values for the sodium layer centroid altitude H_{Na} and column abundance C_{Na} are obtained from studies taking place for over 30 years in São Paulo, (Simonich 1979; Moussaoui 2010), a site whose latitude differs only by one degree from the ESO Paranal Observatory. We believe that the sodium layer parameter statistics on the seasonal and daily variations are valid for Paranal.

Atomic collisions have a significant effect on the sodium states and hence on the LGS return flux. Since mesospheric sodium is rarefied (the total mass of global mesospheric sodium is about 600 kg), Na–Na collisions are negligible compared to Na–N_2 and Na–O_2 collisions. Most of these collisions are binary (collision of two molecules). One important effect of collisions is to change the velocity of the atoms, causing diffusion of optically pumped atoms in velocity space, sometimes called v-damping (Happer 1987). Since the masses of N_2 and O_2 molecules are comparable to that of Na atoms, one can assume that every collision completely randomizes their velocity. The collision rate of a gas of particle mass M_1 with another gas type of particle mass M_2 and number density n_2 is given by (Wright 2004)

$$\gamma_{12} = n_2\sigma_{12}\sqrt{\frac{8k_{\mathrm{B}}T}{\pi}\left(\frac{1}{M_1}+\frac{1}{M_2}\right)}, \tag{2}$$

where $k_{\mathrm{B}} = 1.3807\times10^{-23}$ J/K is Boltzmann's constant and $\sigma_{12} = \pi(r_1+r_2)^2$ is the collisional cross section with the effective particle radii r_1, r_2. Measuring these radii for velocity-changing collisions is difficult; here we just assume the Van-der-Waals radii of $r_{\mathrm{Na}} = 227$ pm, $r_{\mathrm{N_2}} = 250$ pm, and $r_{\mathrm{O_2}} = 245$ pm[7], (Fishbane 2005). The effect of other gas species is negligible. With these numbers, we have, for example, $\sigma_{\mathrm{Na-N_2}} = 0.72\times10^{-14}$ cm^2 and $\gamma_{\mathrm{Na-N_2}} = 3.98\times10^{-10}$ cm^{-3} s$^{-1}\times n_{\mathrm{N_2}} = 1/(62.8\,\mu$s) at the sodium centroid ($n_{\mathrm{N_2}} = 4.0\times10^{13}$ cm^{-3}).

The sodium layer has a median *FWHM* thickness of 11.1 km and its median centroid lies at $H_{\mathrm{Na}} = 92$ km (Moussaoui 2010). The gas pressure decreases exponentially with altitude and the collision rate varies across the layer by about one order of magnitude, as shown by the MSISE-90 atmospheric model. We compute the mean collision rate of Na with N_2 and O_2, based on a table of $n_{\mathrm{N_2}}$, $n_{\mathrm{O_2}}$, and T_{Na} as functions of altitude, weighted by the assumed Gaussian sodium density distribution. The result, which we will use throughout this work, is $\gamma_{\mathrm{vcc}} = \gamma_{\mathrm{Na-N_2,O_2}} = 1/(35\,\mu$s), which is three times higher than Milonni's (1999) assumption of $1/(100\,\mu$s). Since the sodium abundance and layer thickness and altitude are highly variable and its profile often deviates significantly from Gaussian, one cannot expect a high accuracy in this parameter.

The other important relaxation mechanism beside v-damping is spin-exchange relaxation or S-damping (Happer 1987, Sect. 13), in particular for Na–O_2 collisions. Spin relaxation time constants have been measured between rubidium and metastable triplet helium (He*, Dmitriev 2008), as well as between rubidium and H_2, O_2, and N_2, (Nagengast 1998) and sodium and various gases (Ramsey 1964; Kartoshkin 1998). A major difficulty with such measurements is that the overwhelming contribution to S-damping of Na in the mesosphere is due to collisional spin exchange with O_2, however, in gas cells O_2 oxidizes Na quickly and hence this particular cross section is hard to determine experimentally. Theoretical calculations of the cross section involve Born-Oppenheimer molecular potential curves of doublet/quartet surfaces for Na–O_2, analogous to the singlet/triplet curves for Na–Na and have not yet been carried out to our knowledge.

We estimate $\sigma^{\mathrm{S}}_{\mathrm{Na-O_2}} = 0.5\times10^{-14}$ cm^2 at 185 K, based on spin-exchange cross section measurements of Na-He* and O_2-He. However, only 1/2 of this cross section is effective in our case (Dmitriev 2008, Eq. (3)), although the details of the cross-section calculation are under investigation at the moment. Setting $\sigma_{12} = \sigma^{\mathrm{S}}_{\mathrm{Na-O_2}}/2$ in Eq. (2), we obtain $\gamma_S = 1/(680\,\mu$s) at 92 km altitude, which is close to the value $\gamma_S = 1/(640\,\mu$s) that Milonni (1999) finds through fitting to experiment. Note, however, that Milonni's initial guess was $\sigma^{\mathrm{S}}_{\mathrm{Na-O_2}} = 1.0\times10^{-14}$ cm^2, and he does not apply the scaling factor of 1/2. Performing the same sodium density weighted averaging over altitude as above, we obtain $\gamma_S = 1/(490\,\mu$s), which will be used throughout this work. We will discuss the sensitivity of the Na return flux to variations in γ_S and γ_{vcc} in the following section.

The rms lateral velocity $v_\gamma = d\gamma_{\mathrm{ex}}$ describes the sodium atom exchange into and out of the beam, where $d \approx 23$ cm is the median *FWHM* mesospheric speckle diameter (see the following section), and γ_{ex} is the atom exchange rate. We assume that v_γ

[6] MSISE-90 atmospheric model online at NASA website http://ccmc.gsfc.nasa.gov/modelweb/atmos/msise.html.

[7] Atomic beam scattering experiments yield significantly larger cross sections. We will provide details in a forthcoming publication. Online atomic radius list http://www.ccdc.cam.ac.uk/products/csd/radii/.

consists of four components that we sum in quadrature since in general they have uncorrelated directions:

(a) gas diffusion orthogonal to the beam;
(b) mesospheric wind orthogonal to the beam;
(c) beam wander caused by atmospheric turbulence; and
(d) LGS beam slewing due to star tracking.

Each of these contributions can be estimated:

(a) the diffusion coefficient of Na in air (mostly N_2) can be calculated using the Chapman-Enskog formula (Cussler 1997), yielding $D_{\rm Na} = 8.56\times10^4\,{\rm cm^2/s}$, close to Milonni's assumption of $D_{\rm Na} = 1.0\times10^5\,{\rm cm^2/s}$. The effective lateral diffusion velocity across the laser speckle is hence $\sqrt{2/3}D/d = 30\,{\rm m/s}$, where we apply the factor $\sqrt{2/3}$ since we consider only the diffusion orthogonal to the beam. Note that $D_{\rm Na}$ scales like $\sqrt{T_{\rm Na}}/n_{\rm N_2}$. At an altitude of about 104 km the mean free path of sodium exceeds d and the atomic motion within the beam is no longer diffusive (the mean lateral ballistic velocity is then 370 m/s);
(b) we use the horizontal wind model HWM07 which computes zonal and meridional winds at selected mesospheric altitudes and times (Drob 2008). We find a median horizontal wind speed magnitude at Paranal of 20 m/s. Nocturnal fluctuations by a factor of 2 are common;
(c) physical-optics simulations show an rms beam wander in the mesosphere of about 20 cm ($\zeta = 30°$), (Holzlöhner 2008), a value supported by analytical approximations (Andrews 2005, Ch. 12, Eq. (51)). The beam wanders on the time scale of $\tau_{\rm beam} = d/(\text{atmospheric wind speed}) \approx 23\,{\rm cm}/10\,{\rm m/s} = 23\,{\rm ms}$, leading to a beam wander velocity of 8.7 m/s;
(d) the tracking speed of the laser beam in the mesosphere at $\zeta = 30°$ is about $(2\pi/24\,{\rm h})\times L = 7.6\,{\rm m/s}$, where $L = X(H_{\rm Na} - H_{\rm tele}) \approx 103\,{\rm km}$ is the line-of-sight distance to the guide star centroid with the geometrical length extension factor (airmass) $X = \sec(\zeta)$, equaling the secant of the zenith angle ζ.

Summing these four velocities in quadrature yields $v_\gamma = 38\,{\rm m/s}$ and hence $\gamma_{\rm ex} = 1/(6.0\,{\rm ms})$.

3.2. Mesospheric spot size

Given a certain launched laser power, the spot size and shape determine the mesospheric irradiance and thus have a strong impact on the return flux, particularly in the presence of strong optical pumping and for small magnetic field polar angles θ. The instantaneous mesospheric laser spot size has been simulated using physical optics (Holzlöhner 2008). Atmospheric turbulence produces a fast changing (timescale a few milliseconds) speckle pattern on the sky due to diffraction, where the speckles have a *FWHM* diameter of about

$$d = \frac{L\lambda}{2w}, \tag{3}$$

and w is the $1/e^2$ irradiance radius of the laser beam at the projector. The number of speckles and their beam wander are governed by the seeing, and the pattern changes on the time scale of a few milliseconds. Note that the medium/long-term spot size as observed on the ground is significantly larger than d, and it does, in contrast to d, depend directly on the Fried length r_0 (Fried 1966), which is a size scale over which atmospheric phase variations remain below 2π. For a typical $r_0 = 5{-}25\,{\rm cm}$, assuming an outer turbulence scale of $L_0 = 25\,{\rm m}$, there is a single strong central speckle and a couple of much weaker satellite speckles.

Table 2. Mesospheric spot parameters for a 40 cm launch telescope under standard conditions ($P = 20\,{\rm W}$, $\zeta = 30°$)

Seeing (″)	WFE (nm)	$I_{P/2}$ (W/m^2)	$FWHM_{\rm eff}$ (cm)	d (cm)
0.6	70	79.1	30.0	22.5
0.6	100	59.1	34.7	24.3
1.0	70	43.5	40.4	23.8
1.0	100	33.5	46.1	26.1

The LGS return flux depends in general nonlinearly on the mesospheric laser irradiance I, and the return light has to pass the turbulent atmosphere again on the downlink to reach the telescope; thus the irradiance distribution $I(x, y)$, as it would appear on a screen at the mesosphere, cannot be directly observed. To account for the effect of turbulence on the return light and characterize speckle pattern statistically, we collect statistics over many simulated realizations of $I(x, y)$ for different turbulence phase screens. We rewrite the usual optical power integral

$$P\,(T_{\rm a})^X = \int I\,{\rm d}A = \int_0^{I_{\rm max}} I\frac{{\rm d}A}{{\rm d}I}\,{\rm d}I, \tag{4}$$

as an integral over irradiance up to the maximum value $I_{\rm max}$, where A is area orthogonal to the beam and $(T_{\rm a})^X$ is the atmospheric transmission along the line of sight (zenith angle ζ). The quantity ${\rm d}A/{\rm d}I$ can be thought of as a histogram of mesospheric laser irradiance. We define $I_{P/2}$ by

$$\frac{P\,(T_{\rm a})^X}{2} = \int_0^{I_{P/2}} I\frac{{\rm d}A}{{\rm d}I}\,{\rm d}I = \int_{I_{P/2}}^{I_{\rm max}} I\frac{{\rm d}A}{{\rm d}I}\,{\rm d}I, \tag{5}$$

representing an irradiance of "50% power in the bucket", which will be convenient to compute laser efficiencies later (note that usually $I_{\rm max} \gg 2I_{P/2}$). In order to model a realistic LGS beam scenario, we assume a $D = 40\,{\rm cm}$ LT, a launched Gaussian beam of $1/e^2$ (in irradiance) radius $w = 0.72D/2 = 14.4\,{\rm cm}$, two different seeing values of 0.6″ and 1.0″ (site monitor seeing at 500 nm and zenith), and total wavefront errors (WFE) of the launched beam of 70 nm rms ($\approx\lambda/8$) and 100 nm rms ($\approx\lambda/6$). We simulate the actual mesospheric irradiance distribution and $I_{P/2}$ using physical optics, and record the equivalent beam diameter $FWHM_{\rm eff}$ that a single Gaussian spot of the same mesospheric power and same $I_{P/2}$ would have, as well as the speckle size d, as in Holzlöhner (2008). Table 2 summarizes the results. The mean of $I_{P/2}$ on lines 2 and 4 equals 46 W/m^2, which we will use as the reference irradiance in this work. The median values of d in the last column are somewhat above the analytical prediction of Eq. (3) of 21.2 cm, mostly due to the finite WFE.

3.3. Flux quantities

In the following, we define five flux quantities used in this article:

– our simulations compute the return flux per solid angle Ψ as the number of photons per atom and per unit time spontaneously emitted in the direction of the launch telescope, as observed in the mesosphere, with units of photons/s/sr/atom;
– in order to compare different laser formats at similar irradiances, one can divide Ψ by the laser irradiance (in W/m^2) in the mesosphere to derive the specific atomic return flux $\psi = \Psi/I$ in units of photons/s/sr/atom/(W/m^2), where area is measured in the mesosphere orthogonal to the beam. Most of our results are expressed in this quantity;

– to compute the expected return flux on a receiver at a distance L from the fluorescing atoms, we begin by integrating Ψ over the receiver area A orthogonal to the beam, subtending the solid angle A/L^2 to obtain the quantity $F_{\rm m}$;
– the photon flux on the detector Φ (unit photons/s/m^2) at the sodium column abundance $C_{\rm Na}$ (unit atoms/m^2) equals

$$\Phi = \frac{C_{\rm Na} X (T_{\rm a})^X F_{\rm m}}{L^2}. \tag{6}$$

The airmass X appears in the numerator because the sodium column along the laser beam scales like the airmass (note that the distance L grows by the same factor). We do not account for laser power depletion with increasing propagation distance in the sodium layer because only about $\sigma \times C_{\rm Na} \approx 10^{-15}\,{\rm m}^2 \times 4 \times 10^{13}\ {\rm m}^{-2} \approx 4\%$ of the laser photons interact with any sodium atoms under the standard conditions of Table 1, the other 96% travel unused into space;
– in order to compare LGS systems at similar powers but different laser formats, beam spot sizes in the mesosphere, atmospheric transmission, and zenith angle, we can divide $F_{\rm m}$ by the laser power in the mesosphere $P(T_{\rm a})^X$ to arrive at the figure of merit quantity $s_{\rm ce}$ in units of photons/s/W/(atoms/m^2)

$$s_{\rm ce} = \frac{F_{\rm m}}{P\,(T_{\rm a})^X} = \frac{\Phi L^2}{P\,(T_{\rm a})^{2X} C_{\rm Na} X}, \tag{7}$$

where $(T_{\rm a})^X$ appears quadratically in the denominator of the last term, accounting for both up- and downlink. The quantity $s_{\rm ce}$ is hence the photon flux on the ground, corrected for its dependence on sodium centroid height and abundance, airmass, atmospheric transmission, and, to first order, launched laser power (since $s_{\rm ce}$ depends strongly on θ, we will only compute it for $\theta = \pi/2$ in this work). We will compare LGS laser beam efficiencies based on $s_{\rm ce}$. Note that in our definition $s_{\rm ce}$ is not a slope efficiency (which would be proportional to $\partial F_{\rm m}/\partial P$); see also d'Orgeville (2000).

4. Results

We compute ψ using the method and parameters described above. Using the standard conditions of Table 1, we obtain $\psi = 258$ ph/s/sr/atom/(W/m^2). In the following, we first provide some numerical validations including scans of $\psi(I)$, followed by optimization studies of ψ when varying light polarization ellipticity angle χ, repumping frequency offset $\Delta f_{\rm ab}$, repumping power fraction q, and laser linewidth Δf. Unless otherwise noted, the standard conditions of Table 1 apply.

4.1. Some numerical validations

Figure 1 shows a comparison between the analytical Na absorption cross sections given by Eqs. (10), (11) in (Milonni 1998) at $T = 185$ K (dashed red line, the sum of two Gaussians) and the simulated effective cross section

$$\sigma = \frac{h\nu W}{I}, \tag{8}$$

where $\nu = c/\lambda$ is the center frequency of the D$_2$a line, with c the vacuum speed of light, and W is the actual rate of spontaneous emissions at irradiance I (solid blue curve; the inverse of W is known as the cycle time). The abscissa shows detuning of the (main) laser line from the D$_2$a line center. The agreement is excellent. We add the caveat that this agreement is necessary, but not sufficient to prove the validity of our algorithm since effects like Larmor precession, recoil, and stimulated emission have no effect at low irradiance as the Na atom is in thermal equilibrium.

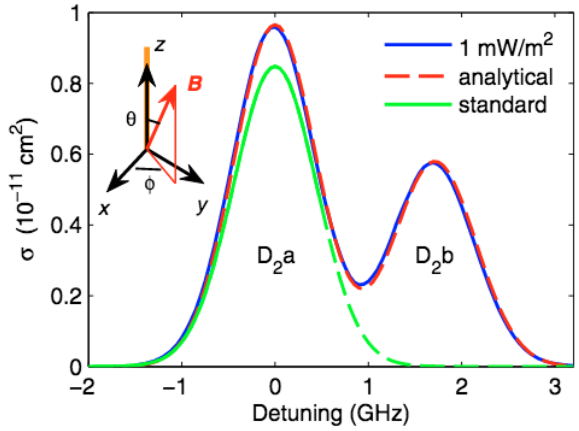

Fig. 1. Absorption cross section σ vs. detuning from the Na D$_2$a line center. Solid blue: simulation at $I = 0.001$ W/m^2 ($q = 0$), dashed red: analytical cross section, green: simulation of effective cross section at standard conditions ($I = 46$ W/m^2, $q = 0.12$). Inset: reference coordinate system.

The steady-state spontaneous emission rate W cannot exceed $1/(2\tau) = 1/(32.5\,{\rm ns})$, and hence σ tends to zero in the limit of infinite I. At $I = 46$ W/m^2 and $q = 0.12$ (green curve), the reduction in σ is still modest, however. We render the tail of the green curve towards the D$_2$b line center at 1.772 GHz dashed, where our computational simplification of letting the "D$_2$a laser line" only excite the D$_2$a Na transitions, and analogously allowing the "repumping" line to only excite the D$_2$b transitions, whenever repumping is used ($q > 0$), breaks down. Once the detuning approaches the D$_2$b line center, this assumption obviously becomes invalid. By contrast, the blue curve was computed for $q = 0$ and without using this simplification, and it is valid for any frequency offset.

The inset in Fig. 1 sketches the definition of the spherical angles θ and ϕ of the $\boldsymbol{B}$-vector in a coordinate system where the laser beam is projected along the z-axis. The major axis of the polarization ellipse for non-circular polarization is parallel to x.

Figure 2 shows the simulated atomic velocity distribution under standard conditions, except that Larmor precession and repumping are absent ($\theta = q = \gamma_{\rm ex} = 0$). The abscissa shows relative atomic velocity away from the receiver in frequency units (proportionality constant $1/\lambda$). Recoil is usually associated with a frequency redshift, whereas we display the shift towards the blue. We choose this convention since a recoiled atom becomes resonant with a blueshifted laser line.

The blue curve represents the occupation histogram from the Monte Carlo rate-equation simulation Exciter after sampling 10^6 different atomic velocities within the Doppler distribution (8.5×10^6 Monte Carlo steps simulating 26.6 s of physical time). The green curve is a Gaussian with the theoretical Doppler *FWHM* width of 1.033 GHz at $T_{\rm Na} = 185$ K, representing the thermal equilibrium, and the magenta curve shows the occupation probability obtained from the Bloch-equation simulation. Finally, the cyan curve depicts for comparison the simulated return flux spectrum in the atomic frame, which in the present case of single-frequency excitation is close to the sodium natural line shape of a Lorentzian with a *FWHM* of $1/(2\pi\tau) = 9.8$ MHz (plotted at arbitrary vertical scale).

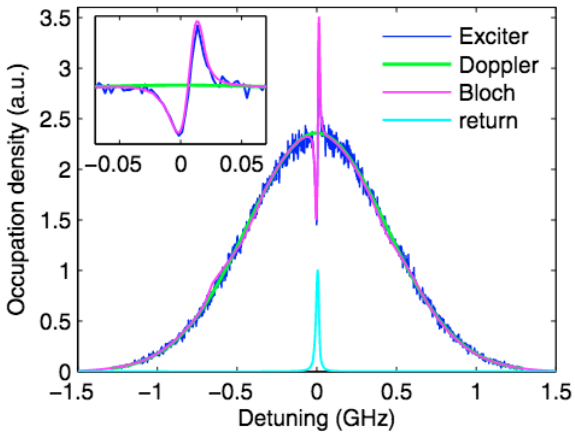

Fig. 2. Atomic velocity distribution under standard conditions (but $\theta = q = 0$), blue: Exciter, green: Doppler profile, magenta: Bloch equations, cyan: return light spectrum in the atomic frame. Inset: zoom on line center.

The effect of spectral hole burning is quite striking; in fact the occupation at the D_2a line center is depleted to 64% below the green Doppler curve. The atomic population, as seen from the telescope, is blue-shifted within about one velocity group. We observe that spectral hole burning due to recoil is in general exacerbated if repumping is applied, presumably due to the larger number of excitations per time. On the other hand, hole burning is mitigated when the laser bandwidth is extended at constant laser power because of the reduced spectral irradiance.

In Exciter, we increment the Doppler shift of the simulated atom by 50 kHz each time a spontaneous emission occurs, which is correct on average. The agreement between Exciter and the Bloch equations is excellent, giving us confidence that the Gaussian velocity distribution and recoil are properly modeled.

At $I = 46\,\mathrm{W/m^2}$, Exciter simulates a spontaneous emission every $9.5\,\mu$s on average. Of all emissions, 10.2% are stimulated and 89.8% are spontaneous, and 70.6% of all atomic transitions occur along $(F = 2, m = 2) \leftrightarrow (F' = 3, m' = 3)$, indicating efficient optical pumping. We conclude that besides suffering from recoil, we are also starting to saturate this transition. At $I = 100\,\mathrm{W/m^2}$, 17.9%, and at $I = 1000\,\mathrm{W/m^2}$, 55.2% of all emissions are stimulated, respectively. On average, one spontaneous emission occurs every $5.1\,\mu$s and $1.1\,\mu$s for these respective irradiances.

Figure 3 shows three semilogarithmic plots of $\psi(I)$ for the standard conditions of Table 1 unless noted otherwise, but neglecting exchange with thermal Na atoms outside the beam ($\gamma_{\mathrm{ex}} = 0$, which is not implemented in Exciter, but causes only a small difference). We hence simulate a single-frequency laser ($\Delta f \to 0$) tuned to the peak of the D_2a line. Solid curves show ψ obtained from the Bloch method, and the symbols indicate the results of Exciter. The green and red curves and symbols represent the case of laser beam parallel to the geomagnetic field ($\theta = 0$) with and without repumping, hence in the absence of Larmor precession, respectively. The blue and magenta curves and symbols are the same as green and red, respectively, but with the laser orthogonal to the field ($\theta = \pi/2$). Figure 3a shows the case of circular, and Fig. 3b that of linear polarization, the blue and magenta curves for $\theta = \phi = \pi/2$ (note the difference in vertical scale).

We can make a number of interesting observations. First, the impact of the magnetic field is profound and reduces the return

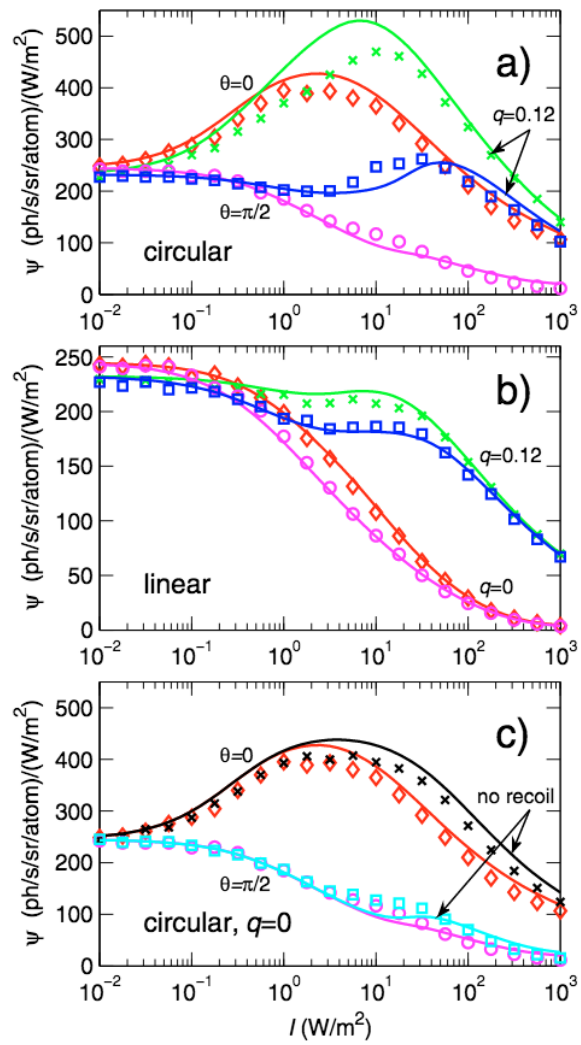

Fig. 3. Specific return flux $\psi(I)$. Lines: Bloch equations, symbols: Monte Carlo rate-equation simulation *Exciter*. **a)** Green, crosses: $\theta = 0$, $q = 0.12$; red, diamonds: $\theta = 0$, $q = 0$; blue, squares: $\theta = \pi/2$, $q = 0.12$ (standard conditions); magenta, circles: $\theta = \pi/2$, $q = 0$ (all with circular polarization and $\gamma_{\mathrm{ex}} = 0$). **b)** Same as **a)**, but for linear polarization. **c)** Red and magenta lines, diamonds and circles: as in **a)**; black, crosses and cyan, squares: same, respectively, without recoil.

flux strongly, at some irradiances by several times. At very low irradiance ($I = 10^{-2}\,\mathrm{W/m^2}$), the atom is in thermal equilibrium and all magnetic sublevels are nearly equally populated. Optical pumping sets in with increasing I if using circular polarization, but Larmor precession is powerful enough to completely suppress it at $\theta = \pi/2$, as evident from the monotonically falling magenta curve. Conversely, in the absence of Larmor precession ψ strongly peaks near $I = 2\,\mathrm{W/m^2}$. The Larmor precession period equals

$$\tau_{\mathrm{L}} = \frac{h}{\mu_{\mathrm{B}}|g_F|B}, \tag{9}$$

where μ_{B} is the Bohr magneton and g_F is the Landé factor that depends on F ($g_F = \mp 1/2$ for the $F = 1$, 2 sodium ground states, respectively). On Paranal, $\tau_{\mathrm{L}} \approx 6.3\,\mu$s (159 kHz) and at SOR we find $\tau_{\mathrm{L}} \approx 3.0\,\mu$s (333 kHz, $B = 0.48$ G).

The green and blue curves portray the "healing" effect of repumping ($q = 0.12$, i.e., 12% of the laser power shifted to D_2b). In the absence of Larmor precession, the peak is more pronounced and shifted to higher I (green). The highest impact occurs when the influence of the magnetic field is highest ($\theta = \pi/2$), where ψ remains shallow until 80 W/m^2 and then decays gently. This finding refutes the often heard notion in the LGS community that "one should always stay away from the circular polarization saturation irradiation ($I_{\mathrm{sat,circular}} = 62.6$ W/m^2 to avoid saturation".

At very low I, repumping is ineffective and even slightly decreases the return flux due to the smaller cross section of the D_2b transition. At high I, repumping can readily compensate the degrading effect of Larmor precession; in its absence, ψ decays to zero. For linear polarization, this decay even occurs for $\theta = 0$ (red curve) due to depopulation of the upper ground state. Conversely, circular polarization "rescues" many atoms into the $(S, F = 2, m = \pm 2) \leftrightarrow (P, F' = 3, m' = \pm 3)$ transition, in which they are safe from downpumping.

Note that besides increasing the return flux by several times, a flatter function $\psi(I)$ also leads to smaller observed spot sizes since spatial power-broadening is reduced, a very welcome bonus.

The agreement between the Bloch calculation and Exciter is very good in almost all cases, given the completely different nature of the two methods, with the Bloch code usually yielding the higher values of ψ. Exciter finds the magnetic resonance bump at smaller I due to difficulties with the proper simulation of two concurrent effects on similar, but not equal, time scales in our Monte Carlo rate-equation. Also the agreement between the green curve and the green crosses is somewhat poor around $I = 0.2$–20 W/m^2, presumably due to the simplified way in which Exciter models S-damping and/or the absence of coherences.

Figure 3c shows the impact of recoil. The red and magenta curves and symbols are as in subplot a), while black and cyan crosses and squares denote the same, respectively, but neglecting recoil. The magnetic resonance is better visible in the cyan than in the magenta curve. Recoil leads to a significant reduction in ψ above 2 W/m^2.

Figure 4a shows ψ as a function of the Larmor frequency $1/\tau_L$ (blue curve) at $I = 1$ W/m^2. The red dashed curve, overlapping the solid blue curve, is a fit function composed of the sum of two Lorentzians of different widths, centered at the origin, plus a constant term. The (half-)width of the narrower Lorentzian (517 Hz $= 0.25\gamma_S$) is determined by the S-damping resonance, and that of the broader Lorentzian (17.9 kHz $= 0.63\gamma_{\mathrm{vcc}}$) by the velocity-changing collision rate, and the widths change proportionally when varying γ_S or γ_{vcc}. However, both resonances are somewhat power-broadened. The geomagnetic field is strong enough at $I = 1$ W/m^2 to place us on the lowest terrace of the blue curve, as indicated by the vertical lines. The blue diamonds show the result of Exciter for comparison, also exhibiting the terraces.

Figure 4b shows the corresponding relative populations of the five S, $F = 2$ upper ground state sublevels ($m = -2 \ldots 2$), where the solid lines indicate Bloch equations and dotted lines Exciter. For $1/\tau_L > 300$ Hz, the sublevel populations collapse to the same value due to Larmor-induced sublevel mixing. Conversely, for $1/\tau_L < 300$ Hz, the populations diverge and the laser pumps the $m = 2$ sublevel (blue) most strongly. When increasing the irradiance to $I = 46$ W/m^2 (not shown in the plot), the curves in b) would look similar, but the divergence point shifts upward to ≈1 kHz. Furthermore, when plotting the

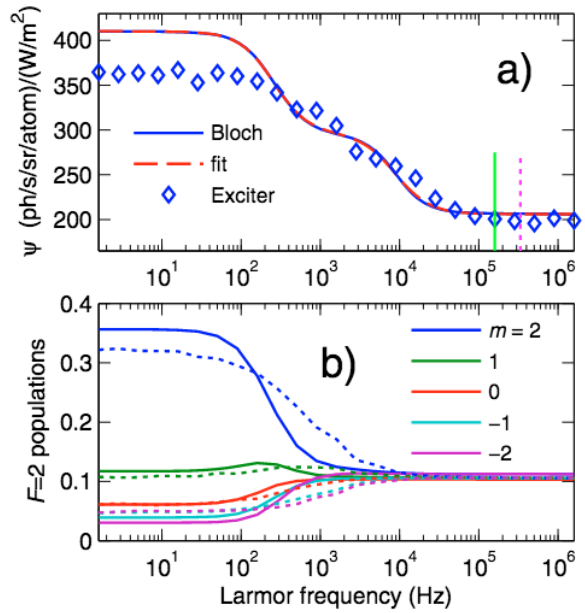

Fig. 4. Magnetic field impact. **a)** Blue curve: ψ as a function of the Larmor frequency $1/\tau_L$ at $I = 1$ W/m^2. Red dashed curve (almost obscuring the blue curve): fit (sum of two Lorentzians). Blue diamonds: Exciter. Solid green (dashed magenta) lines: $1/\tau_L$ at Paranal (SOR). **b)** $F = 2$ fractional sublevel populations, solid (dashed) curves: Bloch (Exciter) simulation.

Table 3. Sensitivity of ψ to a 1% perturbation in some simulation parameters under standard conditions.

Name of perturbed variable	Symbol	ψ change (%)
Mesospheric laser irradiance	I	0.025
Geomagnetic field in mesosphere	B	−0.33
Average mesospheric temperature	T_{Na}	−0.48
Beam atom exchange rate	γ_{ex}	0.0025
Weighted v.c.c.* rate	γ_{vcc}	0.15
Weighted spin-exchange rate at T_{Na}	γ_S	0.013
Recoil frequency (50 kHz)		−0.24

Notes. (*) v.c.c. = velocity-changing collision.

sublevel populations at $I = 46$ W/m^2 as a function of θ, one observes that the magnetic field at Paranal is just strong enough to collapse the populations for $\theta \to \pi/2$. In other words, by scanning θ across the sky with a narrow-band 20-W-class laser, we can observe sodium excitation all the way from full optical pumping to no pumping at all, leading to a severe return flux penalty, as shown in the following figures.

Table 3 lists the sensitivity of ψ w.r.t. a 1% perturbation in some simulation parameter p, more precisely $\psi(1.01p)/\psi(p) - 1$, where all other parameters are those of Table 1. A value of b% in the last table column thus indicates that $\psi(p) \propto p^b$ in some range around the chosen value of p. We have selected only those parameters that we will not study in greater detail in the following subsections (except I). In addition, we have excluded those parameters around which ψ is stationary ($\psi'(p) = 0$), and also those parameters whose influence on the observed return flux is obviously linear, such as C_{Na}.

From Table 3, we notice that with the parameters of Table 1 the sensitivity to changes in I is small. A comparison with Fig. 3b (dashed blue curve) shows that $\psi(I)$ is very shallow near $I = 46$ W/m^2 (the slope is actually weakly positive due to the

magnetic resonance bump), meaning that $\Psi(I) = \psi I \propto I$, i.e. the absolute photon return grows linearly with the irradiance. The dependence of ψ on B, however, is strong: Switching from $B = 0.23$ (Paranal) to $B = 0.48$ (SOR, factor 2.11) decreases ψ by a factor of 0.76! The influence of temperature is significant as well since the width of the velocity distribution scales like $T_{\rm Na}^{1/2}$, and conversely its normalization (the number of Na atoms per velocity group) scales like $T_{\rm Na}^{-1/2}$. However, increasing $T_{\rm Na}$ from 185 K to 200 K, which may be a typical seasonal variation, reduces ψ by only 3.7%, and hence common temperature variations do not directly influence ψ much (we note that temperature influences the sodium abundance). Both $\gamma_{\rm ex}$ and γ_S have a small influence on ψ, mainly due to the presence of repumping, as Milonni (1999) has also noted (for $q = 0$, the sensitivities are 0.049% and 0.56%, respectively).

We can draw two lessons here: There is little point in spending much effort trying to improve the spin-exchange cross section $\sigma^{\rm S}_{\rm Na-O_2}$ estimate, and, secondly, repumping makes ψ more robust towards some parameter variations, leading to higher stability in numerical simulations and possibly also in experiment. The variation of ψ with $\gamma_{\rm vcc}$ is much larger than with γ_S, and at first sight surprisingly, the derivative is positive. We explain the positivity by the fact that collisions mitigate spectral hole burning due to recoil (neglecting recoil, the derivative is −0.089%). Finally, we have constants and λ (more precisely $h/(m_{\rm Na}\lambda^2) = 50.0$ kHz, with the atomic mass of Na $m_{\rm Na} = 3.819 \times 10^{-26}$ kg), in order to demonstrate the importance of proper recoil modeling at $I > 1$ W/m^2.

In the following subsection, we will show that the laser parameters of Table 1 are close to optimal, given the other conditions of the table. We focus on the case $\theta = \pi/2$ where the laser beam is directed orthogonal to the geomagnetic field (the worst case, for which LGS lasers must be designed to achieve a given return flux requirement).

4.2. Optimization of ψ

4.2.1. Polarization ellipticity angle

Figure 5 plots ψ as a function of the laser polarization ellipticity angle χ. To our knowledge, this is the first publication to discuss $\psi(\chi)$ for LGS. The axis limits ±1 of the quantity $4\chi/\pi$ denote circular polarization (the poles of the Poincaré sphere; in our convention, $4\chi/\pi = +1$ pumps towards increasing m), and $\chi = 0$ indicates linear polarization. The curves pertain to different combinations of θ and ϕ, the polar angle and azimuth of the $\boldsymbol{B}$ vector in a system where the laser points along z (note that for $\theta = 0$, the azimuth ϕ becomes meaningless at any light polarization. Conversely, when using any laser that is not purely circular polarized, ϕ *does* influence the return flux, which is often forgotten. When using purely linear polarized light, $\theta = \pi/2$, $\phi = 0$ is equivalent to setting $B = 0$ within our convention, while $\phi = \pi/2$ induces the strongest effect from Larmor precession.)

The cosine-like shape of $\psi(\chi)$ presents an initially gradual decrease of the return flux from $4\chi/pi = \pm 1$, meaning that high polarization purity is not required when pumping the sodium with circularly polarized light. If one is willing to accept a decrease in ψ of 5% along the solid red curve, it is enough to maintain $4|\chi|/\pi \geq 0.8$, i.e., down to an ellipticity angle of $|\chi| = 36°$. The polarization extinction ratio (PER) in dB is given by PER $= -20 \log_{10} \tan|\chi|$ and assumes the values of 0 and ∞ for circular and linear polarization, respectively. The condition

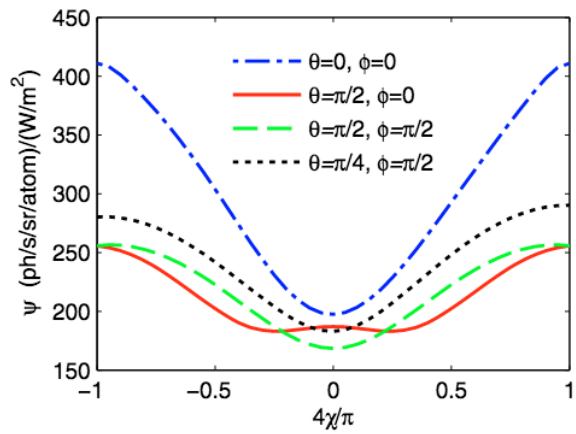

Fig. 5. ψ as a function of laser polarization ellipticity angle χ, where $4\chi/\pi = \pm 1$ (0) marks circular (linear) states. The curves indicate different combinations of the magnetic field polar angle θ and azimuth angle ϕ. Note that $\psi(\chi)$ is highest for circular polarization in all cases.

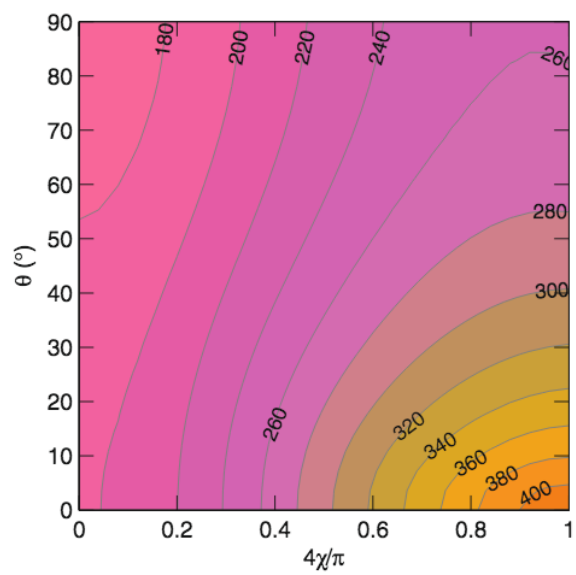

Fig. 6. Contour plot of $\psi(\chi, \theta)$ in ph/s/sr/(W/m^2) for magnetic azimuth $\phi = \pi/2$ at $I = 46$ W/m^2.

of $4|\chi|/\pi \geq 0.8$ implies PER ≤ 6.4 dB. This insensitivity is good news for the design of launch telescope optics.

Figure 6 shows a contour plot of $\psi(\chi, \theta)$ in ph/s/sr/(W/m^2) for $\phi = \pi/2$ (worst case) under standard conditions. Current LGS systems, even SOR's FASOR laser, operate at lower "$P/2$" irradiances than $I_{P/2} = 46$ W/m^2 and/or at linear polarization, for which $\psi(\theta)$ varies slowly. At higher I and circular polarization, $\psi(\theta)$ is a steeper function (along the right vertical plot edge). For $\theta > 45°$, also $\psi(\chi)$ varies slowly near $4|\chi|/\pi = 1$, indicating again that the circular polarization purity does not have to be very high.

4.2.2. Repumping frequency offset

Figure 7 shows ψ as a function of $\Delta f_{\rm ab}$, the repumping frequency offset between D_2a and D_2b, relative to 1.7178 GHz, for two single-frequency laser lines and $q = 0.12$ at $I = 1$ W/m^2 (dashed green), $I = 10$ W/m^2 (dash-dotted blue), and $I = 46$ W/m^2 (solid

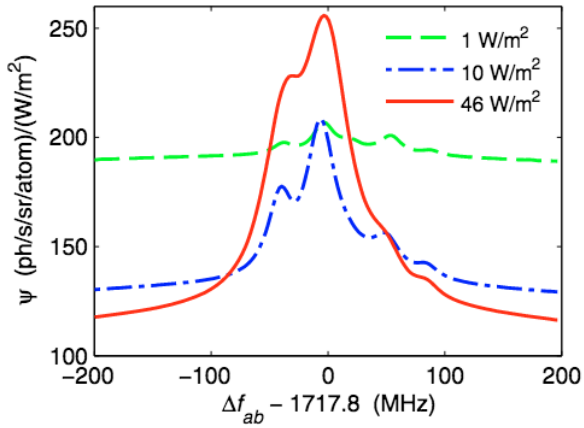

Fig. 7. ψ as a function of repumping laser line frequency offset $\Delta f_{\rm ab}$ at $I = 1\,\mathrm{W/m^2}$ (dashed green), $I = 10\,\mathrm{W/m^2}$ (dash-dotted blue), and $I = 46\,\mathrm{W/m^2}$ (solid red).

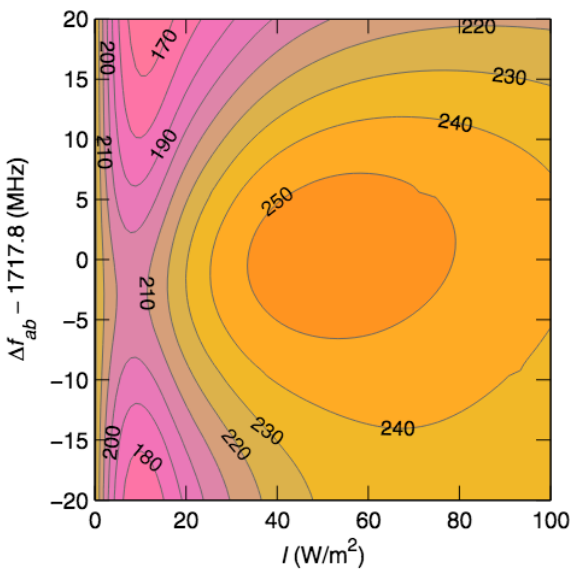

Fig. 8. Contour plot of $\psi(I, \Delta f_{\rm ab})$ in ph/s/sr/(W/m^2).

red). The repumping from $(S, F = 1) \rightarrow (S, F = 2)$ requires excitation to the states $(P, F' = 1)$ or $(P, F' = 2)$ since no transitions $(S, F = 1) \rightarrow (P, F' = 3)$ are allowed.

Figure 8 is a contour plot of $\psi(I, \Delta f_{\rm ab})$, zooming into the region of $\Delta f_{\rm ab} = 1717.8 \pm 20\,\mathrm{MHz}$. In order to harness the full improvement of repumping, one needs to adjust $\Delta f_{\rm ab}$ with a precision of a few MHz, particularly when at intermediate irradiance ($I \approx 10\,\mathrm{W/m^2}$). At larger irradiance, power-broadening washes out the peak (a laser beam has irradiances $0 \le I \le I_{\rm max}$ in the mesosphere, located along a horizontal line in the diagram). The tolerance in $\Delta f_{\rm ab}$ is so narrow because repumping is most efficient if a given Na atom that has been downpumped to the $F = 1$ lower ground state can be reexcited before its velocity changes due to a collision, for which the frequency offset of the repumping laser line should lie between the $(S, F = 1) \rightarrow (P, F' = 1, 2)$ transition frequencies minus the $(S, F = 2) \rightarrow (P, F' = 3)$ transition frequency that the main laser line is tuned to, i.e., close to 1717.8 MHz.

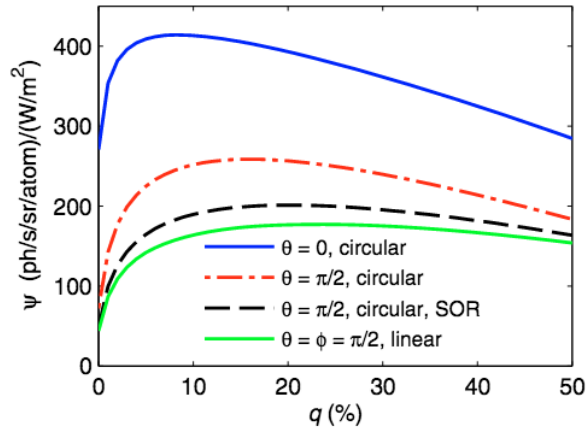

Fig. 9. ψ as a function of repumping power fraction q for different field angles θ. Dash-dotted red curve: standard conditions, solid blue: $\theta = 0$ (circular polarization, no Larmor precession), dashed black: standard conditions, but $B = 0.48\,\mathrm{G}$ (SOR), solid green: linear polarization ($\theta = \phi = \pi/2$).

4.2.3. Repumping power fraction

Figure 9 portrays the calculated $\psi(q)$ for different magnetic field polar angles θ and field strengths B. The dash-dotted red curve is for standard conditions of Table 1, the solid blue curve for $\theta = 0$ (i.e., circular polarization and no Larmor precession), the dashed black curve is for standard conditions, but with the magnetic field at SOR, and the solid green curve is for linear polarization (worst case $\theta = \phi = \pi/2$).

All curves peak around $q = 8$–25%, and the maximum occurs at larger q the stronger the magnetic field effect is. Note that $\psi(q)$ peaks at $q > 0$ even in the absence of Larmor precession (blue curve) since there is always a chance that atoms decay to the lower ground state. Moreover, $\psi(q)$ is very steep at $q = 0$, rewarding even the weakest repumping, which is the reason why broadline lasers ($\approx$2 GHz) often do reasonably well, despite their poor spectral overlap with $\sigma(\nu)$ (see Fig. 1). Our simulations, however, indicate that a narrow-band laser with 12% repumping beats the return flux of a single-line 2 GHz-linewidth laser by a factor of 3.7 under standard conditions (see next subsection).

For circular polarization we find $\psi(q = 0.12)/\psi(q = 0) \approx 3.5$ at $I = 46\,\mathrm{W/m^2}$, underlining again that *repumping is extremely beneficial, in particular in future LGS systems involving high irradiance.*

Figure 10 shows six semilogarithmic contour plots of $\psi(I, q)$ (note the different color scales of the plots). The blue crosses indicate the point ($I = 46\,\mathrm{W/m^2}$, $q = 0.12$). Plot a) exhibits ψ for linear polarization at Paranal for $\theta = \phi = \pi/2$, which only varies weakly with B. At the blue cross, $\psi = 169$ ph/s/sr/(W/m^2) (for $q = 0$, it is only 44 ph/s/sr/(W/m^2)!). Plot b) shows the same for circular polarization ($\psi = 258$ ph/s/sr/(W/m^2) at the blue cross, which is close to the maximum of ψ in Plot b) and lies within the magnetic resonance "island"). Plot d) shows the ratio $\psi(I, q, 4\chi/\pi = 1)/\psi(I, q, \chi = 0)$. Circular polarization at $\theta = \pi/2$ only improves the return flux at Paranal if $I \ge 10\,\mathrm{W/m^2}$ (at smaller θ, there is a much higher gain, as indicated by Fig. 3). The improvement at the blue cross is 1.52 (with the B-field at SOR, it would be only 1.2, but can reach 2.0 for smaller θ). We have limited the plot range in the lower right corner of d) to 1.8 for better rendering; in reality, the value exceeds 3. Plot e) shows the same as b), but for the B-field of SOR. As noted in Fig. 9, the optimal q lies closer to 19% under this condition.

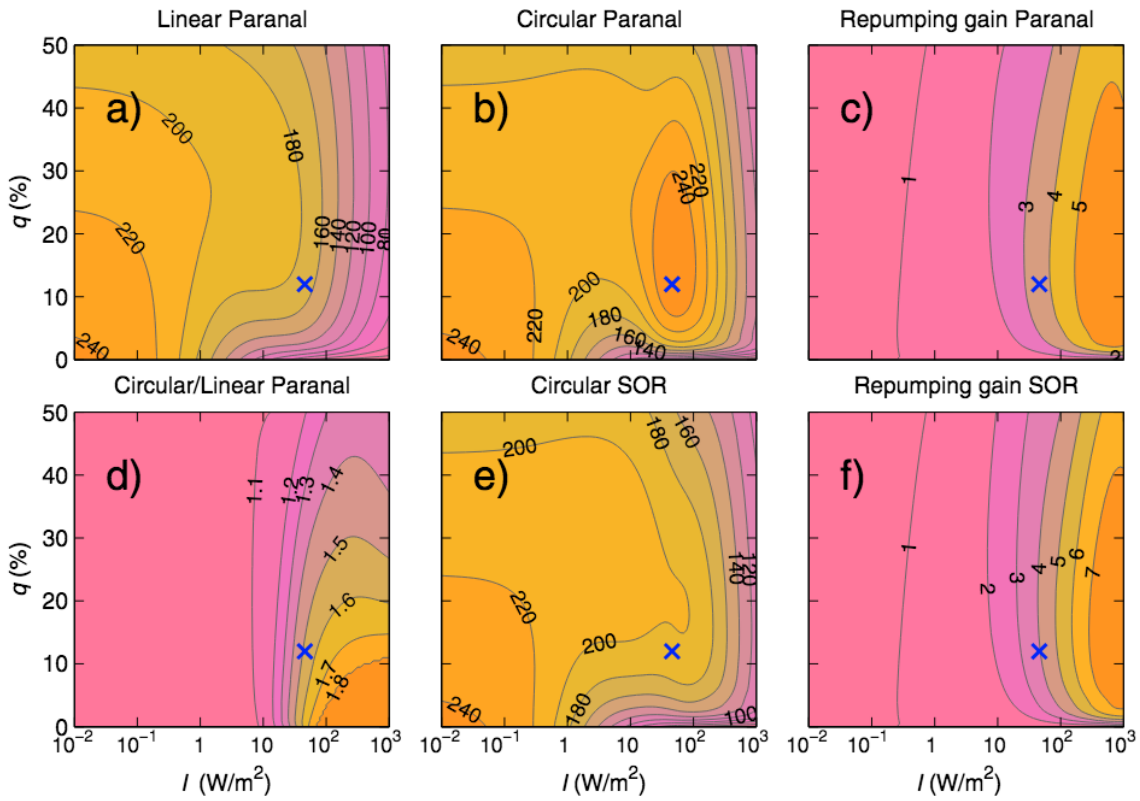

Fig. 10. **a), b)** Contour plots of $\psi(I, q)$ in ph/s/sr/(W/m^2) at Paranal for linear and circular polarization, respectively; **d)** the ratio ψ(circular)/ψ(linear) at Paranal; **e)** same as **b)**, but for SOR geomagnetic field; **c), f)** repumping gain $\psi(I, q)/\psi(I, q = 0)$ at Paranal and SOR, respectively, circular polarization. Blue crosses: $I = 46$ W/m^2, $q = 0.12$.

Note that even at $q = 0.5$ (equal power in D_2a and D_2b), $\psi \approx 164$ ph/s/sr/(W/m^2) is not much below its optimum of 201. Plot c) depicts the gain in ψ when turning on repumping at standard conditions, i.e., $\psi(I, q)/\psi(I, q = 0)$. Plot d) shows the same for SOR. At the blue crosses $\psi(q = 0.12)/\psi(q = 0)$ equals 3.6 and 4, respectively.

4.2.4. Laser linewidth

So far, we have only simulated single-frequency line lasers. We now turn to lasers with Lorentzian lines of finite bandwidth. Figure 11 shows two contour plots of $\psi(I, \Delta f)$ for conditions at Paranal and SOR. The specific return is highest near the dashed blue lines, hence near 10 W/m^2/MHz (100 W/m^2 per natural linewidth of sodium of 9.8 MHz) for Paranal and near 17 W/m^2/MHz for SOR. For irradiances below about 20 W/m^2, this linearity does not hold anymore and $\Delta f \to 0$ will yield higher return flux. Conversely, at $I \gg 1000$ W/m^2, Δf is no longer negligible compared to the Doppler width, and hence the absorption cross section falls off in the wings of the laser spectrum (our simulations for $q > 0$ lose accuracy for wide bandwidths, see the discussion of Fig. 1). In the upper left region of the plot, ψ decreases due to low pumping that is too weak to overcome the population equalization from Larmor precession, and in the lower right we suffer from saturation. We note that d'Orgeville (2000) has conducted a related study (d'Orgeville's Fig. 8 differs from ours in that its horizontal axis shows laser power and not irradiance, and it is rendered in double logarithmic scale).

Based on the dashed blue lines in Fig. 11, the optimum *FWHM* laser bandwidth can be estimated by $\Delta f_{\rm opt} \approx (0.025\, I_{P/2} - 0.5)/B$, where $\Delta f_{\rm opt}$ is in MHz, $I_{P/2}$ in W/m^2 with $20 \le I_{P/2} \le 1000$ W/m^2, and B in Gauss. We expect this optimal spectral power density to only depend on the relaxation time scales. This scaling relationship is good news for future LGS systems, since it means that we can achieve high return flux even at very large irradiances, as long as we keep increasing the laser bandwidth. Lasers with microsecond pulses designed for mesospheric spot tracking or lidar with duty cycles of 1:20–1:100, and hence high peak powers, may take advantage of this possibility.

4.3. Optimization of laser beams

In this subsection, we extend the analysis to entire laser beams by carrying out weighted integrals of $\psi(I)$ for (Gaussian) spot profiles, from which we compute $s_{\rm ce}$ (Eq. (7)).

To begin, we conduct a comparison with the beam return flux computed by Milonni (1999). We apply our Bloch code to Milonni's Na conditions of $B = 0.5$ G, $q = 0$, $\theta = 30°$, $\zeta = 0°$, $P = 1$ W, $2 \times I_{P/2} = 0.52$ W/m^2, circular polarization ($4|\chi|/\pi = 1$), no recoil, $\gamma_{\rm ex} = 0$, $T_{\rm Na} = 200$ K, $T_{\rm a} = 1.0$, $\gamma_{\rm vcc} = 0$, $\gamma_S = 1/(100\,\mu$s$)$) and obtain $s_{\rm ce} = 335$ ph/s/W/(atoms/m^2), in contrast to Milonni's value $s_{\rm ce} = 240$ ph/s/W/(atoms/m^2) from Eq. (30) of that paper. If we switch to $\gamma_S = 1/(640\,\mu$s$)$ (long-dashed curve in Milonni's Fig. 6a), we obtain $s_{\rm ce} = 359$ ph/s/W/(atoms/m^2). For the combination $\gamma_{\rm vcc} = 1/(100\,\mu$s$)$, $\gamma_S = 1/(640\,\mu$s$)$, we find $s_{\rm ce} = 303$ ph/s/W/(atoms/m^2), underlining the importance of properly modeling diffusion in atom velocity space. We suspect

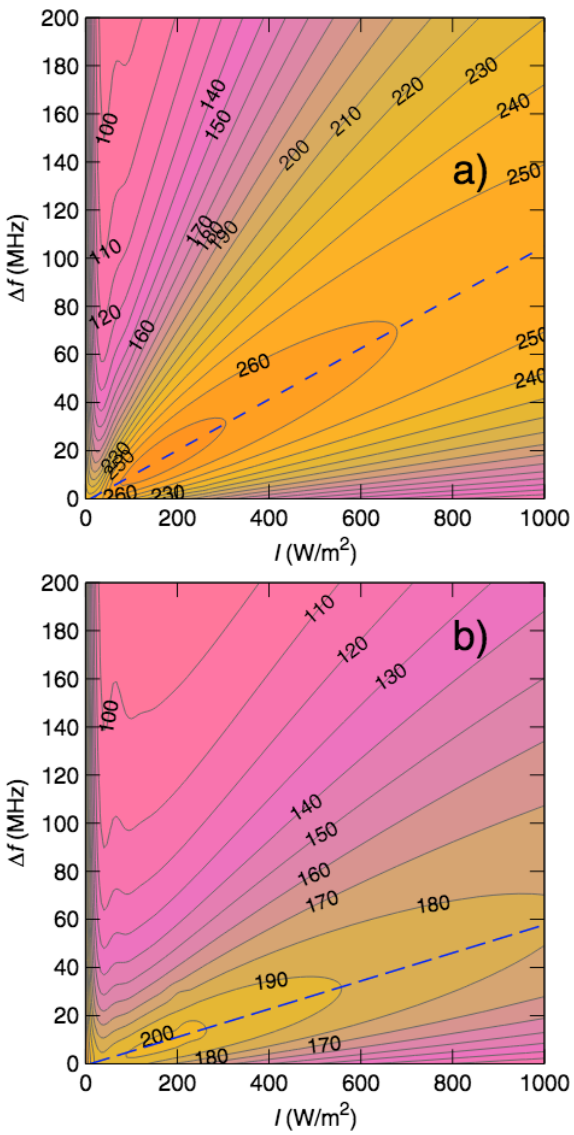

Fig. 11. **a)** Contour plot of $\psi(I, \Delta f)$ in ph/s/sr/(W/m^2) for standard conditions (Paranal). **b)** Same, but for the geomagnetic field of SOR. The optimal spectral irradiance is near 10 and 17 W/m^2/MHz, respectively (dashed blue lines).

that the discrepancy in the flux results is partly due to Milonni's (1999) greatly simplified S-damping formula Eq. (18), which tends to overestimate spin relaxation.

Figure 12 shows a plot of the beam efficiency s_{ce} for different geomagnetic field strengths at $\zeta = 30°$ (solid red: Paranal, dashed green: Mauna Kea, dash-dotted blue: SOR). The dotted magenta and solid black lines show s_{ce} for Paranal at $P = 217$ W ($I_{P/2} = 500$ W/m^2) and $P = 435$ W ($I_{P/2} = 1000$ W/m^2), respectively. At these irradiances, the $s_{ce}(\Delta f)$ peaks at 38 MHz and 75 MHz, respectively, without losing much of its magnitude compared to $P = 20$ W. We expect that pulsed lasers with pulse durations much longer than 16 ns can enjoy this high specific return. Note that the numerical similarity of $s_{ce} \leq 245$ ph/s/W/(atoms/m^2) with typical values of ψ in ph/s/sr/(W/m^2) is a mere coincidence, and the two quantities should not be confused.

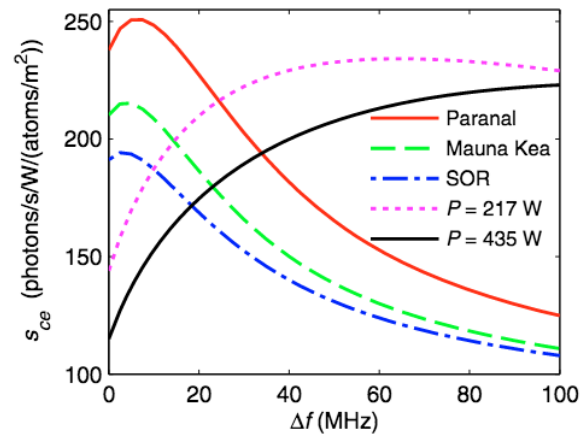

Fig. 12. Beam efficiency s_{ce} as a function of *FWHM* laser bandwidth (Δf) for a $P = 20$ W laser at Paranal (solid red curve, standard conditions), Mauna Kea (dashed green), and SOR (dash-dotted blue), depending on the local geomagnetic-field strengths ($P = 20$ W, $\theta = \pi/2$). Dotted magenta (solid black): Laser at Paranal for $P = 217$ W ($P = 435$ W).

We add the caveat that the laser bandwidth is defined here as the *short-term bandwidth*, as opposed to the apparent bandwidth obtained from a long-term spectral measurement of a laser whose central frequency is slowly drifting, or being chirped.

5. Conclusions

In this article, we describe a modeling method to accurately determine the photon return flux from sodium LGS using Bloch (density matrix) equations. Numerical simulations are crucial, since it is not easy to achieve the desired optimization experimentally.

We summarize some optimization conclusions for cw sodium LGS lasers as follows:

1. The next generation of 20 W-class (launched) cw laser sodium LGS will achieve unprecedented mesospheric irradiances near $I_{P/2} = 50$ W/m^2 ($I_{P/2}$ = "50% power in the bucket irradiance") in good seeing conditions, using launch telescopes with 30–50 cm clear aperture diameter.
2. Atomic Larmor precession due to the geomagnetic field B can completely suppress optical pumping and thus strongly reduce the LGS return flux, depending on the orientation between the laser beam and the field lines. LGS systems must be dimensioned for the beam pointing that yields the lowest return, i.e., laser beam orthogonal to $\boldsymbol{B}$.
3. In the future LGS irradiance regime, circular polarization will significantly elevate the return flux, with a rather relaxed polarization extinction ratio of PER ≤ 6.4 dB. The polarization chirality (sense) does not matter.
4. Repumping (excitation of the D_2b line) with 10–20% of the laser power in combination with circular polarization increases the return flux further by a factor of 3–4. Repumping can moreover alleviate spatial power-broadening and hence reduce the observed LGS spot size.
5. The optimum *FWHM* laser bandwidth can be estimated for a Lorentzian line shape by $\Delta f_{\rm opt} \approx (0.025\, I_{P/2} - 0.5)/B$, where $\Delta f_{\rm opt}$ is in MHz, $I_{P/2}$ in W/m^2 ($20 \leq I_{P/2} \leq 1000$ W/m^2), and B in Gauss. As a rule of thumb, the laser bandwidth in MHz should approximately equal the launched laser power in Watt divided by six, assuming a diffraction-limited spot

size in good seeing. Employing lasers with a single line of 2−3 GHz bandwidth is usually several times less efficient.

6. A laser with the above properties can achieve a specific return of s_{ce} = 200−250 photons/s/W/(atoms/m^2) at a low-B location such as in northern Chile and s_{ce} = 150−200 photons/s/W/(atoms/m^2) at a high-B location such as New Mexico (all values for laser beam orthogonal to $\boldsymbol{B}$).

We expect a numerical accuracy of ±10% in our results of ψ for a given parameter set. However, many physical simulation parameters such as spin relaxation and velocity-changing collision cross sections should be measured more accurately (at mesospheric temperatures). The corresponding relaxation rates depend on gas pressure and temperature and thus vary exponentially with altitude. Moreover, the assumption that velocity-changing collisions are memoryless (complete velocity reset after scattering) is very strong and may need to be refined. In practice, the absolute return flux uncertainty is completely dominated by sodium abundance and altitude distribution fluctuations (for instance, raising the altitude by 6 km causes a reduction of γ_{vcc} from $1/(35\,\mu s)$ to $1/(100\,\mu s)$, diminishing s_{ce} from 245 to 205 photons/s/W/(atoms/m^2)). The accurate return flux computation of a realistic LGS system requires averaging along the beam, accounting for altitude-dependent temperature, gas concentrations, and laser irradiance. Despite these caveats, we do not expect the qualitative conclusions of this work to change when the parameter values are made more precise.

We also compare the Bloch simulation results with our Monte Carlo rate-equation simulation *Exciter* and find good agreement. However, such Monte Carlo rate-equation methods are based on numerous assumptions, and they always need to be validated against more rigorous methods such as a Bloch equation calculation. Moreover, our Bloch code is orders of magnitude faster than Exciter, with the runtime advantage quickly growing with the desired level of accuracy. Our Bloch simulation code can simulate any alkali and is publicly available on our websites[8].

In this work, we treat only steady-state sodium excitation with cw lasers. Pulsed lasers, with pulse durations close to or shorter than the sodium lifetime of 16 ns, will be dealt with in a forthcoming publication. However, we surmise that our present results are valid for microsecond laser pulses that are useful for mesospheric spot tracking and lidar. On-sky experiments to validate our results with a mobile 20 W-class laser unit are being prepared at ESO at the moment, and are expected to yield results in 2010.

In conclusion, our simulations indicate that we have only begun to realize the full capability of sodium LGS, to be harvested by upcoming generations of laser-assisted AO, both with cw and pulsed lasers. The future of sodium LGS, so to speak, looks very bright.

Acknowledgements. We thank Craig Denman, Paul Hillman, Peter Hoffmann, Victor Kartoshkin, Ed Kibblewhite, Peter Milonni, Steve Morgan, Brian Patton, John Telle, Yan Feng, Nourredine Moussaoui, and Luke Taylor for their valuable input. We would like to give special credit to Will Happer, the father of sodium LGS, for his generous advice. This work was supported in part by the NGA NURI program.

References

Andrews, L. C., & Phillips, R. L. 2005, Laser Beam Propagation through Random Media (SPIE Press, Bellingham), 2nd edn.
Bellanger, V., Courcelle, A., & Petit, A. 2004, Comp. Phys. Comm., 162, 143
Bradley, L. C. 1992, J. Opt. Soc. Am. B, 9, 1931
Budker, D., Gawlik, W., Kimball, D. F., et al. 2002, Rev. Mod. Phys., 74, 1153
McClelland, J. J., & Kelley, M. H. 1985, Phys. Rev. A, 31, 3704
Corney, A. 1977, Atomic and Laser Spectroscopy (Oxford: Oxford University Press)
Cussler, E. L. 1997, Diffusion. Mass Transfer in Fluid Systems 2nd edn. (Cambridge: Cambridge University Press)
Denman, C. A., Drummond, J. D., & Eickhoff, M. L. 2006, Proc. SPIE, 6272, 62721L
Dmitriev, S. P., Dovator, N. A., & Kartoshkin, V. A. 2008, Tech. Phys. Lett., 34, 693
Drob, D. P., et al. 2008, J. Geophys. Res., 113, A12304
Drummond, J., Denman, C., & Hillman, P. 2007, ed. S. Ryan, 1215, E67
Fishbane, P. M., Gasiorowicz, S. G., & Thornton, S. T. 2005, Physics for Scientists and Engineers (Prentice-Hall, Upper Saddle River)
Fried, D. L. 1966, J. Opt. Soc. Am., 56, 1372
Guillet de Chatellus, H., Pique, J.-P., & Moldovan, I. C. 2008, J. Opt. Soc. Am. A, 25, 400
Happer, W. 1972, Rev. Mod. Phys., 44, 169
Happer, W., & Van Wijngaarden, W. A. 1987, Hyperfine Interactions, 38, 435
Happer, W., MacDonald, G. J., Max, C. E., & Dyson, F. J. 1994, J. Opt. Soc. Am. A, 11, 263
Hillman, P. D., Drummond, J. D., Denman, C. A., & Fugate, R. Q. 2008, Proc. of the SPIE, 7015, 70150L
Holzlöhner, R., Bonaccini Calia, D., & Hackenberg, W. 2008, Adaptive Optics Systems, Proc. of the SPIE, 7015, 701521
Holzlöhner, R., Bonaccini Calia, D., & Hackenberg, W. 2009, ESO Technical Report VLT-TRE-ESO-11875-3940, Issue 1 (available upon request)
Hubin, N. 2009, Proc. of AO for ELT conference, abstract 118
Kartoshkin, V. A. 1998, Opt. and Spectr., 85, 177
Milonni, P. W., & Thode, L. E. 1992, Appl. Opt., 31, 785
Milonni, P. W., Fugate, R. Q., & Telle, J. M. 1998, J. Opt. Soc. Am. A, 15, 217
Milonni, P. W., Fearn, H., Telle, J. M., & Fugate, R. Q. 1999, J. Opt. Soc. Am. A, 16, 2555
Morris, J. R. 1994, J. Opt. Soc. Am. A, 11, 832
Moussaoui, N., Holzlöhner, R., Hackenberg, W., & Bonaccini Calia, D. 2009, A&A, 501, 793
Moussaoui, N., Clemesha, B., et al. 2010, A&A, in press
Nagengast, W., Nass, A., Grosshauser, C., Rith, K., & Schmidt, F. 1998, J. Appl. Phys., 83, 5626
d'Orgeville, C., Rigaut, F., & Ellerbroek, B. L. 2000, Proc. SPIE, 4007, 131
Patat, F. 2004, The Messenger, ESO Publication, 118, 11
Pique, J.-P., Moldovan, I. C., & Fesquet, V. 2006, J. Opt. Soc. Am. A, 23, 2817
Pfrommer, T., Hickson, P., & She, C.-Y. 2009, Geophys. Res. Lett., 36, L15831
Ramsey, A. T., & Anderson, L. W. 1964, Il Nuovo Cimento, 32, 1151
Ressler, N. W., Sands, R. H., & Stark, T. E. 1969, Phys. Rev., 184, 102
Simonich, D. M., Clemesha, B. R., & Kirchhoff, V. W. 1979, J. Geophys. Res., 84, 1543
Taylor, L., Friedenauer, A., et al. 2009, Proc. CLEO 2009, postdeadline PDA.7
Telle, J., Drummond, J., et al. 2006, Proc. of the SPIE, 6215, 62150K-1
Telle, J., Drummond, J., Hillman, P., & Denman, C. 2008, Proc. of the SPIE, 6878, 68780G-1
Thomas, S. J., Gavel, D., Adkins, S., & Kibrick, B. 2008, Proc. SPIE, 70155L
Ungar, P. J., Weiss, D. S., Riis, E., & Chu, S. 1989, J. Opt. Soc. Am. B, 6, 2058
van der Vorst, H. A. 1992, SIAM J. Sci. Comp., 13, 631
Wright, M. R. 2004, An Introduction to Chemical Kinetics (Wiley)

[8] ESO Laser Systems Department website http://www.eso.org/sci/facilities/develop/lgsf/; LGS extension to Atomic Density Matrix package, http://budker.berkeley.edu/ADM/ (requires Mathematica v. 6 or higher).

2.9 Modular Reconfigurable Dye Laser of Undergrad Lab - AJP

A nice text detailing how to set up a simple dye laser

AMERICAN JOURNAL of PHYSICS

A modular, reconfigurable-cavity, pulsed dye laser for the advanced undergraduate laboratory

John E. Sohl and Stephen G. Payton

Citation: American Journal of Physics **65**, 640 (1997); doi: 10.1119/1.18621
View online: http://dx.doi.org/10.1119/1.18621
View Table of Contents: http://scitation.aip.org/content/aapt/journal/ajp/65/7?ver=pdfcov
Published by the American Association of Physics Teachers

Articles you may be interested in

Modular spectrographs for undergraduate laboratories
Am. J. Phys. **79**, 716 (2011); 10.1119/1.3581500

Continuous pulse duration variation in quenched cavity dye laser
Rev. Sci. Instrum. **74**, 945 (2003); 10.1063/1.1532837

A visible extended cavity diode laser for the undergraduate laboratory
Am. J. Phys. **68**, 925 (2000); 10.1119/1.1285896

An introduction to laser modeling studies with a nitrogen-pumped dye laser
Am. J. Phys. **67**, 803 (1999); 10.1119/1.19128

A high-school dye laser project
Phys. Teach. **35**, 72 (1997); 10.1119/1.2344597

This article is copyrighted as indicated in the article. Reuse of AAPT content is subject to the terms at: http://scitation.aip.org/termsconditions. Downloaded to IP: 158.104.100.45 On: Thu, 03 Sep 2015 22:53:57

A modular, reconfigurable-cavity, pulsed dye laser for the advanced undergraduate laboratory

John E. Sohl and Stephen G. Payton
Department of Physics, Weber State University, Ogden, Utah 84408-2508

(Received 10 October 1996; accepted 31 January 1997)

The modular pulsed dye laser described is extremely easy to build, is quickly reconfigurable into different laser cavity designs, and is usable for experiments in spectroscopy. The laser can be constructed with readily available optical components and simple hand tools. This laser is designed primarily to illustrate the performance differences of three different dye laser cavity designs: the Littrow grating (Hänsch) cavity, and both the single- and double-grating grazing incidence cavities. In the double-grating configuration, the laser's linewidth of 0.007 nm is on the order of ten times narrower than many commercially available pulsed dye lasers. Thus the laser also has excellent performance as a spectroscopic tool. Construction, typical performance, and application details are described. © *1997 American Association of Physics Teachers.*

I. INTRODUCTION

Dye lasers, a common tool in spectroscopy laboratories, are occasionally found in advanced undergraduate laboratories. Hilborn[1] and Alfrey[2] have described the construction of homemade dye lasers that are appropriate for undergraduate use. Several manufacturers[3] produce compact, rugged, and relatively inexpensive dye lasers suitable for undergraduate spectroscopy experiments. In this paper, we describe a ''modular'' dye laser that was designed both for experiments in laser physics and in spectroscopy. Use of standard, commercially available, optical components makes this dye laser extremely simple to build. The modular approach allows a student to rearrange the optical components into different laser cavity configurations in a matter of minutes. The performance of the laser is better than many commercially available models, thus this dye laser is also suitable for undergraduate research.

Many advanced laboratory experiments can be accomplished with dye lasers. Brandenberger[4] has edited conference proceedings describing the usefulness of laser/optics laboratory experiences for undergraduates. Included in the proceedings are several applications of dye lasers such as Raman scattering, laser-induced fluorescence, and the excitation of sodium Rydberg states. Arnett *et al.*[5] describe a simple optogalvanic spectroscopy experiment. Several laser manufacturers also provide lists of potential experiments.[6–8]

Like the lasers described by Hilborn and Alfrey, this laser can be used for spectroscopy. As a spectroscopic tool, this laser is appropriate for all the experiments referenced above. When assembled in the double-grating grazing incidence dye laser configuration, the laser delivers research quality performance, producing a linewidth that is on the order of ten times narrower than many commercially available dye lasers.

Our primary goal was to design a laser specifically for experiments on laser cavity physics. Because of its modular design, students can quickly configure this laser's cavity into at least three different designs. Students then compare and

 © 1997 American Association of Physics Teachers

This article is copyrighted as indicated in the article. Reuse of AAPT content is subject to the terms at: http://scitation.aip.org/termsconditions. Downloaded to IP: 158.104.100.45 On: Thu, 03 Sep 2015 22:53:57

contrast the efficiency, linewidth, and stability of the different laser cavities. Thus the system provides not only an excellent introduction to dye laser design, but to the function of lasers in general.

This laser system, as described, can initially be built in less than two days using mostly ''off-the-shelf'' components. The few remaining components are easily constructed with a drill press and hand tools. The total cost of this dye laser was less than $3,300, nearly an order of magnitude less expensive than most commercial dye lasers. Once the initial construction and preassemblies are complete, upper-division students can assemble and operate this laser in less than an hour. Finally, with the addition of a few more components, further laser design experiments (e.g., other cavity designs, amplification stages, etc.) can be made available to the students.

II. BACKGROUND

An impressive array of literature is available on all aspects of lasers. A delightful and thorough introduction to the physics, designs, techniques and applications of lasers has been presented by Schewe.[9] Another good starting point is O'Shea and Peckham's[10] Resource Letter on lasers. The basic theory of dye lasers in particular has been described in detail by Hilborn.[1] (Ganiel[11] has performed a more rigorous treatment for the advanced reader.)

Dye lasers require the standard components of any laser—an energy source (the pump laser), an active medium (the laser dye), and a resonant cavity. In addition, dye lasers require a method of isolating a narrow range of wavelengths out of the broad range over which the laser dye will allow lasing to occur. Almost universally, a diffraction grating is introduced into the laser cavity to disperse unwanted wavelengths, allowing amplification of only the desired wavelength. There are only two orientations in which diffraction gratings are commonly used: the Littrow mount and the grazing incidence configuration. Of the three cavities described in this paper, the first uses the Littrow mount, the second uses the grazing incidence configuration, and the third uses a combination of the two.

Several performance characteristics of each laser cavity configuration can be readily measured by students. We chose to measure the linewidth, the background noise (amplified spontaneous emission), the mode structure and the efficiency.

A. The pump laser

The pump laser acts as the power supply for a dye laser. There are two requirements for the pump laser: the wavelength must be shorter than the desired output wavelength of the dye laser and the pump laser must be powerful enough to drive the dye laser above the lasing threshold.

While nearly any medium- to high-power laser can be used as the pump, in practice pulsed lasers are easier to use than continuous lasers. For pulsed light sources the average power remains low while the peak power can be quite high, easily into the megawatt range. Good candidates for the pump laser are the nitrogen-ion, Nd:YAG, and the excimer. The pump laser can be either purchased or constructed.

The excimer laser is probably not a good choice for a student laboratory because of the toxic and expensive gases needed. (A single mistake can rapidly pump $500 worth of xenon into the atmosphere.) Building your own is not really a viable option; although conceptually straightforward, excimer lasers are constructed from materials inert to the excited halogen gases used to create the excimer molecules. The advantages of the excimer laser are: high repetition rates, high peak power output, easy operation, and simple maintenance.

Nd:YAG lasers are not easy to build and require some expertise to maintain. However, Yang[12] *et al.* have described a homemade Nd:YAG laser. One advantage of this type of pump laser is that the output can be either green (532 nm) or ultraviolet (either 355 or 266 nm). The green output has the advantage of being easier to see. This makes it easier to control stray beams for the sake of eye safety. Also, many red laser dyes are more efficient when pumped with 532-nm light than with UV light. Finally, the beam quality of Nd:YAG lasers is generally very high.

Probably the best choice for the undergraduate laboratory is the nitrogen ion laser. The N_2^+ laser is easy to operate and maintain, and comparatively inexpensive to purchase or build. Hilborn,[13] and others,[14–16] have described many designs for homemade N_2^+ lasers. (It should be noted that careful attention must be paid to the choice and design of the capacitors, if you choose to build your own nitrogen laser.[17,18]) An inexpensive, albeit relatively low power, nitrogen laser is manufactured by Laser Science, Inc. (model VSL-337). More powerful nitrogen lasers are available from Photon Technology International, Inc. and Laser Photonics, Inc., among others. A more comprehensive listing of suppliers may be found in the annual buyers guide edition (August) of *Physics Today*.

If you are comfortable with possibly having to repair a laser, there are several dealers of used lasers.[19,20] The nitrogen laser is an especially good choice for this because of its simplicity and ease of maintenance. Both of our nitrogen pump lasers are secondhand and have worked well for us with only minor repairs.

On the other hand, a pump laser is not completely necessary. Dye lasers can also be pumped with high intensity flash lamps such as the one described by Alfrey.[2] While we have not tried it, it is conceivable that one could construct a flash lamp powered dye laser using the modular cavity approach described in this paper.

B. General cavity configurations

1. The Littrow mount laser

Hänsch[21] describes a narrow-linewidth dye laser that is typical of the Littrow mount cavity. This basic design, still used by many dye lasers on the market today, is shown in Fig. 1. In general, the diffraction grating's light dispersion can be described as

$$m\lambda = a(\sin\,\theta + \sin\,\phi), \tag{1}$$

where m is the diffraction order (typically between 1 and 4), λ is the peak wavelength, a is the spacing of the lines on the grating, ϕ is the angle from the normal to the incoming light, and θ is the angle from the normal to the outgoing light. In the Littrow configuration the angles of the incoming and outgoing light are the same for one of the diffraction orders. Thus, with $\theta = \phi$ we obtain

$$m\lambda = 2a\,\sin\,\theta. \tag{2}$$

Effectively, the diffraction grating behaves as a wavelength-specific end mirror. A particular wavelength can be selected by rotating the diffraction grating about an axis perpendicu-

This article is copyrighted as indicated in the article. Reuse of AAPT content is subject to the terms at: http://scitation.aip.org/termsconditions. Downloaded to IP: 158.104.100.45 On: Thu, 03 Sep 2015 22:53:57

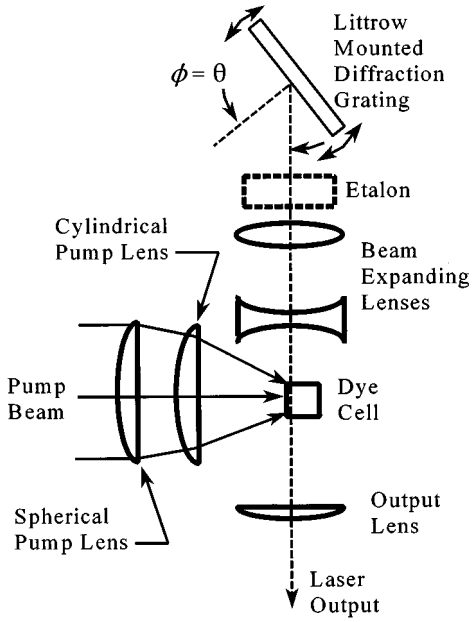

Fig. 1. The standard Hänsch design dye laser cavity configuration. Rotating the grating changes the laser's output wavelength. Hänsch used the etalon to narrow the laser's linewidth. Common practice is to not use the etalon. The first surface reflection from the Plano side of the output lens functions as the cavity's end mirror. The output lens also collimates the beam.

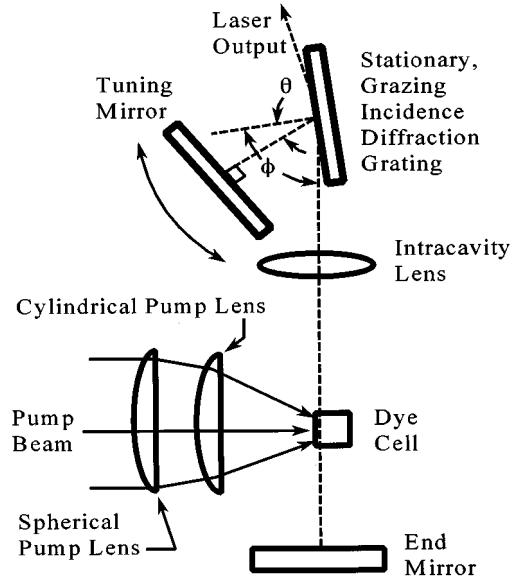

Fig. 2. The single-grating, grazing incidence dye laser cavity configuration. Rotating the tuning mirror around the diffraction grating changes the laser's output wavelength. The intracavity lens collimates the beam. The zeroth diffraction order is the output beam.

lar to the cavity and parallel to the rulings of the grating.

The linewidth, $\Delta\lambda$, of a diffraction grating is inversely proportional to the product of the number of grating lines illuminated, N, and the diffraction order,[22] specifically,

$$\Delta\lambda = \frac{\lambda}{mN}. \tag{3}$$

The total number of lines that are illuminated is N, which is equal to the number of lines per unit length of the diffraction grating (a fixed quantity) times the length of that portion of the grating that is illuminated. The purpose of the beam-expanding telescope inside a Littrow mount dye laser is to increase the number of lines on the diffraction grating that are illuminated, thereby increasing the spectral resolution of the laser. The beam-expanding telescope also serves to collimate the diverging beam leaving the dye cell. This ensures that the rays striking the diffraction grating are approximately parallel.

In most commercial Littrow mount dye lasers a system of two or more prisms is used in place of the beam-expanding telescope. This allows the beam to be expanded in only one dimension thus making the laser more efficient. A prismatic beam expander is substantially more expensive and more challenging to design. For our purposes we decided that the additional output power was not worth the added expense.

2. The single-grating grazing incidence dye laser

The grazing incidence dye laser uses a stationary diffraction grating oriented with the grating normal at approximately 89° to the axis of the laser cavity as shown in Fig. 2. The grazing incidence dye laser does not need an intracavity beam expander because the orientation of the diffraction grating intrinsically maximizes N.

For the grazing incidence dye laser (hereafter referred to as the GIDL) the wavelength is determined from Eq. (1) as

$$m\lambda = a(\sin\,\theta + \sin\,\phi) \approx a(\sin\,\theta + 1), \tag{4}$$

where we have approximated $\sin\,\phi = \sin(89°) \approx 1$. Tuning of the laser wavelength is accomplished by rotating a flat mirror about an axis oriented perpendicular to both the laser cavity and the grating normal and through the center of the surface of the grating.

3. The double-grating grazing incidence dye laser

The third laser design that students can easily configure our system into is a common modification of the GIDL where the flat tuning mirror is replaced with a second diffraction grating in a Littrow mount configuration. A closeup of this change is shown in Fig. 3. With two diffraction gratings in the cavity, the dispersion of unwanted wavelengths is substantial.

C. Laser linewidth

Iles[23] has performed a theoretical analysis of the linewidth for each of the three cavities described in this paper. We can characterize the diffraction gratings by defining α (for the Littrow mounted grating) and β (for the grazing incidence grating) as the ratios of the diffraction order to the grating line spacing. That is, $\alpha = m_1/a_1$ and $\beta = m_2/a_2$, where m is the diffraction order and a is the grating line spacing. Correcting for several typesetting errors in Iles paper, we can estimate the linewidths for the various cavities. For the Hänsch laser, Iles predicts the linewidth to be

$$\Delta\lambda_H = \frac{4\sqrt{2}\lambda}{\pi L\alpha}, \tag{5}$$

where L is the length of the illuminated portion of the diffraction grating. For the single diffraction grating GIDL. Iles predicts the linewidth to be half that of a comparable Hänsch laser, i.e.,

This article is copyrighted as indicated in the article. Reuse of AAPT content is subject to the terms at: http://scitation.aip.org/termsconditions. Downloaded to IP: 158.104.100.45 On: Thu, 03 Sep 2015 22:53:57

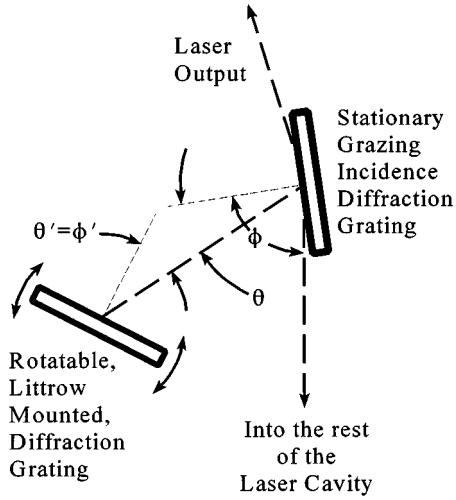

Fig. 3. The double-grating, grazing incidence dye laser (GIDL) cavity configuration. This figure shows only the differences from the single-grating GIDL. Rotation of the Littrow mounted grating controls the wavelength.

$$\Delta\lambda_s = \frac{2\sqrt{2}\lambda}{\pi L\beta}. \tag{6}$$

The double diffraction grating configuration is more complicated. Iles' result is

$$\Delta\lambda_D = \frac{2\sqrt{2}\lambda}{\pi L\left(\alpha + \frac{\beta}{2}\left[\frac{2\alpha\lambda - \alpha^2\lambda^2}{1-\left(\frac{\beta\lambda}{2}\right)^2}\right]^{1/2}\right)}. \tag{7}$$

This is roughly equivalent to the single diffraction grating situation but with an additional term in the denominator that accounts for the extra dispersion generated by the second diffraction grating. Using the parameters for our laser cavities, the predicted linewidths are 0.034, 0.0068, and 0.0023 nm, respectively.

Obtaining an accurate measurement of the linewidth is most easily done with an etalon.[24,25] The result of the measurement, $\Delta\lambda_{\text{meas}}$, is actually the convolution of the laser's actual linewidth, $\Delta\lambda_{\text{laser}}$, and the instrument's resolution, $\Delta\lambda_{\text{etalon}}$. This is approximately described as

$$\Delta\lambda_{\text{meas}} = \sqrt{(\Delta\lambda_{\text{etalon}} + \Delta\lambda_{\text{laser}})^2}. \tag{8}$$

Optimally, the resolution will be fine enough to not affect the measurement significantly. The resolving power of the etalon is the free spectral range (FSR) divided by the finesse. At $\lambda = 540$ nm, our etalon has a finesse of 40 and a FSR of 0.058 nm. Thus, the resolving power of this etalon is approximately 0.058 nm/40=0.0015 nm. For the double-grating GIDL cavity, the linewidth, as measured by the etalon, was 0.0072(2) nm. (The uncertainty is statistically determined from fitting the peak to a Gaussian line shape.) Using Eq. (8), we find that the actual linewidth of the laser is 0.0070(2) nm. Since this is within the uncertainty, we conclude that we don't need to routinely correct our measurements for the effect of the instrument.

Another method for measuring the linewidth is to drive an atomic transition with the laser. This can be done by setting up any of a number of experiments as mentioned above. We used a Ne hollow cathode discharge tube (HCDT) and the optogalvanic effect.[14] The primary broadening source in the atomic lines in a HCDT is from the Doppler effect. A reasonable estimate of the temperature inside the discharge is 400 K from which we can estimate the Doppler broadening to be approximately 0.002 nm. Our narrowest measurement of the Ne line was 0.0059(2) nm, this deconvolves to 0.0056(2) nm. Note that this error is greater than the fitting uncertainty.

The linewidth disagreement in the etalon and HCDT measurements is likely due to inaccuracies in curve fitting and systematic sources of error in the measurements. One such source of error is the physical size of the photodiode used to measure the etalon fringes. Another potential source of error is deviations from linearity (for signal versus intensity) in the photodiode or HCDT.

D. Amplified spontaneous emission (ASE)

Lasing occurs when an initial spontaneous photon propagating along the axis of the laser cavity starts the chain reaction of stimulated emission that we know as laser light. For most lasers this is the end of the discussion, but for dye lasers the situation is different. Laser dyes are designed to support lasing over a bandwidth of tens of nanometers. Dye laser cavities must reject all but a very narrow bandwidth of photons for amplification. For example, the cavity for the grazing incidence dye laser typically reduces the emission bandwidth of the dye by four orders of magnitude. ASE is the result of spontaneous photons being amplified by either a single pass through the cavity or feedback from unwanted internal reflections. ASE is essentially broadband background noise in the laser output.

Completely eliminating ASE is impossible, but it can be reduced. For example, simply orienting the sidewalls of the dye cell exactly perpendicular to the axis of the laser cavity can quickly demonstrate serious ASE. Internal reflections from the sides of the dye cell will form a broadband resonant cavity. The effect can be readily observed by monitoring the laser output with a diffraction grating, or by observing a single slit diffraction pattern. With the slit, all fringe contrast will be washed out when broadband lasing occurs. For the diffraction grating, the output spot will spread over a much larger region. The effect is so strong, when the laser linewidth changes from 0.006 to 60.0 nm, that even a simple prism will detect it. ASE caused by internal reflections in the dye cell is easy to resolve; simply rotate the dye cell a few degrees about an axis parallel to the pump beam so that the laser cavity axis is not perpendicular to the faces of the dye cell.

Other sources of ASE, for example, surface reflections from optical components inside the laser cavity, are not as easy to control. Rotating all the optics a few degrees so that no first surface reflections can be amplified is one solution. However, this also causes astigmatism in the laser beam. We require that the students deliberately orient at least one optical component such that a stray reflection is amplified. The students then rotate the component slightly while monitoring the beam quality.

E. Cavity mode structure

No laser is truly monochromatic. Beyond the issue of a finite bandwidth, most lasers contain several closely spaced emission lines arising from longitudinal modes inside the cavity. For a typical resonant cavity with plane mirrors, the

This article is copyrighted as indicated in the article. Reuse of AAPT content is subject to the terms at: http://scitation.aip.org/termsconditions. Downloaded to IP: 158.104.100.45 On: Thu, 03 Sep 2015 22:53:57

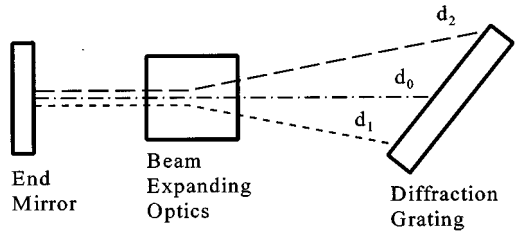

Fig. 4. A simplified diagram of a typical dye laser cavity. Notice the different cavity lengths, d_0, d_1, and d_2. A poorly defined cavity length is only one of the complications involved in calculating the cavity mode structure for a dye laser. A Hänsch laser is shown, but the problem is even more pronounced in the grazing incidence cavities.

spacing between modes is described by $\Delta\lambda = \lambda^2/(2nd)$, where n is the index of refraction and d is the cavity length. (The mode spacing is a direct result of the requirement that an integral number of half-wavelengths fit inside a resonant cavity.) Unlike most lasers, the cavity length is not a well-defined quantity for dye lasers. This is because of the tipped ''mirror'' formed by the diffraction grating (see Fig. 4). Other complexities arise because the active medium (the optically pumped laser dye) is only a small part of the cavity; thus neither the index of refraction nor the laser gain is constant inside a dye laser.[26]

An etalon will readily display the modes of a dye laser if the laser modes are more closely spaced than the free spectral range of the etalon. It turns out that the mode structure of a dye laser is far more dependent on careful alignment than on cavity length. In use, a dye laser is usually scanned in wavelength; therefore, the optical alignment must be robust throughout the tuning range of the laser. Each of the three laser cavities described in this paper have different behavior with respect to cavity modes. Typical results are reported below.

F. Laser safety

There are two primary safety concerns for dye laser users: light and laser dyes. It is not the purpose of this article to address these issues at length. However, there are a few easy precautions that all dye laser users should follow.

An excellent overview of laser hazards and safety has been written by Weichel *et al.*[27] The Optical Society of America's Laser Safety Committee[28] has addressed specifically the issues related to ultraviolet laser light such as the lasers used for optically pumping the dye laser. Moseley[29] has written a more current and extremely detailed review article on both ultraviolet and laser radiation safety.

In addition to retinal damage from direct exposure to laser beams, the lens tissue can also be damaged by the UV pump laser. The 337-nm laser light from an N_2^+ pump laser is right at the edge of the range that causes cataracts. Additionally, with UV light, skin exposure should also be avoided as much as is practical. Skin effects include erythema (sunburn), accelerated aging of the skin and photocarcinogenisis (skin cancer).

Because the laser light is pulsed, the average power may be only a few milliwatts, yet the peak power can be quite high. The pump laser can easily exceed 1 MW and the dye laser's peak power can be in the range of 10 kW. Common sense is the best first defense, but careful planing can help. You should have an adequate supply of UV blocking laser safety goggles. All stray laser beams should be monitored, preferably blocked. Be alert to first surface reflections from laboratory equipment and furniture, e.g., glass cabinet doors and windows. It is good laser laboratory practice to keep all laser beams in a single horizontal plane. Then, make sure that no chairs are available that would place an occupant's eyes on the same level as the laser beam plane. The general direction of the laser beams should be away from doors or other traffic areas. Access doors must have warning lights and signs.

Laser dyes introduce a hazard not present with other laser types. The dyes themselves have not generally had complete tests done on the toxilogical and mutagenic properties. (The current test results[30] indicate that many laser dyes are generally safe, though be aware that some laser dyes are known mutagens.) All liquid laser dyes use solvents. Usually the solvents, e.g., methanol, are easy to handle. However, some laser dyes require solvents such as DMSO. DMSO is difficult to handle without risking the direct absorption of laser dyes into the body. Since dyes requiring DMSO are easy to avoid, we recommend that they not be used in the undergraduate laboratory. All laser dyes should be mixed in a fume hood or other area with adequate ventilation. Gloves and eye protection should be worn whenever dyes are handled. Premixed dye solutions should be kept tightly capped. The laser dye powder often gets spilled in minute amounts and seems to get everywhere, hence the mixing area should be carefully wiped down after each use.

III. BUILDING AND USING THE LASER

A. Components

We have attempted to minimize the use of parts requiring specialized machining. This laser can be constructed almost completely from off-the-shelf optical components. The minimum tools needed to manufacture the specialized components are a hacksaw, a drill press, and an 8-32 tap. A complete listing of parts and suppliers is in Appendix A. The dye laser (sans the pump laser) can be built for less than $3,300 and will outperform lasers costing more than $20,000.

Most of the optical components need only be of standard student laboratory quality. The only exceptions are the dye cells, pump beam lenses and diffraction grating(s).

For the dye cells, spectrometer cuvettes, commonly used in chemical analysis equipment, are readily available and work well. Most campus chemistry department stock rooms stock these. If you are using UV light for the pump then you will want a quartz dye cell. A glass dye cell might also work since the optical path thickness is small enough that the UV absorption and reflection losses should be about 25%. (The quartz dye cell will have about an 8% loss.) If your pump laser is powerful enough then this loss will probably not be critical. (We have not tried glass cells.) We found that plastic dye cells will not work due to strong absorption of the UV pump beam. Additionally, some of the laser dyes stain the plastic aggressively. The dye cell must have a securely sealing top to reduce evaporation of the dye solvent.

An improvement to the system is to use a flowing dye cell or a dye cell stirrer. This will allow for higher repetition rates without saturating the laser dye. We found that a simple, unstirred dye cell provides stable operation at ten pulses per second (pps) but becomes unstable at 15 pps. Lower pump power will likely offset this limitation.

This article is copyrighted as indicated in the article. Reuse of AAPT content is subject to the terms at: http://scitation.aip.org/termsconditions. Downloaded to IP: 158.104.100.45 On: Thu, 03 Sep 2015 22:53:57

The pump beam lenses should be constructed of UV transparent material such as silica. The cylindrical lens is the most expensive. Some laser manufacturers might have overstock and/or damaged cylindrical silica lenses on hand that can be purchased at a reduced price. A small chip in the lens will not affect its use unless it is near the vertex.

For the grazing incidence dye laser, purchasing a diffraction grating that is blazed for this purpose is best. However, we found that any high quality grating with 1200–2400 lines/mm can be used, although the efficiency will be less. Good potential sources of free, high quality diffraction gratings are chemistry and geology departments. For example, we obtained several top quality diffraction gratings (and other optics) from an atomic absorption instrument that was being surplused as scrap by our chemistry department.

The optics mounts should be as sturdy as possible. However, we deliberately shook each mount and found that only the dye cell, tuning mirror/grating and diffraction grating mounts really needed to be of the highest quality.

Being able to scan the dye laser wavelength with a stepper motor is extremely useful. The step sizes must be small enough to provide five or more steps across the full width at half-maximum of the laser linewidth. We found that elaborate gearing systems were much more difficult to use than a microstepping circuit for the stepper motor. Microstepping circuits are commercially available that can be controlled by transistor–transistor logic (TTL) digital input–output (I/O) signals from a computer data acquisition card.

Many moderately priced rotation stages have substantial lateral motion of the control knob while rotating the stage. These stages will work if the stepper motor drive linkage can adapt to this. We successfully used a chain and sprocket drive train along with a microstepper circuit. This was substantially easier than earlier attempts that used flex shafts and universal joint couplings.

B. Assembly

The components we used are listed in Appendix A along with a note describing the position of that component. Because the goal of this project was to have a laser that students could quickly reconfigure, we have placed every optical component in its own permanent mount. Students can safely bolt down the components that they do not need off to the side on the breadboard. Permanently mounted components also lessen the potential for damage to the optical components. Unfortunately, the current design requires direct handling of the most delicate element—the diffraction grating. Currently, this is done only with the instructor present.

In Appendix A we have described which mounts hold which optics for the initial assembly. Once the optical components are mounted, students can shuffle them around on the breadboard to match the cavity configurations shown in Figs. 1, 2, and 3. Appendix B gives an outlined approach to setting up each individual laser cavity. Figure 5 is a photograph of the optical components arranged for the double-diffraction grating GIDL. The black baseplate was removed, and the spacing between the optics increased, for photographic clarity.

The effects of the pump beam include the eventual breakdown of the laser dye caused by photochemical interactions. Some laser dyes will only last for a few hours of use. There is no visual way to know when the laser dye is exhausted since the dye will still fluoresce. So, if your attempts at lasing fail for no apparent reason, try using fresh laser dye.

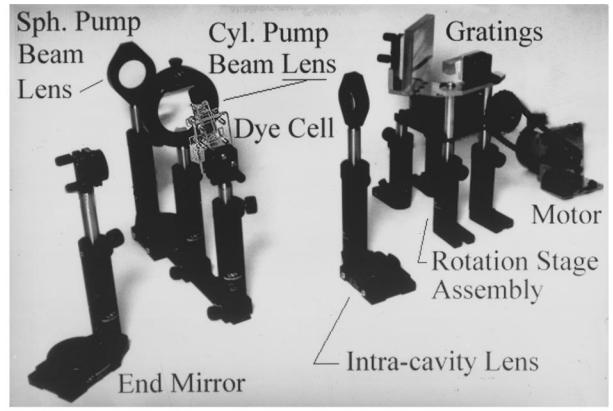

Fig. 5. The double-grating grazing incidence dye laser. For clarity, the black baseplate was removed for the photograph. Students can reconfigure the laser into the different cavity designs by simply rearranging the optical assemblies. Only the rotational stage assembly requires direct handling of the optical components. The motor is used to scan the laser's output wavelength by rotating the stage.

C. Measurement

The primary goal of this work is for the student to be able to change the cavity design quickly, then measure the effects of that change. A secondary goal is to have a laser that is useful for projects in spectroscopy. Both goals require measurement equipment. The cost of measurement equipment can easily exceed the cost of the laser, although several ways exist to reduce that expense.

Laser parameters that students might measure include the linewidth, ASE, efficiency, polarization, and beam divergence. Since diffraction gratings produce polarized light, all dye lasers are polarized. The beam divergence depends primarily on the adjustment of the output lens, or, for the GIDL, on the intracavity lens. Therefore, beam divergence depends less on the laser cavity and more on careful adjustment.

The linewidth can be measured with an etalon, by scanning an atomic transition, or by using a high resolution spectrometer. By far the easiest and fastest choice is the etalon. An etalon also aids in final adjustment of the laser. A student quality Fabry–Perot interferometer will work but ours was not nearly as efficient as a high quality etalon. We also attempted to use a Michelson interferometer but the resolution was completely inadequate. Etalons typically cost several thousand dollars; however, Perkalskis and Freeman[25] describe the construction of a homemade etalon for a fraction of this cost. Dye laser manufacturers sometimes have etalons available that are obsolete stock or over-stock accessories that they will sell for a reduced price. The etalon also provides a simple and accurate method for measuring the ASE, as is described below. Etalons are useful for other experiments too, e.g., measuring the Zeeman effect can be easily done with an etalon.

One of the easiest ways to scan an atomic transition is by using neon in a hollow cathode discharge tube (HCDT). Arnett *et al.*[31] have described the technique in detail. HCDTs cost about a tenth that of an etalon. We obtained ours for no cost from the chemistry department; while the HCDT no longer functioned for their atomic absorption instrument, it worked well for our purposes. Try to obtain several tubes since not all tubes have a stable discharge current. Of the three tubes we obtained only two were usable.

This article is copyrighted as indicated in the article. Reuse of AAPT content is subject to the terms at: http://scitation.aip.org/termsconditions. Downloaded to IP: 158.104.100.45 On: Thu, 03 Sep 2015 22:53:57

Table I. Comparison of the three cavity configurations for the homemade dye laser and a commercial dye laser. The results reported are ''typical,'' not ''best.''

Laser cavity	Linewidth[a] (nm)	Efficiency (%)	Noise[b] (%)	Stability[c]
Hänsch	0.16(3)	5	15	poor
single-grating GIDL	0.011(5)	2	10	good
double-grating GIDL	0.0073(2)	2	4	excellent
commercial laser[d]	0.050(2)	N/A[e]	10	fair

[a]Measured using an etalon except the Hänsch configuration that was measured with a 0.25-m spectrometer.
[b]Defined as the fraction of amplified spontaneous emission (ASE) in the total output power.
[c]Defined subjectively as ease of setup, alignment, and smoothness when scanned in wavelength.
[d]Photon Technology International, South Brunswick, NJ, model PL202. This is a single-grating GIDL with the addition of an amplifier stage.
[e]This dye laser has an amplifier stage built in. Thus a direct comparison cannot be made with the homemade laser.

Schreiber *et al.*[32] describe a homemade, high resolution Ebert spectrometer that is precise enough for measuring laser linewidths. We did not complete ours in time for this project but did use a low resolution, 0.25-m, commercial scanning spectrophotometer for measuring the Hänsch dye laser.

Amplified spontaneous emission can be measured with an etalon by measuring the laser power at a fringe peak, at a minimum between fringes, and with the beam blocked. Using the blocked beam reading as the zero power level, the percent ASE is simply obtained from the ratio of the fringe minima to the fringe maxima. Lacking an etalon, a reasonable estimate of the ASE can be made by using a diffraction grating or prism. Disperse the output beam and then measure the power with the lasing portion alternately blocked and unblocked. If you are using a photodiode for power measurement, you will need to add a lens to focus the dispersed beam onto the photodiode.

Efficiency measurements are best accomplished with a laser power meter. An inexpensive alternative is a photodiode. Since you should measure the power of the pump beam, make sure your photodiode will measure in that frequency range. Most photodiodes use glass windows that start to cut off transmission at about 350 nm, so, the 337-nm nitrogen laser output is slightly attenuated.[33] Many photodiode suppliers provide sample circuit diagrams. Photodiode circuits are typically very simple, often involving less than five components.

IV. TYPICAL RESULTS

The dye laser proved to be extremely stable and easy to assemble. The dye laser demonstrated clear differences between three cavity designs. The results presented here are not the best data obtained, but are typical of what should be obtained by students setting up the laser for the first time. We made measurements of the linewidth, the ASE level, and the efficiency. These are compared with that of a commercially made dye laser used as a baseline reference. The results are summarized in Table I.

Optomechanical stability and durability are excellent. The components are generally robust, except for the surface of the diffraction gratings. Aggressive tapping on, and wiggling of, the optical components produced little or no effect in the beam quality with the exception of the mounts for the diffraction grating, tuning mirror/grating, and dye cell.

With practice, we could obtain good laser performance within 15 min when starting with a completely disassembled system. An experienced technician with no formal background in optics or physics was able to obtain excellent laser performance within an hour on the first try. He simply followed a detailed set of instructions on the laser's alignment. Choosing optical mounts that are easy to adjust is advantageous. Several early designs using low-end optical mounts were adequate but much slower to adjust. In particular, mounts with stationary baseplate slots forced one to adjust several degrees of freedom at once for each mount. Being able to slide the optical mount around on the breadboard without rotating the optical component proved to be a significant advantage.

Because students typically approach optical alignment very haphazardly, we have found that they require a detailed procedure. An outline of the alignment procedure is provided in Appendix B.

Based on Iles theoretical analysis, the linewidth of the Hänsch laser should be 0.034 nm, the single-grating GIDL should be 0.0068 nm, and the double-grating GIDL should be 0.0023 nm. With quick alignments, we obtained typical values of 0.175, 0.009, and 0.007 nm, respectively. (With extreme care in the alignment we can obtain values much closer to the theoretical predictions.) The main cause of the increased linewidth was multimode operation. By comparison, the commercial dye laser (Photon Technology International, model PL202) using a single-grating, grazing incidence design produced a linewidth of 0.044(1) nm that, while consistent with their specifications, is much broader than Iles' predictions.

Figures 6, 7, 9, and 10 show typical results for the laser linewidths and tuning stability. For ease of comparison all wavelength axes use the same scale except Fig. 6. A bar on the wavelength axis of Fig. 6 shows the wavelength range of the other figures. The raw data are shown with symbols, and the lines are the results of nonlinear curve fitting to approximately the top half of each peak to a Gaussian. The measured linewidths and uncertainties are all full width at half-maximum (FWHM) and are obtained from the Gaussian curve fit.

Figure 6 was obtained by combining spectrophotometer scans of the neon spectrum from the HCDT and of the laser. The spectrophotometer's resolution is 0.052(4) nm as determined by measuring the neon line. Figure 6 is interesting because it shows that the laser is operating on at least three separate paths within the laser cavity. Other attempts at aligning the Hänsch laser cavity resulted in one or two peaks. Overall, this cavity required more care than the other designs to obtain the best operation. Linewidths on the order of 0.2 nm, as shown for the three peaks in Fig. 6, were typical for this cavity even when operating with a single peak. Hänsch added an intracavity etalon to narrow the linewidth substantially (shown by a dashed box in Fig. 1). This is still common today in many commercial Hänsch design, dye lasers.

The ASE level shown in Fig. 6 is misleading. Since these data were taken with a spectrometer, the correct method to determine the ASE level would be to integrate the area under the curve (excluding the laser lines) rather than reading the instantaneous level as can be done with measurements using

This article is copyrighted as indicated in the article. Reuse of AAPT content is subject to the terms at: http://scitation.aip.org/termsconditions. Downloaded to IP: 158.104.100.45 On: Thu, 03 Sep 2015 22:53:57

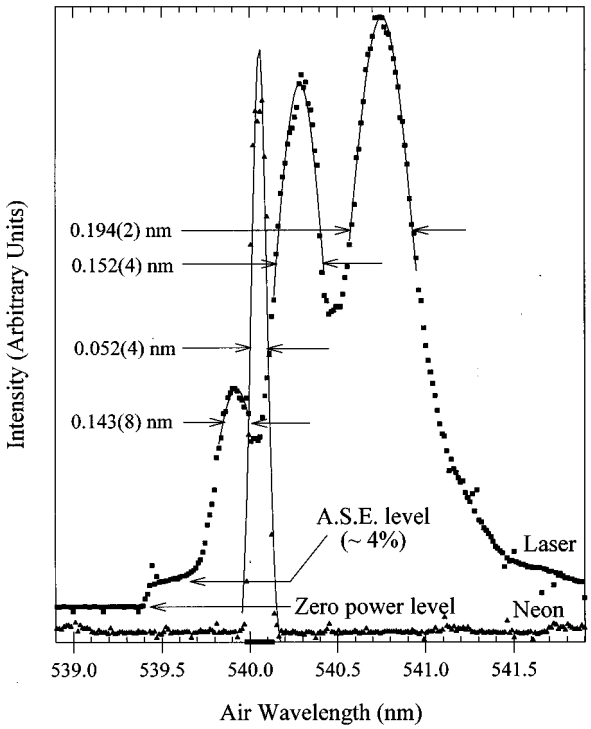

Fig. 6. The laser's spectral output when configured as a Hänsch dye laser, measured using a 0.25-m spectrometer. The neon spectral line was scanned separately for calibration and to determine the resolution of the spectrometer. The amplified spontaneous emission (ASE) level indicates the amount of broadband noise in the laser's output. The horizontal bar on the wavelength axis near 540.0 nm indicates, for comparison, the spectral range covered in Figs. 7, 9, and 10.

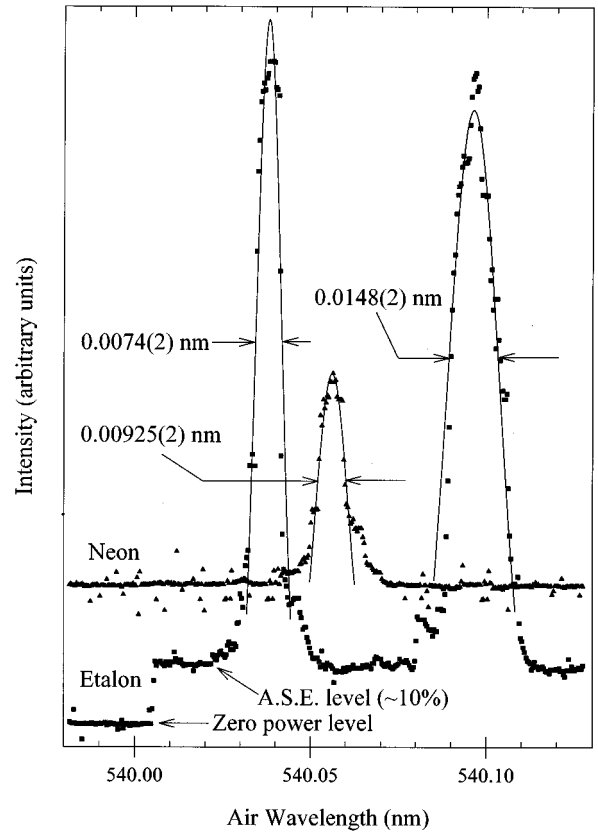

Fig. 7. The spectral output from the laser when configured as a single-grating, grazing incidence dye laser. The etalon fringes and optogalvanic spectra were simultaneously measured while the laser was scanned in wavelength. Note the progression in linewidth as the laser mode structure changes.

the etalon. However, the approach used in Fig. 6 does provide a sense of the level of the background noise in the laser output.

Figures 7, 9, and 10 are simultaneous measurements of the etalon fringes and optogalvanic effect in the HCDT while scanning the laser wavelength. For the sake of clarity, we have plotted only every other data point. We scanned the laser with a microstepping stepper motor providing more than 30 steps within the FWHM of the laser line. (A later version of the drive circuit reduced this resolution by a factor of 2. The reduced resolution is still more than adequate and has improved the data collection rate.) At the start of each scan, we blocked the laser beam into the etalon to determine a zero power level. The ASE is then determined as described in the previous section.

The single-grating GIDL performance is shown in Fig. 7. Note the progression in linewidth as the laser scanned upward in wavelength. Changes in the mode structure caused this. At the start of the scan, the cavity was lasing predominantly on one or two adjacent longitudinal modes. [Typical etalon fringes for this situation are shown in Fig. 8(a).] At the second etalon fringe, at 540.97 nm, the cavity is lasing on multiple adjacent modes. [Figure 8(b) shows typical etalon fringes when the laser is running on multiple modes.] By the next etalon fringe (not shown in Fig. 7) the linewidth was back to 0.007 nm and the cavity was again running nearly single mode. This is a common problem with narrow linewidth lasers when they are being scanned. The phenomenon is known as ''mode hopping.''

The added spectral dispersion provided by a second diffraction grating significantly improved the stability of the laser cavity, as is shown in Fig. 9. Longer scans with this design proved much more stable than similar scans with the single diffraction grating GIDL. This laser cavity routinely provided the easiest alignment for the highest quality resolution. The 60% reduction in ASE compared with the single grating design is an additional benefit of the extra dispersion contributed by the second grating.

The commercial dye laser's performance is shown in Fig. 10. Notice the noise in the peaks caused by instability in the mode structure. Students can easily see this by looking at the etalon fringes. Each fringe consists of many fine fringes all with unstable intensity levels. This is manifested as noise in the neon peak in Fig. 10. (Because of an equipment failure, Fig. 10 is actually the result of combining two scans obtained a few minutes apart. Thus, the noise peaks do not line up between the two signals.)

The laser efficiency is determined by taking the ratio of the output power of the dye laser to the input power from the pump laser. Again, using typical results rather than ''best'' results, we found that the Hänsch design yielded 5% efficiency. Both the single and double grating GIDLs ran at approximately 2% efficiency. At first glance it would appear that the Hänsch dye laser is the most efficient. This is misleading, however, since often what is important is the spectral energy density. Since the GIDLs operate with on the

This article is copyrighted as indicated in the article. Reuse of AAPT content is subject to the terms at: http://scitation.aip.org/termsconditions. Downloaded to IP: 158.104.100.45 On: Thu, 03 Sep 2015 22:53:57

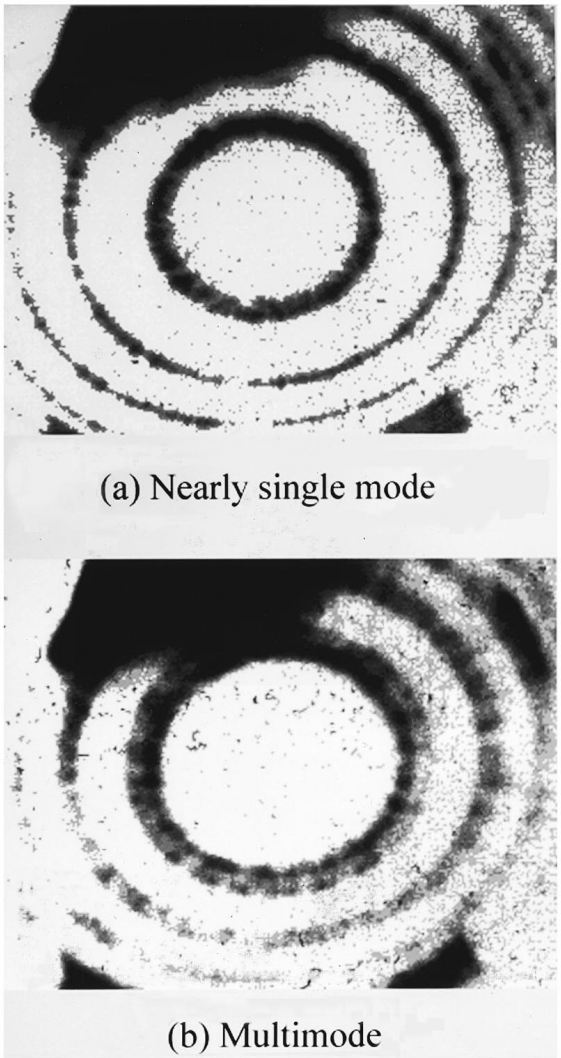

Fig. 8. Final adjustments to the laser are most easily made while monitoring the output with an etalon. In (a) the fringes are crisp and narrow indicating a well defined, narrow linewidth. In (b) the laser cavity is operating on at least two cavity modes resulting in multiple etalon fringes.

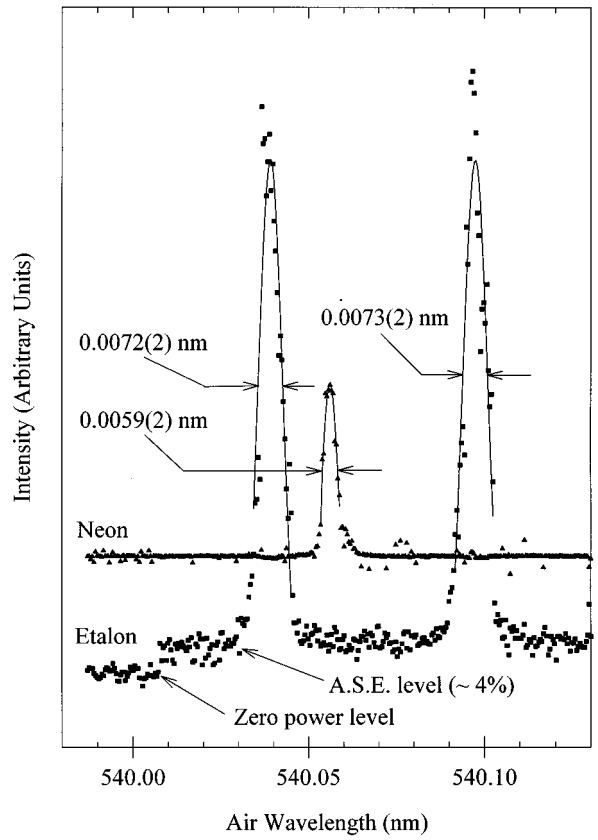

Fig. 9. The spectral output from the laser when configured as a double-grating, grazing incidence dye laser. Data were collected as in Fig. 7. Note the stable, narrow linewidths. Note also the reduction in amplified spontaneous emission (ASE) as compared with Fig. 7.

order of 20 times narrower linewidths, the actual useful energy density is nearly 10 times greater for the GIDLs than for the Hänsch laser.

Finally, we varied the length of the laser cavity for the GIDL designs. No significant effect was detected, just as was predicted by Iles. It seems that longer cavities offset the closer longitudinal mode spacing with higher extinction of unwanted frequencies due to the angular dispersion caused by the diffraction gratings. This analysis fails for extremely short cavities that can operate on a single mode.

V. CONCLUSION

Because of the ease of assembly, stability, and educational value of this experiment, it will become a standard laboratory exercise for our Applied Optics course. Additionally, the laser is visually ''pretty'' to view and has attracted much attention and excited many students.

Due to the dye laser's modular design, this system can easily provide future expandability. With the addition of a few optical parts, students can study other laser cavity designs, e.g., the DiMauro[34] laser. Planned future improvements include the addition of an amplifier stage and adding dye cell stirring or a flow through dye cell. Amplifier stages are extremely efficient, often as high as 35%. Stirring will allow for higher repetition rates. Even without additional improvements, the laser is already useful for spectroscopic work and outperforms many commercial dye lasers.

Purchasing off-the-shelf optics both reduced the development time and added to the ease of assembly. Standard, off-the-shelf optical mounts later replaced several mounts originally manufactured in-house. Given the comparatively low cost of high quality optical mounts, we do not feel it is worth the labor to make your own.

ACKNOWLEDGMENTS

This work was supported in part by National Science Foundation- Instrument and Laboratory Improvement Grant No. DUE-9351951. Support in the form of two grants from the Weber State University Research, Scholarship and Professional Growth Committee is gratefully acknowledged. We also thank the Departments of Chemistry and Geoscience for the donation of nonworking and/or unwanted hollow cathode discharge tubes and spectrometers.

This article is copyrighted as indicated in the article. Reuse of AAPT content is subject to the terms at: http://scitation.aip.org/termsconditions. Downloaded to IP: 158.104.100.45 On: Thu, 03 Sep 2015 22:53:57

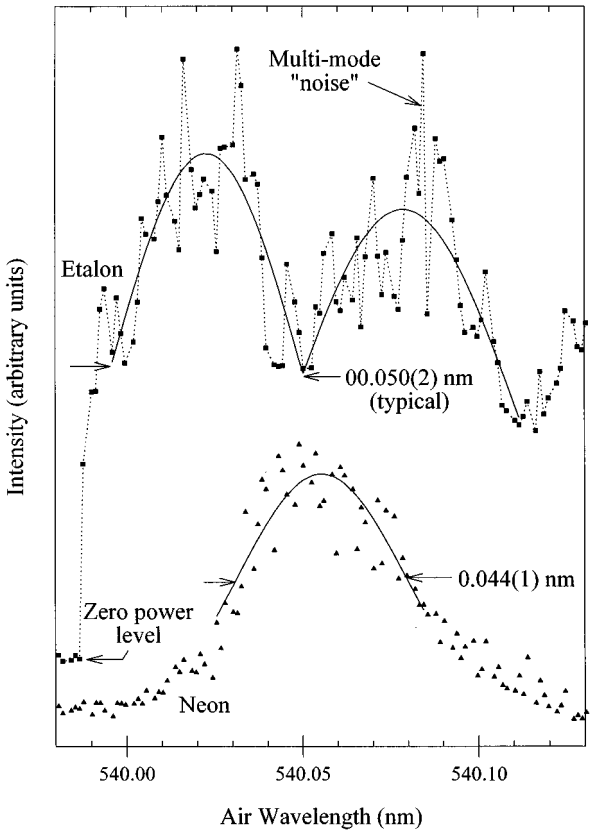

Fig. 10. The spectral output from a commercial dye laser that uses the single-grating grazing incidence design. Data were acquired using the same methods as for Figs. 7 and 9. An ASE measurement is not possible with this data because of our choice of free spectral range for the etalon. (An ASE level of 10% was determined using an external diffraction grating.) Unstable mode structure inside the laser cavity causes the noise in the data.

APPENDIX A: PARTS LIST AND INITIAL ASSEMBLY

A detailed list of all items used to construct this laser system is shown in Table II. Of course, any comparable products will work, we have listed specific suppliers for reference only. Prices are dynamic and are also listed for reference only. The height of the laser cavity above the breadboard is chosen to match the pump laser's beam height. Changing the length of the support posts (items with part number prefixes ''SP-'') and post holders (part numbers starting with ''VPH-'') can easily adapt the height of the dye laser to any pump laser. No values (focal lengths, grating constants, etc.) are critical. Costs can be reduced by several hundred dollars by: using lower quality lenses (except the pump beam lenses), using a glass dye cell, substituting the less convenient B-05 style base for the BUP-2 base, choosing not to build the Hänsch cavity, using cheaper optics mounts (except as noted in the text), and/or building most of the components in-house.

Several simple homemade adapters are used for attaching optics to the rotation stage. Construction details are described below, while Fig. 11 shows these various adapters in use. The sprocket (see Fig. 11) was bored out to fit the rotation stage knob. Two set screws keep the sprocket from slipping when the motor is running the stage.

The diffraction gratings and tuning mirror can be secured to the mounting plates (see Fig. 12) with either epoxy or double-back sticky tape. (Do not use foam-based tapes.) We made the mounting plates from aluminum measuring 0.25 $\times$1.0$\times$1.0 in. A 0.25-in.-diam, 0.5-in. long pin was glued into a matching hole centered in the plate. This pin was inserted until flush with one side of the plate. No dimensions are critical, except the pin diameter. The pin must be chosen such that it will fit into the MM-1, or equivalent, mounting hole.

We hold the grazing incidence diffraction grating above the rotation stage with the support plate shown in Fig. 13. The plate is attached with two 2.50-in.-long 8-32 screws through two standoffs to two of the support posts that hold the stage; see Fig. 11. (The standoffs are made from 0.375-in.-diam rods, with 8-32 clearance holes drilled lengthwise through the axes.) The standoffs hold the support plate above the stage. The third hole in the plate is for attaching the mounting that holds the diffraction grating.

The tuning optic, Littrow mount diffraction grating or tuning mirror, is attached to the rotation stage with the bracket shown in Fig. 14(a). The baseplate holes match the surface of the rotation stage and the mount for the tuning optic is attached with the vertical spacer shown in Fig. 14(b).

We attach the dye cell to the MM-1, or equivalent mount, with the holder shown in Fig. 15. As was done for the diffraction grating mount (Fig. 12), the dye cell holder has a 0.50-in.-long pin glued into the 0.25-in. hole. Except for the pin, we constructed this holder of plastic so that the dye cell will not be scratched. The dye cell is sandwiched between the clamps [Fig. 15(a)] and the main holder [Fig. 15(b)] with four 8-32 screws.

The cylindrical pump beam lens does not completely fit inside its mount. We attached it to the LH2-150R holder with two spots of hot glue.

APPENDIX B: LASER ALIGNMENT

An orderly approach to alignment cannot be over-stressed. Following is an overview to the typical alignment procedure. We have assumed that the assemblies mentioned in Appendix A have already been completed.

For all laser cavity designs:

(1) Wear UV laser safety goggles. For an UV light detector, use a business card or other white paper stock: the UV light will cause the card to fluoresce in the blue.
(2) Insert the spherical pump beam lens.
(3) Insert the cylindrical pump beam lens.
(4) Insert the dye cell with laser dye, tip the dye cell away from vertical a few degrees about the optical axis of the pump beam. Make sure the dye cell front surface is perpendicular to the pump beam by verifying that the first surface back-reflection is centered on the pump beam lenses.
(5) Adjust the pump beam lenses such that the dye cell width is completely illuminated and the focus of the line is as sharp as possible. Rotate the cylindrical lens about the optical axis until the fluorescence beams exiting the sides of the dye cell are horizontal.

For the GIDL cavity designs:

(1) Insert the intracavity lens. Adjust the lens such that the output is collimated and centered on the original fluorescence spot on a distant screen.

This article is copyrighted as indicated in the article. Reuse of AAPT content is subject to the terms at: http://scitation.aip.org/termsconditions. Downloaded to IP: 158.104.100.45 On: Thu, 03 Sep 2015 22:53:57

Table II. Parts list for the reconfigurable, homemade dye laser and support equipment.

Qty	Description	Part number	Function	Our supplier[a]	Unit cost[b]
1	breadboard	SA-12	1 ft×2 ft baseplate, mounting holes on 1-in. centers	Newport Corp., Irvine, CA	$427.00
1	6-in. rail	MRL-6	pump optics mounting for focus slides	Newport	38.00
2	rail carrier	MCF	pump optics rail slides (focus adjustment)	Newport	20.00
1	rotory stage	481-A-S	for wavelength tuning, holds Figs. 9 and 10	Newport	360.00
4	base	B-05	supports rotation stage	Newport	8.50
4	post holder	VPH-3	supports rotation stage	Newport	13.00
4	support post	SP-3	supports rotation stage	Newport	7.00
6	post holder	VPH-4	supports for dye cell, end mirror, all lenses	Newport	15.00
6	support post	SP-4	supports for dye cell, end mirror, all lenses	Newport	8.00
4	base	BUP-2	supports for dye cell, end mirror, all lenses	Newport	63.00
1	lens mount	LM-2R	rotatable for 2-in. cyl. pump beam lens	Newport	39.00
1	lens holder	LH2-150R	holds cyl. pump lens in above mount	Newport	26.00
1	lens holder	LH-150	mounting for spherical pump beam lens	Newport	21.00
4	mirror mount	MM-1	for both gratings, dye cell, end mirror	Newport	44.00
1	mirror holder	MM-1H	GIDL end mirror holder, fits into MM-1	Newport	7.00
1	lens holder	MM2-1A	for Hänsch output lens	Newport	54.00
2	lens holder	LH-100	mounting of Hänsch beam expander lenses	Newport	18.00
1	mirror mount	MM-2	for 2-in. GIDL tuning mirror	Newport	51.00
1	UV lens	A115100	spherical pump lens 38 mm diam., $f=254$ mm	Esco Products, Oak Ridge, NJ	146.00
1	UV lens	B115030	cyl. pump beam lens, 38 mm, $f=76.2$ mm	Esco Products	174.00
1	biconvex lens	KBX058	GIDL intracavity lens, 1-in. diam., $f=75.6$ mm	Newport	27.00
1	planoconvex	KPX082	Hänsch lens/end mirror, 1-in., $f=50.2$ mm	Newport	29.00
1	biconcave lens	KBC046	Hänsch beam expander, 1-in., $f=-25.0$ mm	Newport	30.00
1	biconvex lens	KBX070	Hänsch beam expander, 1-in., $f=150.0$ mm	Newport	24.00
1	dye cell	23H-10 mm	polished on four sides with stopper	NSG precision Cells, Inc., Farmingdale, NY	118.00
1	1-in. mirror	10D20BD.1	GIDL end mirror	Newport	98.00
1	2-in. mirror	20D20BD.1	GIDL wavelength tuning mirror	Newport	217.00
1	grating	135.2400D21	GIDL diffraction grating, 2400 lines/mm (This grating is blazed for use in GIDLs)	American Holographic, Fitchburg, MA	265.00
1	grating	unmarked	Littrow mount grating, 1440 lines/mm	scavanged (Perkin–Elmer)	0.00
1	laser dye	C540A, 1 g	almost any laser dye will work	Exciton, Dayton, OH	44.00
1	drive circuit	7100-DB	for microstepper control of stepper motor (Kit form, you supply box and power.)	Am. Sci. Instrument Corp, Smithtown, NY	175.00
1	stepper motor	M061-CS02	remote control of wavelength scanning	Slo-Syn	110.00
1	sprocket	25B21	21 tooth, drill out to fit rotation stage knob	U.S. Tsubaki	5.34
1	sprocket	25B10	10 tooth, for stepper motor shaft	U.S. Tsubaki	4.02
1	16-in. chain		connect motor and stage sprockets	U.S. Tsubaki	5.60
1	screw kit	SK-25A	screws for attaching mounts to baseplate	Newport	46.00
3	mounting	Fig. 12	adapts optics to MM-1 mounts (see Fig. 11)	homemade	0.00
1	support	Fig. 13	holds gazing incidence grating (see Fig. 11)	homemade	0.00
2	spacers		support plate spacers (see Fig. 11)	homemade	0.00
1	bracket	Fig. 14	holds tuning optics (see Fig. 11)	homemade	0.00
1	holder	Fig. 15	dye cell holder, fits into MM-1 mount	homemade	0.00
The following items are not specifically part of the dye laser but are useful or required support items:					
6	Ne–N goggles	G-LGS-NN	safety goggles	Newport	196.00
1	etalon	EA201-7S1-7S2	linewidth testing	TecOptics, Merrick, NY	4,487.00
1	HCDT		neon spectrum	surplus	0.00
2	integrator	SR250	data acquisition and averaging	Stanford Research Systems, Sunnyvale, CA	2,990.00
1	nitrogen laser	UV-1000	pump source	Molectron (now Laser Photonics) Orlando, FL (used laser)	$4,001.00

[a]Part numbers and suppliers are listed for reference only, any roughly equivalent component will work.
[b]Prices were accurate at time of submittal.

(2) Install the end mirror and adjust it such that its reflected spot is centered on the previous spot.
(3) Mount the diffraction grating such that the rulings are as perpendicular to the laser cavity as possible. (This is a one time adjustment.)
(4) Insert the rotation stage/diffraction grating assembly such that the diffraction grating intersects the collimated fluorescence beam at about 89° from the grating normal. Part of the beam will spill past the surface. The second spot is the zeroth diffraction order. Adjust the angle of the diffraction grating such that the angle between the spilled beam and the diffracted beam is 2°. Take care to illuminate the diffraction grating as uniformly and completely as possible.
(5) Attach either the Littrow mounted diffraction grating or the tuning mirror to the rotary stage. Position the optic to

This article is copyrighted as indicated in the article. Reuse of AAPT content is subject to the terms at: http://scitation.aip.org/termsconditions. Downloaded to IP: 158.104.100.45 On: Thu, 03 Sep 2015 22:53:57

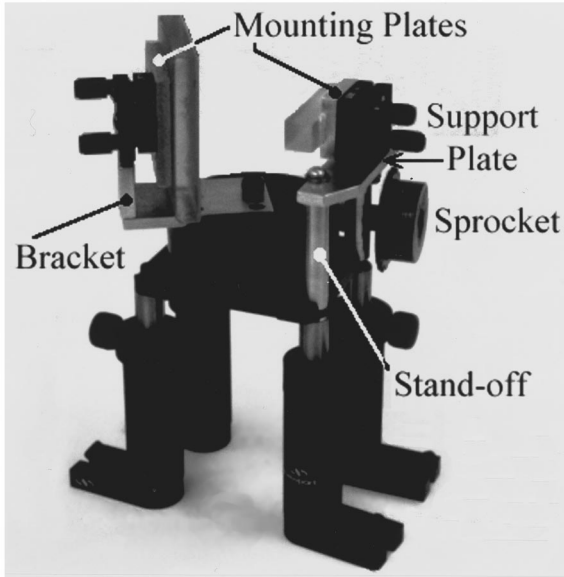

Fig. 11. A closeup view of the rotational stage assembly. The diffraction gratings and tuning mirror are glued to the mounting plates. The standoffs (two are required) and the support plate are only used for the grazing incidence laser cavity.

retroreflect the brighter of the two first-order diffraction lines from the grazing incidence diffraction grating.

(6) While monitoring the remaining first-order diffraction line from the grazing incidence diffraction grating, adjust the tuning optic such that laser speckles appear both in this diffraction order and in the output beam.
(7) Use an etalon or other measuring method to make minor adjustments to optimize the laser cavity alignment.

For the Hänsch dye laser cavity design:

(1) Insert the negative focal length beam expanding lens. Adjust the lens such that the output is centered on the original fluorescence spot on a distant screen. Rotate the lens about a vertical axis just enough that any first surface reflections do not return through the dye cell for unwanted amplification. (Skew lenses cause astigmatism, do not rotate any of the lenses more than needed.)

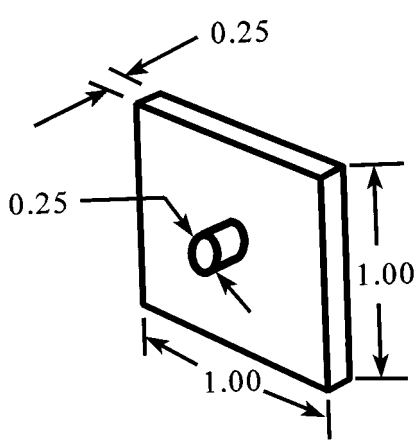

Fig. 12. The aluminum mounting plate (three required) used to hold the diffraction gratings and tuning mirror to the adjustable optical mounts. The protruding pin inserts into the adjustable optical mount.

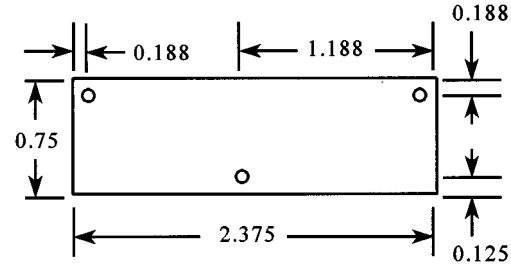

Fig. 13. The support plate for the grazing incidence diffraction grating. The plate is constructed from 0.25-in.-thick aluminum. Figure 11 shows the support plate in use.

(2) Insert the positive focal length beam expanding lens. Adjust the lens such that the output is collimated and centered on the previous fluorescence spot on a distant screen. Again, rotate the lens slightly to keep reflections out of the active region of the dye cell.
(3) Install the output lens/end mirror and adjust it such that its back reflected spot is centered on the previous spot. This lens should be installed with the Plano side toward the inside of the laser cavity.
(4) Mount the diffraction grating such that the rulings are as perpendicular to the laser cavity as possible. (This is a one time adjustment.)
(5) Rotate the diffraction grating such that a specific wavelength reflects back into the laser cavity. (The Littrow mount condition.) The laser should be operating now.
(6) While monitoring the quality of the output, make small adjustments to optimize the alignment.

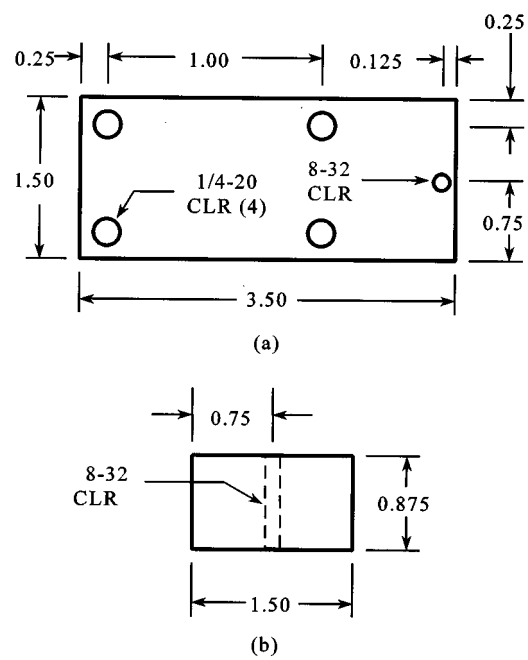

Fig. 14. This bracket holds the tuning optic (a diffraction grating or plane mirror) to the rotation stage. The base bracket (a) bolts to the surface of the stage and the vertical spacer (b) is used between the optical mount and the base bracket. Both items are constructed from 0.25-in.-thick aluminum. Figure 11 shows this bracket in use.

This article is copyrighted as indicated in the article. Reuse of AAPT content is subject to the terms at: http://scitation.aip.org/termsconditions. Downloaded to IP: 158.104.100.45 On: Thu, 03 Sep 2015 22:53:57

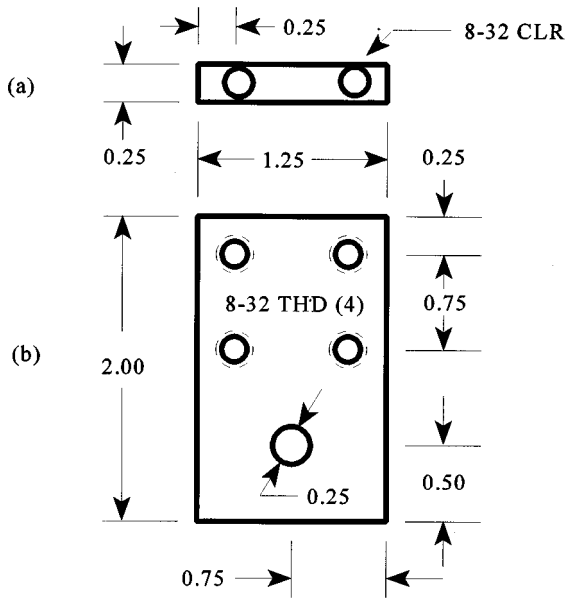

Fig. 15. The dye cell holder. This is constructed from 0.25-in.-thick plastic (we used Lexan). Two of the clamping pieces (a) are needed. The dye cell is sandwiched between the clamping pieces and the main holder (b) using four, 1-in.-long 8–32 screws. A 0.5-in.-long, 0.25-in.-diam pin is glued into the 0.25-in. hole on the main holder. This pin fits into the optical mount used to hold the dye cell assembly.

[1]R. C. Hilborn, ''Design and construction of simple, nitrogen-laser-pumped, tunable dye lasers,'' Am. J. Phys. **46**, 565–572 (1978).

[2]A. J. Alfrey, ''Flashlamp-pumped dye laser as an undergraduate lab project,'' Am. J. Phys. **49**, 776–781 (1981).

[3]Laser Science, Inc., 26 Landsdowne St., Cambridge, MA 02139, produces a small Hansch design dye laser. Reference the annual (August) Buyers Guide issue of Phys. Today for more manufacturers.

[4]J. R. Brandenberger, *Proceedings of Laser Physics and Modern Optics in Liberal Arts Colleges*, Appleton, WI, 22–23 June 1987 (Lawrence University Press, Appleton, WI, 1987).

[5]K. Arnett, R. Anderson, and R. Alexander, ''Modern spectroscopy with a spectrometer by the optogalvanic effect,'' Am. J. Phys. **49**, 767–772 (1981).

[6]H. P. Grieneisen, *The Nitrogen Laser-Pumped Dye Laser: An Ideal Light Source for College Experiments* (Laser Science, Inc., Cambridge, MA, 1984).

[7]F. H. Wirth, *Dye Laser Experiments for the Undergraduate Laboratory* (Laser Science, Inc., Cambridge, MA, no date given, approximately 1984).

[8]*Nitrogen Dye Laser Applications to Physics and Chemistry Courses in Colleges and Universities* (Laser Photonics, Inc., Orlando, FL, 1992).

[9]P. F. Schewe, ''Lasers,'' Phys. Teach. **19**, 534–547 (1981).

[10]D. C. O'Shea and D. C. Peckham, ''Resource Letter L-1: Lasers,'' Am. J. Phys. **49**, 915–925 (1981).

[11]U. Ganiel, A. Hardy, G. Neumann, and D. Treves, ''Amplified Spontaneous Emission and Signal Amplification in Dye-Laser Systems,'' IEEE J. Quantum Electron. **QE-11**, 881–892 (1975).

[12]D.-H. Yang, T. L. Breeden, and H. J. Metcalf, ''Home-built Nd-YAG laser for general laboratory use,'' Appl. Opt. **24**, 1899–1901 (1985).

[13]R. C. Hilborn, ''An inexpensive reliable, high power molecular nitrogen laser,'' Am. J. Phys. **44**, 1172–1176 (1976).

[14]R. S. Kunabenchi, M. R. Gorbal, and M. I. Savadatti, ''Simple nitrogen laser,'' Am. J. Phys. **50**, 568–569 (1982).

[15]M. Feldman, P. Lebow, F. Raab, and H. Metcalf, ''Improvements to a home-built nitrogen laser,'' Appl. Opt. **17**, 774–777 (1978).

[16]E. Armandillo and A. J. Kearsley, ''High-power nitrogen laser,'' Appl. Phys. Lett. **41**, 611–613 (1982). Of special note, they report peak power outputs in excess of 5 MW.

[17]G. J. Havrilla, R. B. Green, and T. O. Trask, ''Capacitor modification for the Schenck–Metcalf nitrogen laser,'' Appl. Opt. **17**, 3525–3527 (1978).

[18]A. Fried and C. W. Mathews, ''Ceramic capacitor failures in nitrogen lasers: A solution,'' Appl. Opt. **16**, 3077 (1977).

[19]Laser Resale, Inc., 54 Balcom Rd., Sudbury, MA 01776, 508-443-8484, http://www.laserresale.com

[20]OE Technologies, Box 703, LaMadera, NM 87539, 505-583-2482.

[21]T. W. Hänsch, ''Repetitively Pulsed Tunable Dye Laser for High Resolution Spectroscopy,'' Appl. Opt. **11**, 895–898 (1972).

[22]Eugene Hecht, *Optics* (Addison-Wesley, Reading, MA, 1987), p. 428.

[23]M. K. Iles, ''United Single-Pass Model of Linewidths in the Hänsch, Single- and Double-Grating Grazing-Incidence Dye Lasers,'' Appl. Opt. **20**, 985–988 (1981).

[24]An etalon is a Fabry–Perot interferometer with fixed mirrors, see any optics text, e.g., E. Hecht, *Optics* (Addison-Wesley, Reading, MA, 1987), pp. 368–371.

[25]B. S. Perkalskis and J. R. Freeman, ''Fabry-Perot interferometers for lecture demonstrations and laboratories,'' Am. J. Phys. **64**, 1210–1212 (1996).

[26]*Atomic, Molecular, & Optical Physics Handbook*, edited by G. W. F. Drake (AIP, Woodbury, NY, 1996), pp. 784–794.

[27]H. Weichel, W. A. Danne, and L. S. Pedrotti, ''Laser Safety in the Laboratory,'' Am. J. Phys. **42**, 1006–1013 (1974). Note: While this is an old article, it is still reasonably current and well worth posting in the laser laboratory.

[28]OSA Laser Safety Committee, ''Don't be ultraviolated!'' Opt. News **7**, 18–21 (1988).

[29]H. Moseley, ''Ultraviolet and laser radiation safety,'' Phys. Med. Biol. **39**, 1765–1799 (1994).

[30]Material Safety Data Sheets (MSDS) are available from the laser dye manufacturers. Dyes that cover the visible spectrum are available that have low biological hazard levels, e.g., Stilbene 420, Coumarin 481, Coumarin 540 A, Rhodamine 6G, and Kiton Red 620.

[31]K. Arnett, R. Anderson, and R. Alexander, ''Modern spectroscopy with a spectrometer by the optogalvanic effect,'' Am. J. Phys. **49**, 767–772 (1981).

[32]C. L. Schreiber, E. Y. Wong, and D. Johnston, ''Low-cost, high-resolution Ebert spectrographs for a teaching laboratory,'' Am. J. Phys. **39**, 1333–1336 (1971).

[33]Our measurements comparing a laser power meter with photodiode response at 337 and at 540 nm indicates that you can get reasonable efficiency estimates using a photodiode if you multiply the 337-nm photodiode reading by 4.1. This seems to take into account both the effects of the glass window and the declining responsivity of the silicon photodiode. N.B., This may be strongly dependent on your particular photodiode.

[34]R. Smith and L. F. DiMauro, Appl. Opt. **26**, 855–859 (1987).

RENORMALIZATION

[Renormalization is] just a stop-gap procedure. There must be some fundamental change in our ideas, probably a change just as fundamental as the passage from Bohr's orbit theory to quantum mechanics. When you get a number turning out to be infinite which ought to be finite, you should admit that there is something wrong with your equations, and not hope that you can get a good theory just by doctoring up that number.

Paul Adrien Maurice Dirac, in *A Question of Physics: Conversations in Physics and Biology*, conducted by Paul Buckley and F. David Peat (Routledge and Kegan Paul, London, 1979), p. 39.

This article is copyrighted as indicated in the article. Reuse of AAPT content is subject to the terms at: http://scitation.aip.org/termsconditions. Downloaded to IP: 158.104.100.45 On: Thu, 03 Sep 2015 22:53:57

2.10 W.M. Keck Observatory AO System

IOPscience

This site uses cookies. By continuing to use this site you agree to our use of cookies. To find out more, see our Privacy and Cookies policy.

The W. M. Keck Observatory Laser Guide Star Adaptive Optics System: Overview

Peter L. Wizinowich, David Le Mignant, Antonin H. Bouchez[1], Randy D. Campbell, Jason C. Y. Chin, Adam R. Contos[2], Marcos A. van Dam, Scott K. Hartman, Erik M. Johansson, Robert E. Lafon

Published 2006 February 9 • © 2006. The Astronomical Society of the Pacific. All rights reserved. Printed in U.S.A.

Publications of the Astronomical Society of the Pacific, Volume 118, Number 840

W. M. Keck Observatory, 65-1120 Mamalahoa Highway, Kamuela, HI 96743; peterw@keck.hawaii.edu

Lawrence Livermore National Laboratory, P.O. Box 808, Livermore, CA 94550

[1] Current address: Caltech Optical Observatories, Mail Code 105-24, California Institute of Technology, 1200 East California Boulevard, Pasadena, CA 91125.

[2] Current address: Ball Aerospace, 10 Longs Peak Drive, Broomfield, CO 80021.

[3] Current address: Center for Adaptive Optics, University of California, Santa Cruz, 1156 High Street, Santa Cruz, CA 95064.

Received 2005 September 12
Accepted 2005 October 31
Published 2006 February 9

Peter L. Wizinowich *et al* 2006 *PASP* **118** 297

https://doi.org/10.1086/499290

Buy this article in print

Abstract

The Keck Observatory began science observations with a laser guide star adaptive optics system, the first such system on an 8–10 m class telescope, in late 2004. This new capability greatly extends the scientific potential of the Keck II Telescope, allowing near–diffraction-limited observations in the near-infrared using natural guide stars as faint as 19th magnitude. This paper describes the conceptual approach and technical implementation followed for this system, including lessons learned, and provides an overview of the early science capabilities.

Export citation and abstract BibTeX RIS

1. INTRODUCTION

Adaptive optics (AO) systems have been in use on astronomical telescopes since the early 1990s (Graves et al. 1994; Rousset et al. 1994; Rigaut et al. 1998). From the beginning, astronomers recognized the limitations of AO due to the need to use relatively bright stars to measure the wave-front distortions introduced by Earth's atmosphere. To increase the very limited sky coverage of these systems, they have therefore looked for ways to create their own beacons using lasers. The most feasible of these approaches for very large telescopes is to use a sodium-wavelength laser to excite the sodium atoms in Earth's mesosphere (Foy & Labeyrie 1985; Thompson & Gardner 1987). Although experiments with various lasers have been performed at a number of observatories, only a few laser guide star (LGS) based science papers have been published (McCullough et al. 1995; Hackenberg et al. 2000; Perrin et al. 2004), and until recently only the Lick 3 m telescope sodium LGS system has been performing LGS observations on a regular basis (Max et al. 1997). The Lick system was joined in late 2004 by an operational sodium LGS system on the Keck II Telescope.

The W. M. Keck Observatory consists of two 10 m diameter optical/infrared telescopes separated by 85 m, located on the summit of Mauna Kea in Hawaii. Natural guide star (NGS) AO systems have been in operation on the Keck II and Keck I Telescopes since 1999 (Wizinowich et al. 2000a, 2000b) and 2000, respectively. The science instruments behind the AO system have included KCAM, a simple near-infrared imaging engineering camera; NIRSPEC, a near-infrared spectrograph (McLean et al. 1998); NIRC2, a near-infrared camera designed explicitly for AO (K. Matthews et al. 2006, in preparation); an interferometer that combines the light from both telescopes (Colavita et al. 2004); and OSIRIS, an OH-suppression infrared integral field spectrograph (Larkin et al. 2003).

The Keck II AO system was designed from the start to be an LGS system. The laser was fabricated by Lawrence Livermore National Laboratory (LLNL) and delivered in 1998 (Friedman et al. 1998) to a laboratory at Keck headquarters, where it was further engineered by a team of LLNL and Keck personnel. It was integrated with the telescope in 2001 in time for an end-of-the-year first projection of the laser onto the sky. This milestone was followed by continued laser and LGS AO development. The first closed-loop tests with the laser occurred in late 2003. Shared-risk science observations began in late 2004, and 30 LGS AO science nights have been allocated in the second half of 2005.

The nature and limitations of a sodium-wavelength LGS require numerous modifications with respect to an NGS-based AO system. Section 2 discusses these LGS AO issues and the conceptual approaches we chose to address them, as well as the technical implementation of the resulting LGS components. Section 3 describes the laser, associated operational issues, and the laser guide star. We then describe the LGS AO operations, including observing strategy (§ 4) and the early science capabilities (§ 5). Implementing the first LGS AO system on a large telescope has presented numerous challenges, and this paper attempts to share the lessons learned in this process. A separate paper (van Dam et al. 2006) describes the LGS AO system's performance and algorithms in more detail.

2. IMPLEMENTATION

In order to orient the reader, we first provide a schematic of the LGS AO control approach taken in the Keck system. We then review, at a schematic level, the LGS AO issues and the solutions chosen for the Keck system (somewhat as a perspective on historical development). Finally, we describe the physical implementation of the Keck system.

2.1. LGS AO Control

A schematic view of the major Keck LGS AO components is presented in Figure 1. The NGS and LGS light collected by the telescope are reflected off the tip-tilt mirror (TTM), the deformable mirror (DM), and the infrared (IR) transmissive dichroic. The infrared light is transmitted to the science camera. The sodium-wavelength light is transmitted through a sodium-transmissive dichroic to the wave-front sensor (WFS). Since the LGS is not at infinity, it comes to a focus after the NGS focus.

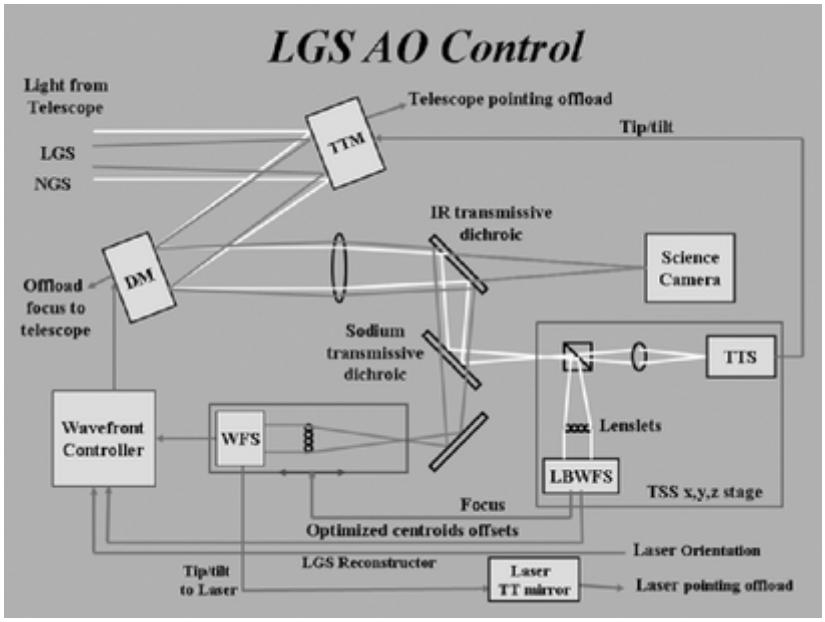

Fig. 1.— Schematic representation of the Keck LGS AO system components. The light from the telescope is reflected off a TTM and DM. The infrared light is transmitted through an IR-transmissive dichroic to the science instrument. The visible light from the NGS and LGS is reflected off this dichroic. The NGS light is reflected off a sodium-transmissive dichroic to a TTS and LBWFS mounted on an (x, y, z) TSS. The transmitted LGS light goes to a WFS mounted on a focus stage. The resulting control loops are described in the text.

The WFS is mounted on a translation stage to keep it conjugate to the sodium layer as a function of zenith angle. The tip-tilt error is used to drive the laser uplink TTM, which in turn offloads to a larger stroke mirror used for laser pointing corrections. The tip-tilt–removed centroid errors measured by the WFS go to the wave-front controller that drives the DM. The DM offloads its time-averaged focus to the telescope control system, which pistons the secondary mirror to compensate.

The visible light reflected off the sodium-transmissive dichroic goes to the tip-tilt sensor (TTS) and low-bandwidth wave-front sensor (LBWFS). A beam-splitter cube transmits 80% of the light to the TTS, since tip-tilt needs to be corrected at a high bandwidth, and reflects 20% to the LBWFS. The TTS and LBWFS are mounted on an (x, y, z)-translation stage (TSS) to acquire and track an off-axis NGS.

The tip-tilt error measured by the TTS is used to drive the TTM, which in turn offloads to the telescope pointing. The focus error measured by the LBWFS is used to keep the WFS conjugate to the sodium layer. The time-averaged centroid errors measured by the LBWFS are used to remove the LGS-induced aberrations by adjusting the WFS centroid offsets. The LGS reconstructor changes as a function of the laser orientation with respect to the WFS.

This last point about laser orientation deserves an explanatory background paragraph, since it is mentioned several times in the next section and is somewhat unique to Keck. In the Keck II case, the laser projects from the elevation ring of the telescope. As the telescope moves in elevation, the laser projector and telescope pupil change in orientation with respect to the fixed Nasmyth platform location of the AO system. In addition, the sky rotates with respect to the AO system as the telescope moves in azimuth and elevation. The first element on the AO bench is a derotator, which can be used to keep either the sky or the pupil fixed with respect to the AO system, but not both. In general, observers prefer to keep the science object orientation fixed on the science instrument, resulting in a changing orientation of the Keck pupil and laser on the WFS. Since the Keck pupil is an irregular hexagonal shape (due to its 36 hexagonal segments), we already had to solve the problem of a rotating pupil for NGS AO (Stomski & Shelton 2000). This is done by continually determining which WFS subapertures are illuminated, and building and loading new reconstructor matrices on this basis. The impact of a rotating off-axis laser projection is among the LGS AO issues addressed in the next section. The NGS and LGS reconstructors are discussed in van Dam et al. (2004) and (2006), respectively.

2.2. LGS AO Issues and Approach

An overview schematic of the LGS AO issues and the solutions we have chosen is shown in Figure 2.

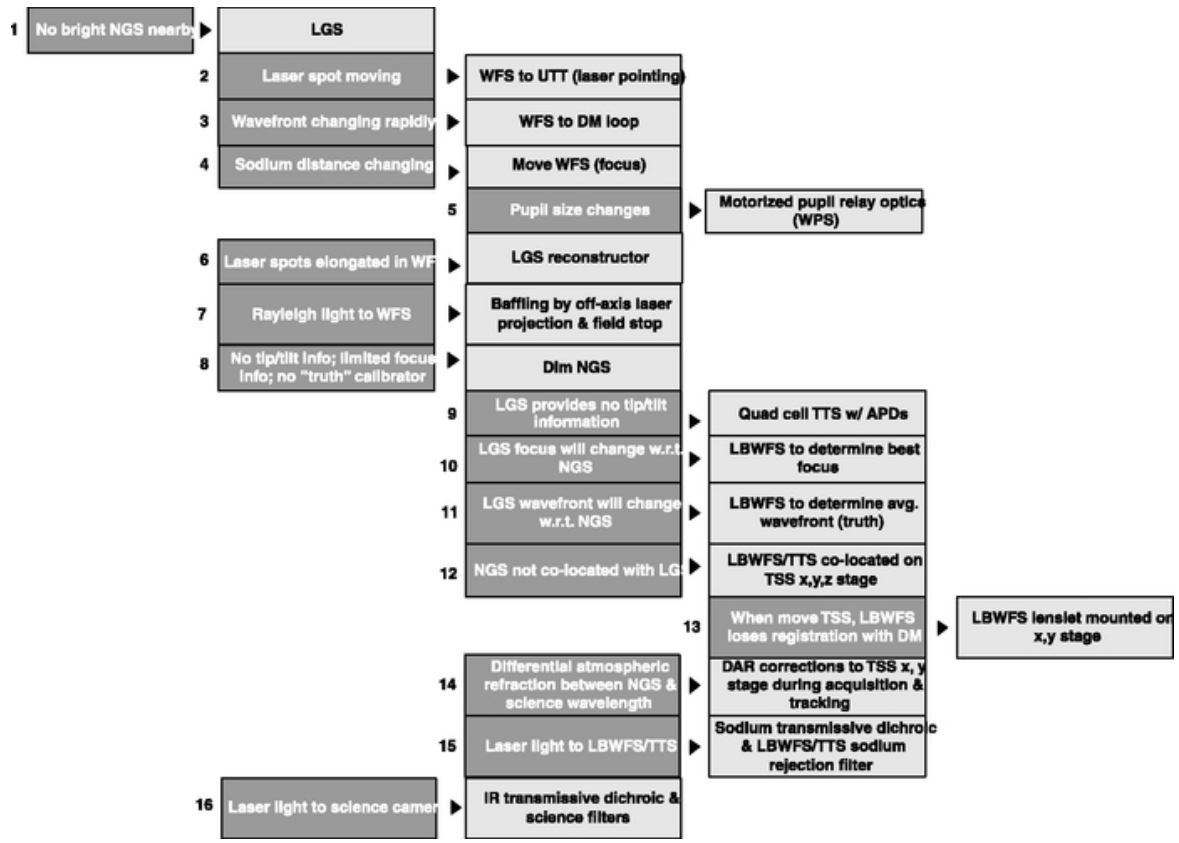

Fig. 2.— Solutions tree for LGS implementation issues. LGS-specific issues are shaded in dark gray below their associated parent topic, and their chosen solution is indicated with an arrow. Individual issues are called out by a number referenced in the text.

In NGS AO, the wave-front distortions introduced by the turbulence in Earth's atmosphere are measured using the light from a star or compact astronomical object. Since the atmosphere changes both temporally and spatially, the NGS must be bright and near the science target. For the Keck NGS AO systems, the NGS must be brighter than 14th magnitude and within 30" of the science target. This limits NGS AO observations to only a small fraction of the sky. The lack of a bright nearby NGS for a hypothetical science target is shown as item 1 in Figure 2. One solution is to use an LGS, specifically a sodium-wavelength LGS in our case.

As shown in Figure 2, there are complications introduced when using an LGS.

Item 2.— The laser spot moves on the sky, due to tilt introduced in the upward path by a combination of atmospheric turbulence, laser launch-tube flexure, telescope vibrations, and wind shake. To overcome this LGS spot motion, the laser launch

optics includes a tip-tilt mirror (referred to as uplink tip-tilt, or UTT) to stabilize laser pointing. The UTT error signal is provided by the WFS, which observes the LGS light. The Keck WFS is a high-bandwidth (up to 670 Hz) Shack-Hartmann system with 20 subapertures across the Keck primary mirror.

Item 3.— Rapid atmospheric turbulence–induced changes in the wave front are corrected by changing the shape of a DM using the tip-tilt–removed wave front measured by this WFS, in the same way as for NGS AO.

Item 4.— In NGS mode, the WFS is located in the same focal plane as the science instrument (i.e., conjugate to infinity), which ensures that the WFS drives the DM to maintain focus on the science instrument. In LGS mode, the WFS needs to be conjugate to the sodium layer so that the LGS is in focus on the WFS. As the telescope moves away from the zenith, the distance to the sodium layer increases, and the WFS focus must be moved back toward the NGS focus to stay conjugate to the sodium layer. The required focus shift as a function of zenith angle ξ is given by

$$Z(h, \xi) = fh/(h - f\cos\xi) - f = (f^2\cos\xi)/(h - f\cos\xi), \tag{1}$$

where h is the height of the sodium layer above the telescope at zenith, and f is the focal length of the telescope (f = 150 m for Keck). For h = 90 km, the Keck WFS focus shift varies from 250 mm at the zenith to 125 mm at a zenith angle of 60°. To avoid having the H-band Strehl ratio degraded by more than 10%, the focus must be maintained to an accuracy of 0.17 mm. The approach taken in the Keck system was to mount the WFS on a focus stage that tracks as a function of the zenith angle.

Item 5.— Translating the WFS in focus also changes the distance to the pupil (i.e., the DM). To compensate, one of the elements of the WFS pupil relay optics is translated. This maintains the pupil size on the WFS lenslet array.

Item 6.— In NGS AO, the reference beacon imaged in each WFS subaperture is identical, regardless of pupil location. In LGS AO, however, each subaperture sees an elongated image of the approximately 10–15 km thick layer of sodium illuminated by the laser. This is due to perspective elongation as one moves off the axis of the laser projection telescope. The elongation is a function of the distance off the laser projector axis and is in the direction of the laser projector. This is particularly bad in the Keck II laser implementation, since the laser projector is located on the side of the telescope. The subaperture on the far side of the telescope from the projector (~12 m from the projector) exhibits an elongation as long as 3″ for a 10 km thick layer at an altitude of 90 km. Figure 3 (*middle*) shows an acquisition camera image of this LGS elongation versus distance obtained by unstacking the 36 primary-mirror segments of the Keck Telescope; the bright spot on the right side of this image is the Rayleigh-scattered light from air molecules in the lower atmosphere, indicating the side where the laser projector is located. This elongation introduces several challenges. One is that the optimal (x, y) gains for each subaperture are functions of the length and direction of the elongation, and the other is that these gains change as the pupil (and hence laser projector) rotates. This gain versus position correction is handled in the LGS wave-front reconstructor, and the reconstructor is updated as the telescope pupil rotates with respect to the AO system. The LGS reconstructor algorithm takes two inputs to estimate spot size in each subaperture: the FWHM of the laser spot as seen from near the launch telescope, and the maximum elongation observed at the far edge of the pupil. Both of these are measured nightly from acquisition camera images of the unstacked primary-mirror segments. Projecting the laser from behind the secondary mirror instead of from the side of the telescope would have considerably reduced the complexity of this issue (and item 11 below), since the magnitude of the elongation would be halved and the impact of pupil rotation could be negligible.

Item 7.— The Rayleigh-scattered light could contaminate the measurements made by the WFS if it reached this sensor. The Rayleigh light is separated from the LGS light due to the off-axis projection of the laser, and this off-axis Rayleigh light is then blocked by the field stop in front of the WFS.

Item 8.— Some critical information cannot be obtained from the LGS. This information can be provided by a faint NGS.

Item 9.— Unfortunately, the LGS does not provide tip-tilt information for the science object, since the laser is deflected in tip and tilt along both its upward and downward paths. A separate TTS observing an NGS can be used to provide this tip-tilt information. NGSs as faint as 19th magnitude can be used with the Keck system's TTS. The error measured by this sensor is used to drive a fast TTM.

Item 10.— A change in the altitude of the sodium layer looks like a focus change to the WFS and is therefore applied to the DM. An LBWFS aimed at the NGS that is being used for tip-tilt is employed to sense this error. The WFS focus stage position is adjusted to drive the time-averaged focus measured by the LBWFS to zero. The new focus-stage position is then used to reestimate the sodium layer altitude to optimize the focus-stage tracking rate (Summers et al. 2004).

Item 11.— The wave front measured by the WFS is different when an LGS is used than when an NGS is used. In particular, the LGS elongation mentioned under item 6 above results in the measurement of aberrations that one does not want to apply to the DM. These are referred to as semistatic, since they change as the sodium layer thickness or structure changes, as the telescope elevation changes, and as the telescope pupil (and hence laser projector) rotates. In the case of Keck, a LBWFS is used as a truth sensor to correct for these aberrations. The LBWFS determines what centroid offsets should optimally be applied to each subaperture of the fast WFS observing the LGS. The bandwidth of the LBWFS is limited by the magnitude of the available NGS to an exposure time of tens of seconds to a couple of minutes. A model of the LGS aberrations can be used to provide higher bandwidth corrections when the NGS is too faint or when the pupil is rotating more rapidly than can be compensated for by the LBWFS.

Item 12.— The LGS is normally pointed at the science object somewhere in the field of view of the science camera. The NGS can be separated from the science object by as much as about 60″, due to the large isokinetic angle for tip-tilt correction. In the Keck system, the TTS and LBWFS are located on a three-axis TSS to allow off-axis acquisition of this NGS. Focus tracking versus field position is automatically provided by one of these axes to compensate for the curvature of

the focal plane. This axis also provides focus adjustment to match the focal position for different science instruments.

Item 13.— Translation of the LBWFS around the field to acquire the NGS results in a misregistration of the LBWFS's lenslets with respect to the DM (by as much as 0.58 subapertures at the edge of the field). The lenslets are mounted on an (x, y)-translation stage to maintain registration with the DM actuators.

Item 14.— Acquisition and tracking of the NGS on the LBWFS and TTS includes compensation for differential atmospheric refraction (DAR) between the wavelength observed by the science instrument and the tip-tilt sensor, in order to accurately acquire and maintain the science object's position on the science instrument. DAR compensation is a function of the telescope's elevation, the color of the NGS, and the wavelength of the science observation (Stomski et al. 2003).

Item 15.— Due to the faintness of the NGS, the complete rejection of the sodium light becomes crucial. A sodium-transmissive, visible-reflecting dichroic beam splitter is used to reflect the NGS light to the TTS and LBWFS (the transmitted light goes to the WFS). This provides partial rejection. In addition, a narrowband rejection filter (centered on the 589.3 nm laser line) is located in front of the TTS and LBWFS

Item 16.— In the case of infrared science instruments, the sodium light can be rejected through the use of an IR-transmissive dichroic and the science instrument filters and detectors.

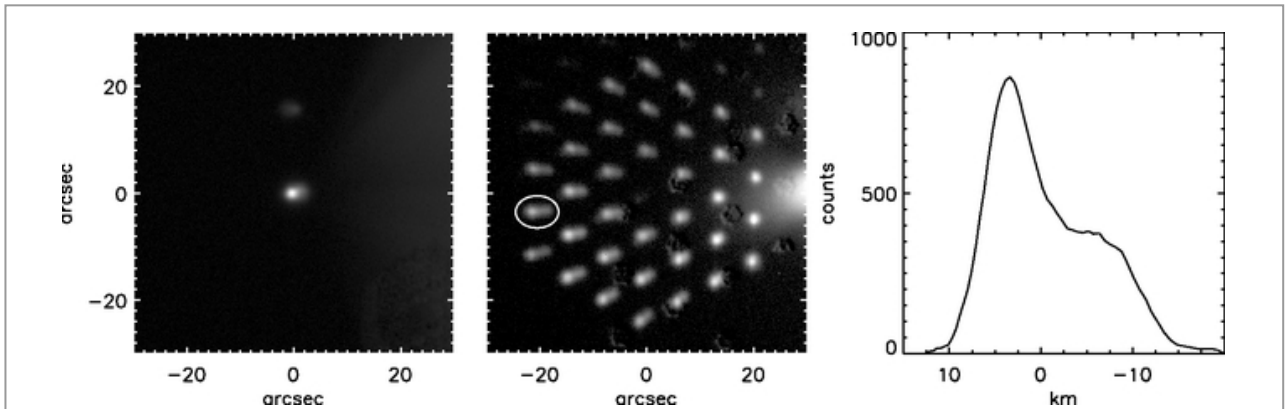

Fig. 3.— Acquisition camera images (*left and middle*; 60″ × 60″) of the Keck LGS at zenith. *Left*: LGS image with a FWHM of 1″.6 × 2″.0 and an equivalent *V* magnitude of 9.8. *Middle*: LGS image taken with the 36 primary-mirror segments unstacked. The laser projector is on the right side of the telescope in these images; the side from which the Rayleigh-scattered light can also be seen. The individual segment image closest to the projector can have a FWHM as small as 1″.0, while the segment images further away can be seen to be elongated toward the projector. The circled segment image in the middle panel was used to produce the relative density structure vs. altitude plot for the sodium layer (*right*); a 35 km altitude range is shown.

2.3. Optomechanical Implementation

The NGS AO facilities are located on the left Nasmyth platforms of the Keck Telescopes at the f/15 focus. The entire facility is enclosed in the thermally insulated enclosure shown in Figure 4, with one room for the AO bench and science instruments, and a second room for the electronics racks.

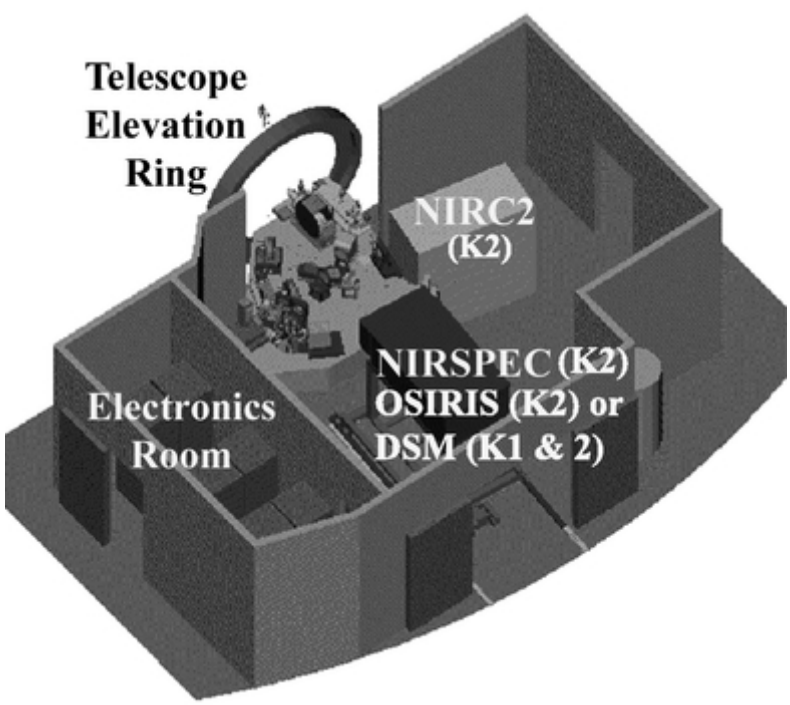

Fig. 4.— Schematic view of the Keck AO enclosure, located on the left Nasmyth platform of the telescope, with its roof removed. Light from the telescope enters the AO bench through the telescope elevation ring.

Science instruments can be positioned at two locations next to the AO bench as shown in Figure 4. NIRC2 is located at a fixed position, while NIRSPEC, OSIRIS, and the dual star module (DSM), which feeds the interferometer in the basement between the two Keck Telescopes, move in on rails to kinematic defining points located beside the AO bench.

Figure 5 provides a top-view schematic of the AO bench. The light from the telescope comes to a focus just inside the derotator (labeled 1 on Fig. 5). The derotator, which consists of three flat mirrors, can be used to keep either the image or the pupil fixed. The next element (2) is a fast tip-tilt mirror consisting of a 203 mm diameter silicon carbide mirror with three piezoelectric actuators. The beam continues to diverge to an off-axis parabola (3) that collimates the light and reimages the primary mirror of the telescope onto the DM (4). The Xinetics, Inc., DM has 349 electrostrictive actuators on a 7 mm spacing, corresponding to 56 cm spacing on the primary mirror. The second off-axis parabola (6) reconverges the light with the same focal ratio and exit pupil location as initially provided by the telescope. The light is split at a visible-reflecting, IR-transmitting dichroic (7). The infrared light (>1 μm wavelength) proceeds either directly to NIRC2 or off a fold mirror (9) to OSIRIS, or off another fold mirror (10) to NIRSPEC. Since NIRSPEC was designed as a seeing-limited instrument, a set of reflective reimaging optics (30–34) was implemented to provide a factor of 10 magnification to take advantage of the increased angular resolution behind AO while maintaining the pupil and image position within NIRSPEC. The light to the DSM that feeds the interferometer is picked off in collimated space by an IR-reflective, visible-transmitting dichroic (5).

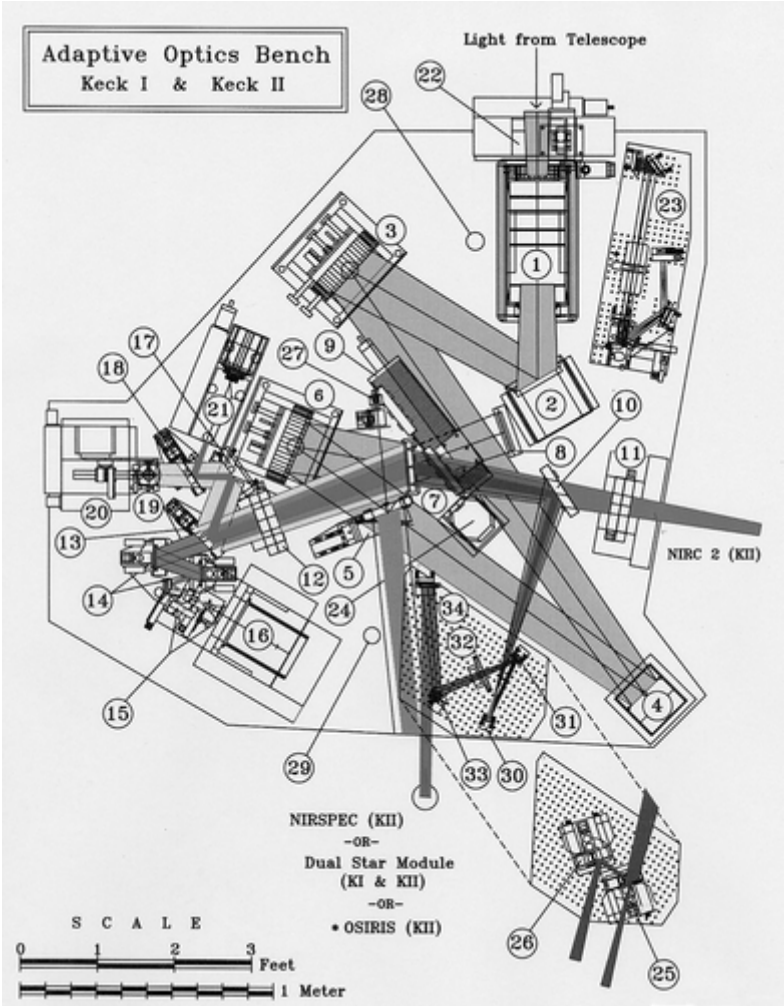

Fig. 5.— Schematic aerial view of the AO optics bench. The numbers are referenced in the text.

The visible-reflecting dichroic (7) sends the visible light toward the various wave-front sensors. A translation stage (13) allows the selection of either a 4% reflective beam splitter for NGS mode or a visible-reflecting, sodium-transmitting dichroic for LGS mode. The transmitted light proceeds to a pair of field-steering mirrors (14), which select an object within the available field of view (up to 40″ off-axis) and direct it down the axis of the Shack-Hartman wave-front sensor optics (15) and camera (16). These optics consist of a field stop, transmissive optics that reimage the DM onto an array of 200 μm square lenslets, and transmissive optics that relay and demagnify the images from the lenslets onto the Adaptive Optics Associates camera. The MIT/LL CCD consists of 64 × 64, 21 μm square pixels. The image from each lenslet is reimaged onto 2 × 2 pixels, with 1 pixel between subapertures. The entire WFS assembly, from the field stop to the camera, is mounted on a translation stage to maintain conjugation to the sodium layer.

A translation stage (18) allows a mirror to be inserted to feed the light toward the 2' diameter field of view of the acquisition camera (21). In LGS mode, this mirror is translated out of the beam, and the NGS light is sent to the LBWFS (19) and the TTS (20), mounted on an (x, y, z)-translation stage, as shown in Figure 6. STRAP is a quadrant avalanche photodiode unit manufactured by Microgate. The light to STRAP is collimated through a filter wheel and then reimaged at a slower focal ratio (f/37.5) onto the quad lenslet of STRAP. After reflection off an 80:20 beam splitter, light heading toward the LBWFS goes through a lens and field stop mounted in a lens-tube assembly. The light is then collimated before passing through a lenslet array mounted on an (x, y) motorized stage. The lenslets are imaged on a Photometrics 512 × 512 CCD detector. The LBWFS lenslets are registered to the DM actuators in a pattern identical to the WFS lenslets, but with 16 × 16 pixels per subaperture instead of 2 × 2 pixels.

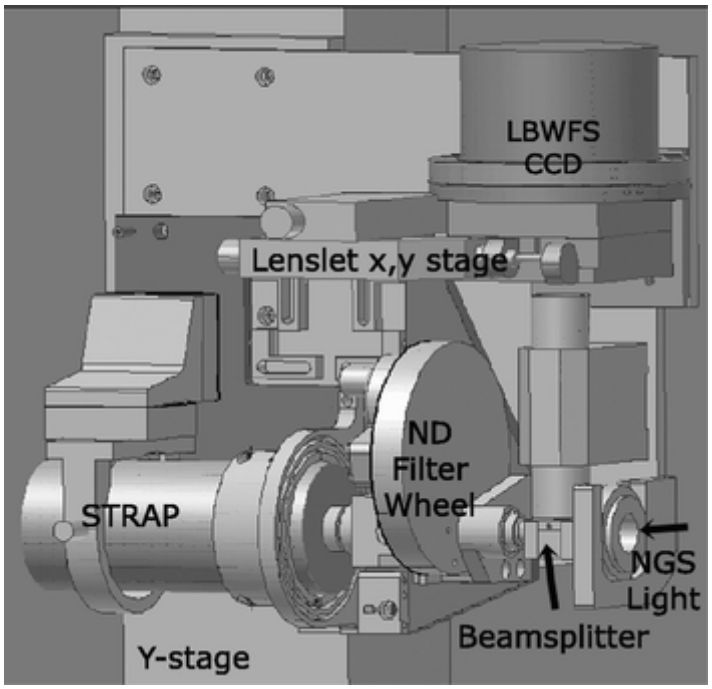

Fig. 6.— CAD drawing of the STRAP tip-tilt sensor and LBWFS.

3. LASER GUIDE STAR

3.1. Laser System

A schematic of the laser system location is shown in Figure 7. A thermally insulated laser room on the dome floor houses six flash-lamp–pumped, frequency-doubled Nd-YAG lasers and a dye master oscillator (DMO), plus associated hardware and safety systems. The DMO is narrowly tuned to the center of the sodium doublet wavelength. The DMO's output is broadened across the doublet with a pair of electro-optic phase modulators and then coupled into a single-mode fiber. The single-mode fiber provides the seed light to a table on the side of the telescope, where it passes through two stages of dye amplification (preamplifier and amplifier stages). The YAG lasers, coupled through multimode fibers, are used to pump the various dye laser and amplification stages. These lasers are *Q*-switched at either 13 or 26 kHz, with pulse durations of 150 ns, and each produces about 40 W of output power. The 26 kHz versions are used to pump the DMO and preamplifier. The four 13 kHz versions, two of which are time delayed to produce an overall 26 kHz pulse rate, are used to pump the amplifier.

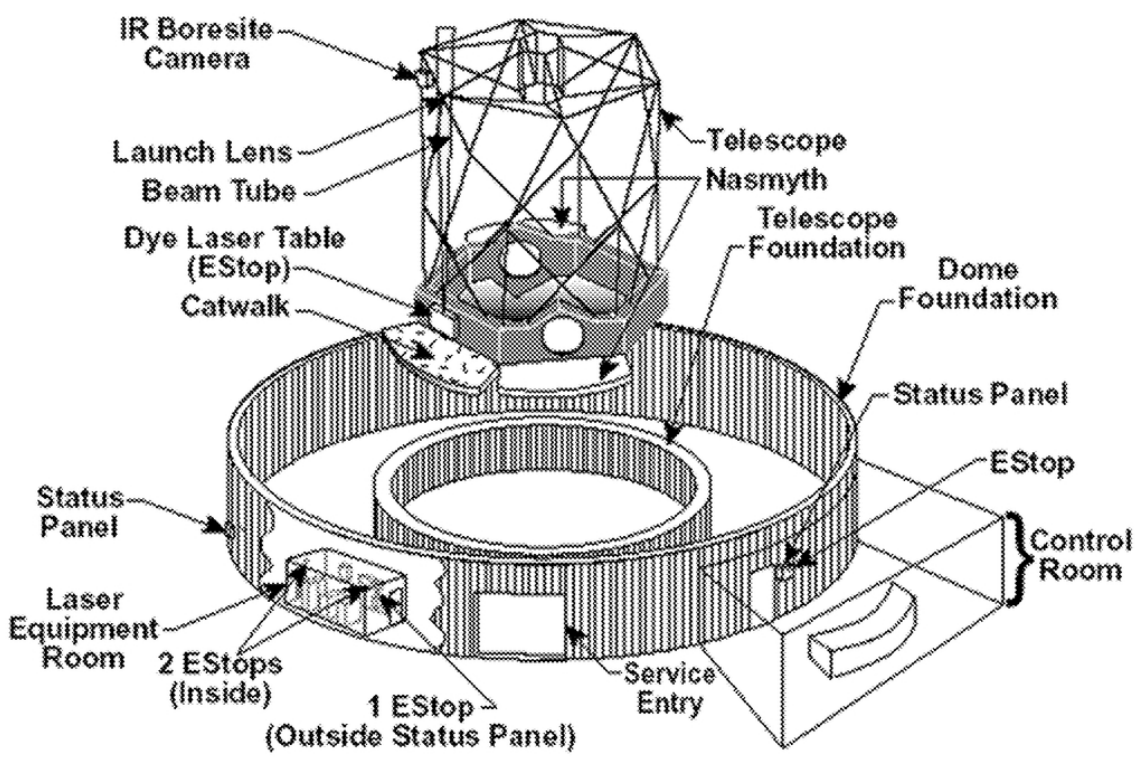

Fig. 7.— Schematic of the location of the laser equipment room on the dome floor, the dye laser table, and the projection telescope (beam tube and launch lens), and the IR boresight camera on the side of the telescope.

A 1.2 × 1.8 m laser table, shown in Figure 8, is located vertically in an enclosure on the elevation ring of the telescope. In addition to the two stages of dye amplifiers, a significant number of transport and formatting optics, and the first element of the projection telescope, this table contains several alignment and diagnostic tools. These tools include power meters, a power-in-the-bucket camera, and pointing and centering cameras. The last element on the laser table is a pointing mirror that is used to center the laser with respect to the science object and to compensate for tilt changes due to flexure and the distance to the sodium layer (Summers et al. 2004).

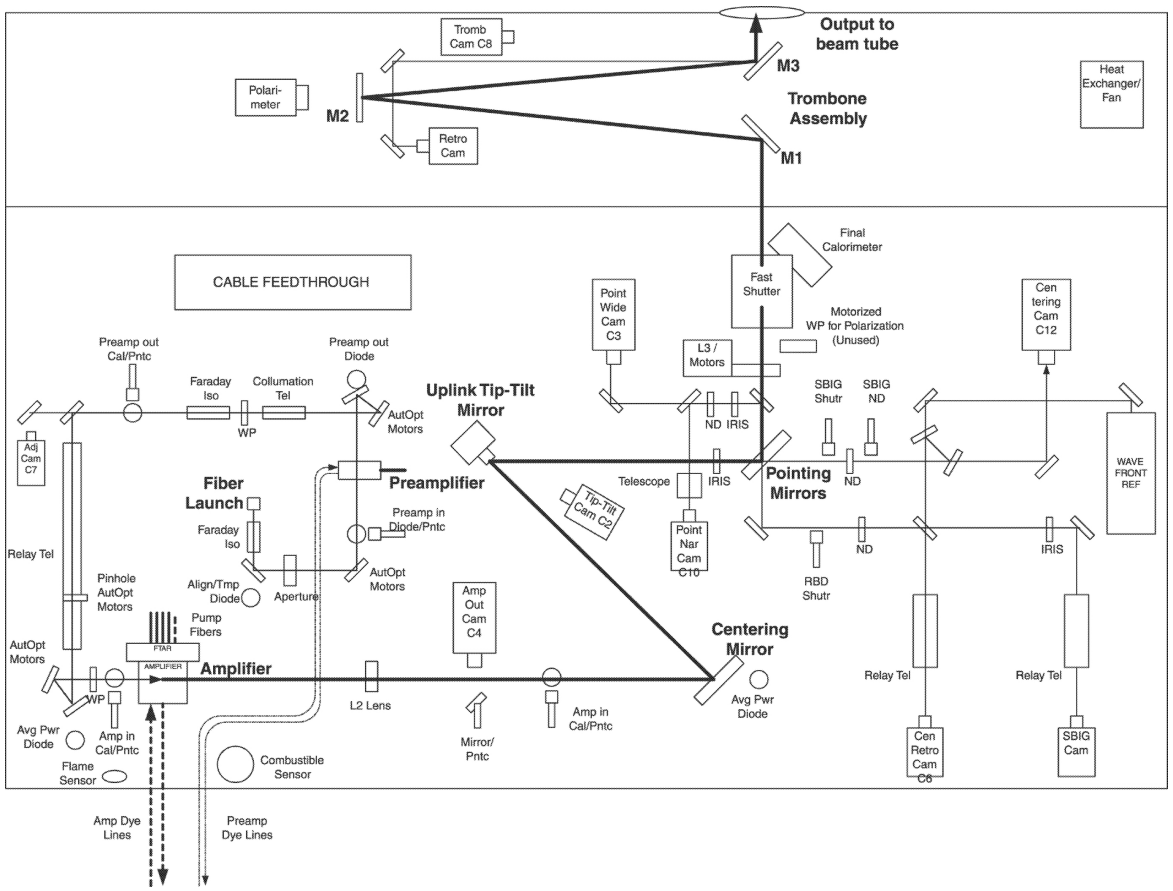

Fig. 8.— Schematic view of the 1.2 × 1.8 m laser table and the trombone assembly mounted on the elevation ring of the telescope. The dark solid line shows the optical path from the laser amplifier cell off of the centering mirror, UTT mirror, and pointing mirror, through a three-mirror trombone assembly to the output up the beam tube. A portion of the light is split off at or near the pointing mirror to several diagnostics cameras. The light path prior to the amplifier begins at the fiber launch (a single-mode fiber from the dye master oscillator on the dome floor) and passes through the preamplifier and various formatting optics.

The final output of the dye laser is sent to the sky through a projection telescope with a 50 cm diameter output lens, mounted to the side of the telescope. Both the laser table and the projection telescope move with the telescope in azimuth and elevation. An extensive programmable logic control safety system is in place to protect personnel and the laser itself.

The major weak point of the current laser system is its overall complexity (nine lasers in total). Failure points include the YAGs, especially the use of flash lamps, and the inherent difficulties of dye lasers, including many dye-cell burns in our early days. The wall-plug efficiency is also low, with ~50 kW producing ~12 W of output power. Sodium-wavelength solid-state lasers, which were unavailable when we started this project, are much less complex and should be far more efficient and reliable.

3.2. Laser Operation and Coordination

Safety systems are in place to protect aircraft and satellites. Our Federal Aviation Administration–approved approach to aircraft safety is to have two spotters outside during all laser operations, with switches to shutter the laser. We also have an IR camera boresighted to the laser that will automatically shutter the laser in the event of aircraft detection. Given Hawaii's location in the middle of the Pacific, we have only had to shutter the laser for an aircraft a couple of times. Our longer term plans include the implementation of a visible wide-field camera system for aircraft detection, and possibly the use of a Hawaii-wide radar feed to alleviate the need for spotters.

Prior to each laser observing run, a list of targets and their observation times is faxed to the Laser Clearinghouse at the US Space Control Center. The Space Control Center faxes back a list of any required blackout periods, to avoid illuminating satellites. This has had minimal impact on our nighttime operations to date, since blackout periods have been rare, but it requires careful preobserving planning.

A laser traffic control system (LTCS) is also in place to ensure that the laser does not contaminate the observations of other telescopes (Summers et al. 2003). All the potentially affected telescopes on Mauna Kea provide their current pointing coordinates to the LTCS via a URL, along with additional parameters such as field of view, and the laser is automatically shuttered by the LTCS when the laser passes through their field of view. The surface brightness of the Keck laser measured by the Subaru Telescope at elevation angles between

45° and 60° was found to be relatively low, roughly equivalent to 19.5 mag arcsec^{-2}; however, the impact could be significant if the intersection were to occur near the LGS itself (Hayano et al. 2003).

See Wizinowich et al. (1998) for a discussion of the coordination and use of laser beacons on Mauna Kea.

3.3. Laser Guide Star

The performance of the LGS AO system depends on the power and beam quality of the laser and the density and structure of the sodium layer. The laser is typically operated at an output power of between 12 and 14 W. Depending on the sodium density, this generates an LGS with an equivalent *V* magnitude of typically 9.5 to 10.5 mag at the zenith (or ~140 to 55 photons s^{-1} cm^{-2}). The return decreases with zenith angle, due to the resulting increase in the distance to the sodium layer and the amount of Rayleigh scatter.

The FWHM of the LGS image as seen by the subapertures closest to the laser launch telescope is typically 1″.0 to 1″.4. As seen in Figure 3, the images appear elongated as the subapertures become farther away from the launch telescope. This elongation has been observed to be 3″.4 FWHM for a sodium layer thickness of approximately 15 km. A fairly commonly observed structure for the sodium layer versus altitude can also be seen in the right panel of Figure 3.

4. OBSERVING OPERATIONS

4.1. NGS Operations

During NGS science operations, the astronomer operates the science instrument from the remote operations room at Keck Observatory's headquarters, and the observing assistant (OA) operates the AO system from the telescope control room on Mauna Kea. The daytime AO calibrations take less than 30 minutes and include calibrating the DM-to-lenslet registration and the non–common-path aberrations between the science instrument and the WFS optical paths. These are performed by a support astronomer using a set of calibration tools. A more thorough set of AO calibrations (WFS lenslet centering, telescope pointing origins, and image sharpening on the science instrument) is performed by an AO expert prior to the first night of an observing run.

At dusk, the OA brings up the AO observing tools and runs a script that automatically configures the AO system for the specific science instrument and telescope (Keck I or II). The OA also acquires each new target before turning over control to the astronomer. The automated tools perform the AO acquisition using the *V* and B - V magnitudes for the NGS provided by the astronomer's star list. The DAR-compensation tool positions the science object at the desired location on the science instrument by compensating for DAR with the field-steering mirrors (FSMs) that feed the WFS. The autosetting tool commands the AO subsystems and the telescope to obtain sky backgrounds and set the WFS frame rate, the tip-tilt and DM gains, and if necessary (for bright objects), the camera gain and WFS neutral density filters; it iterates once, if appropriate, using the photon flux measured by the WFS to find the optimal settings. The OA monitors the status and health of the AO system with dedicated tools that also automatically recover from faults. After slewing to a new target, AO acquisition takes between 30 and 90 s, depending on the object brightness and the sky transparency conditions.

Once the AO acquisition is complete, the astronomer selects the science instrument configuration, including the rotator mode and position angle, and then controls the observing sequence using the science instrument user interfaces. Many possible dithering scripts that are common to near-infrared imaging and spectroscopic observations are commanded from the science instrument user interface. A handshake protocol is used to automatically coordinate the telescope and AO system during these dithers. This includes opening the AO loops, repointing the telescope and FSMs, and closing the AO loops.

The main observing-time overheads in NGS AO observing are telescope slew, telescope fine-acquisition on target (<2 minutes), AO acquisition (90 s), and AO/telescope/instrument handshaking during dither (8–10 s per dither command). When using NIRC2, the NIRC2 setup (20 s for filter/camera moves) and readout (~8 s frame^{-1}) times also impact observing efficiency. Some specific observing modes, such as coronagraphy and spectroscopy, require more setup time to center the target with a 10 mas accuracy behind the focal mask or on the spectroscopic slit. The observing efficiency throughout an AO night ranges from 60% (1–2.5 μm wavelength deep AO imaging) to 30% (survey-mode observing, or 3–5 μm observing that requires lots of frames and dither).

4.2. LGS Operations

LGS AO observing preparations currently start a week prior to an observing run, with a meeting between the support astronomer and the observers. A Web page has been set up to support observation planning.[4] This includes a description of the system and the observing procedures. Also available are software tools for finding suitable NGSs, supporting the generation of star lists, and planning for off-axis observations. All science targets are reviewed for technical feasibility with the support astronomer. Prior to observing, the astronomer also becomes acquainted with the science camera and the specific LGS dithering scripts.

Supporting LGS AO represents a significant load on the Observatory. The minimal LGS-specific operation crew for an observing night includes a laser technician to start up the laser in the afternoon and monitor the laser and LTCS during the early evening, a second laser technician to monitor these systems through the remainder of the night, an LGS AO operator, a support astronomer to monitor and optimize the LGS AO system, and a team of aircraft spotters. This is in addition to an OA who operates the telescope, and a support astronomer for the science instrument. Ultimately, we plan to reduce the LGS-specific operations crew to an afternoon laser technician and a nighttime LGS AO operator. This will be done by implementing automated systems for aircraft detection and laser system monitoring, transferring some responsibilities to the OA, and training the LGS AO operator in system optimization.

Prior to an observing run, about 2 hr of afternoon NGS and LGS AO calibrations and system checkout are performed on the system. Daily start-up and checks of the laser system by a technician take 2 to 3 hr, with a full day of alignments and checks on the first day of the run. The laser also requires considerable routine maintenance and recovery from component failures.

An LGS operator is currently required to operate the LGS system for observing. The long-term plan is to have the OA operate the LGS AO system, as is done for NGS AO observing. So far, one OA has been trained as an LGS AO operator.

Beginning at dusk, a 40 minute routine test procedure is performed to check out the AO system in NGS mode, measure the seeing, acquire and characterize the LGS at zenith, and check out and characterize the AO system in LGS mode on a fairly bright star (R-band magnitude of ~10). Laser propagation is restricted to between 12° twilight after sunset and before dawn.

Acquisition of a new target in LGS AO mode is somewhat complex, due to the requirement that two properties of the sodium layer must be determined before science integrations can begin. One is the altitude of the layer, and the other is the effect of the layer's structure and thickness on the wave front measured by the WFS. Both of these are determined iteratively by observing the wave front of an NGS with the LBWFS while locked on the LGS with the WFS.

The following is a typical LGS AO acquisition sequence: the OA slews to the science target as instructed by the observer and positions the tip-tilt reference NGS on the acquisition camera at a location that coincides with the desired position on the science camera. Using the color information of the star, DAR correction is automatically used to position the STRAP/LBWFS stage for NGS acquisition.

The LGS operator then takes over and, similarly to NGS AO acquisition, uses fully automated scripts to set the subsystem parameters, interact with the telescope for recording background for the various sensors, and acquire the NGS and offset to the science target. The *R*-band magnitude of the NGS is used to set up the LBWFS binning and integration time and the TTS gain and integration time. The tip-tilt loop is closed on the NGS. The laser is projected toward the NGS, and the DM loop is closed on the LGS. LBWFS measurements are then begun on the NGS. The LBWFS measurements are used to (1) optimize the WFS centroids (to correct for the varying extension of the LGS spot across the telescope pupil) and (2) focus the WFS (to be conjugate to the sodium altitude). Since LBWFS integrations are necessarily very long (~120 s) when using a faint NGS ($R > 18$ mag), the initial determination of these properties may be more efficiently done on a nearby bright star prior to acquisition of the science target's NGS. Each LBWFS wave-front measurement is used to iteratively converge on the correct WFS centroid offsets and focus until the measured rms wave-front error has fallen below 200 nm (usually three to five LBWFS integrations). The LGS AO performance is optimized and monitored during the observations. The tip-tilt and DM loop gains and bandwidths can be manually adjusted using an optimization tool that analyzes saved WFS and STRAP telemetry data. If appropriate, the telescope is then offset to the science target. This automatically opens the tip-tilt and LBWFS loops, repoints the telescope and the TTS/LBWFS stage, and recloses these two loops.

The entire acquisition takes 5 minutes for stars brighter than 16 mag, and up to 15 minutes for faint stars (19 mag) or objects that require manual tuning during acquisition (e.g., extended targets with high-intensity backgrounds, such as M31).

Control is then handed back to the astronomer to begin science observations. At the start of an observing sequence, typically both the LGS and the science target are positioned at the center of the science camera. During dithering scripts, the astronomer has the option of leaving the LGS fixed at the center of the science camera field or on top of the science object when the science object is repositioned on the science instrument. In the latter case, if the DM loop is initially closed, then repointing the telescope will automatically open the DM and uplink tip-tilt loops, reposition the laser pointing mirror and the WFS FSMs, and reclose the loops. If the TTS loop is closed, then repointing the telescope will always open the TTS and LBWFS loops, reposition the STRAP/LBWFS stage to reacquire the NGS with DAR corrections, and reclose these loops.

5. THE SCIENCE FACILITY

5.1. NGS Science Capability

The performance of the Keck II NGS AO system is reported in van Dam et al. (2004). The achieved on-axis *H*-band Strehl ratio varies from 0.4 for stars brighter than V = 9 to 0.1 for V = 14. NGSs can be used as far off-axis as 40″.

Keck NGS AO science output has included the publication of 74 refereed science papers as of 2005 October, including seven papers with the interferometer. Keck Observatory staff maintain a bibliography of refereed Keck AO science papers.[5] The mix of these papers is 31% planetary, 54% Galactic, and 15% extragalactic. Solar system science has included observations of planets, especially Neptune and Uranus, moons of planets such as Io and Titan, and asteroids. One feature that has made the Keck II system especially suitable for planetary science is that the WFS can close on objects as large as 4″ in diameter. Galactic science has included companion searches and orbits, circumstellar disks, pre–planetary nebulae, and astrometric and spectroscopic measurements of the stars orbiting the black hole at the center of our Galaxy. Extragalactic science has been limited to faint galaxies near bright stars and galaxies with bright cores, a limitation that has been dramatically reduced with LGS AO.

5.2. LGS Science

5.2.1. Science Demonstration Program

An LGS engineering science program was implemented to test and demonstrate the most challenging observing modes in a realistic way, and to provide an opportunity for early scientific use of the system. Projects spanning planetary, Galactic, and extragalactic astronomy were proposed by members of the Keck user community, and the observations were performed by the Keck AO engineering team during commissioning nights.

Initial engineering science projects included observations of the HK Tau binary disk system during our first closed-loop demonstration in 2003 September, and observations of the Egg pre–planetary nebula in 2004 June (Bouchez et al. 2004). The angular resolutions of the Egg Nebula images are 3 to 4 times higher than that achieved with NICMOS on the *Hubble Space Telescope*.

The Galactic center was observed for 1.5 hr in K' and L' in 2004 July for the primary purpose of comparing LGS AO performance to previous NGS AO data (Ghez et al. 2005). The improvement in performance was dramatic, as shown in Figure 9. In addition, an $80'' \times 80''$ wide-field mosaic in He I and H_2 (1–0) of the region surrounding the Galactic center was also acquired on the same night, in a total observing time of 0.3 hr. These images have provided an excellent demonstration of the wide-field capabilities of the LGS AO system. Since the laser can remain at the center of each element of the mosaic, and the isokinetic angle for the tip-tilt star is large, the image quality remains essentially constant over the entire field.

Observations of the CATS (Center for Adaptive Optics Treasury Survey) fields were proposed to compare LGS and NGS performance on faint extragalactic targets, and to target particularly interesting galaxies (*Chandra* sources and high-redshift candidates) in previously inaccessible CATS fields. A field near guide star GOODS-S19 was observed for 3 hr in 2004 October. The resulting images of merging galaxies have been published in Melbourne et al. (2005).

Solar system engineering science projects have included measuring the system mass of binary Trojan asteroids (Marchis et al. 2005) and Kuiper Belt objects (Brown et al. 2005). Additional projects have included a search for brown dwarf binaries, and images of the Andromeda galaxy shown in Figure 10.

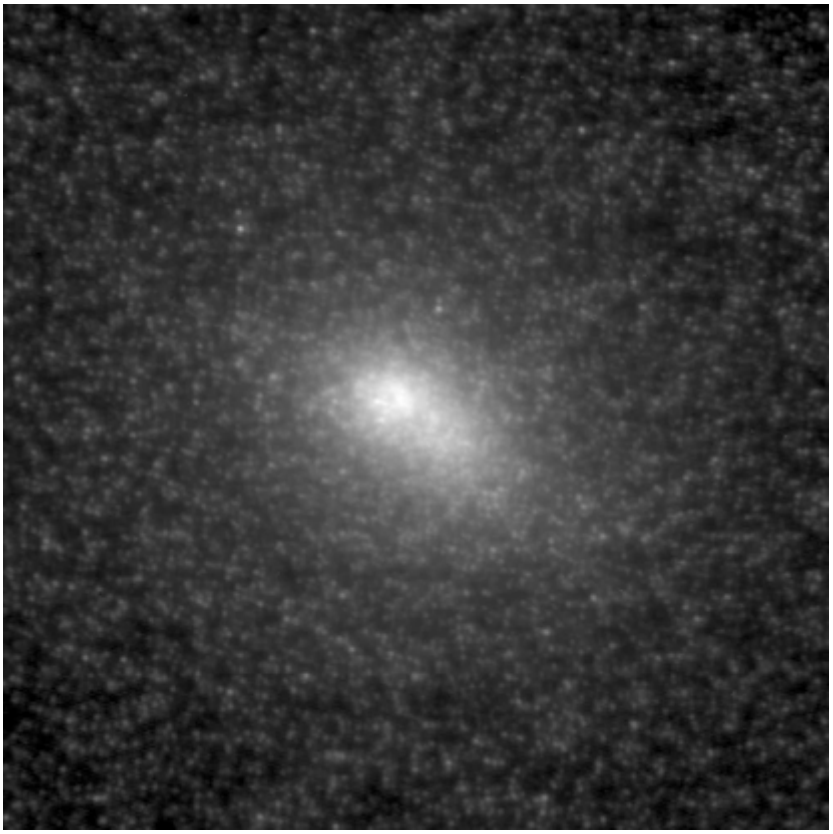

Fig. 10.— A 10″ × 10″ image of the core of the Andromeda galaxy imaged at K' (2.1 μm). A compact cluster 55″ away was used as the tip-tilt reference. The dynamical center of the galaxy, the likely location of a supermassive black hole, is located ~1″ to the lower right of the highest density region. Individual giant stars are clearly resolved throughout the image.

5.2.2. Shared-Risk Science Programs

A restricted number of LGS AO shared-risk science nights with NIRC2 (12) were awarded by the Keck time allocation committees in semester 2005A (February–August), while development continued on the LGS system. As of 2005 October, six refereed papers had been accepted for publication (Gal-Yam et al. 2005; Liu et al. 2005; see also papers cited in § 5.2.1).

5.3. LGS Science Observing Efficiency

The observing time overheads associated with LGS AO are summarized in Table 1. The AO/telescope/instrument handshake during dithers takes 7 s when the LGS is fixed with respect to the center of the science camera, and 20 s when the LGS is moved in order to be

fixed with respect to the science target. NIRC2 overheads remain the same. The average science integration time for two science nights in 2005 March, with three different observers, was 44% of the observing hours.

TABLE 1
LGS AO Observing Overheads

Action	Time
AO setup and laser acquisition (from 12° twilight)	30 minutes
Acquisition of new target (TT ref. $R < 15.5$)	5 minutes
Acquisition of new target (TT ref. $15.5 < R < 19.0$)	10 minutes
Dither with laser move	20 s
Dither without laser move	7 s
Recovery from aircraft or LTCS shuttering of the laser	2 minutes

Note.—These numbers reflect performance as of 2005 July.

The percentage of clear time lost to LGS AO system faults over 12 science nights in 2005 March through July was 12% overall. The time lost was <5% on half of these nights. On two nights, problems with the laser and laser pointing systems, respectively, which are counted as time lost to LGS AO, did not permit laser propagation. On these two nights, we switched to backup NGS AO science programs for half the night.

The average time lost to LTCS collisions during these 12 nights was 17 minutes. We are working with other observatories to minimize the number of these collisions by better understanding the actual impact on their observations. In addition, the Space Control Center has occasionally (once per ~15 nights) required that the laser not be propagated for up to 2 hr, due to a space event, such as a satellite launch.

5.4. Keck LGS Science Capability

The performance of the Keck II LGS AO system is reported in van Dam et al. (2006). The typical achieved on-axis K'-band Strehl ratio varies from 0.35 for NGS stars brighter than R = 10, to 0.27 for R = 16, to 0.1 for R = 19. The performance characterization is an ongoing project that is being documented on the Keck Observatory Laser Guide Star Adaptive Optics observation support Web page (see footnote 3).

During semester 2004B, we demonstrated the following observing modes:

1. Science target <70″ from the tip-tilt (NGS) reference (pupil angle restrictions occur for >55″).

2. NGS reference R<19 in vertical angle (fixed pupil) mode (requires on-axis NGS).

3. NGS reference R<18 in position angle (fixed field) mode, if pupil rotation <2° minute^{-1}.

4. Dithering over up to a 40″ × 40″ square (no faster than every 2 minutes).

5. Observations that require <20 mas positioning accuracy on the science instrument.

6. Observations that require differential atmospheric refraction tracking of the science target (e.g., spectroscopy).

Our user community has been very enthusiastic about the science capability of LGS AO, and increased availability has been strongly encouraged. The number of LGS AO science nights continues to be restricted in semester 2005B (August–January); however, the number of scheduled science nights has been significantly increased to 30, including eight nights with the newly commissioned OSIRIS science instrument. LGS AO development will be quite limited during 2005B to better focus on LGS AO operations, including improved observing automation, better management and maintenance of the laser and AO systems, more training for the observing support group, and completion of the LGS AO performance characterization effort.

6. CONCLUSION

We have described the approach taken in the implementation of a laser guide star system on the Keck II system, as well as the early scientific capabilities. An impressive amount of science has already been achieved with the AO facilities described in this paper, and the future for high angular resolution astronomy at the W. M. Keck Observatory looks extremely promising.

This future includes further improvements to the Keck II LGS AO system, upgrades to the real-time wave-front processor system and wave-front sensor cameras, the implementation of a commercial solid-state laser on the Keck I Telescope, along with laser projection from behind the secondary mirror, and potentially a next-generation LGS AO system.

Financial support for the development and fabrication of the Keck II LGS AO system was generously provided by the W. M. Keck Foundation. This material is based on work supported in part by the National Science Foundation Science and Technology Center for Adaptive Optics, managed by the University of California at Santa Cruz under agreement AST 98-76783, and based on work supported in part under the auspices of the US Department of Energy, National Nuclear Security Administration, by the University of California, Lawrence Livermore National Laboratory, under contract W-7405-Eng-48. Any opinions, findings, and conclusions or recommendations expressed in this material are those of the authors and do not necessarily reflect the views of the National Science Foundation or the US Department of Energy.

The author list reflects those people directly involved in the implementation of the LGS AO system. Many individuals have contributed to the development and implementation of the Keck AO systems and laser over the years, including S. Acton, J. An, K. Avicola, J. Bell, J. Brase, F. Chaffee, J. Chock, L. Chock, R. Cohen, A. Conrad, G. Erbert, H. Friedman, J. Gathright, D. Gavel, A. Gleckler, P. Goude, T. Gregory, M. Hess, K. Ho, H. Jones, K. Kinoshita, T. Kuklo, O. Lai, W. Lupton, I. Lynn, B. Macintosh, J. Maute, C. Melcher, D. McBride, D. Medeiros, R. Mouser, C. Nance, C. Neyman, S. Olivier, T. Saloga, C. Shelton, M. Sirota, R. Sumner, K. Sweeney, K. Waltjen, J. Watson, T. Williams, N. Wong, and the entire support staff of the W. M. Keck Observatory. We would also like to express our appreciation to past and present members of our review committees and AO working groups: E. Becklin, M. Brown, G. Chanan, R. Dekany, P. Everett, R. Fugate, A. Ghez, B. Kibrick, S. Kulkarni, J. Larkin, M. Liu, T. Mast, K. Matthews, J. Nelson, D. Sandler, and M. Troy.

The data presented herein were obtained at the W. M. Keck Observatory, which is operated as a scientific partnership among the California Institute of Technology, the University of California, and the National Aeronautics and Space Administration. The Observatory was made possible by the generous financial support of the W. M. Keck Foundation. The authors wish to recognize and acknowledge the significant cultural role and reverence that the summit of Mauna Kea has always had within the Hawaiian community. We are most fortunate to have the opportunity to conduct observations from this mountain.

Footnotes

4 W. M. Keck Observatory laser guide star adaptive optics observation support Web page, http://www2.keck.hawaii.edu/optics/lgsao.

5 W. M. Keck Observatory astronomical science with adaptive optics bibliography, http://www2.keck.hawaii.edu/library/biblios/aokeck.php.

References

↑ Bouchez A. H. *et al* 2004 *Proc. SPIE* **5490** 321
Crossref

↑ Brown M. E. *et al* 2005 *ApJ* **632** L45
IOPscience (http://iopscience.iop.org/1538-4357/632/1/L45)

↑ Colavita M. M., Wizinowich P. L. and Akeson R. L. 2004 *Proc. SPIE* **5491** 454
Crossref

↑ Foy R. and Labeyrie A. 1985 *A&A* **152** L29

↑ Friedman H. W. *et al* 1998 *Proc. SPIE* **3353** 260
Crossref

↑ Gal-Yam A. *et al* 2005 *ApJ* **630** L29
IOPscience (http://iopscience.iop.org/1538-4357/630/1/L29)

↑ Ghez A. M. *et al* 2005 *ApJ* **635** 1087
IOPscience (http://iopscience.iop.org/0004-637X/635/2/1087)

↑ Graves J. E., Roddier F., Northcott M., Anuskiewicz J. and Monnet G. 1994 *Proc. SPIE* **2201** 502
Crossref

↑ Hackenberg W. *et al* 2000 *A&A* **363** 41

↑ Hayano Y. *et al* 2003 *PASP* **115** 1419
IOPscience (http://iopscience.iop.org/1538-3873/115/814/1419)

↑ Larkin J. *et al* 2003 *Proc. SPIE* **4841** 1600
Crossref

2.11 Continuously Tunable Picosecond Dye Laser

Continuously Tunable Picosecond-Pulse Organic-Dye Laser*

B. H. SOFFER† AND J. W. LINN‡

Union Carbide Corporation, Electronics Division, Korad Department, Santa Monica, California 90406

(Received 24 June 1968; in final form 19 August 1968)

Picosecond-pulse outputs, tunable over a broad spectral range, have been demonstrated in an organic-dye laser. Evidence is presented that no more than a small fraction of the available bandwidth cooperates in mode locking to produce individual short pulses.

Mode locking of organic-dye lasers has been reported recently by several groups[1–3] using mode-locked lasers as pumping sources. Most recently, self-mode locking of a flash-lamp-pumped dye laser has been described.[4] These studies reported the oscilloscopic observation, with subnanosecond resolution, of trains of pulses of considerable modulation, with periods of the round-trip cavity times. The appearance of these possibly instrmentally broadened pulses with proper temporal periodicity is a necessary condition for the existence of some degree of mode locking. We report here the observation of 1×10^{-11} sec pulses generated by a laser-pumped dye laser. Furthermore, without degrading the pulsewidth, continuously tunable outputs of 6 cm^{-1} bandwidth have been demonstrated.

A mode-locked neodymium glass laser was constructed for use as a pumping source for the organic-dye laser. All intracavity reflective elements were set at the Brewster angle and mode locking was effected by the use of a bleachable absorber near the 100% reflector in a cell positioned[5] to minimize the intensity of satellite spikes on the main pulsetrain. The pulse was structured in groups of 10 or 11 individual pulses separated by 1×10^{-10} sec, an interval determined by the internal round-trip time in the cavity output reflector. The surfaces of this glass reflector were wedged at 2′ and one surface was coated with a 30% dielectric reflector creating a low-Q resonator. These groups of pulses themselves were separated by 3×10^{-9} sec, $2L/C$ of the cavity with typically 10–15 sets of pulses between the half-power points. Picosecond pulses were detected by the two-photon excitation of fluorescence technique.[6] A solution of Rhodamine 6G in ethyl alcohol was employed as the fluorescent medium. The second harmonic of this laser generated by an ADP crystal revealed the same pattern of pulses with the same temporal duration of $4\pm1\times10^{-12}$ sec. A solution of Esculin in ethyl alcohol was employed in this case as the two-photon fluorescent medium. The spectral bandwidth of the second-harmonic output was 150 cm^{-1}.

These second-harmonic pulses were used to transversely pump a Rhodamine 6G dye cavity. An ethanolic solution of the dye with decadic absorption coefficient equal to 10 at 530 mμ was contained in a cell constructed with internal and external window surfaces disposed at their respective Brewster angles. The internal length of the cell was 1.15 cm. Laser action in unwanted directions was suppressed by degrading all optical surfaces excepting the windows. Wedged dielectric coated mirrors of ~99% reflectivity and of 60%–90% output reflectivity were employed.

When the dye-laser cavity optical length L_l was made equal to (or to a small submultiple of) the pump cavity optical length L_p and the Rhodamine laser dye cell put at the end of the cavity, trains of fully modulated pulses of periods equal to (or to small submultiples of) the pump pulse were observed with instrumental temporal half-width of 7×10^{-10} sec using a planar photodiode and traveling wave oscilloscope. With $L_p=L_l$ and the laser cell in intermediate harmonic positions L/n, $n=3$, 4; two pulses separated by $2L/nc$ occurred for each pumping pulse with one predominantly intense, as may be expected if one considers that pulses traveling in opposite directions in the cavity reach the dye cell together only once per pump pulse. With the cell centered and $L_l=mL_p/n$; $m/n=2$, 1, $\frac{2}{3}$, $\frac{1}{2}$; $2n/m$ pulses are seen on the traveling wave oscilloscope for each pumping pulse, spaced at 3, $\frac{3}{2}$, 1, and $\frac{3}{4}$ nsec, respectively. These results are an extension of findings reported earlier.[2,3] When the pulse interval approaches the pulse resolution time, the overlap of the instrumentally broadened pulses reduces the apparent modulation drastically. When two or more pulses per pump pulse occur, the first two are of approximately equal intensity and any remaining ones show rapidly diminishing intensity, but with large statistical variations in decay rates on successive pictures. The fluorescent lifetime of Rhodamine 6G has been recently redetermined as 5.5×10^{-9} sec for an approximately equal concentration solution.[7] This time is greater than any of the periods described above, a condition which would diminish the effectiveness of this dye were it used as a passively bleachable absorber to engender mode locking with the cavity dimensions and configurations described above.

* This research is part of Project Defender under the joint sponsorship of the Advanced Research Projects Agency, The Office of Naval Research and the Department of Defense.

† Present address: Hughes Research Laboratories, Malibu, Calif.

‡ Present address: Image Optics, Inc., Santa Monica, Calif.

[1] M. Bass and J. I. Steinfeld, J. Quantum Electron. **QE4**, 53 (1968).

[2] W. H. Glenn, M. J. Brienza, and A. J. DeMaria, Appl. Phys. Letters **12**, 54 (1968).

[3] B. H. Soffer, Quarterly Rept., 10 Jan. 1968. Contr. Nonr-5150(00) ARPA Order No. 306.

[4] W. Schmidt and F. P. Schäfer, Phys. Letters **26A**, 558 (1968).

[5] R. Harrach and G. Kachen, J. Appl. Phys. **39**, 2482 (1968).

[6] J. A. Giordmaine, P. M. Rentzepis, S. L. Shapiro, and K. W. Wecht, Appl. Phys. Letters **11**, 216 (1967).

[7] A. E. Mack, J. Appl. Phys. **39**, 2483 (1968).

However, this is a driven system with periodic gain modulation. The superradiant lifetime over the pumping intensity range employed was found to be greater than 1×10^{-9} and less than 3×10^{-9} sec by removing the cavity reflectors and observing the ability of the emitted radiation to follow stimulation of diminishing periodicity. The effective cavity lifetime including the driven dye-laser cell was inferred from the multipulse decay rates to be between 1 and 2 nsec.

The picosecond pulse structure of the dye laser was observed using the alcoholic solution of Esculin. Multiple exposures were often required and so for convenience the two-photon fluorescence cells were sometimes positioned in the cavity, a procedure empirically justified by the finding of no significant change in the observed pulse shapes. More dispersive, scattering, and generally nonlinearly behaving solvents than ethanol might be expected to cause complications. Several of the cavity configurations mentioned above were tried all yielding similar picosecond pulses patterns. The additional expediency of increasing the f No. of the camera lens with inexpensive positive portrait lenses allowed the use of less sensitive but higher gamma emulsions (Polaroid type 52, $\gamma\sim3.5$ or type 146-L, $\gamma\sim2.5$) to photograph the two-photon-excited fluorescence. This is an aid in densitometrically determining the contrast ratio (see below), as the fractional error in contrast ratio, for an error in optical density, is inversely proportional to gamma.

The structure of the picosecond pulses closely followed that observed for the pump, except that the pulsewidth was $1.1\pm0.1\times10^{-11}$ sec. The contrast ratio was determined to be 2 ± 0.2, and the contrast ratio of the pump pulses was found to be 1.8 ± 0.2. Several approaches have been taken to attempt to realize more of the full mode-locking potential of the ~150 cm^{-1} dye laser bandwidth which might yield pulses as short as $\sim2\times10^{-13}$ sec in duration. However, no significant changes in pulsewidths were noted when the spatial width of the pumping pulse was narrowed from 12 to 1 mm by focusing with a cylindrical lens in order to bound the 10^{-11} sec pulse length, when fine variations were made in the position of the pulse in the dye cell and the position of the cell itself, or when operating the dye laser from 10 to as much as 20 times above threshold. Higher output mirror reflectivities produced only trivially shorter pulses within the estimated deviation.

One condition that might contribute to the pulsewidth is a frequency sweeping of the laser output, a circumstance reported for certain cyanine dye lasers[1,8] It should also be noted that because of the pulse structure of each laser burst in these experiments, each of the picosecond pulses displayed in the two-photon fluorescence technique is actually an average over $>10^2$ discreet pulses. Each pulse may be narrower than the average but broadened by aperiodicity within each 10^{-9} sec group of pulses or from one such 10^{-9} sec pulse to the next. Furthermore, as has recently been discussed,[9,10] two-photon fluorescence pictures of picosecond pulses with contrast ratios of less than three, the maximum value which can be obtained as for example in the case of fully mode-locked operation, are fraught with uncertainties about the actual nature of the pulses. Contrast ratios of two which are observed here might indicate a free running oscillation[10] or random (initial condition) mode-locked laser.[9] It should further be noted that all experimental problems as, for example, scattering and imperfect overlap of the beams, would tend to reduce the observed contrast ratio. Because of this uncertainty we can quote only the bounds of the average peak power between a maximum and a minimum had there been no picosecond pulse content: for the pump $8\times10^6<P(\text{watts})<10^8$; for the dye laser $2\times10^6<P(\text{watts})<2\times10^7$ using an output mirror reflectivity of 60%. A smaller number of picosecond pulses might be expected to yield higher powers. The full beam angle at half-power density was measured as 2.0 mrad by a self-calibrating technique[11] which obviates the problem of film reciprocity.

Efficiently confining the spectral output of the dye laser to 6 cm^{-1}, by replacing one of the cavity mirrors by a diffraction grating as described in an earlier publication,[12] we have demonstrated a continuously tunable source of $1.1\pm0.1\times10^{-11}$ sec pulses over a half-power tuning range of 600 cm^{-1}. Narrowing the spectral output much beyond this would, of course, broaden the pulsewidths. The pulse pattern again resembled the pumping pulse structure and had a measured contrast ratio of 2 ± 0.2. The Rhodamine cell was centered in the cavity with $L_l=L_p$. Using a grating of 2160 lines/mm of approximately constant first-order reflectivity of 58% in the range of interest in the Littrow position and a 100% reflector, the energy output in the zeroth order at the peak of the tuning curve was greater than 50% of that obtained with the 60% dielectric reflector replacing the grating. The full beam angle at half-power density was found to be 4.8 mrad.

It should be noted that pulse duration with narrow spectral output is identical to that obtained with no grating when the full 150 cm^{-1} bandwidth was generated. This indicates that no more than 6 cm^{-1} of the available bandwidth cooperated in mode locking to produce any one short pulse.

The technique described in this paper, providing tunable short pulses, is expected to work well with many families of dyes, both in liquid and plastic[12] hosts covering the entire range from the near ultraviolet to the near infrared. The flash-lamp-pumped self-mode-locked dye laser[4] would also be amenable to this technique. Single tunable picosecond pulses or pulses with other intervals should also be obtainable.

[8] G. I. Farmer, B. G. Huth, L. M. Taylor, and M. R. Kagan, Appl. Phys. Letters 12, 136 (1968).

[9] M. A. Duguay and S. T. Shapiro, *1968 International Quantum Electronics Conference*, Miami, Florida, Paper 4D-4.

[10] H. P. Weber and R. Dandliker, *1968 International Quantum Electronics Conference*, Miami, Florida, Paper N4.

[11] I. M. Winer, Appl. Opt. 5, 1437 (1966).

[12] B. H. Soffer and B. B. McFarland, Appl. Phys. Letters 10, 266 (1967).

3 Citations

3.1 Brackman, LambdaChrome

Brackman, Ulrick, Lambdachrome Laser Dyes, Lambda Physik 3, 2000

3.2 Budker, Optical Magnetometry

Budker, Dmitry, and Romalis, Michael. Optical Magnetometry. Nature Physics 3, 2007.

3.3 Fan, Improving LGS through Polarization Switching

Fan, Tingwei, Tianhua Zhou, and Yan Feng. "Improving sodium laser guide star brightness by polarization switching." Scientific reports 6 (2016).

3.4 Fugate, Measuring Wavefront Distortion

Fugate, Robert Q., and D. L. Fried. "Measurement of atmospheric wavefront distortion using scattered light from a laser guide-star." Nature 353.6340 (1991): 144.

3.5 Gale, Kilohertz Picosecond Dye Laser

Gale, G. M., B. Pedersen, and P. Schanne. "Kilohertz picosecond distributed-feedback dye laser system." Optics Communications 76.2 (1990): 138-142.

3.6 Kane, Pulsed Laser Architecture

Kane, Thomas J., Paul D. Hillman, and Craig A. Denman. "Pulsed laser architecture for enhancing backscatter from sodium." SPIE Astronomical Telescopes+ Instrumentation. International Society for Optics and Photonics, 2014.

3.7 Kibblewhite, Physics of LGS

Kibblewhite, Edward. "The physics of the sodium laser guide star: Predicting and enhancing the photon returns." In Advanced Maui Optical and Space Surveilance Technologies Conference. 2009.

3.8 Rampy, Toward Optimization of pulsed LGS

Rampy, Rachel, Donald Gavel, Simon M. Rochester, and Ronald Holzlhner. "Toward optimization of pulsed sodium laser guide stars."JOSA B32, no. 12 (2015): 2425-2434.

3.9 Holzlohner, Optimization of CW LGS

Holzlhner, R., et al. "Optimization of cw sodium laser guide star efficiency." Astronomy & Astrophysics 510 (2010): A20.

3.10 Sohl (AJP), Modular Reconfigurable Pulsed Dye Laser

Sohl, John E., and Stephen G. Payton. "A modular, reconfigurable-cavity, pulsed dye laser for the advanced undergraduate laboratory." American Journal of Physics 65.7 (1997): 640-652.

3.11 Watanable, Advancement in Adaptive Optics

Watanabe, Makoto, et al. "Proceedings of SPIE-The International Society for Optical Engineering." Advancements in Adaptive Optics. 2004.

3.12 Wizinowich, W.M. Keck Observatory System

Wizinowich, Peter L., David Le Mignant, Antonin H. Bouchez, Randy D. Campbell, Jason CY Chin, Adam R. Contos, Marcos A. van Dam et al. "The WM Keck Observatory laser guide star adaptive optics system: overview."Publications of the Astronomical Society of the Pacific118, no. 840 (2006): 297.